UNIVERSITY OF SOUTHERN QUEENSLAND

Faculty of Health, Engineering and Sciences

The Applications of Near Infra-Red Fibre Bragg Grating Sensors for Wave Propagation Based Structural Health Monitoring of Thin Laminated Composite Plates

A thesis submitted by

Mohd Hafizi Bin Zohari

in fulfilment of the requirements of

Doctor of Philosophy

2014

Abstract

This thesis contributes to the research and development towards achieving better structural health monitoring (SHM) system for composite structures. Composites are widely used in critical engineering applications due to the advantage of higher specific strength and stiffness compared to other conventional materials. However, composite laminates have a very high probability of unexpected damage development during service. This study uses fiber Bragg grating (FBG) sensor to create a practical and robust SHM tool based on monitoring the acoustic emission, in order to provide continuous information of the structure's condition. The remarkable capability of using the FBG sensors for dynamic sensing has been demonstrated, in particular for the wave propagation based SHM. Combined with FBG sensor technologies, the wave propagation based SHM such as acoustic emission (AE), ultrasonic evaluation and acousto-ultrasonics becomes more exciting. The FBG sensor has the ability of acquiring both static and dynamic strains with a single sensor. Besides, the physical size of FBG sensor provides greater access to embed them in composite structures without significantly affecting its structural properties. This study also emphasizes some drawbacks in the use of piezoelectric sensors in the wave propagation based SHM of composite structures, specifically in the AE applications. In most optical fiber based SHM applications to date, people have used only FBG sensors with wavelength 1550 nm. The FBG sensors with this wavelength are commonly used in industries such as telecommunications and health. However, there is an option of using near infra-red (NIR) FBG range which is comparably cheap in terms of total system design, yet offers the same performance of a conventional 1550 nm range FBGs. This research work presents the NIR FBG dynamic sensing system, as a wave propagation-based SHM system for monitoring the damages in thin glass fiber reinforced composite plates. The NIR-FBG sensor system has been validated successfully, in particular for thin composite plate's applications. The sensor system has shown its unique capability whereby it can be applied in the area which cannot be accessed by standard piezoelectric based system. The developed NIR FBG sensor system has shown its competitiveness and ability to replace the piezoelectric sensors in the 'wave propagation based SHM' of laminated composite plates.

List of Publications Arising from this Study

The following publications were produced during the period of candidature:

Hafizi, Z. M., Epaarachchi, J., Nizwan, C. K. E., and Lau, K. T., "Non-velocity Based Analysis of Passive Ultrasonic Signal for Source Location Detection in Composite Plates: A Pilot Study", *IOP Conf. Series: Materials Science and Engineering* Vol. 36, 012008, 2012.

Hafizi, Z. M., Epaarachchi, J. and Lau, K. T., "An Investigation of Effective Detection Length of a Localized Micro-failure in a Laminated Thin Composite Plate Using FBG Sensor Integrated AE System", *8th Asian-Australasian Conference on Composite Materials (ACCM-8)*, Kuala Lumpur, Malaysia, 6 8 November 2012.

Hafizi, Z. M., Epaarachchi, J. and Lau, K. T., "Modal Acoustic Emission Investigation for Progressive Failure Monitoring in Thin Composite Plates under Tensile Test", *Key Engineering Materials*, vol 558, 2013, pp 65-75.

Hafizi, Z. M., Epaarachchi, J. and Lau, K. T., "Wave Propagation Scattering due to Defect on Thin Composite Plates", *Journal of Mechanical Engineering and Sciences (JMES)*, vol 5, 2013, pp 602-610.

Hafizi, Z. M., Kahandawa, G. C., Epaarachchi, J., Lau, K. T., Canning, J., and Cook, K., "NIR Fibre Bragg Grating as Dynamic Sensor: An Application of 1D Digital Wavelet Analysis for Signal Denoising", *The 4th International Conference on Smart Materials and Nanotechnology in Engineering (SMN 2013)*, Gold Coast, Australia, 10 12 July 2013.

Hafizi, Z. M., Kahandawa, G. C., Epaarachchi, J., Lau, K. T., Canning, J., and Cook, K., "An Application of Near Infra-Red Fibre Bragg Grating as Dy-

namic Sensor in SHM of Thin Composite Laminates", *International Workshop On Structural Health Monitoring (IWSHM2013)*, Stanford University, Stanford, CA USA, 10 - 12 September 2013.

Kahandawa, G. C., Hafizi, Z. M., Epaarachchi, J. and Lau, K. T., "Detecting delamination in a composite structure using an Embedded FBG AE hybrid System", *7th Australasian Congress on Applied Mechanics (ACAM 7)*, Adelaide, Australia, 9-12 December 2012.

Hafizi, Z. M., Epaarachchi, J. and Lau, K. T., "The Investigation of Acoustic Emission Signal Attenuation for Progressive Failure Monitoring in Fibreglass Reinforced Composite Laminates", *International Journal of Automotive and Mechanical Engineering (IJAME)*, vol 8, 2013, pp 1464-1478.

Hafizi, Z. M., Epaarachchi, J. and Lau, K. T., "NIR-FBG Based Sensor System With Single FBG Sensor for Dynamic Measurement of Thin Laminated Composite Plates", *Sensors and Actuators A: Physical*, draft submitted.

Hafizi, Z. M., Epaarachchi, J. and Lau, K. T., "Impact Location Determination on Thin Laminated Composite Plates Using the NIR-FBG Sensor System", *NDT & E International*, draft submitted.

Certification of Dissertation

I certify that the ideas, designs and experimental work, results, analyses and conclusions set out in this dissertation are entirely my own effort, except where otherwise indicated and acknowledged. The work is original and has not been previously submitted for assessment in any other course or institution, except where specifically stated.

Mohd Hafizi Bin Zohari

0061015567

_____

Signature of Candidate

_____

Date

ENDORSEMENT

Supervisory Team

_____	_____
Dr. Jayantha Ananda Epaarachchi Signature of Principle Supervisor	Prof. Dr. Alan Kin-tak Lau Signature of Associated Supervisor
_____	_____
Date	Date

Acknowledgments

I would like to express my deepest appreciation to all those who provided me the possibility to complete this Ph.D. thesis. A special gratitude I give to my supervisor, Dr Jayantha Ananda Epaarachchi and co-supervisor, Professor Dr Alan Lau, whose contribution in stimulating suggestions and encouragement, helped me to coordinate my project especially in writing this thesis.

Furthermore, I would also like to acknowledge with much appreciation the crucial role of the staff of Faculty of Health, Engineering and Science (formerly known as Faculty of Engineering and Surveying) and the Centre of Excellence in Engineered Fibre Composites (CEEFC), who gave the permission to use all required equipment and the necessary materials to complete the project. Special thanks go to my teammates in the Structural Health Monitoring group, Dr Gayan Kahandawa, Eris Eliandy and Joshua Peauril, who help me to solve many problems and offer suggestions regarding this project. I also like to thank the University Malaysia of Pahang together with the Ministry of Higher Education, Malaysia for scholarship support.

Last but not least, many thanks go to my family, especially my lovely parent, Tn. Hj. Zohari Muda and Pn. Hjh. Azizon Abdullah who always pray for my success. Not to forget, the Malaysian Community of Toowoomba, who have given a lot of support and help along my stay in Toowoomba. And, I would like to thank my loved ones, Mrs Nor Irmanuhi Abdul Wahab, who has supported me throughout the entire process, both by keeping me harmonious and helping me putting pieces together. Not to forget my kids, princess Aisyah and prince Faris, who always waiting for me in front of the door each time I'm back home. I will be grateful forever for your love.

Mohd Hafizi Bin Zohari

UNIVERSITY OF SOUTHERN QUEENSLAND
February 2014

Contents

List of Figures

List of Tables

Notation

σ	Stress
ε	Strain
σ_{ij}	2×2 stress matrix
E	Young's modulus
C	Stiffness tensor
ν	Poisson's ratio
Q	Stress-reduced stiffness
τ	Shear stress
γ	Shear strain
G	Shear modulus
d	Plate thickness in Lamb's wave frequency equations
ω	Angular frequency
k	Wave number
c_p	Phase velocity
c_g	Group velocity
c_L	Longitudinal wave velocity
c_T	Transverse wave velocity
ρ	Density
u, v, w	Displacement components of a point on the midplane
ψ_i	rotations of the normal to the midplane about the i-axis. $i = x, y$
h	Thickness
N	Force on a plate

M	Moment on a plate
ϵ	Strains vector
K	Plate curvatures
A_{ij}	Extensional stiffness matrix
B_{ij}	Coupling stiffness matrix
D_{ij}	Bending stiffness matrix
r	Layer's of laminates
I_i	Moment of inertia
c_e	Extensional velocity
c_f	Flexural velocity
c_s	Shear wave velocity
$\kappa_{i,j}$	Shear correction factors
$f(t)$	Signal function in time domain
f, f_i	Frequency
t	Time
$\widehat{\tau}$	Time shift (in Continuous Wavelet Transform)
$F(\omega, \widehat{\tau})$	Magnitude of Short Time Fourier Transform (STFT) in the function of ω and $\widehat{\tau}$
WT_f	Continuous Wavelet Transform (CWT) of a function
$\psi(t)$	Basic wavelet or mother wavelet
s	Scale
ω_0	Wavelet centre frequency
DWT_f	Discrete Wavelet Transform of a function
$b_i(f)$	Arrival time of a specific frequency, f
L, l_i	Length
A	Sound wave attenuation
α	Attenuation coefficient
$\widehat{\beta}$	Decay constant
$\widehat{E}$	Photon's energy

$\widehat{h}$	Planck's constant
λ	Wavelength
c	Speed of light in vacuum
$\widehat{E}_c$	Energy of the conduction band
$\widehat{E}_v$	Energy of the valence band
I	Current
P	Power
q or e	Electron charge
η	Quantum efficiency
T	Temperature
R	Responsivity
n	Refractive index
Λ	Grating period
$\widehat{k}$	Order of the grating
$\widehat{\alpha}$	Thermal expansion
ξ	Thermo-optic coefficient
p_e	Effective photo-elastic constant
p_n	Poisson probability distribution
N	Mean number of photoelectrons detected at $\triangle t$
SNR	Signal to noise ration
$\mathbf{k}$	Wavespace vector
nm	nanometer
Hz	Hertz
kHz	kilohertz
MHz	megahertz

Acronyms and Abbreviations

SHM	Structural Health Monitoring
NDE	Nondestructive Evaluation
FBG	Fiber Bragg Grating
AE	Acoustic Emission
ELE	Elastic Emission
MAE	Modal Acoustic Emission
MEMS	Microelectromechanical System
NIR	Near Infra Red
PZT	Piezoelectric Transducer
GFRP	Glass Fibre Reinforced Plastic
CFRP	Carbon Fibre Reinforced Plastic
NDT	Nondestructive Testing
FSDT	First-Order Shear Deformation Theory
CLPT	Classical Laminated Plate Theory
FFT	Fast Fourier Transform
STFT	Short Time Fourier Transform
CWT	Continuous Wavelet Transform
DWT	Discrete Wavelet Transform
FRP	Fiber Reinforced Polymer
PAC	Physical Acoustic Corporation
FTC	First Threshold Crossing

DAQ	Data Acquisition
RMS	Root Mean Square
LED	Light Emitting Diode
SLED	Superluminescence Light Emitting Diode
DFB	Distributed Feedback
DBR	Distributed Bragg Reflector
VCSEL	Vertical Cavity Surface Emitting Lasers
SML	Single-Mode Lasers
MML	Multi-Mode Lasers
FP	Fabry - Perot
PD	Photo Detector
PIN	p-type and n-type semiconductor layers
AVD	Avalanche Photodiodes
SNR	Signal to noise ratio
FBG-AE	An AE system with FBG sensor as the sensor head
NIR-FBG	FBG sensors in NIR range wavelength
FEA	Finite Element Analysis

Chapter 1

Introduction

1.1 Research background

Composite materials are some of the most interesting materials which pull engineering experts into a new era of designing advanced structures. The dramatic increase of its applications not only involves engineering structures, but also expands to the daily usage equipment such as electronic circuits, sports gear and also in medical devices. However, it is important to look at the development of composite-based structures' failure monitoring systems, especially when it involved in the critical applications such as aerospace (Mandalgiri 1999), infrastructures (Hollaway 2010, Einde et al. 2003) and wind turbines (Ciang et al. 2008, Brondsted et al. 2005). For that reason, Structural Health Monitoring (SHM) began to be incorporated seriously in composite studies.

There are a number of SHM systems that can be used for composite structures. However the main question to be asked, which is the best? The question may lead to the search for robust and practical systems; and possibly can lead to the development of smart structures!

1.1.1 Structural Health Monitoring (SHM)

SHM is an emerging research field with a number of applications particularly in the assessment of a critical structure's condition. SHM may be described as a revolution in structural integrity assessment techniques. The ultimate objective for SHM system is to provide as much information, at every minute, about the

current state of the structure. The state or condition of the structure must be the same as in the original design at all times to ensure optimal performance during service. It is a difficult job, given that the structure is always subject to aging and exposure to outside elements such as damages and accidents.

The major motivations that contribute to the continuing development of SHM technology are to improve the reliability and security of the structure as well as to reduce the long term maintenance costs. Consistently monitored structures will provide a high level of confidence to the end users. Furthermore, it is a very serious and important issue when touching on security matters.

SHM is relatively young, but it shows promising results especially with the integration of existing non-destructive evaluation (NDE) technology into SHM systems such as ultrasonic evaluation, Acoustic Emission methods and Fiber Bragg Gratings (FBG) sensors (Black 2008). In general, NDE tool is only a part of a complete SHM system. NDE technique can provide the diagnostic information of the current state of the structure. Meanwhile, SHM system involves the integration of sensors, data gathering, transmitting the data for analysis and processing of the information itself, which will direct to enable full management of the structure involved. In summary, Boller & Meyendorf (2008) stated that:

SHM is the integration of sensing and possibly also actuation devices to allow the loading and damaging conditions of structure to be recorded, analyzed, localized and predicted in a way that non-destructive testing becomes an integral part of the structure.

SHM for Composite Structures: Future Smart Structures

In composite structures, the damages are complex. They can develop and propagate slowly from inside the composite layers (e.g. matrix cracks, delamination and matrix-fibre debonding). As a result, it will affect the material properties such as material strength and stiffness. Hence, the assimilation of SHM systems in composite structures offer an ability to give continuous and real time information of its circumstances under critical loading applications.

The integration of SHM into composite structures will lead to the development of smart composite structures. Smart structures can be described as a structure that can adapt in any changing surroundings. In other words, smart structure can automatically respond; whether in the form of physical or chemical reaction, to ensure that it can survive in any situation without causing a major disaster to the components or the users.

Consider the changing environment which is always taking place in this century, such as climate change and the impact of natural disasters. The civil structures such as buildings and bridges need to utilize the benefit of smart structures. It also applied to other applications as well, such as turbine blades and aircraft wings. Both of them are usually exposed to changing extremes of fluid flow surround them, thus can cause enormous deformation that can affect performance, or, most frightening, cause a catastrophic.

1.1.2 Wave propagation based SHM

Most of composite structures are made of thin plates or shells. When it comes to the thin plate structures, SHM techniques based on the study of wave propagation are seem to be very popular. There has been an enormous amount of research work published in this area. However, the wave propagation based SHM for thin composite structures has a significant scope, because it involved various types of promising monitoring systems such as acoustic emission (AE), ultrasonic evaluation and acousto-ultrasonic. They share the same basic principle; that is investigating the structures' condition by means of wave propagation analysis method.

The acousto-ultrasonic area is fast growing at present and its concept, in general, is the same as the Lamb wave inspection (Wilcox 1998). Both techniques involve scanning the whole structure during inspection, which leads to extra time and also need higher level of interpretor. Meanwhile, the AE technique offers a very good ability in term of global monitoring of structures during in service. Furthermore, ultrasonic, acousto-ultrasonic and lamb waves inspection techniques belong to the active SHM while AE is passive SHM (see Section 1.1.3).

The frequency range for ultrasonic, acousto-ultrasonic and Lamb wave inspection is up to Megahertz (MHz). All of them are in a group of active monitoring and required actuator which actively supply the input signal wave propagation. The MHz range will assure that no other propagation that can interfere with the signals, thus provide reliable results. However, operating in very high frequency ranges may conflict with the severe wave attenuation in short distances, especially involving the high damping materials such as composites.

Meanwhile, the working frequency range for AE is around 1 kHz to 2 MHz; which include from the audible sound to the ultrasound range (Carlos 2003). AE method is highly dependent on the energy of the wave propagation from the source. AE signals that travel at high frequency (e.g. 200 kHz - 2 MHz), are susceptible to the

attenuation effect and cannot propagate over long distances. However, this range is common for the usage in metallic structures. Whereas, for the propagation at low frequency range of AE signal (e.g. below 10 kHz), it is susceptible to background noise, although they can spread to larger distances. Note that, the AE with 10 kHz or 20 kHz and below, is also known as low frequency elastic emission (ELE) (Schiavi et al. 2011, Lacidogna et al. 2010).

AE is one of the strongly identified NDE technique, which has been used for many decades. It fits uniquely to the idea of SHM due to its multiple phenomenological advantages (Muravin et al. 2010). In addition, AE also well known as a highly sensitive method for detection of various types of damage using a small number of sensors, thus very attractive for SHM (Wilcox et al. 2006). But, in composites, the challenge for a reliable AE results is still significant due to the anisotropic behavior of the materials. Fortunately, many studies were done to investigate the potential of AE method for SHM of composite structures to become more quantitative, leading to a more general result and not case specific (Scholey et al. 2010, Scholey et al. 2009), especially with the Modal Acoustic Emission (MAE). The details of MAE will be explained further in the next chapter.

There are no clear arguments for any techniques to be labelled as the best method in SHM. It depends on the specific needs of the monitoring system for the structures under examination, such as budget, size of the structures and inspection period. However, AE was chosen as the wave propagation based method to be used in this research work. It is based on some advantages such as a passive process (only associated with sensing process) and better in term of global monitoring.

1.1.3 Active and passive monitoring in the SHM system

SHM system can be passive or active (Balageas 2010). The good explanation of both modes of sensing can be shown in the Figures 1.1 and 1.2. In an active sensing mode, the actuator will produce a constant, pre-selected signal to the structure being monitored, and all responses will be detected by the sensor network. These responses will determine the condition of the material being monitored, such as the location and size of the damages, the damage's type and the changes in material properties. For damage monitoring in composite materials, ultrasonic testing is the most widely used for active monitoring system (Staszewski et al. 2009).

Meanwhile, in a passive monitoring mode, the sensor network will continuously

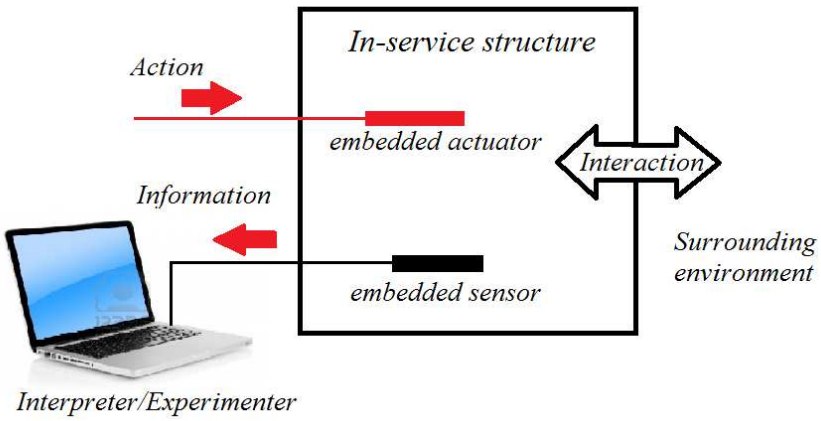

Figure 1.1: Active monitoring system (Balageas 2010).

'listen' to the signal that is produced by a variety of sources from the structure being monitored. For instance, signals from external impacts and propagating cracks. An example of a passive monitoring system which is popular and extensively used is the Acoustic Emission (AE) monitoring (Staszewski et al. 2009).

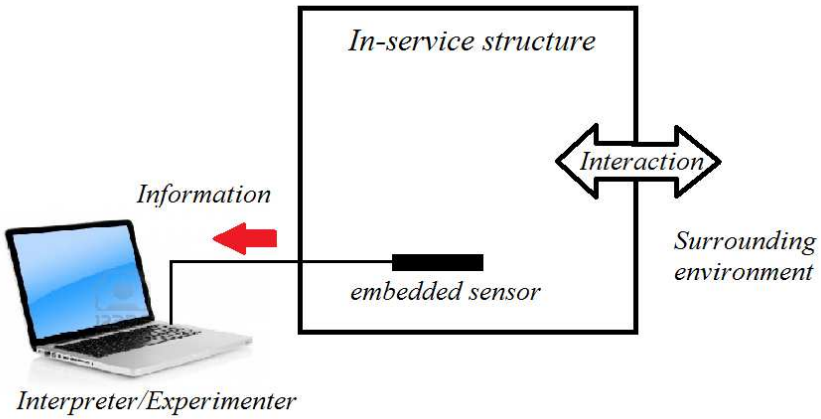

Figure 1.2: Passive monitoring system (Balageas 2010).

This Ph.D. work will emphasize on the passive technique as it only involves the process of 'receiving' the information from monitoring activities. Therefore, ensuring that the focus will be only the signal acquisition's part or in other words, the sensing process.

1.1.4 Issues on piezoelectric sensors for SHM of composite structures and the rise of FBG sensor technologies

In general, the SHM system requires three critical components, namely; a sensor network, integrated hardware and analysis software to continuously monitor the in-service structures (Beard et al. 2005). There are several types of sensors which are available for SHM, such as piezoelectric, fiber-optic, Microelectromechanical systems (MEMS) and traditional strain gauges. All these sensors are good, yet depending on their use in different structures under examination.

Among all these sensors, the piezoelectric sensors have been considered the best as they also can work as an actuator, hence making it possible for active and passive monitoring. Although piezoelectric sensors are excellent, they also have some significant drawbacks. For instance, the problem of the sensor attachment to the structure or sensor mounting, particularly in composite structures.

For any wave propagation-based SHM, it is very significant to have a good sensor system which has high efficiency in signal transfer, onto the sensors. At the transducer, the wave propagations on the examined structures will be captured before they are channeled to the data storage or post-processing part. If the signals obtained by the sensors are questionable due to an error in the acquisition process, consequently, the entire information provided by the SHM system also cannot be trusted.

It is best for a sensor or sensor system to be embedded in the structure at all times to enable the continuous monitoring. In other words, the sensor must be a part of the structure itself; in which case is quite difficult to do when using a piezoelectric sensor. Note that, embedding sensors into the composite laminates also can solve the sensor mounting problem which will be explained further in next chapters.

Although there is a variety of recent studies, which attempt to utilize the technology of embedded piezoelectric sensors (layered or 'fiber' type) for online fault detection in composite structures (Wu & Chang 2006, Brunner et al. 2004, Yan & Yam 2002, Giurgiutiu & Zagrai 2002), yet the sensor attachment (and their interconnections part) problem is still strongly debated. To produce piezoelectric sensors that can be implanted between composite layers, require good manufacturing technology and also high cost.

In the meantime, there are studies that attempt to prove that this technology does not affect the material properties as well as being the cause of the damage

propagation in composite structures, such as the research work done by (Paget & Levin 1999). Undoubtedly, embedding the piezoelectric sensors into composite structures is certainly not giving a negative impact if it is prepared properly and perfectly bonded to the composite matrix or laminates. However, problems occur when there is imperfection in the internal bonding between the sensors and the composites, such as those reported by (Wang & Zou 2013). In their numerical study, inter-facial imperfections gave a significant effect on the mechanical behavior of the specimens studied.

Some of the practical issues regarding the deficiencies of the piezoelectric sensors, particularly in SHM, has been discussed in a few case studies in chapter three. It is believed these drawbacks can be overcome in the future because more studies are still on going. However, these weaknesses of the piezoelectric sensors are one of the reasons for current researchers to choose other alternatives. For instance, the Fiber Bragg Grating (FBG) sensor for dynamic sensing. This optical type sensor has much more benefits, such as its non-conductive nature and low transmission loss. Moreover, for some applications such as in SHM of aerospace structures, the FBG sensors are one of the best (Kahandawa 2012). Figure 1.3 shows an example of piezoelectric layer and FBG sensor that used in composite structures.

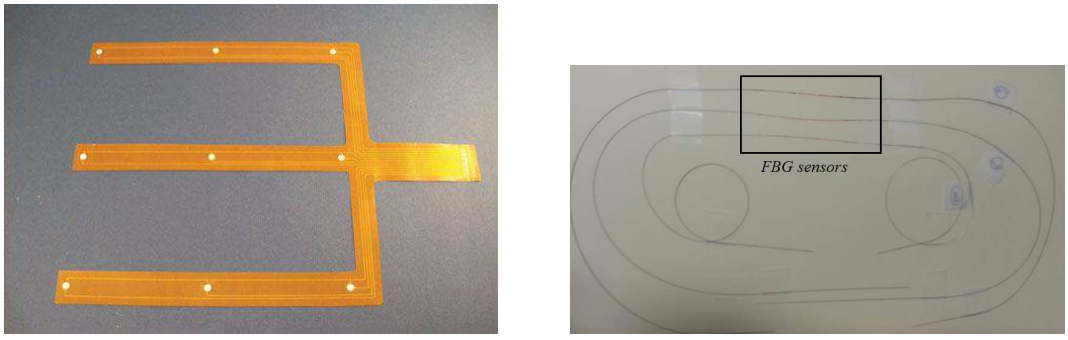

(a) SMART Layer, from Acellent Technologies.

(b) FBG sensors in SHM laboratory, USQ.

Figure 1.3: Example of piezoelectric layer (SMART) and FBG sensors for composite structures

FBG technology can be considered as one of the fastest growing topics and mostly discussed in the field of fiber optic sensors during late 20^{th} century (Rao 1999). Nowadays, they are becoming one of the interesting topics as studied by numerous SHM researchers (Chen & Shin 2010, Kahandawa et al. 2012, Kim 2004, Panopoulou et al. 2011, Wild & Hinckley 2010, Wild & Hinckley 2007, Zou et al. 2012). Although this fibre optic technology is established and interesting for static measurement, but there are some recent studies that attempt to use

this FBGs as a dynamic sensor (Majumder et al. 2008, Chen & Shin 2010).

Certainly, embedding fibre optic sensors in composite laminates is not a significant issue as the size of the optical fibre is relatively small compared to the reinforced fibers (Beukema 2012, Takeda et al. 2005). Not only that, it also has the benefit of having a closer look at the defects in between composite layers (Kahandawa et al. 2012). Besides, FBG sensor has advantage in term of capturing the frequency responses in wave propagation based SHM for composite structures. As it is embedded (or surface-glued), the sensors will acquire all the wave propagation's frequencies regardless of the out-plane or in-plane motion.

The excellent potential of the FBGs for the applications in dynamic measurement, lead to the focus of this study; the use of FBG sensors for AE (FBG-AE). Please note that, the applications of FBG sensors not only limited to be applied in the AE technique, yet it also can be used for the other wave propagation based SHM systems. As explained earlier, the FBG sensor offers the innovative solution to the problem faced by the transducer part (piezoelectric sensor) in the traditional SHM systems, particularly for monitoring of composite structures.

1.2 Research Concept and Objectives

One of the main objectives in this research project was the development of the Fiber Bragg Grating (FBG) sensor system for dynamic response measurement. This FBG-based systems then can be used for damage detection with any wave propagation based SHM, particularly in FBG-AE system. It should be noted that the AE technique was selected to use in this project as the practical example to apply the NIR-FBG dynamic sensor system in SHM applications. One of the innovations to be highlighted in this project is the use of FBG sensors in the near infra-red (NIR) range, $\sim$ 830 nm, as an alternative to the applications of the conventional 1550 nm FBG sensors. The use of NIR-FBG sensors will lead to the cheaper system compared with the expensive 1550 nm FBG sensors.

This project utilized the embedded and the surface-glued NIR-FBG sensor on the composite test panels, and the ability of this system for composite SHM will be extensively investigated and explored. Several tests regimes were performed to compare its performance with conventional piezoelectric transducer (PZT) in the AE applications, and also with the 1550 nm FBG dynamic sensing system. Figure 1.4 shows the general overview of research concept for this PhD work.

Towards achieving the above primary objective, the related aims associated with

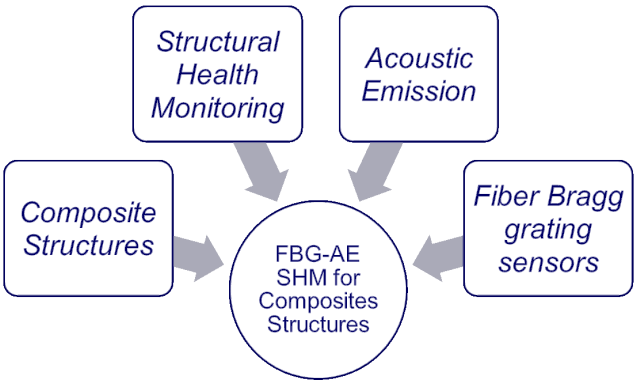

Figure 1.4: Research concept overview

it are identified as follows:

1. To investigate the use of AE in composite structures, especially regarding its applicability and robustness for SHM of composite structures.
2. To develop the FBG dynamic sensing utilizing the Near-Infra-Red FBG sensors.
3. To implement FBG-AE system in plate-like composite laminates for damage monitoring.

The outcome from this research was is, a developed NIR-FBG dynamic sensor system which is robust and practical for SHM purposes. As a boundary condition, this work will be limited only for a specific applications; linear source location mapping and failure characterization of matrix cracks. In this research, the main material used was the glass fibre/epoxy composites. It has well known material properties and well established analysis. This study focused only the mechanical aspect and response of the glass fibre/epoxy composites. Thus, other properties such as chemical and thermal aspects and responses were left for further research topics.

1.3 Overview of the Dissertation

This dissertation is organized as follows:

Chapter 1 outlines the background, research gap, significance and objectives of this study.

Chapter 2 describes the theory of acoustic wave propagation on thin composite plates. Furthermore, the advance time-frequency analysis, wavelet transform, will be explained. The overview of fibre reinforced composite materials are also discussed in this chapter.

Chapter 3 discussed the use of AE in composite thin laminates, and how the internal damages of composite laminates can be the source of AE wave propagation. A few case studies will be presented regarding several issues on the Modal Analysis of AE signals a.k.a Modal Acoustic Emission (MAE). The non-velocity based source mapping based on wave energy attenuation is also discussed as well as the effective distance issue of the propagating AE signals.

Chapter 4 discusses the development of the FBG dynamic sensing for the FBG-AE system. The use of Near-Infra-Red (NIR) FBGs for dynamic sensing will be introduced. Note that, the theory behind the development of this novel system is also presented as the NIR FBG dynamic sensing may require a different arrangement compared to commonly available FBG dynamic systems.

Chapter 5 demonstrates the validation of a newly developed system and some applications for small scale SHM.

Chapter 6 concludes the dissertation and suggests further work in the area of 'NIR FBG dynamic sensing' as the complete FBG-AE system.

Chapter 2

Acoustic Wave Propagation on Thin Laminated Composite Plates

2.1 Chapter overview

This chapter explains the acoustic wave propagation on thin composite plates. Prior to the basic information on the acoustic wave propagation being presented, the mechanics of fiber reinforced materials will be described in the first section. This is necessary due to the dependency of wave propagation in thin composite plates to the material properties and the fiber direction.

The study of acoustic wave propagation can be applied to the determination of internal damage characteristics of composite plates, as every single damage, will release 'burst' energy that can be the source for acoustic wave propagation. It is important to understand the behavior of wave propagation, that is, due to events such as impacts or internal damage of composite plates. This is to ensure the accuracy and reliability of the information which is contained in wave signals before it captured by the sensors.

Besides the propagation theory, the signal processing technique is also presented in this chapter. One of the most recent and advance time-frequency analysis, the wavelet transform, will be exploited further especially for its potential in making the wave-propagation-based SHM to be more attractive and reliable.

2.2 Fibre Reinforced Composite Materials

Composite materials are modern and advanced material which have a growing number of applications in this century. They offer the advantage of high strength and stiffness but with low density, thus resulting in weight reduction while maintaining the excellent performance of the materials.

By definition, a composite material consists of two or more materials which together produce desirable properties that cannot be achieved with any of the constituents alone (Reddy 2004). The ability to have a variety of 'ingredients' in the composite material, allows it to become more multi-functional. Despite the well-known advantage, which is high strength-to-weight ratio, this composite material can also be designed to be used as insulation, fire retardant, corrosion resistance, noise reduction and many more.

One of the constituents in composite materials is called matrix, which is a continuous phase and acts as the 'binding' materials. The matrix can be polymer, metal or ceramic. Each of these types of matrix will give different effects to the overall performance of the composite material. For instance, a polymer matrix has a low strength and stiffness and generally brittle, whereas, a metal matrix will usually provide high strength and stiffness, but high ductility (Campbell 2010).

Meanwhile, the other constituent is the reinforcement. This reinforcing phase provides most of the strength and stiffness values to a composite material. The reinforcement part can be divided into two types; continuous or discontinuous form. Each one will provide different advantages. For instance, composite materials with continuous reinforcement are relatively easy to be fabricated; and they are also evenly distributed in the matrix materials, thus giving higher strength and stiffness. On the other hand, the discontinuous type of reinforcement is relatively cheaper.

2.2.1 Equation of anisotropic elasticity

Composite materials are non-isotropic. The anisotropic behavior makes the materials more complex to be analyzed numerically or experimentally. Material properties of an anisotropic body will often depend upon the orientation of the applied forces and/or moments. The direction dependence of properties is a result of inter-atomic bonds, which are stronger in one direction than in other directions (Reddy 2004).

Note that this section will only review in brief, the generalized Hooke's Law particularly for the unidirectional GFRP symmetric laminates, loaded at angle 0^o or 90^o, which is in the scope of this research work. The environmental effect such as temperature and moisture, were not included into analysis as all the experiments were done in controlled surroundings. Several textbooks had described this topic very clearly such as Reddy (2004) and Abrate (1998).

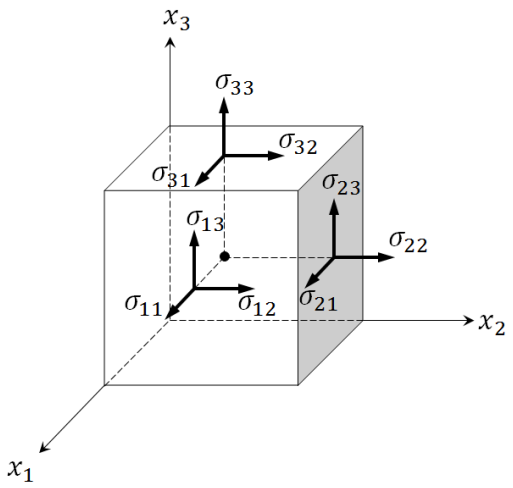

Figure 2.1: Notation used for the stress components in Cartesian rectangular coordinates.

Prior to further explanation regarding this subject, the clarification about the notation and terminology used is necessary. The notations as indicated in figure 2.1 will be consistently applied throughout this dissertation. Meanwhile, a summary of some of the important terminology can be found in Appendix A.

From the *Hooke's law* for elastic materials, the stress, σ and strain, ε relation for an isotropic material can be written as,

$$\sigma = E\varepsilon \tag{2.1}$$

Equation 2.1 indicates that the relationship between stress and strain for isotropic material is independent of the direction of the applied uniaxial force. Therefore only one elastic constant, E (Young's modulus) is required.

Meanwhile, for more general stress-strain relation in any solid media, the expression (*generalized Hooke's law*) can be described as,

$$\sigma_{ij} = C_{ijkl}\varepsilon_{kl} \tag{2.2}$$

where C is the *stiffness tensor*. Considering the simplifications that occurred when the material possesses some symmetry properties, the stiffness tensor C_{ijkl} is reduced to elements of a 6×6 matrix (Reddy 2004, Datta & Shah 2009). Thus, the equation becomes,

$$\sigma_i = C_{ij}\varepsilon_j \tag{2.3}$$

or in matrix form,

$$\begin{Bmatrix} \sigma_1 \\ \sigma_2 \\ \sigma_3 \\ \sigma_4 \\ \sigma_5 \\ \sigma_6 \end{Bmatrix} = \begin{bmatrix} C_{11} & C_{12} & C_{13} & C_{14} & C_{15} & C_{16} \\ C_{21} & C_{22} & C_{23} & C_{24} & C_{25} & C_{26} \\ C_{31} & C_{32} & C_{33} & C_{34} & C_{35} & C_{36} \\ C_{41} & C_{42} & C_{43} & C_{44} & C_{45} & C_{46} \\ C_{51} & C_{52} & C_{53} & C_{54} & C_{55} & C_{56} \\ C_{61} & C_{62} & C_{63} & C_{64} & C_{65} & C_{66} \end{bmatrix} \begin{Bmatrix} \varepsilon_1 \\ \varepsilon_2 \\ \varepsilon_3 \\ \varepsilon_4 \\ \varepsilon_5 \\ \varepsilon_6 \end{Bmatrix} \tag{2.4}$$

2.2.2 *Orthotropic* materials

All unidirectional laminae are individually *orthotropic*. Consider the x_1 axis is oriented along the fiber direction. For *orthotropic* material, the stiffness in x_1 is larger than stiffness in the x_2 direction. In the meantime, both stiffness values are not the same as in the x_3 direction. The difference between an *isotropic* and an *orthotropic* material can be best explained by Figure 2.2.

For the unidirectional GFRP laminates; which can be considered as *orthotropic*, the number of elastic coefficients is reduced to 9 only (Reddy 2004). Therefore equation 2.4 can be simplified as,

$$\begin{Bmatrix} \sigma_1 \\ \sigma_2 \\ \sigma_3 \\ \sigma_4 \\ \sigma_5 \\ \sigma_6 \end{Bmatrix} = \begin{bmatrix} C_{11} & C_{12} & C_{13} & 0 & 0 & 0 \\ C_{12} & C_{22} & C_{23} & 0 & 0 & 0 \\ C_{13} & C_{32} & C_{33} & 0 & 0 & 0 \\ 0 & 0 & 0 & C_{44} & 0 & 0 \\ 0 & 0 & 0 & 0 & C_{55} & 0 \\ 0 & 0 & 0 & 0 & 0 & C_{66} \end{bmatrix} \begin{Bmatrix} \varepsilon_1 \\ \varepsilon_2 \\ \varepsilon_3 \\ \varepsilon_4 \\ \varepsilon_5 \\ \varepsilon_6 \end{Bmatrix} \tag{2.5}$$

where each of the stiffness coefficients can be expressed in terms of the engineering

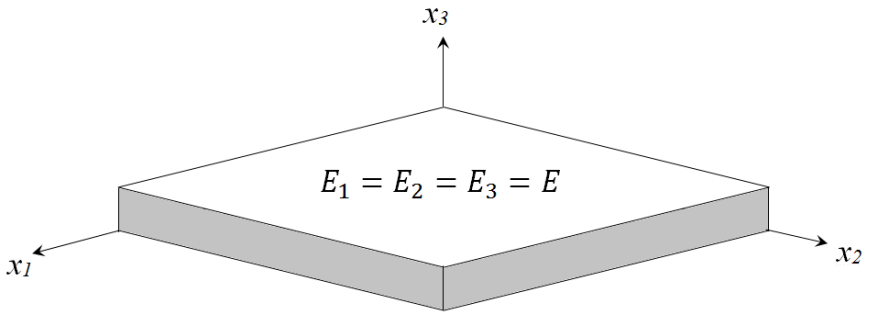

(a) *Isotropic* plate.

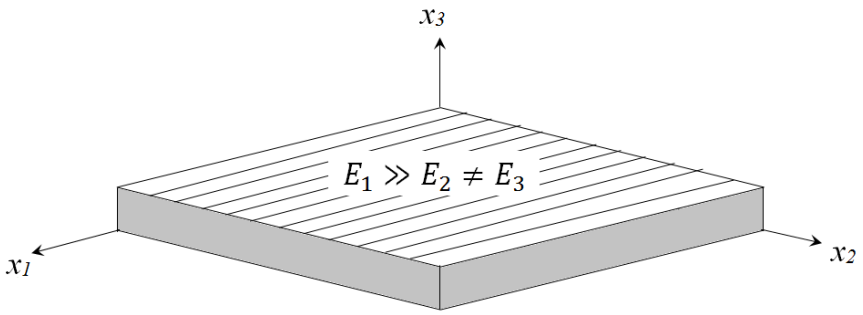

(b) *Orthotropic* plate.

Figure 2.2: Different between an *isotropic* and an *orthotropic* plate.

constants (Reddy 2004, Lempriere 1968),

$$
\begin{aligned}
C_{11} &= (1-\nu_{23}\nu_{23})/E_2E_3\Delta \\
C_{12} &= (\nu_{21}-\nu_{31}\nu_{23})/E_2E_3\Delta = (\nu_{12}-\nu_{32}\nu_{13})/E_1E_3\Delta \\
C_{13} &= (\nu_{31}-\nu_{21}\nu_{32})/E_2E_3\Delta = (\nu_{13}-\nu_{12}\nu_{23})/E_1E_2\Delta \\
C_{22} &= (1-\nu_{13}\nu_{31})/E_1E_3\Delta \\
C_{23} &= (\nu_{32}-\nu_{12}\nu_{31})/E_1E_3\Delta = (\nu_{23}-\nu_{21}\nu_{13})/E_1E_3\Delta \\
C_{33} &= (1-\nu_{12}\nu_{21})/E_1E_2\Delta \\
C_{44} &= G_{23}, C_{55} = G_{31}, C_{66} = G_{12} \\
\Delta &= (1-\nu_{12}\nu_{21}-\nu_{23}\nu_{32}-\nu_{31}\nu_{13}-2\nu_{21}\nu_{32}\nu_{13})/(E_1E_2E_3)
\end{aligned}
\tag{2.6}
$$

and ν_{ij} is the respective *Poisson's ratio*. For unidirectional fiber-reinforced material, the stiffness along the fibers (longitudinal) can be referred to E_L, and for the direction transverse to the fibers, E_T commonly used; or,

$$\begin{aligned} E_1 &= E_L \\ E_2 &= E_T \end{aligned} \tag{2.7}$$

All the engineering parameters can be determined experimentally using an appropriate test.

2.2.3 Specially plane-stress state of *orthotropic* plates

With respect to the x_1x_2 plane, the stress strain relation of an *orthotropic* material in a plane-stress state can be expressed as,

$$\begin{Bmatrix} \sigma_1 \\ \sigma_2 \\ \sigma_6 \end{Bmatrix} = \begin{bmatrix} Q_{11} & Q_{12} & 0 \\ Q_{12} & Q_{22} & 0 \\ 0 & 0 & Q_{66} \end{bmatrix} \begin{Bmatrix} \varepsilon_1 \\ \varepsilon_2 \\ \varepsilon_6 \end{Bmatrix} \tag{2.8}$$

where the Q_{ij} is called the plane stress-reduced stiffness. In term of engineering constants, it can be written as,

$$\begin{aligned} Q_{11} &= E_1/(1-\nu_{12}\nu_{21}) \\ Q_{22} &= E_2/(1-\nu_{12}\nu_{21}) \\ Q_{12} &= \nu_{12}E_2/(1-\nu_{12}\nu_{21}) = \nu_{21}E_1/(1-\nu_{12}\nu_{21}) \\ Q_{66} &= G_{12} \end{aligned} \tag{2.9}$$

Meanwhile, the transverse shear stresses are related to the transverse shear strains by the relations,

$$\begin{aligned} \begin{Bmatrix} \sigma_4 \\ \sigma_5 \end{Bmatrix} &= \begin{bmatrix} Q_{44} & 0 \\ 0 & Q_{55} \end{bmatrix} \begin{Bmatrix} \varepsilon_4 \\ \varepsilon_5 \end{Bmatrix} \\ Q_{44} &= G_{23} \\ Q_{55} &= G_{13} \end{aligned} \tag{2.10}$$

By including the shear stress, τ and shear strain, γ, therefore the equation 2.8 can be written as,

$$\begin{Bmatrix} \sigma_1 \\ \sigma_2 \\ \tau_{12} \end{Bmatrix} = \begin{bmatrix} Q_{11} & Q_{12} & 0 \\ Q_{12} & Q_{22} & 0 \\ 0 & 0 & Q_{66} \end{bmatrix} \begin{Bmatrix} \varepsilon_1 \\ \varepsilon_2 \\ \gamma_{12} \end{Bmatrix} \tag{2.11}$$

with

$$\tau_{ij} = \gamma_{ij} G_{ij} \tag{2.12}$$

2.3 Wave Propagation Theory

Before going deeper into the acoustic signal's propagation on a composite plate, it is important to review some of the wave propagation theory. In solid media, a number of different types of sound waves are possible. Generally, a *wave* can be characterized in space by oscillatory patterns that are capable of maintaining their shape and propagating in a stable manner. Wave propagation is often described as *wave modes*. For thin plates, where the wavelength is larger than the plate thickness, *plate wave* is predicted.

The propagation of a *plate wave* mode in composite plates has been investigated since the 1980's as reported by Prosser et al. (1992). In the early 90's, Prosser et al. (1992) had shown their interest in determining the extensional and flexural wave velocities in a thin-walled graphite/epoxy tube through an experimental study and successfully found a good agreement between theoretical calculations and experimental results. Approximately a year later, Prosser & Gorman (1994) had reported the same study but using composite plates.

Before discussing further details of the plate theories, it is good to review the history of wave and vibration studies. Here, is the summary of some important chronology (Graff 1975).

- 6^{th} Century B.C., Pythagoras studied the origin of musical sounds and the vibrations of strings.
- 1638, Galileo described the vibrations of pendulums, the phenomenon of resonance and the factors influencing the vibrations of strings.

- 1678, Robert Hooke formulated the law of proportionality between stress and strain for elastic bodies.
- 1686, Newton investigated the speed of water waves and the speed of sound in air.
- 1700, Sauveur calculated vibrational frequency of stretched strings.
- 1713, Taylor worked out a completely dynamical solution for the vibrations of a string.
- 1744, Leonard Euler (1744) and Daniel Bernoulli (1751) developed the equation for the vibrations of beams and obtained the normal modes for various boundary conditions.
- 1747, D'Alembert derived the equation of motion of a string and solved the initial-value problem.
- 1755, Bernoulli developed the principle of superposition and applied it to the vibrations of strings.
- 1759, Lagrange analysed the string of a system of discrete mass particles.
- 1815, Madame Sophie Germain developed the equation for the vibrations of a plate.
- 1821, Navier investigated the general equations of equilibrium and vibration of elastic solids.
- 1828, Poisson investigated the propagation of waves through an elastic solid; and found that longitudinal and transverse waves could exist. Cauchy (1830) obtained a similar result.
- 1882, Hertz developed the first successful theory for impact.
- 1887, Rayleigh investigated the propagation of surface waves on a solid.
- 1888, Rayleigh and Lamb (1889) developed the frequency equation for waves in a plate according to exact elasticity theory.
- 1904, Horace Lamb made the first investigation of pulse propagation in a semi infinite solid.
- 1917, Horace Lamb found the *Lamb waves*.
- 1921, Timoshenko developed a theory for beams that accounted for shearing deformation.

- 1930, Donnell studied the effect of a non-linear stress-strain law on the propagation of stress waves in a bar.
- 1951, Mindlin presented an approximate theory waves in a plate that provided a general basis for development of higher-order plate and rod theories.
- 1955, Perkeris presented the solution to Lamb's problem of pulse propagation in a semi-infinite solid.

2.4 Lamb's Wave Propagation in Composite Thin Plates

According to Lamb (1917), the term *Lamb's wave* refers to a wave type existing in a plate with planar dimension far greater than its thickness; that requires free upper and lower boundaries to maintain the propagation. In the early years after Horace Lamb found the *Lamb's waves*, not many researchers had intention to utilize the wave theory. However since the 1990's, during the rapid development of computing devices, the application of Lamb wave-based applications started to explode (Su & Ye 2008). In past decades, a lot of studies have utilized Lamb wave theory for Non-destructive Testing (NDT) purposes, especially for ultrasonic inspection of thin plates (Tsuda 2006, Lam et al. 2009, Diamanti & Soutis 2010).

Lamb's waves can be used for NDT in two fields. First, wave phase velocity, thickness calculation and elastic properties determination, and second, fault or damage detection (Diamanti & Soutis 2010). Lamb wave-based evaluation is very successful nowadays due to its excellent capability to travel in a long distance even in high attenuation materials and it is also highly sensitive to internal structural damage (Su & Ye 2008).

According to Lamb's wave theory, two major wave modes exist; symmetric and antisymmetric wave modes (Diamanti & Soutis 2010). Symmetrical Lamb wave mode (S modes) move in a symmetrical fashion along the mid-plane of the plate. This is sometimes called the extensional mode because the wave is stretching and compressing the plate in the wave motion direction (Figure 2.3). Meanwhile, the Asymmetrical Lamb wave mode (A modes) is often called the flexural mode because a large portion of the motion moves in a normal direction to the plate, and a little motion occur in the direction parallel to the plate (Figure 2.4).

Surgeon & Wevers (1999) have discussed the relation of these wave modes with the source orientation due to failure mechanisms in composite plates. They pro-

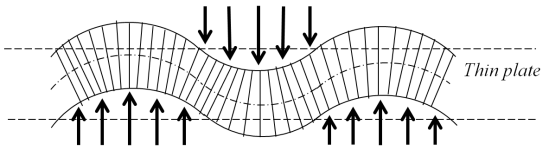

Figure 2.3: Asymmetric wave mode

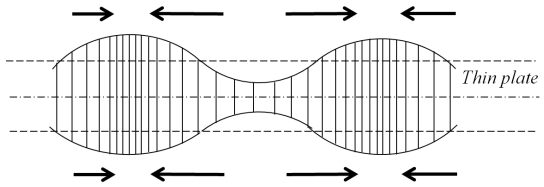

Figure 2.4: Symmetric wave mode

posed an interesting suggestion; *matrix cracks and fiber fracture will generate an extensional wave mode while delamination is expected to produce a flexural wave mode* (Figures 2.5). Recently, Scholey et al. (2010) published a report that proved the hypothesis by Surgeon & Wevers (1999).

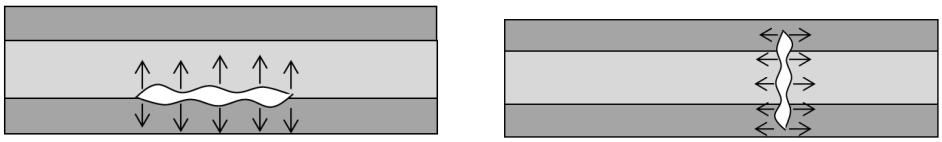

(a) Out of plane motion caused by delamination growth.

(b) In plane motion caused by matrix cracking.

Figure 2.5: Source orientation due to failure mechanisms.

2.4.1 Theory and fundamentals of Lamb's Wave

The dispersion curves of both modes can be derived from Lambs characteristic equation. For symmetrical vibrations, the equation can be written as (Lamb 1917),

$$\frac{\tan \beta d/2}{\tan \alpha d/2} = -\frac{4\alpha\beta k^2}{(k^2 - \beta^2)^2} \tag{2.13}$$

while the asymmetrical mode can be expressed as (Lamb 1917),

$$\frac{\tan \beta d/2}{\tan \alpha d/2} = -\frac{(k^2 - \beta^2)^2}{4\alpha\beta k^2} \tag{2.14}$$

where $\alpha = \sqrt{\frac{\omega^2}{c_L^2} - k^2}$, $\beta = \sqrt{\frac{\omega^2}{c_T^2} - k^2}$ and $k = \omega/c_p$. The parameters d, ω , k, c_p, c_L and c_T are the plate thickness, angular frequency, wave number, phase velocity, longitudinal wave velocity and transverse wave velocity respectively. The c_L and c_T are defined by equation 2.15 and 2.16 respectively,

$$c_L = \sqrt{\frac{E(1-\nu)}{\rho(1+\nu)(1-2\nu)}} \tag{2.15}$$

$$c_T = \sqrt{\frac{E}{2\rho(1+\nu)}} \tag{2.16}$$

Equation 2.13 and 2.14 also know as *Rayleigh-Lamb frequency equations*. These equations obviously produce two distinct types of wave modes: symmetric, S_i and antisymmetric, A_i mode; where $i = 0, 1, 2, 3, ...$ Meanwhile, the relation between the group velocity and phase velocity can be expressed as (Lam et al., 2009),

$$c_g = \frac{dkc_p}{dk} = c_p + k\frac{dc_p}{dk} \tag{2.17}$$

There is many software available in the market which can predict the dispersion curves based on the *Rayleigh-Lamb frequency equations*. For instance, Imperial College London promoted *DISPERSE*, a commercial interactive software that can calculate for any multi-layered structures such as composite laminates, sandwich plates and other glued structures. However, there is also free software available such as *Vallen Dispersion* and *PACShare Dispersion Curves*.

The Lamb wave dispersion equation does not clearly consider the propagation direction and magnitude, especially when dealing with anisotropic plates. Rhee et al. (2007) and Su & Ye (2009) have discussed very well on this matter and proposed the calculation of group velocities with consideration of the magnitude and direction from the slowness surface. Besides, the phase velocity of Lamb waves is also dependent on the stiffness of the laminates; as described by Lam et al. (2009). However, a few researchers have used the *Rayleigh-Lamb frequency*

equations to predict source location on composite specimens with reasonable accuracy (Jeong & Jang 2000, Jing-Pin et al. 2006, Jingpin et al. 2008, Oskouei & Ahmadi 2008).

2.4.2 First-Order Shear Deformation Theory (FSDT) for composite plate analysis

Lamb waves propagation also can be calculated using laminated plate theories. There are several laminated plate theories that can be used for wave propagation analysis in composite plates such as Classical Laminated Plate Theory (CLPT) and Mindlin-Reissner plate theory. Note that the Mindlin-Reissner plate theory also can be called the First-order Shear Deformation Theory (FSDT).

The FSDT showed better agreement with the experimental measurements, compared to classical plate theory (CLPT), particularly for the case of acoustic wave propagation, as reported by Prosser & Gorman (1994) (Figure 2.6). According to them, FSDT gives better result, than CLPT because FSDT includes the effect of shear deformation and rotator inertia.

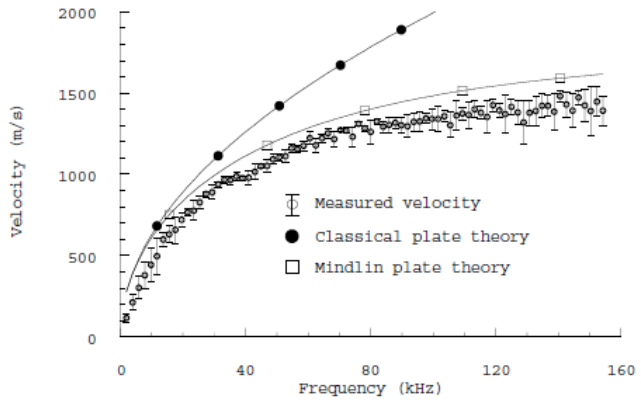

Figure 2.6: CPT vs FSDT prediction for flexural waves velocity (Prosser & Gorman 1994).

For the case of low frequency acoustic waves, approximately below 500 kHz, the lower order of plate theories, such as FSDT, still can predict the lamb wave dispersion curves very well. However for a higher range of frequencies, Wang & Yuan (2007) proposed the higher order plate theory for more accurate results.

In this review, the FSDT approximation will be detailed out in order to understand the behavior of acoustic propagation in thin laminated composite plates. The theory was well discussed by Abrate (1998) and Reddy (2004).

The displacement field according to FSDT can be written as (Abrate 1998),

$$\begin{aligned} u(x,y,z) &= u_0(x,y) + z\psi_x(x,y) \\ v(x,y,z) &= v_0(x,y) + z\psi_y(x,y) \\ w(x,y,z) &= w_0(x,y) \end{aligned} \tag{2.18}$$

where u_0, v_0, w_0 are the displacement components of a point on the mid-plane. ψ_x and ψ_y are the rotations of the normal to the mid-plane about the y and x axis respectively. Figure 2.7 shows these displacements.

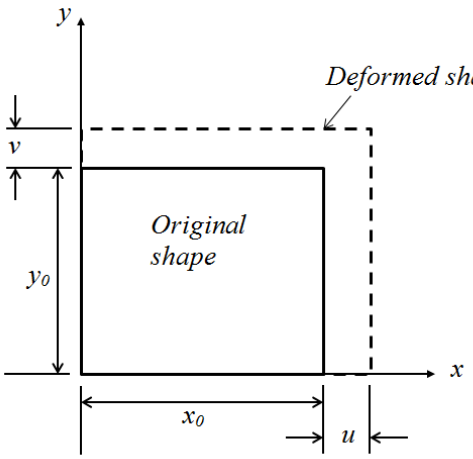

(a) Normal displacement.

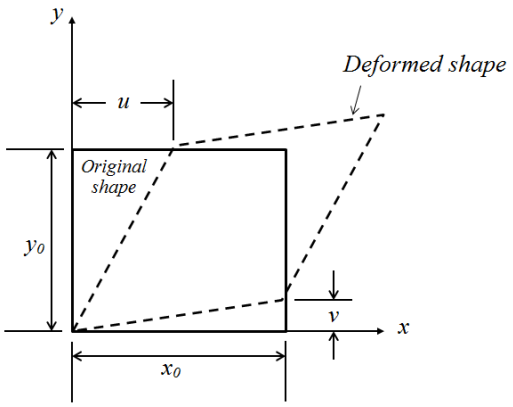

(b) Shear displacements.

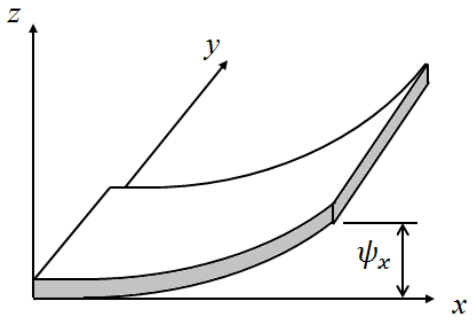

(c) Bending displacements.

Figure 2.7: Displacements of a plate.

For a plate with thickness h and the origin of the global coordinate system is located at the mid-plane (Figure 2.8), the in-plane force resultant, the bending moment and the shear force resultants can be defined as equations 2.19, 2.20 and 2.21, respectively (Abrate 1998).

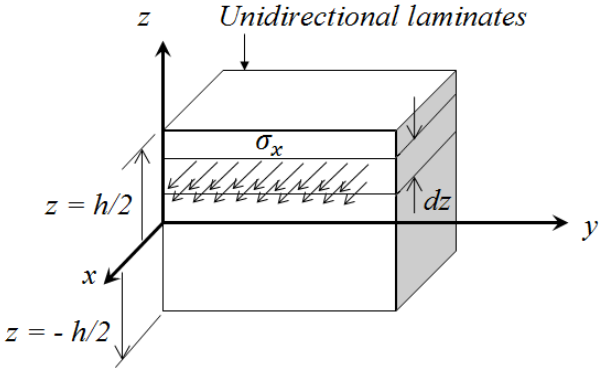

Figure 2.8: Definition of stress resultant.

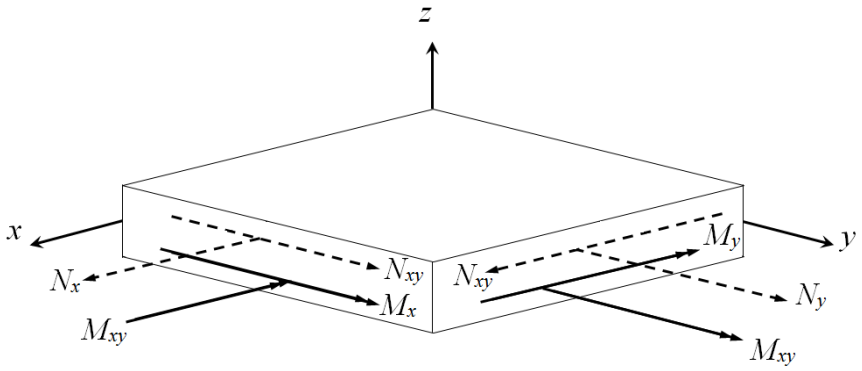

Figure 2.9: Force and moment resultants on a plate.

$$(N_x, N_y, N_{xy}) = \int_{-h/2}^{h/2} (\sigma_{xx}, \sigma_{yy}, \sigma_{xy}) dz \tag{2.19}$$

$$(M_x, M_y, M_{xy}) = \int_{-h/2}^{h/2} (\sigma_{xx}, \sigma_{yy}, \sigma_{xy}) z dz \tag{2.20}$$

$$(Q_x, Q_y) = \int_{-h/2}^{h/2} (\sigma_{xz}, \sigma_{yz}) dz \tag{2.21}$$

Meanwhile, the strain-displacement relations can be written as (Abrate 1998),

$$\begin{Bmatrix} \epsilon_{xx} \\ \epsilon_{yy} \\ \epsilon_{xy} \end{Bmatrix} = \begin{Bmatrix} \frac{\partial u_0}{\partial x} \\ \frac{\partial v_0}{\partial y} \\ \frac{\partial u_0}{\partial y} + \frac{\partial v_0}{\partial x} \end{Bmatrix} + z \begin{Bmatrix} \frac{\partial \psi_x}{\partial x} \\ \frac{\partial \psi_y}{\partial y} \\ \frac{\partial \psi_x}{\partial y} + \frac{\partial \psi_y}{\partial x} \end{Bmatrix} \tag{2.22}$$

or

$$\{\epsilon\} = \{\epsilon_0\} + z\{K\} \tag{2.23}$$

where ϵ_0 is the vector of mid-plane strains and K is the plate curvatures.

Using the relations defined by equations 2.19, 2.20 and 2.21, the constitutive equation for a laminate can be written as,

$$\begin{Bmatrix} N_x \\ N_y \\ N_{xy} \\ M_x \\ M_y \\ M_{xy} \end{Bmatrix} = \begin{bmatrix} A_{11} & A_{12} & A_{16} & B_{11} & B_{12} & B_{16} \\ A_{12} & A_{22} & A_{26} & B_{12} & B_{22} & B_{26} \\ A_{16} & A_{26} & A_{66} & B_{16} & B_{26} & B_{66} \\ B_{11} & B_{12} & B_{16} & D_{11} & D_{12} & D_{16} \\ B_{12} & B_{22} & B_{26} & D_{12} & D_{22} & D_{26} \\ B_{16} & B_{26} & B_{66} & D_{16} & D_{26} & D_{66} \end{bmatrix} \begin{Bmatrix} \epsilon_{xx} \\ \epsilon_{yy} \\ \epsilon_{xy} \\ K_x \\ K_y \\ K_{xy} \end{Bmatrix} \tag{2.24}$$

where

$$A_{ij} = \Sigma \overline{Q}_{ij}|_r (z_r - z_{r-1}) \tag{2.25}$$

$$B_{ij} = \frac{1}{2} \Sigma \overline{Q}_{ij}|_r (z_r^2 - z_{r-1}^2) \tag{2.26}$$

$$D_{ij} = \frac{1}{3} \Sigma \overline{Q}_{ij}|_r (z_r^3 - z_{r-1}^3) \tag{2.27}$$

and the subscript r refers to the r^{th} layer of the laminates.

The A_{ij} matrix is called the extensional stiffness matrix. As discussed in the previous section, the term A_{16} and A_{26} are zero for plane stress state of *orthotropic* laminates. Meanwhile, the matrix D_{ij} is called the bending stiffness matrix and relates to the amount of plate curvatures with the bending moments. The B_{ij} matrix is called the coupling stiffness matrix and it vanishes when symmetric lay-up is used.

By applying Hamilton's principle to get the motion equations in terms of the force and moment resultants, and using all values in equation 2.24, gives the equations

of motion for general laminate in term of displacements (Abrate 1998).

$$\frac{\partial N_x}{\partial x} + \frac{\partial N_{xy}}{\partial y} = I_1 \ddot{u_0} + I_2 \ddot{\psi_x} \tag{2.28}$$

$$\frac{\partial N_{xy}}{\partial x} + \frac{\partial N_y}{\partial y} = I_1 \ddot{v_0} + I_2 \ddot{\psi_y} \tag{2.29}$$

$$\frac{\partial Q_x}{\partial x} + \frac{\partial Q_y}{\partial y} + q = I_1 \ddot{w_0} \tag{2.30}$$

$$\frac{\partial M_x}{\partial x} + \frac{\partial M_{xy}}{\partial y} - Q_x = I_3 \ddot{\psi_x} + I_2 \ddot{u_0} \tag{2.31}$$

$$\frac{\partial M_{xy}}{\partial x} + \frac{\partial M_y}{\partial y} - Q_y = I_3 \ddot{\psi_y} + I_2 \ddot{v_0} \tag{2.32}$$

where $I_2 = 0$ for a symmetric lay-up.

FSDT solution for harmonic wave propagation

For harmonic wave propagation in thin plates, three main wave modes is predicted; extensional or symmetric (S), in-plane shear or shear horizontal (SH) and flexural or antisymmetric (A) modes. The *SH* waves can exist in both *A* and *S* modes.

Consider the x-axis is taken to be parallel to the fiber axis. For symmetric modes, the term qS_n $(n = 0, 1, 2, 3, ...)$ is designated for the dominant extensional component which is propagating along the x-axis; and qSH_{2n} is for the dominant component which propagates toward the x-axis but polarized in the y-axis. Meanwhile for antisymmetric modes, a similar thing occurs where the qA_n and qSH_{2n-1} components are generated (Wang & Yuan 2007). Usually the term $q = quasi$ is ignored to ease the presentation.

In a homogeneous isotropic material, the extensional mode propagates with a

dispersionless velocity (Prosser et al. 1992),

$$c_e = \sqrt{\frac{E}{\rho(1-v^2)}} \tag{2.33}$$

where E is Youngs modulus, v is Poissons ratio and ρ is density. In composite materials, the extensional velocity wave propagation is dependent on the in-plane stiffness coefficients. From equations of motion (equations 2.28 and 2.29) for a symmetrically balance laminate, the in-plane extensional or S wave velocity is (Abrate 1998, Reddy 2004, Prosser et al. 1992),

$$c_e = \sqrt{\frac{A_{11}}{\rho}} \tag{2.34}$$

and the shear wave is,

$$c_s = \sqrt{\frac{A_{66}}{\rho}} \tag{2.35}$$

for wave propagation, in the x-direction. Meanwhile for the y-direction, the in-plane extensional wave velocity is,

$$c_e = \sqrt{\frac{A_{22}}{\rho}} \tag{2.36}$$

and the shear wave is the same as equation 2.35.

For the flexural wave propagation in an isotropic thin plate with thickness h, its velocity can be written as (Prosser et al. 1992),

$$(c_f)^2 = \sqrt[4]{\frac{D}{\rho h}}(\sqrt{\omega}) \tag{2.37}$$

where D is the bending stiffness which is can be expressed as,

$$D = \frac{Eh^3}{12(1-v^2)} \tag{2.38}$$

and ω is the frequency in radians/sec. In composite laminates, flexural or transverse wave velocities are a function of bending stiffness coefficients, D_{ij} and transverse shear stiffness coefficients, A_{ij}. However the A_{ij} matrix needs to include the shear correction factors, κ_i and κ_j; when usually $\kappa_i \times \kappa_j$ is equal to 5/6 (Abrate 1998, Prosser & Gorman 1994, Datta & Shah 2009).

$$A_{ij} = \kappa_i \kappa_j \times \int_{z=-h/2}^{z=h/2} \overline{Q}_{ij}|_r (z_r - z_{r-1}) \tag{2.39}$$

In the case of unidirectional laminates, from the equations of motion which were derived earlier, the dispersion relation can be expressed as (Prosser & Gorman 1994, Jeong & Jang 2000),

$$(D_{11}k^2 + A_{55} - I\omega^2)(A_{55}k^2 - \rho^*\omega^2) - (A_{55}k)^2 = 0 \tag{2.40}$$

for wave propagation in the x-direction, and

$$(D_{22}k^2 + A_{44} - I\omega^2)(A_{44}k^2 - \rho^*\omega^2) - (A_{44}k)^2 = 0 \tag{2.41}$$

for wave propagation in the y-direction. Solving for the wave number, k as a function of circular frequency, ω yields a cubic relationship to k^2. Then, the phase velocity, c_p is determined as a function of frequency using the relationship $c_p = \omega/k$. The relation between the group velocity c_g and phase velocity c_p is $c_g = \frac{d\omega}{dk}$.

Results from Jeong & Jang (2000) reveal a very good agreement between theoretical calculation and experimental measurements for the dispersion of flexural waves as shown in Figure 2.10. In their study, they use pencil lead breaks as a source for generating low frequency flexural waves; and measured the difference of wave arrival time between two sensors, with known distance.

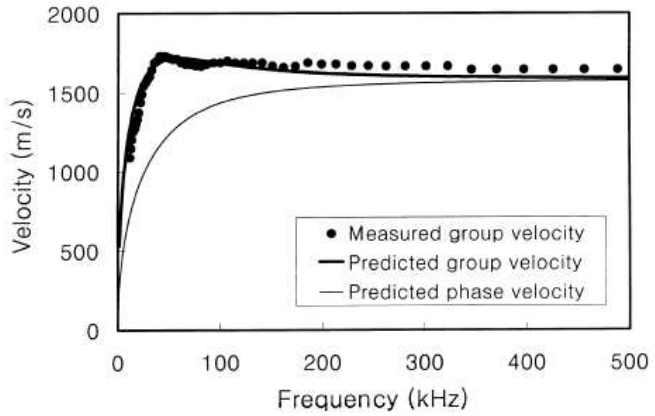

Figure 2.10: Comparison between theoretical calculation and experimental measurements for the dispersion of flexural waves (Jeong & Jang 2000).

2.4.3 Case study - numerical results

Datta & Shah (2009) have proposed the solution for the equations of motion for layered media using the *Stiffness Method*. They also produced a useful program for the numerical prediction of phase velocity and group velocity. Note that developing a numerical solution is not the scope of this research work. The details of the software can be found in Appendix A.

The program deals with the transversely isotropic or quasi-isotropic material and applied the FSDT approximation. Since the scope of this study was using the glass reinforced fiber in an epoxy matrix, the numerical solution offered through the software can be utilized. Note that, for transverse isotropy, the stiffness value, $C_{12} = C_{13}$, $C_{22} = C_{33}$, $C_{55} = C_{66}$, $C_{44} = \frac{C_{22}-C_{23}}{2}$ (Datta & Shah 2009), and this is applicable for glass-epoxy laminates.

Consider a $270mm \times 123mm$ unidirectional GFRP thin laminated plate, $[0^o]_8$ with thickness (H) of $4.25mm$. The engineering constant values can be referred as in the Table A.2 and A.3 in the Appendix A. The C_{ij} matrix as in equation 2.5 was calculated and the result can be expressed as,

$$[C_{ij}] = \begin{bmatrix} 57,403 & 3,570 & 3,570 & 0 & 0 & 0 \\ 3,570 & 21,185 & 6,905 & 0 & 0 & 0 \\ 3,570 & 6,905 & 21,185 & 0 & 0 & 0 \\ 0 & 0 & 0 & 7140 & 0 & 0 \\ 0 & 0 & 0 & 0 & 8,963 & 0 \\ 0 & 0 & 0 & 0 & 0 & 8,963 \end{bmatrix} \tag{2.42}$$

All values are in the unit MPa (or MN/m^2).

Velocity and slowness surfaces plot for the GFRP sample

The polar plot of normalized phase velocity surfaces against the propagation angle, as produced by the program can be shown in Figure 2.11. The phase velocity polar plot indicates the direction dependency of all three velocity modes to the angle of propagation. Velocities are normalized with respect to the pure shear wave velocity, $c_s = 2117ms^{-1}$ which was computed using the equation 2.35.

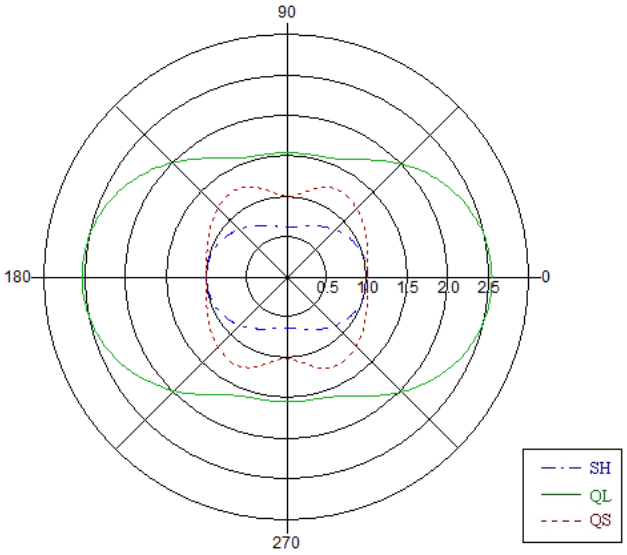

Figure 2.11: The polar plot of normalized phase velocity surfaces vs the propagation angle (degrees)

Figure 2.12 shows the slowness profile of the sample. The theory for the plots were discussed thoroughly by Datta & Shah (2009). The velocity and slowness surface plots show the high dependencies of longitudinal properties to the angle of propagation. This can be avoided by using multiple angle lay-up of laminates (Su & Ye 2009). The transverse velocity seems not to vary much against the different propagation angles. These plots are very important when studying the Lamb waves propagation in the next section.

Dispersion curves for the GFRP sample

In the meantime, the numerical computation (through the software) calculated up to 5 modes of velocity curves as indicated in the Figures 2.13 and 2.14. Note

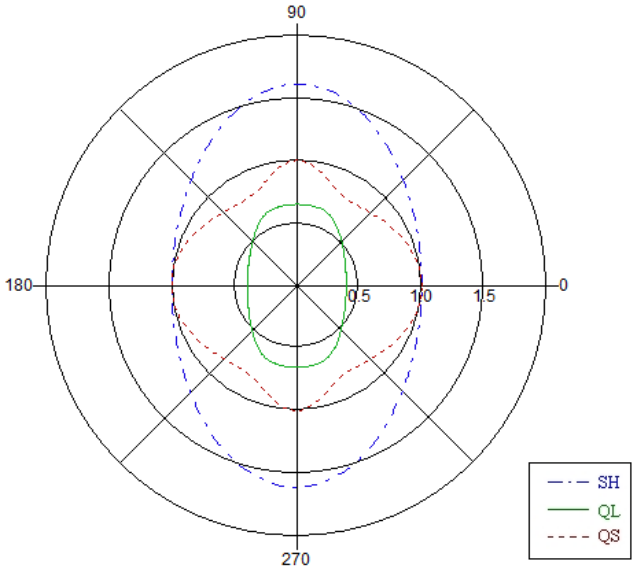

Figure 2.12: The slowness profile for the sample.

that, the velocities (phase velocity, c_p and group velocity, c_g) were normalized with respect to pure shear wave velocity, $c_s = 2117ms^{-1}$,

$$NormalizedVelocity = \frac{c_i}{c_s} \tag{2.43}$$

for $i = p, g$, while the normalized frequencies were calculated as,

$$NormalizedFrequency = \frac{\omega \times H}{c_s} \tag{2.44}$$

where ω denotes the frequency (radian/time) and H refers to the half thickness of plate.

However, this research work is only interested on the fundamental mode of wave propagation. Acoustic waves with a spectrum higher than 200 kHz must be avoided to assure no interference with other modes of propagation; and it can be done by applying appropriate signal filtering. As a consequences, complicated analysis can be avoided.

The fundamental modes of the phase velocity and group velocity curves for the sample are presented in Figure 2.15 and 2.16 respectively. In both figures, the dispersion curves calculated by the *Rayleigh-Lamb frequency equations* have also been included, for comparison.

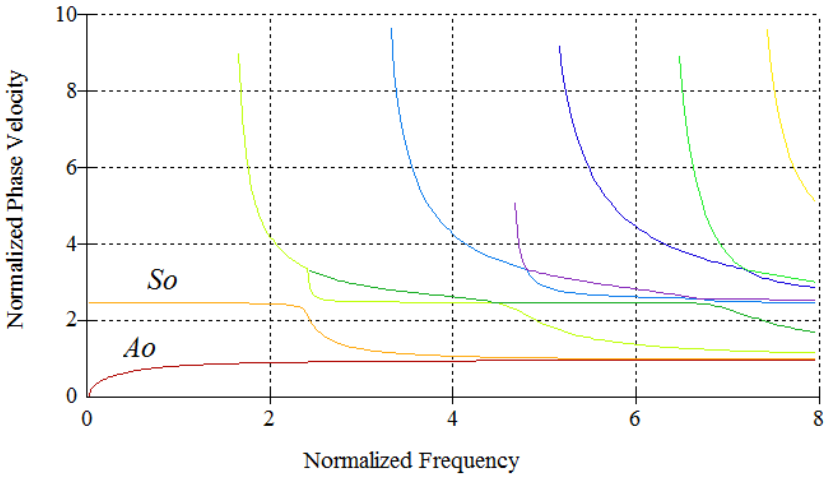

Figure 2.13: Phase velocity curves of the sample.

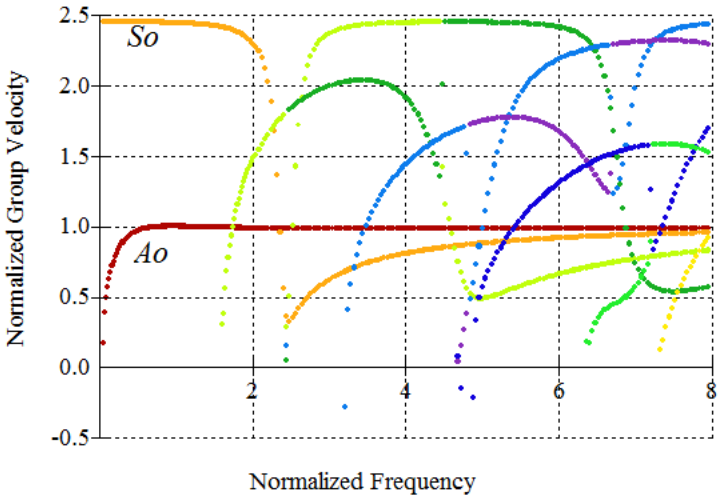

Figure 2.14: Group velocity curves of the sample.

Note that, the calculation using the *Rayleigh-Lamb frequency equations* was done using the *PACshare Dispersion Curves* software. It is obvious that, the flexural waves velocity approximation from both FSDT and the *Rayleigh-Lamb frequency equations*, have good agreement. However, there is a big different in terms of extensional waves velocity determination.

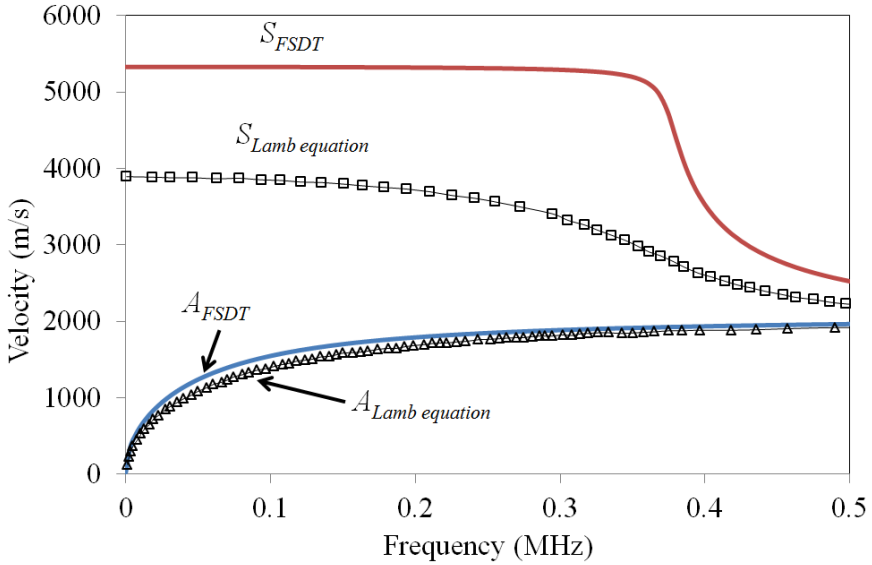

Figure 2.15: The fundamental curves for antisymmetric mode A_0 and symmetric mode S_0 for phase velocity.

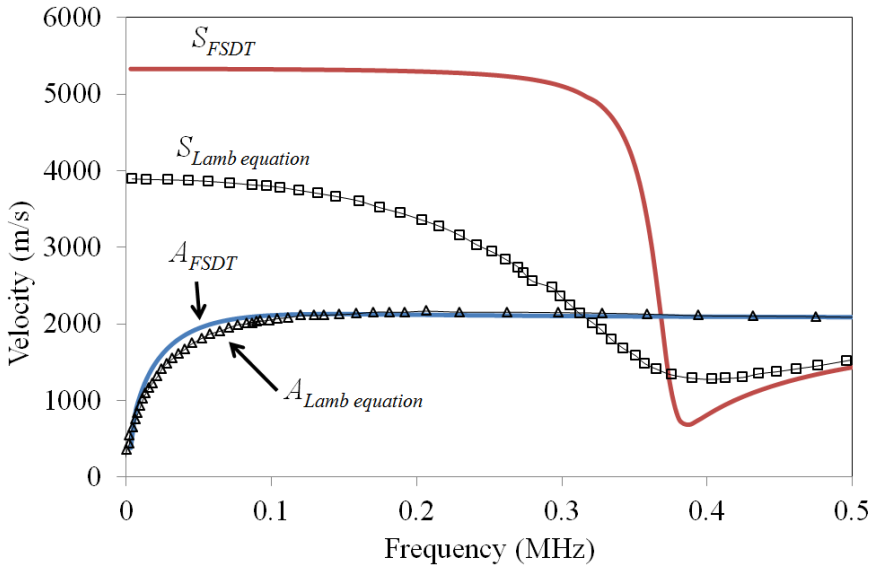

Figure 2.16: The fundamental curves for antisymmetric mode A_0 and symmetric mode S_0 for group velocity.

2.5 Time-frequency Signal Analysis

Spectral analysis is one of the most important analyses when dealing with acoustic waves. Fast Fourier Transform (FFT) is a well known and useful tool for spectrum analysis. Despite its ability to provide the details of signal's frequency content,

FFT actually is unable to show the time information of the signal. Therefore, a time-frequency analysis is needed.

The main goal for a time-frequency analysis is to look for the detail time information for a specific frequency to occur in a signal. For the case of plate waves analysis, it is important to identify the arrival time of wave modes to the sensors. This is due to each wave mode propagating with different frequencies. Therefore the prediction of the source location for damages (e.g. by impacts or cracks), can be more accurate and reliable with the use of time-frequency analysis.

Note that, the conventional source location prediction techniques using the time arrival of full signal have a significant potential of errors, according to some research works (Ziola 1991, Jiao et al. 2004). More details will be explained in the Section 3.4.1.

There are different types of signal transformation methods available for this analysis. Two most commonly used are the Short Time Fourier Transform (STFT) and the wavelet analysis. Both time-frequency analysis techniques are actually an advanced signal processing approach and have been using widely for signal analysis

There is an on going debate on the performance of the two approaches. However, it depends on its applications as discussed by Giurgiutiu & Yu (2003) in their work. They reported that STFT is easy to use and not complex to understand, meanwhile, wavelet analysis can be applied for wider applications. However, in terms of accuracy and resolution, wavelet analysis is better (Daubechies 1990) than STFT.

For a particular case such as damage source location using *Modal Acoustic Emission*, both types of time-frequency analysis can be used. The details will be explained further in the next chapter. In the meantime, there are a number of researchers who have successfully used wavelet analysis and came out with good accuracy (Hamstad et al. 2002, Jing-Pin et al. 2006, Oskouei & Ahmadi 2008). Yet, Hafizi, Epaarachchi & Lau (2012) also have shown the suitability of source mapping using STFT in their work, however the results show quite a large error. This case study will be furthered explain in the Section 3.5.

This Ph.D. work utilized the wavelet analysis, since this technique also has a signal 'denoising' capability. The next sections will explain in brief, the wavelet's topic: particularly the Continuous Wavelet Transform (CWT) and Discrete Wavelet Transform (DWT).

2.5.1 Continuous Wavelet Transform (CWT)

Before working with the details of any wavelet transform, the understanding of the STFT is essential. Conceptually, the STFT is the 'windowed' version of FFT, where in every small time frame, a FFT analysis was done to produce the magnitude F as a function of frequency, ω and time shift, $\widehat{\tau}$. Mathematically, the STFT can be expressed as,

$$F(\omega, \widehat{\tau}) = \int_0^t f(t)\omega(t - \widehat{\tau})e^{-j\omega t}dt \tag{2.45}$$

Meanwhile, the Figure 2.17 shows how STFT maps a time domain signal into time-frequency representation. The main drawback of the STFT is the window function, $\omega(t)$ is fix through the analysis. As consequences, the details of frequency information will be sacrificed if time resolution is increased and vise versa. Fortunately, this time-frequency 'compromising' can be improved by using the wavelet analysis.

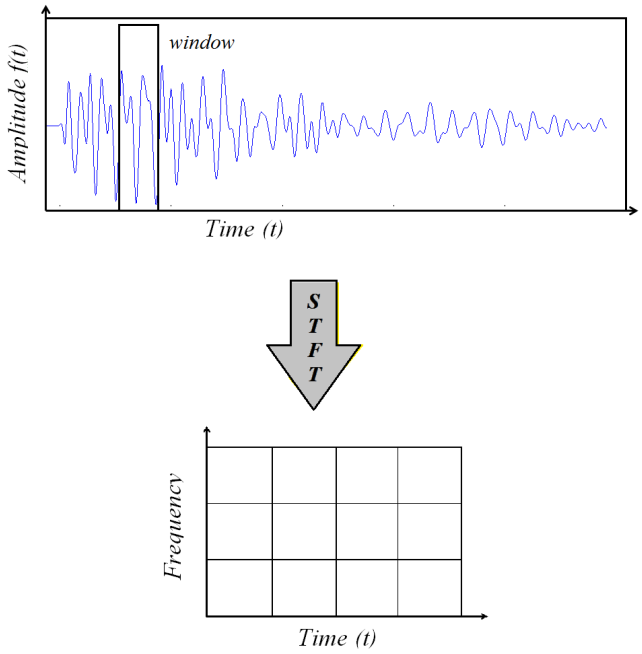

Figure 2.17: The demonstration of how STFT mapping a time domain signal into a time-frequency result.

The Wavelet analysis or Continuous Wavelet Transform (CWT) also able to express the time-frequency representation for continuous-time (analog) signals. The

CWT of a function, as defined by Chui (Chui 1992), can be expressed as,

$$WT_f(s,\widehat{\tau}) = \frac{1}{\sqrt{s}}\int_{-\infty}^{\infty} f(t)\psi^*(\frac{t-\widehat{\tau}}{s})dt \tag{2.46}$$

where $s > 0$ and the superscript * indicates the complex conjugate. The term $\psi(t)$ is the basic wavelet. The parameter s in equation 2.46 stands for the scale of basic wavelet and is related to signal frequency. Meanwhile, the parameter $\widehat{\tau}$ stands for shift or position of basic wavelet and it can be related to the time of the signal. Plotting wavelet transform magnitude, WF_f on $s-\tau$ axis gives the time-frequency view of a signal with improved time and frequency resolution compared to STFT.

There are many basic wavelets of *wavelet families* available such as Haar, Daubechies, Biorthogonal, Coiflets, Symlets, Morlet, Mexican Hat, Meyer, Gaussian, Complex Gaussian, Shannon and Frequency B-Spline. The appropriate wavelet choice will give better results in a time-frequency analysis.

In this work, the Morlet wavelet as shown in Figure 2.18 was used for CWT. This wavelet is identical to the Gabor wavelet (Simonovski & Boltezar 2003) and has a similar shape as an impulse (Lin 2001). It can be defined as (Simonovski & Boltezar 2003, Lin 2001),

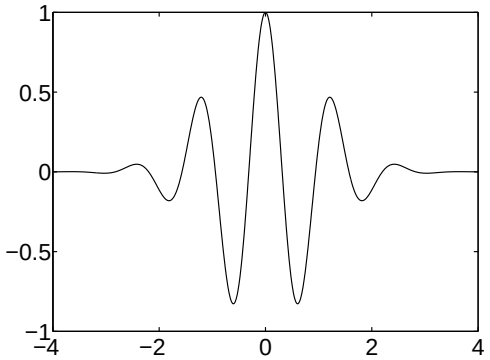

Figure 2.18: The shape of the Morlet wavelet

$$\psi(t) = (\exp^{-i\omega_0 t} - \exp^{-\omega^2/2})\exp^{-t^2/2} \tag{2.47}$$

The scale, s can be related to the frequency by this relation,

$$\omega = \omega_0/s \tag{2.48}$$

where the wavelet center frequency, ω_0 is depending on the sampling frequency and the selected minimum scale; as explained by Simonovski and Boltezar (Simonovski & Boltezar 2003).

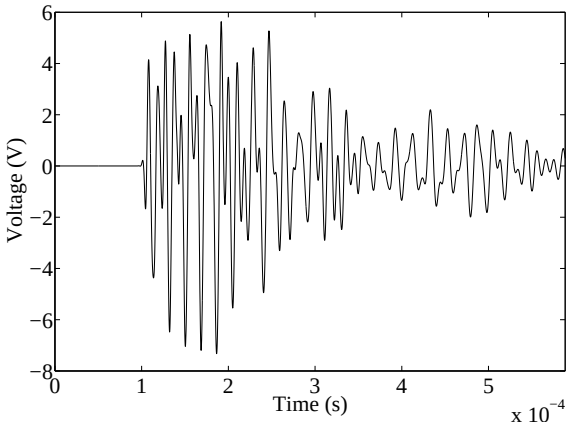

Figure 2.19: AE burst signal.

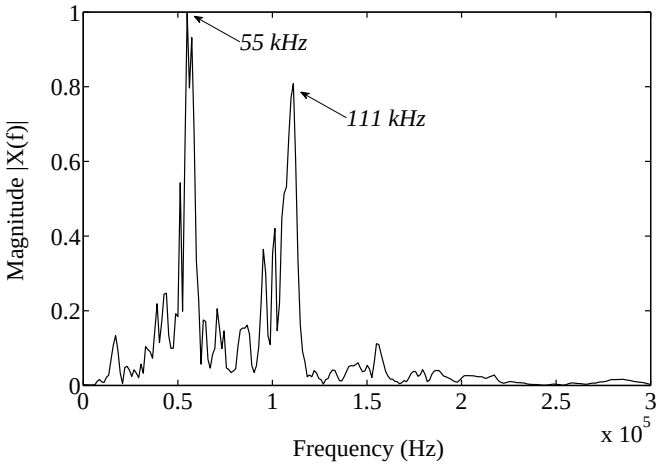

Figure 2.20: FFT of the signal shown in 2.19

Consider an analog signal, $f(t)$ in the time domain, as shown in Figure 2.19. The respective FFT analysis for the signals can be presented as in the Figure 2.20. Meanwhile, the Figures 2.21 and 2.22 show the time-frequency representation, STFT and CWT respectively, for the time domain signal as shown in Figure 2.19. It is obvious that the CWT offers an excellent resolution for both time and frequency.

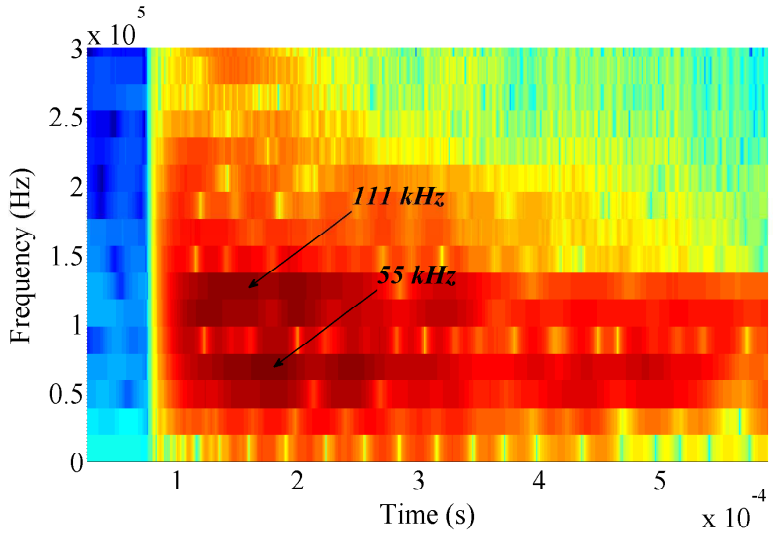

Figure 2.21: STFT representation.

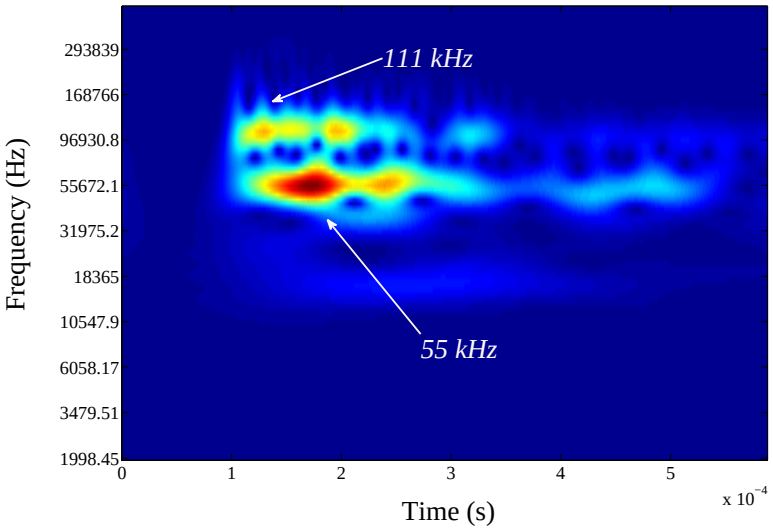

Figure 2.22: CWT representation.

2.5.2 Discrete Wavelet Transform (DWT)

Despite of the excellent resolution of CWT for time-frequency representation, it is actually impractical in real applications. Therefore a sampled version of CWT, the Discrete Wavelet Transform (DWT), was introduced for many applications such as noise filtering or signal 'denoising' (Ergen 2012). DWT decomposed any signals into several levels of approximations and details. The parameter s and τ (as is Equation 2.46) which is continuous in CWT, can be discretized by

introducing a dyadic grid (Ergen 2012, Tsai 2002),

$$\begin{aligned} s &= 2^{-m} \\ \widehat{\tau} &= n2^{-m} \end{aligned} \tag{2.49}$$

Therefore the $WT_f(s,)$ in Equation 2.46 can be written in discrete version, $DWT_f(m,n)$,

$$DWT_f(m,n) = \int_{-\infty}^{\infty} f(t)\psi^*_{m,n}(t)dt \tag{2.50}$$

where $\psi^*_{m,n} = 2^{-m}\psi(2^m t - n)$ is the dilated and translated version of the mother wavelet $\psi(t)$. According to Figure 2.23, more levels of decomposition can 'dismantle' the signal into more details. This unique capability of wavelet transform actually works with a series of low-pass and high-pass filters, which can be used for 'denoising'.

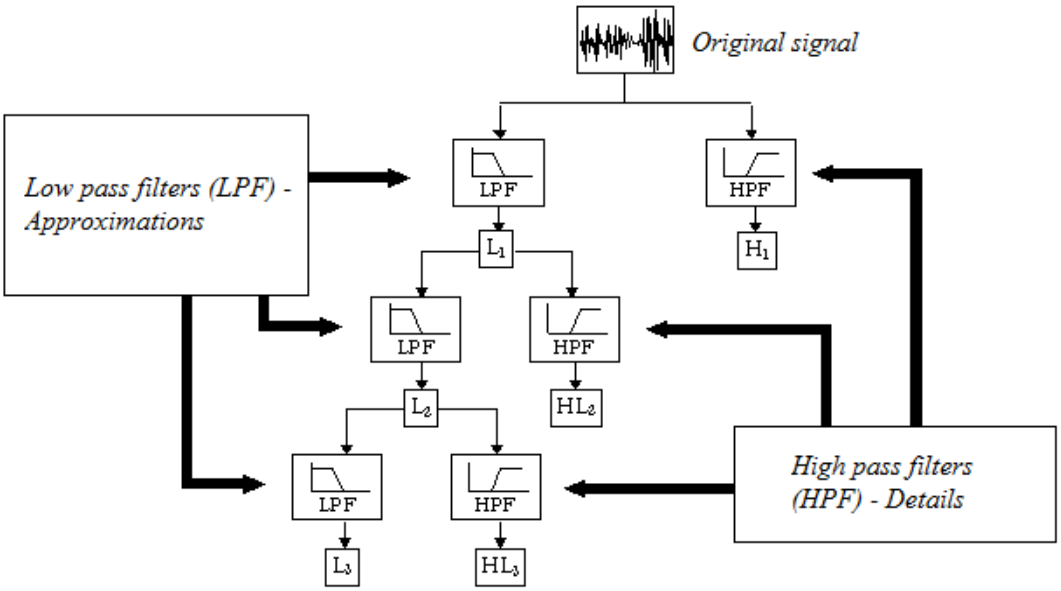

Figure 2.23: Discrete wavelet decomposition tree or filter bank (Altmann 1996).

There are several types of mother wavelet or wavelet families that can support DWT, such as Symlets, Daubechies, Coiflets, Haar and Bi-orthogonal wavelets. Any wavelet can be chosen arbitrarily as long as they are in these wavelet families. In this study, a Daubechies wavelet (dbN) was preferred. It is an established mother wavelet in normal application and can give exact reconstruction. In other words, any wavelet order in this family can be selected arbitrarily since all of them

can provide no loses during signal reconstruction. In particular, db20 (Figure 2.24) was chosen as it has a high number of vanishing moments. Thus it presents a better representation of a polynomial information in the signal.

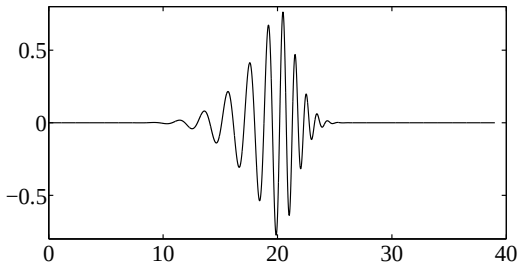

Figure 2.24: The db20 wavelet

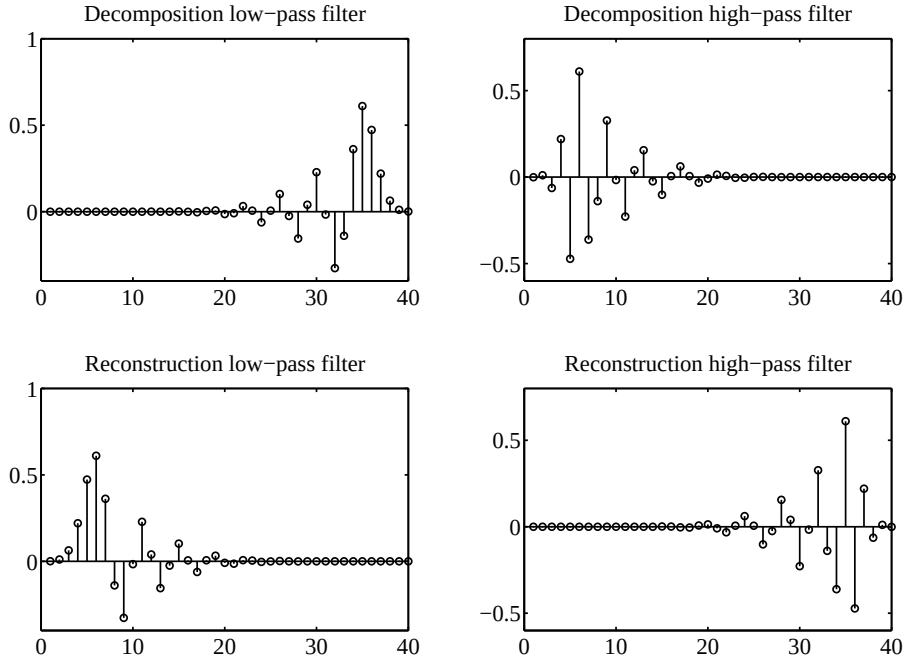

Figure 2.25: Analysis and synthesis filters for db20 wavelet.

However, for DWT analysis, the analysis and synthesis filters are more important than the associated scaling function and wavelet since it is more related to the low-pass and high-pass filter as described in Figure 2.23. The analysis (decomposition) and synthesis (reconstruction) filters of the db20 wavelet can be shown as in Figure 2.25. For comparison, the db4 wavelet and the analysis and synthesis filters of lower order dbN wavelet (db4) are also presented, as indicated in Figure 2.26 and Figure 2.27 respectively.

The DWT will be used in the chapter 4, during the 'denoising' process of noisy signals. Further analysis will be described along with the results presented.

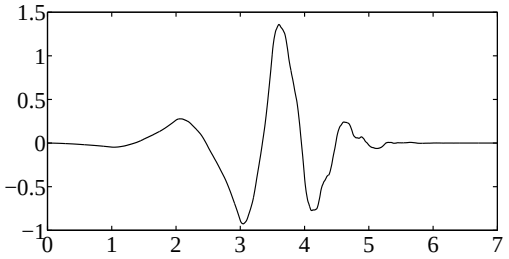

Figure 2.26: The db4 wavelet

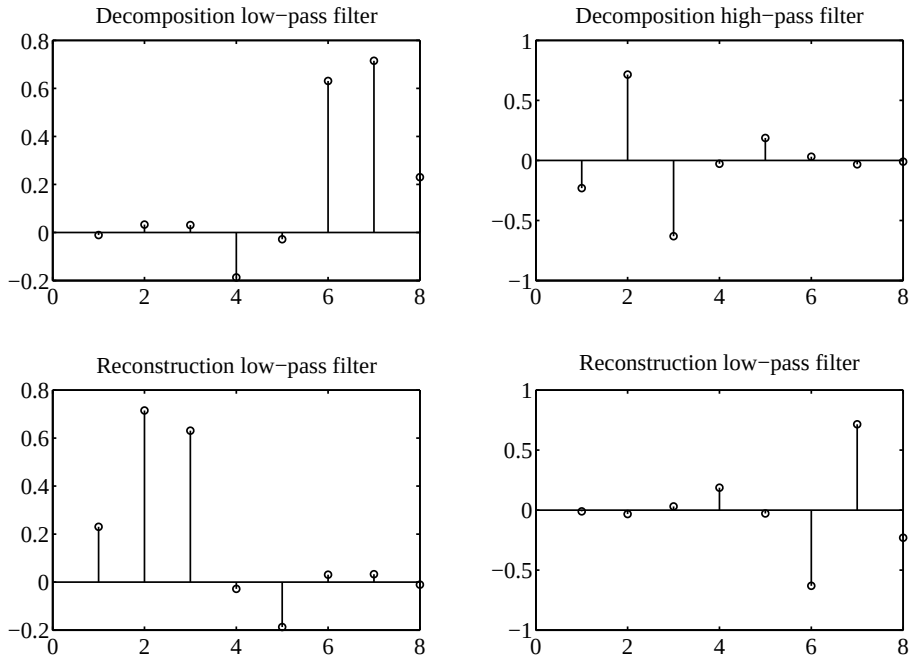

Figure 2.27: Analysis and synthesis filters for db4 wavelet.

2.6 Chapter Summary

This chapter has reviewed some basic information regarding acoustic wave propagation in thin laminated composite plates. It is important to emphasize that the propagation of waves in a thin composite plate is considered as Lamb waves. This assumption will be continued in the next chapter, because of its importance in showing the relationship between the propagation of waves with the characterization of damage in a composite structure. Not only that, enough knowledge of the Lamb waves will allow an accurate mapping of a damage, or the external impact. All the brief knowledge supplied, is a good foundation in understanding wave propagation due to AE sources; particularly for the purpose of MAE analysis.

Chapter 3

Use of MAE for Damage Detection in Composite Thin Laminates

3.1 Chapter Overview

One of the main focus of this study is to apply the wave propagation analysis of Lamb waves on the composite thin plates. It is necessary as most of the wave propagation based SHM utilized this theory. To narrow the research scope, Acoustic Emission (AE) was chosen to be performed as the monitoring technique in this research work. The significance of AE as wave propagation based SHM has been explained briefly in Chapter One.

This chapter will describe thoroughly about the AE technique. The explanation will be more particular to a modal analysis of acoustic emission or *Modal Acoustic Emission* (MAE), particularly for progressive damage monitoring in thin laminated composite plates.

In the first section, failure modes in fibre reinforced composite material will be introduced due to its relation to the AE source. It will be followed by a brief description of the AE technique and its application for composite materials. A few case studies will be presented, especially regarding the MAE method for thin laminated composite plates.

3.2 Failure Mode in Fibre Reinforced Composite Material

Unlike the homogeneous isotropic materials, where the information is considered adequate (although current research is still ongoing), more info is required for the study of failure in composite materials. It is due to limited research work that has been done in the area of the damage behaviour of composites. Its micro-structures are different from the typical isotropic materials; consequently, the failure behaviour in composites are complex as described by usual plasticity theory or crack growth concepts (Reifsnider 1998).

Theoretically, an AE system can easily detect an imperfection in loaded composite structures. When a load is applied on a composite laminate, in the micro level, it will starts deforming. Consequently, the elastic strain energy will be stored inside the material. If there is a growing micro-crack, the stored energy being released by the propagation of the crack and transient AE waves will be generated.

Each wave's signal, from different types of failure mechanisms, generates different signal features which can be identified by proper signal analysis. It contains useful information such as crack energy, source orientation, size of the crack and the failure mechanism involved. This feature extraction study has become of great interest nowadays, mainly involving composite failure characterization (Bohse 2000, Godin et al. 2004, Gutkin et al. 2011). Furthermore, with an appropriate number of AE sensors, an accurate mapping of the damage can be done.

Composite materials display a wide variety of failure mechanisms, such as fiber failure, matrix cracking, buckling and delamination (Orifici et al. 2008). The damage development usually is a combination of multiple failure modes. This damage accumulation will result in the final failure to the composites (Reifsnider 1998). Proper examination of this damage accumulation and its correlation with acoustic emission signals will give a significant contribution towards the better monitoring system for composite structures. Three main damage modes which are usually considered are micro-cracking, delamination and fiber fractures (Reifsnider 1998).

3.3 Basic Principles of an AE System

AE is increasingly popular in the last few decades, especially in the health monitoring of structures such as buildings, bridges, wind turbines and transport vehicles. In a rock mechanisms study, AE was also called a microseismic activity

(Leaird 1980). From the geology field in early 1900, AE has emerged into structural health monitoring research lately. This technique became established today, owing to its ability to reveal, in advance, of any impending failure in structures, but more than that, this method be used for real-time monitoring.

Acoustic emission can be defined as high frequency acoustic signals that are released when a material experiences stress or strain (Shull & Tittmann 2002). According to the standard, ASTM-E1316-13D (2013), the term 'acoustic emission' is referred to the class of phenomena whereby the transient elastic waves are generated by the rapid release of energy from localized sources within the material. The AE waves travel in the medium of solid materials (e.g. concrete, metals, composites) and can be easily captured by AE sensory systems as shown in Figure 3.1.

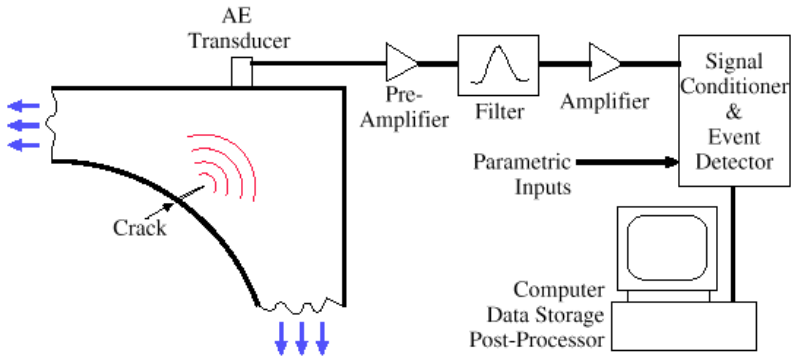

Figure 3.1: Typical AE system (Huang et al. 1998).

An AE transducer acts like the human ear, whereby it collects all the acoustic activity from its surroundings. In particular, the acoustic signals can be from the materials flaws, cracks or impact. Listening to the AE activities, which propagate from the structure being monitored, is like a one-way communication between the examiner and the structure itself. The physical motion of the AE waves will be transformed into electrical signals by the appropriate transducers and submitted to a computer for analysis. Typically for metallic structures, an AE system operates in a range of 20 kHz to 2 MHz in frequency.

The AE technique is sometimes expressed as a 'passive ultrasonic' method. The AE technique differs from a commercial ultrasonic method in one significant aspect, whereby it doesn't require the ultrasonic wave as input (Miller & v. K. Hill 2005). The energy released is from the source itself, therefore leads to the main drawback in the AE method, whereby the sources can contain a large amount of information, and complex signal analysis is needed to be done to interpret the data. However, with current development in computer technology, complex signal analysis can be done and, as a result, feature extractions of AE signals can be performed easily.

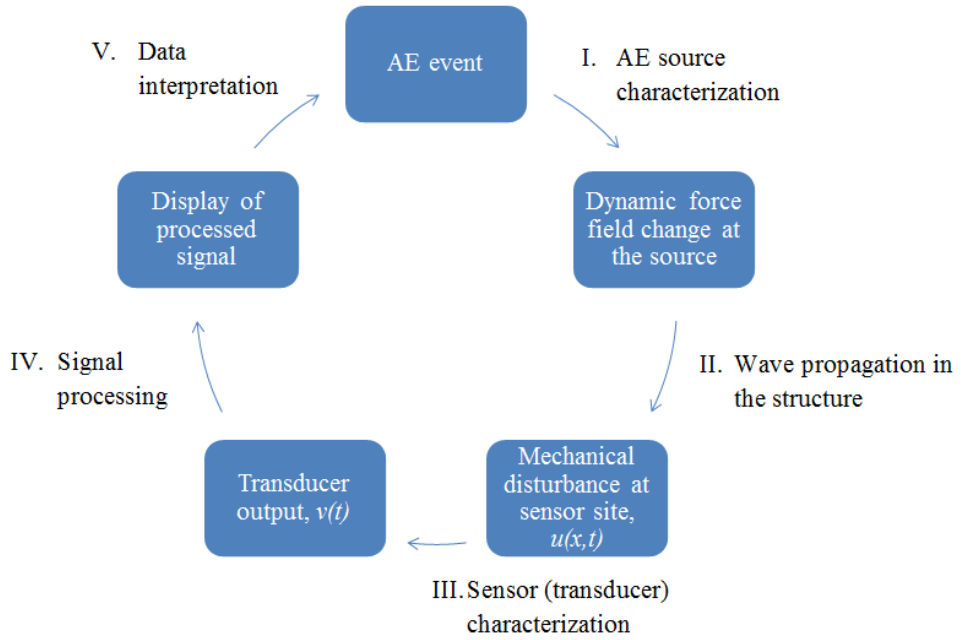

Figure 3.2: The causal chain of AE signal analysis (Eitzen & Wadley 1984).

Eitzen & Wadley (1984) had presented a useful summary of the whole AE examination process. The framework contains source generation, evolution, signal transduction and signal processing. The sequence of the process can be shown as in Figure 3.2. The general procedure reveals that there are five important aspects to understand in order to achieve the best results from the AE system;

1. AE source characterization
2. Wave propagation in the structure
3. Sensor characterization
4. Signal processing
5. Data interpretation

The first two items were already touched in the previous sections. The rest of the items will be discussed further in the next section and onwards.

3.4 Issues of AE in Composites

There are two main focuses in the application of AE for composite materials; that is the precise mapping the failure location and the identification of the failure characteristics (Eitzen & Wadley 1984). Unfortunately, up to date, both are still in need of improvement prior to become practically established in the field. Further studies are indispensable when dealing with composite materials, especially when almost all the relevant information about the existing AE techniques, are mainly dedicated for the metal structures.

Despite some attempts to incorporate the wave propagation theory composite plates, as discussed in the Chapter Two, the results of up to date studies are still in an early stage, particularly in AE for SHM. For instance, recently, Scholey et al. (2009) have suggested a model that requires several inputs including source waveforms, phase velocity and attenuation, for quantifying the performance of AE systems on a plate-like structure. Meanwhile, Scholey et al. (2010) have also introduced a procedure for determining the minimum specimen size necessary to make quantitative AE measurements. Meanwhile, Muravin et al. (2010), also shows great attention for AE in SHM whereby he presented the fundamental principles and standard approach for systematic development of new AE SHM procedures and applications.

Although the issues discussed in the next subsection were focused on the AE technique, in general, these also involve the other wave propagation based SHM systems.

3.4.1 Source localizations

There are no differences in the AE source localization techniques, either when it comes to metallic materials or composites. As mentioned earlier, the mapping of damages in thin composite plates can be done by using the appropriate number of AE sensors. For instance, in one-dimensional mapping, two sensors must be used. While for two-dimensional mapping, at least three sensors are needed. On the other hand, more than four sensors are required for three-dimensional applications.

However, the most important issues in the failure localization in composite plates is the accuracy in determining the time arrival of an AE signal to sensor. It is difficult but possible, especially when it involved anisotropic materials. A proper use of wave propagation theory can improve the accuracy of the predicted

AE wave propagation in thin laminated composite plates (Hafizi, Epaarachchi & Lau 2012), and it was discussed thoroughly in the previous chapter, and will be shown in the case study later.

The ability to obtain more accurate results may change the perspective of AE techniques, from just a global qualitative observation of structures, into a quantitative type of monitoring. Several studies had been done to investigate the potential of AE techniques for health monitoring of composite structures towards quantitative evaluation (Scholey et al. 2009, Scholey et al. 2010). Thus, leading into more general results and not case specific.

The study of AE waves should be back to basics in order to obtain accurate and consistent results (Eitzen & Wadley 1984). Meaning that, researchers should understand the mechanics of AE waves, propagating from the source to the transducer. The traditional thought that the AE system work as a black box which produces a lot of data to be interpreted; without understanding of the physical data itself is not right.

Instead, each piece of data that reaches the sensor must be taken into account as it will contain useful information if analyzed properly. Therefore, the Modal Acoustic Emission (MAE) is becoming popular nowadays, especially when it involves thin plate structures. MAE is a better concept of how Acoustic Emission signals should be treated, particularly for source location and failure characterization. In other words, MAE can offer the theoretical background for acoustic emission analysis.

By using MAE, AE signals are interpreted as mechanical waves that propagate through any structure in a variety of modes and have the characteristics of dispersion and attenuation. The example of typical AE wave traveling on thin plate can be seen as in Figure 3.3. The figure reveals that two main wave propagations exist: which are extensional and flexural waves.

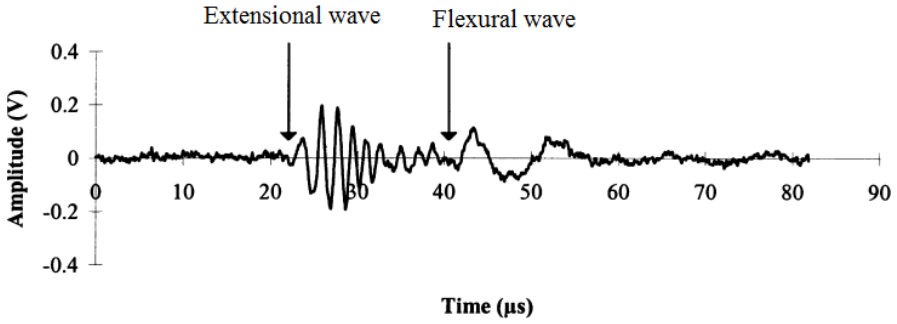

Figure 3.3: Extensional and flexural waves (Surgeon & Wevers 1999).

The MAE analysis utilized the Lamb's wave theory. Thus, the laminated plate theory, FSDT, which was explained in the previous chapter, can be referred to for better understanding. However, the use of FSDT require the exact material properties. For the case of some properties are unknown, Scholey et al. (2006) have proposed the use of *QAE-Forward* model, and the experimental results show a good agreement with the theoretical values.

Beside the FSDT, MAE also exploits the time-frequency analysis such as, wavelet or STFT analysis particularly for source localization. The advance in signal processing algorithms and assimilation of AE theory for plate-like structures (Surgeon & Wevers 1999, Morscher 1999, Prosser et al. 1995), make MAE well known in AE field.

The AE source localization using MAE approach was known to start since 1990s, when the theoretical study of AE by mean of plate wave analysis were published by Prosser (1991), Prosser et al. (1992), Prosser & Gorman (1994) and Prosser et al. (1995). The extensional component of AE wave seems not a big issue since it was predicted not dispersive in nature. However, the study of flexural modes becoming an interesting topic, and leading to the work done by Jeong & Jang (2000) and Jeong (2001). They reported the ability to measure the time arrival of flexural waves using wavelet analysis. Since then, few researchers attempted to determine the source localization by measuring the arrival time of extensional and flexural waves, and they reported better results compared to the conventional threshold-based technique (Jingpin et al. 2008, Oskouei & Ahmadi 2008).

In the conventional threshold method, the time arrival of an AE signal is determined by threshold crossing technique. The first AE envelope which cross the preset threshold is considered as the arrival of AE signal. When the AE wave is dispersive and attenuate over a distance, it may cause an error, since the original AE wave will not be in the same form when it reaches the transducer. The error size also varies, depending on the preset value of the threshold. Figure 3.4 show the example of how possible error can occur by the threshold crossing technique.

The red-dotted line in Figures 3.4a and 3.4b indicate the actual time arrival of the whole AE envelope at two different distances from AE source. However, according to the threshold crossing method, there is a possibility that the threshold will miss the actual arrival time of AE wave as shown in Figure 3.4b. Although there is an option to choose variable thresholding, whereby the threshold value is changed base on the power ratio of the signal (in unit dB), yet the possibility of the error to occur is still high.

The threshold crossing technique uses only one velocity for the arrival time of

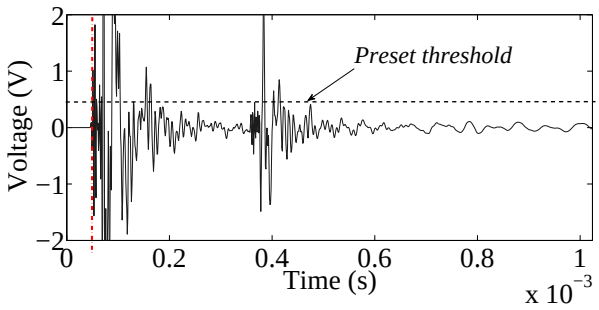

(a) AE signal obtained at 20 mm from the source.

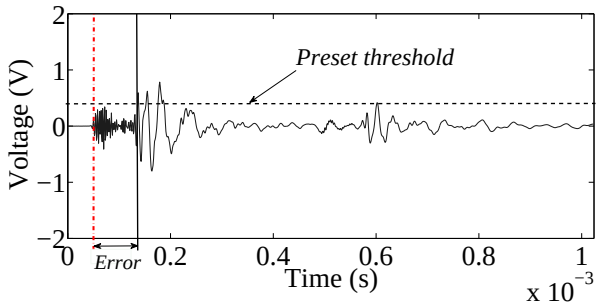

(b) AE signal acquired at 140 mm from the source.

Figure 3.4: Possible time arrival errors caused by the usual threshold method.

AE wave packet; that is the extensional wave velocity. Consider the situation in Figure 3.4b where the threshold detected the arrival of flexural velocity (have a lower frequency than the extensional mode). As a consequence, significant error will occur in the source location determination because the velocity of extensional and flexural modes are a significantly different value!

According to the MAE technique, the arrival time of the AE wave is measured based on the arrival of extensional and flexural wave modes, particularly for thin plates. The time-frequency analysis is needed to achieve this goal, whereby the arrival times are determined by the arrival of peak frequencies that represent the arrival of each mode. Figures 3.5a and 3.5b are the Continuous Wavelet Transform (CWT) version of the AE signals as in Figures 3.4a and 3.4a, respectively. By the CWT, time arrival variation of two wave modes at different distances can be observed significantly. As a result, the source location determination of AE become more accurate, and reliability was increased.

Consider one-dimensional source mapping with an AE system as shown in Figure 3.6. Based on MAE, there are two ways for an AE source location determination; using one sensor measurement or two sensor measurement.

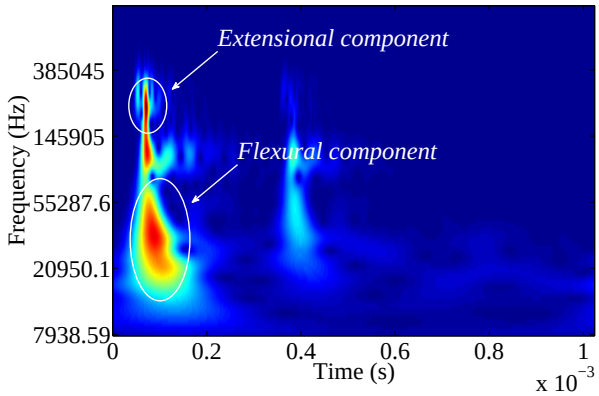

(a) CWT of AE signal which acquired at 20 mm from the source.

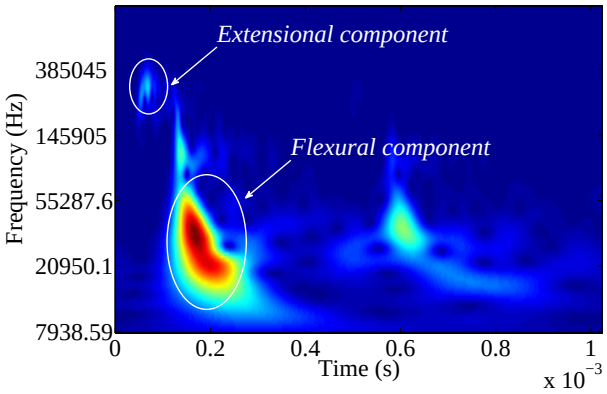

(b) CWT of AE signal which acquired at 140 mm from the source.

Figure 3.5: CWT of AE signals that show the different time arrival of extensional and flexural wave modes.

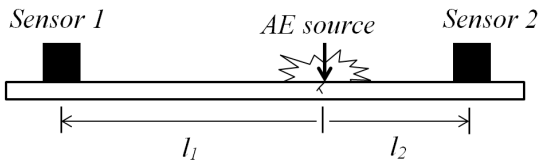

Figure 3.6: Setup for one dimensional source localization.

By using the arrival time of particular wave mode to two sensors; the group velocity c_g at certain frequency, f, can be described by (Jeong 2001),

$$c_g(f) = \frac{l_2 - l_1}{b_2(f) - b_1(f)} \tag{3.1}$$

where $b_1(f)$ and $b_2(f)$ are the arrival time of the specific frequency to sensor 1 and 2, respectively.

Based on Equation 3.1, Jingpin et al. (2008) had presented the general source determination equation for broader situation, where the two different modes could exist. For l_2 calculation, the equation can be expressed as,

$$l_2 = \frac{Lc_g^l(f_2) - c_g^l(f_1)c_g^k(f_2)[b_2(f_2) - b_1(f_1)]}{c_g^l(f_1) + c_g^k(f_2)} \tag{3.2}$$

where the $c_g^l(f_1)$ and $c_g^k(f_2)$ are the group velocities of l and k mode at frequency f_1 and f_2, $b_1(f_1)$ and $b_2(f_2)$ denote the arrival times of l and k mode at frequency f_1 and f_2 to sensor 1 and 2. For the case of only one dominant mode in an AE signal, thus $l = k$. The equation also applicable for $f_1 = f_2$ or $f_1 \neq f_2$.

Meanwhile, if two or more dominant frequencies exist in an AE signal, single sensor source localization is possible. However, it only can measure the distance, not the direction of the source. The general equation for one sensor measurement can be written as (Jiao et al. 2004, Jingpin et al. 2008),

$$l_2 = [b(f_1) - b(f_2)]/[\frac{1}{c_g^l(f_1)} - \frac{1}{c_g^k(f_2)}] \tag{3.3}$$

where the $b(f_1)$ and $b(f_2)$ refer to the arrival times of l and k modes at frequency f_1 and f_2 to sensor 2. This single sensor measurement also can be done for $f_1 = f_2$, but must have two dominant wave modes in a signal. However, if only one mode is dominant ($l = k$), then essentially $f_1 \neq f_2$.

3.4.2 Failure characterizations

Many studies have successfully predicted material properties and classified the failure mechanisms of composites by analyzing AE signals (Jalili et al. 2010, Arumugam et al. 2010, Bohse 2000, Marec et al. 2008). In the early stages, it was common for researchers to obtain a large amount of data and use the statistical figures to explain the material failures qualitatively. This style of AE data interpretation still becomes interest for some researchers (Gutkin et al. 2011, Godin et al. 2004, Johnson 2002). Instead of only qualitatively looking at the statistical data, they extracted the related features of AE signals and matched with the failure mechanism accordingly. Later, they used an artificial neural

network to predict the possible occurrence of the next failure with new AE signals. The results were promising, except the technique for data clustering or 'features matching' between the AE signals and failure mechanisms need to be improved to get an accurate prediction.

Multiple failures always occur during mechanical testing of composite samples, e.g. static tensile testing, double cantilever test and compression test. Usually for feature matching purposes, some researchers defined the range of some AE parameters such as amplitude or peak frequency that can be referred to the occurrence of a particular failure or failure modes. Table 3.1 show the summary of failure modes and the respective AE amplitude range, as described by Huguet et al. (2002). Meanwhile, Figure 3.7 is the summary done by Gutkin et al. (2011) in attempt to collect more information, to be included in their pattern recognition algorithm.

Table 3.1: Failure modes and the respective AE amplitude ranges (Huguet et al. 2002).

Failures	AE amplitude ranges (dB)
Matrix cracking	40 - 55
Debonding	60 - 65
Pull-out	65 - 85
Fibre fracture	85 - 95
Delamination	45 - 70

Instead of using typical AE parameters in the time domain such as signal energy and amplitude, there are other options; that is by using the time-scale descriptors from wavelet analysis. According to Marec et al. (2008), this method can provide better discrimination of damage mechanisms than time-based descriptors.

Meanwhile, Oskouei et al. (2009) also did the characterization by implementing the wavelet analysis. In the end, they concluded that matrix cracking was dominated in the frequency range of 125 - 200 kHz; while debonding occurred in the range of 250 - 310 kHz and the fiber breakage dominated at 375 - 440 kHz. The results agreed well with the summary that is described in Figure 3.7.

Although there are plenty more reported studies attempting to use this traditional method of AE analysis for composite materials, quantitative results are still difficult to be achieved. This 'bulky' approach will collect all AE data without seriously considering the buried noise signals in the waveforms although some filtering was done during the measurement process.

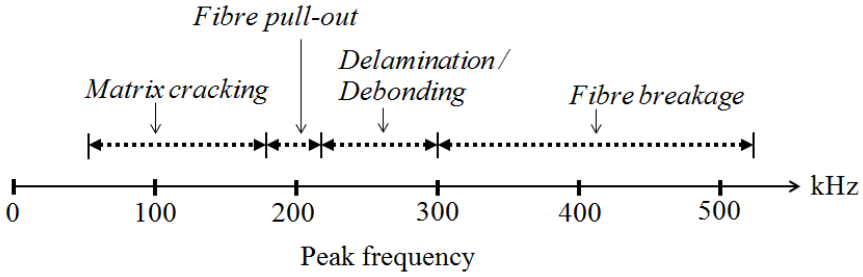

(a) Reported by de Groot et al. (1995).

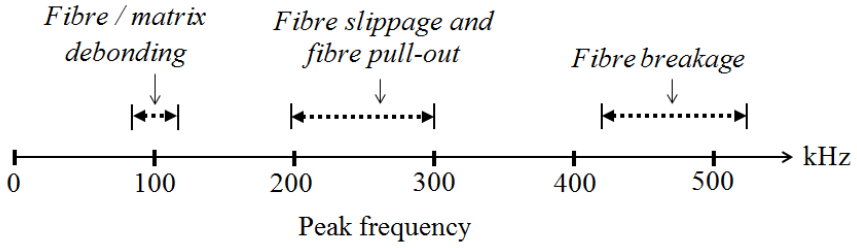

(b) Reported by Jimenez et al. (2004).

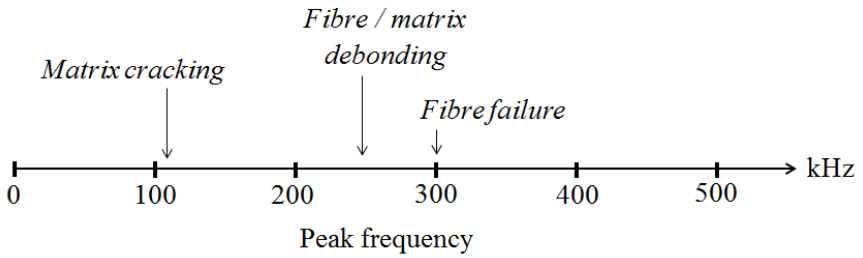

(c) Reported by Qi (2000).

Figure 3.7: Summary of some frequency ranges defined by several researchers (Gutkin et al. 2011).

Fortunately, modern computer technology helps solving this problem where individual wave analysis of an AE signal can be done. Thus, failure mechanisms can be recognized more precisely. Obviously this is referred to the MAE.

MAE analysis can reveal the orientation of the AE source as discussed by Gorman & Prosser (1991) and Surgeon & Wevers (1999). The relation between AE wave modes and the source orientation caused by failure mechanism was already discussed in Chapter Two, Section 2.4.

Meanwhile, Scholey et al. (2010) had performed the experiment that clearly shows how matrix cracking and delamination can be distinguished by detail investigation the AE wave modes. They found that, matrix cracking are dominated by symmetric, S_0 wave mode while the antisymmetric wave mode, A_0, dominates

the events due to delamination growth. The essential part that need to be highlighted in their experimentation is the placement of sensors. Sensor pairing must be used in order to specify which wave mode is dominant in an AE signal (Hafizi et al. 2013). The details of measurement's mechanism is presented in a case study, in the next section.

3.5 Case Study: Single-channel AE for Source Mapping

As mentioned earlier, MAE treats AE signals as mechanical waves that propagate through a thin structure in a variety of modes. Analyzing these different modes of AE signals will give a more accurate result of failure characterization and source location detection. Moreover, it has also made single sensor source location possible (Jiao et al. 2004).

In some research works, only standard pencil break tests were performed to prove the findings (Jing-Pin et al. 2006, Jingpin et al. 2008, Oskouei & Ahmadi 2008). Even though the results were reasonably good, almost all works were only up to case specific but not competent enough to apply for a wide range of materials, such as composite materials. The fact that a pencil break test is only created by an external AE source, makes almost all previous studies invalid for real cases, such as in a composite laminates micro-failure characterization study where the sources are produced internally. This case study was aimed to report and discuss the MAE investigation on thin composite laminates sample under tensile test.

A standard static tensile test (ASTM-D3039/D3039M-08 2008) was carried out on a 250 mm $\times$ 25 mm fiberglass epoxy resin plate with thickness of 2.64 mm. The unidirectional laminate with stacking sequence $[0^o]_4$ was fabricated using the hand lay-up method. The experimental set-up was as shown in Figure 3.8.

Meanwhile, Figures 3.9 and 3.10 show the dispersion curves generated for the sample with density value 1559 kg/m^3 and thickness 2.64 mm. The dispersion curves were generated by *PACShare Dispersion Curves* free software. It is observed that, when the excitation frequency is smaller than 400 kHz, only fundamental modes; S_o (Symmetric) and A_o (Asymmetric) exist.

An artificial notch with approximately 3 mm length was created and located 75 mm from each sensor to initiate crack and AE activity. Two piezoelectric sensors were coupled to the surface of the plate and were placed 150 mm apart from each

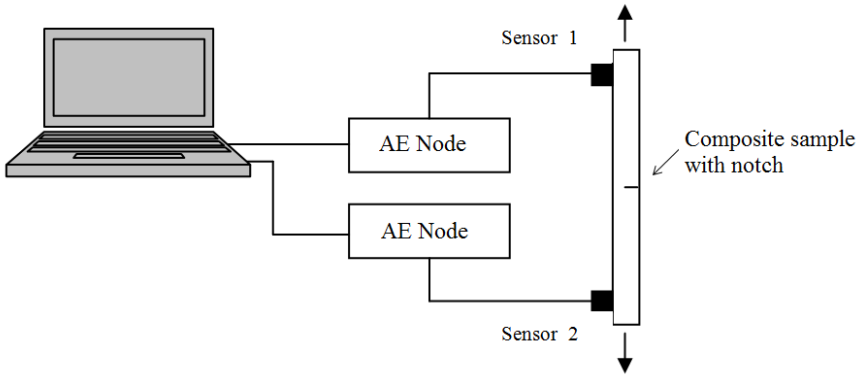

Figure 3.8: Set-up of the test for case study 3.5.

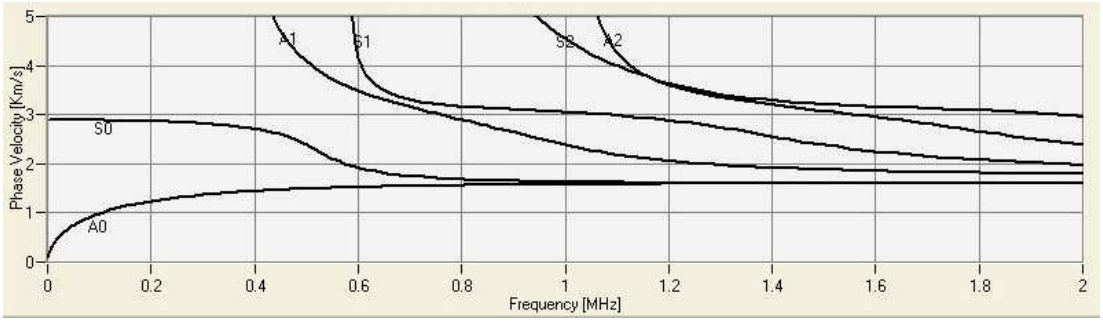

Figure 3.9: Phase velocity dispersion curves.

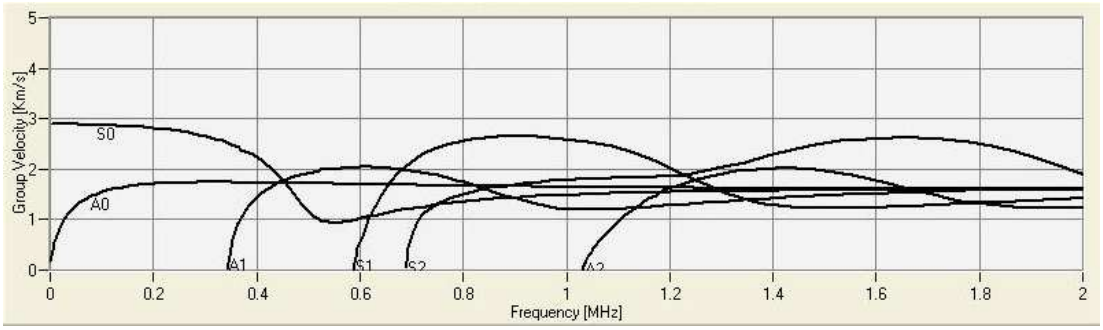

Figure 3.10: Group velocity dispersion curves.

others. The sensors were individually connected to two PAC AE Node Systems (data acquisition from Physical Acoustic Corporation) for waveform acquisition and were synchronized with the help of *AE Win* software. All the received signals were analogue filtered to the range of 20 kHz 200 kHz. The sampling rate for acquisition was set to 5 Mega samples per second and threshold was set to 45 dB. In the *AE Win* software, the first time threshold crossing (FTC) was chosen for the source location detection. All acquired waveforms were stored in a computer for further analysis.

3.5.1 Results and discussion for the single-channel AE for source mapping case study

Table 3.2 provide the tensile test result summary of a few samples. Meanwhile, the stress-strain plot of the samples is as shown in Figure 3.11.

Table 3.2: Summary of tensile test result.

Specimen	Average thickness (mm)	Average width (mm)	Peak stress (MPa)	Modulus (MPa)	Poisson's ratio
1	2.73	25.84	487.59	21237	0.262
2	2.66	25.48	508.42	22700	0.275
3	2.62	25.37	519.76	22628	0.267
4	2.75	25.31	536.39	21582	0.261
Mean	2.69	25.50	513.04	22037	0.266

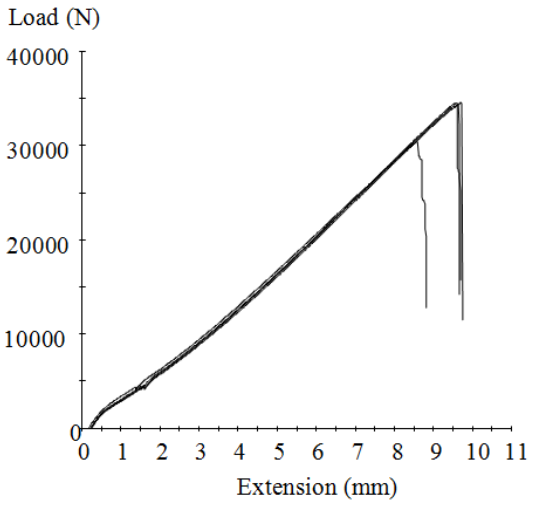

Figure 3.11: Stress vs. strain of the specimens

Alternatively, FSDT also can be used for the dispersion curves prediction. For this purpose, material properties of the GFRP as in the Table 5.2 was used (derived from the tensile test result). Therefore, the predicted curve for group velocity can be shown as in Figure 3.12.

The AE hit numbers and cumulative hits versus time is as shown in Figure 3.13. The result shows the typical AE hits pattern for any GFRP sample under static tensile loading. Most of AE activities will occur very rapidly at the half way point of the loading before final failure.

Table 3.3: Material properties of the sample.

Parameters	Values
E_1	22037 MPa
E_2	7378 MPa
v_{12}	0.266
G_{12} and G_{13}	8741 MPa

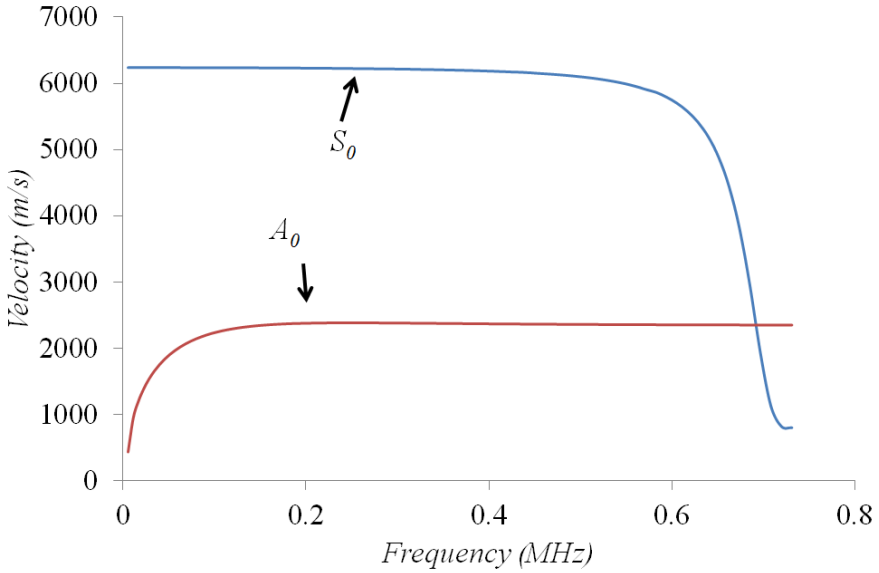

Figure 3.12: Group velocity predicted by FSDT

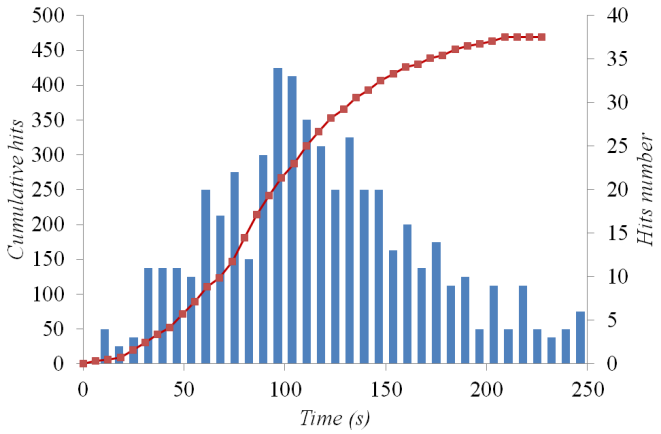

Figure 3.13: AE hit numbers and cumulative hits versus time.

Meanwhile, Figure 3.14 shows the plot for a one-dimensional location prediction by the *AE win* software. The plot indicates that a lot of AE activities are also happening at the grip area. In order to eliminate the AE activities due to the

cracking process at the grip, AE signals were filtered at 70 dB, and the result can be shown as in Figure 3.15. In this study, the AE signals which are above 70 dB can be considered as a powerful signal. These strong signals start to occur after 10 - 11 seconds of the loading; during the beginning of cracking process at notch area, at approximately 30 percent of strain.

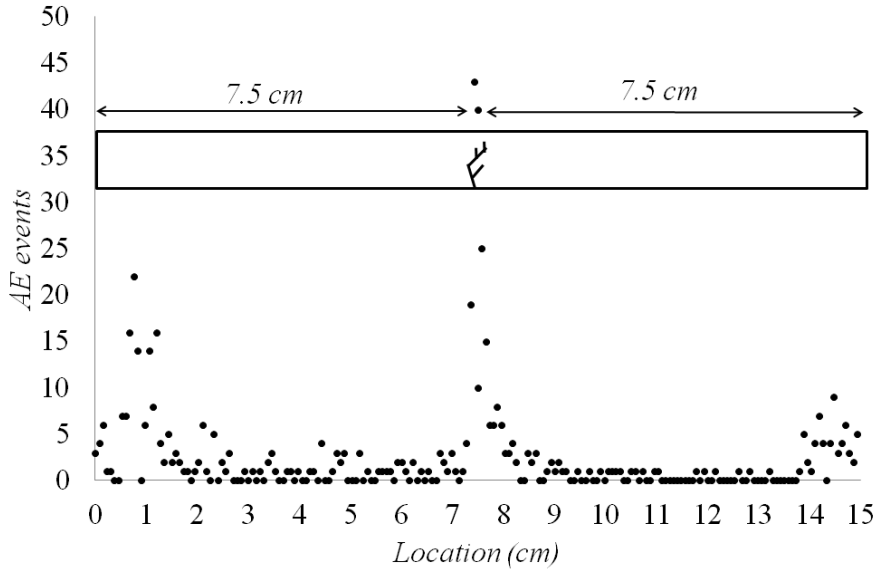

Figure 3.14: One dimensional source localization with two AE sensors.

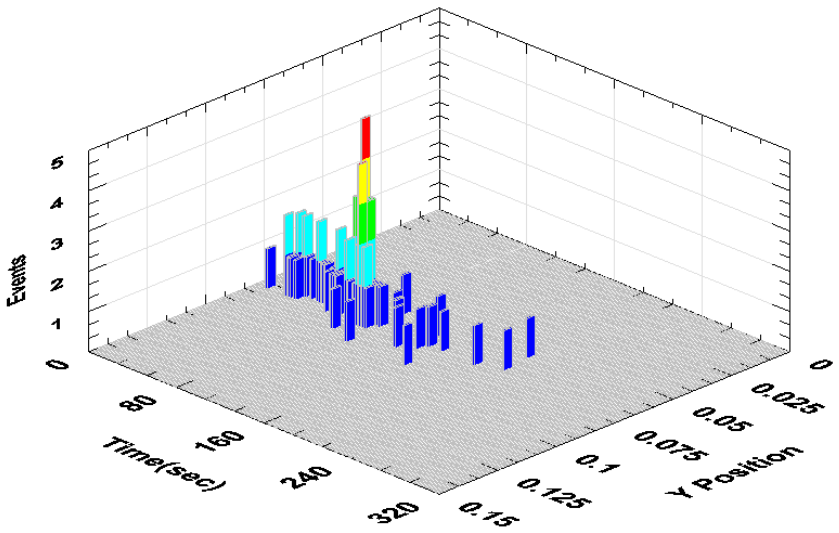

Figure 3.15: AE events at crack location; near notch.

The first event of the AE signal from the filtered data, which was captured by sensor 2, was taken for further analysis. This particular signal was predicted to occur precisely at the crack location. The waveform and its amplitude spectrum can be shown as in the Figure 3.16. Two peak frequencies appeared in the

spectrum analysis, which indicated the existence of two wave modes; extensional and flexural wave modes.

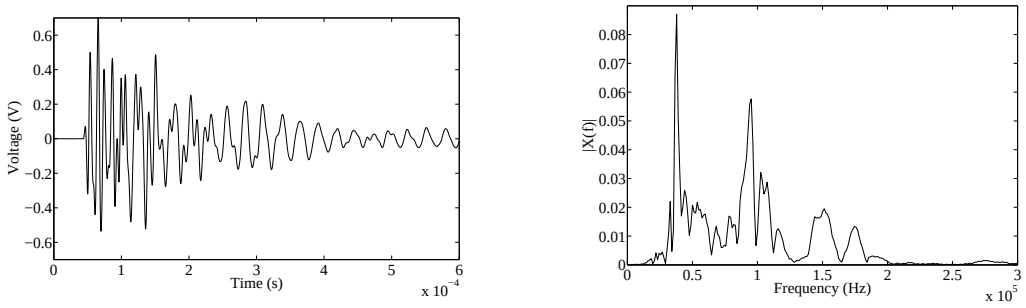

(a) AE waveform. (b) FFT analysis.

Figure 3.16: AE waveform and its spectrum.

MAE analysis

STFT analysis of the waveform successfully displayed the arrival time of each frequency band in the waveform spectrum as shown in Figure 3.17. By calculating the time arrival of two peak frequencies from the dispersion curve (see Figure 3.10); 37 kHz (flexural wave, A_o) and 100 kHz (extensional wave, S_o) and each corresponding group velocities, the location of the AE source can be predicted.

The arrival time for A_o and S_o wave modes were measured as 0.1136 ms and 0.0688 ms, respectively. Meanwhile, according the group velocity dispersion curve, as in Figure 3.10 (Lamb's frequency equation), the wave velocity for A_o and S_o wave modes were 1160 ms^{-1} and 2870 ms^{-1}, respectively. Therefore, the distance between the source location and Sensor 2 can be determined using Equation 3.3. The result was 87 mm; 16 % or 12 mm error compared to the actual position (75 mm).

Meanwhile, based on FSDT, the wave velocity for A_o and S_o wave modes were 1687 ms^{-1} and 6235 ms^{-1}, respectively. As a result, the new calculated distance was 103.6 mm; which was about 38 % relative error.

Time arrival determination of wave modes using STFT clearly revealed a considerable large error. Fortunately, the error can be decreased if a Continuous Wavelet Transform (CWT) analysis is used instead of STFT. CWT performs better time and the frequency resolution compared to STFT thus can lead to more accurate result (Hamstad et al. 2002).

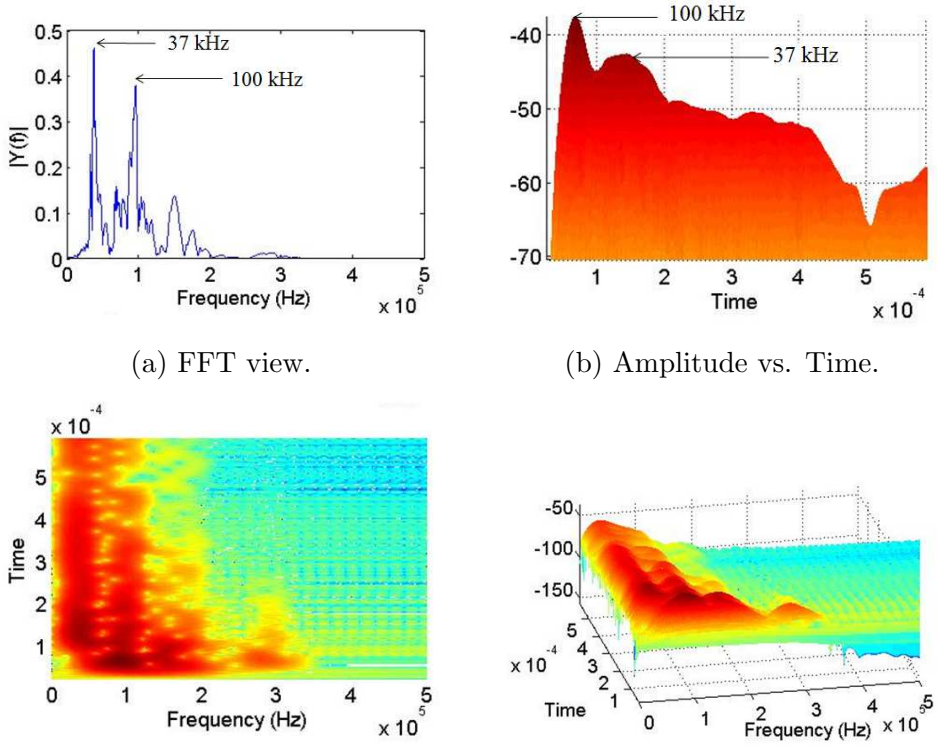

(a) FFT view.

(b) Amplitude vs. Time.

(c) Time vs. Frequency.

(d) 3D view.

Figure 3.17: STFT analysis.

Figure 3.18 shows the CWT of the AE signal; in terms of scale versus time. In the meantime, the CWT also can be viewed by a frequency versus time plot, as shown in Figure 3.19. The mother wavelet used for the analysis was the *Morlet* wavelet. Note that, the scale-time version can give better time resolution; especially for accurate arrival time measurement.

The new time arrival for A_o and S_o wave modes were now measured as 0.1036 ms and 0.0652 ms, respectively. Therefore the new calculated AE source location, based on group velocity curve by Lamb's frequency equation is 74.8 mm; 0.27 % relative error. Meanwhile, if utilizing the group velocity curve approximation by FSDT, the location was measured as 88.8 mm; 17.3 % relative error.

3.5.2 Conclusion for the single-channel AE for source mapping case study

The MAE was proved to be a useful tool for source location prediction, especially with the additional attractively single sensor AE location measurement. In particular, the CWT was shown to have a better time-frequency resolution compared

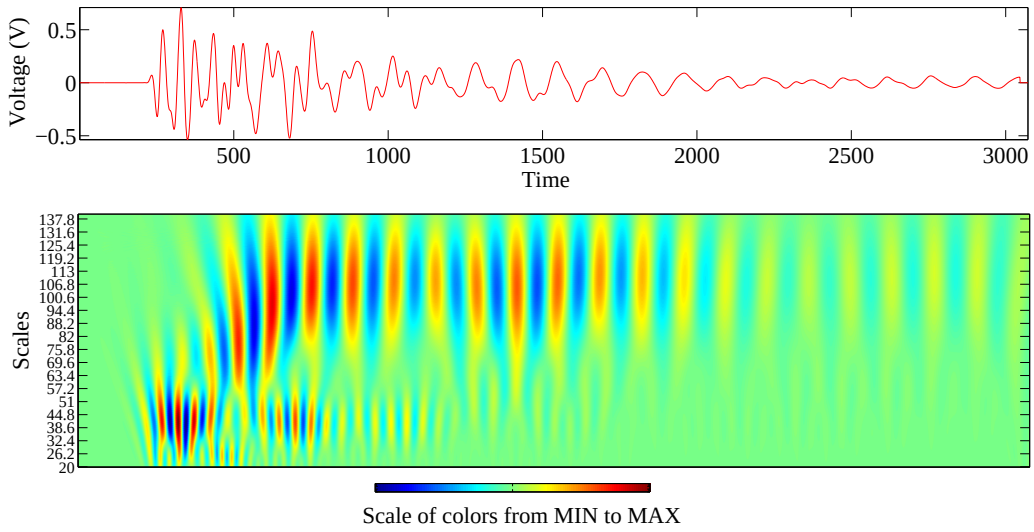

Figure 3.18: CWT analysis of the waveform; scale vs time.

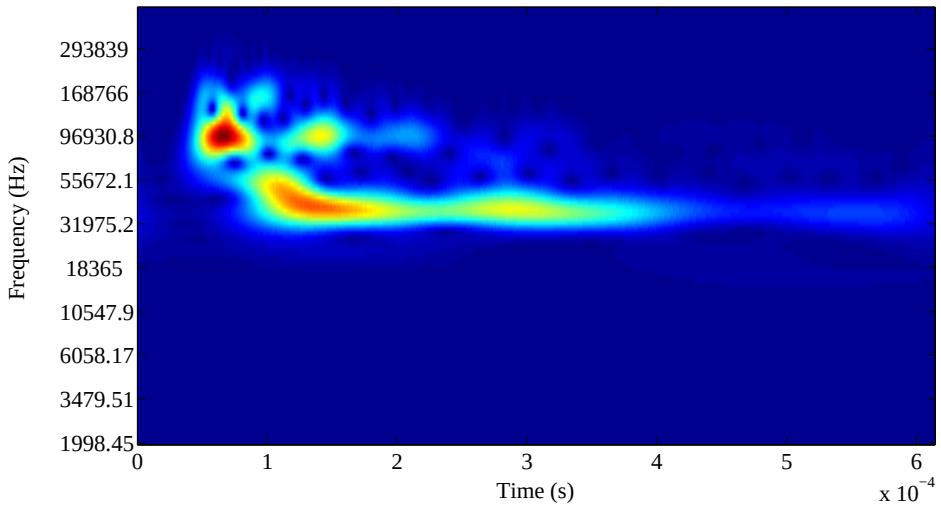

Figure 3.19: CWT analysis of the waveform; frequency vs time.

to STFT, thus provided a much more accurate result.

This case study also revealed that the dispersion curve approximation by FSDT was unable to give an exact result for the AE source mapping. It was maybe due to the inaccurate determination of the material properties during tensile testing. In other words, it was as the result of a significant variation of local material properties due to the hand lay-up process during sample's fabrication. However, the approximation of the dispersion curve by using Lamb's frequency equation was able to indicate a good result, particularly for unidirectional laminates.

3.6 Case Study: GFRP Plates Under Tensile Test

This case study also attempted to report and discuss the MAE investigation on thin composite laminate samples under tensile tests. However, the main objective was to observe the behavior of AE signals if the source was from micro-cracking.

As proposed by Surgeon & Wevers (1999), matrix cracks and fiber fracture will generate extensional wave mode signals while delamination is expected to produce flexural wave mode signals; as explained in chapter 2. Therefore, it is expected that matrix cracking and fiber fracture will give *in-phase* signals from two sensors, where each is located on the top and bottom surface of composite plates; as shown in the setup in Figure 3.20. Meanwhile, *out-of-phase* signals are predicted if the AE source is from delamination.

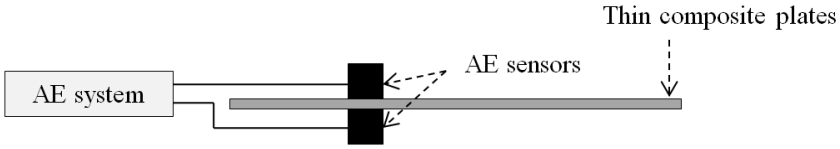

Figure 3.20: Set-up for AE wave mode determination

A unidirectional, 400 mm × 400 mm × 2.9 mm thin fibreglass epoxy resin plates with stacking sequence $[0^o]_4$ was prepared using the hand lay-up method. Later, the plate was cut into smaller piece; 250 mm × 25 mm (250 mm length is in fibre direction) with 6 mm notch, for tensile test. Four AE sensors (Physical Acoustic Corporation, *R*6) with a resonance frequency 60 kHz were attached on the sample and numbered as in Figure 3.21.

All sensors were connected individually to four single channels Physical Acoustic Corporation (PAC) AE Node systems and the systems were combined to create a four channel AE system for data acquisition. All AE Nodes were set to sample AE data at 5 Mega-samples per-second (MS/s) with a threshold at 45 dB. AE signals were analog filtered between 20 kHz to 200 kHz. The full experimental set-up is shown in Figure 3.21 and Figure 3.22 and the tensile test was done at the rate of 2 mm per minute.

Before starting the tensile test, a pencil lead break (Hsu-Nielsen test) was done on the sample; 50 mm from sensor 3. Two sets of Hsu-Nielsen tests were done; one on the surface or x-y plane (for flexural source) and another one on the edge or *y-z* plane (for extensional source). The Hsu-Nielsen test results can be used for source location determination using MAE technique and also for the verification

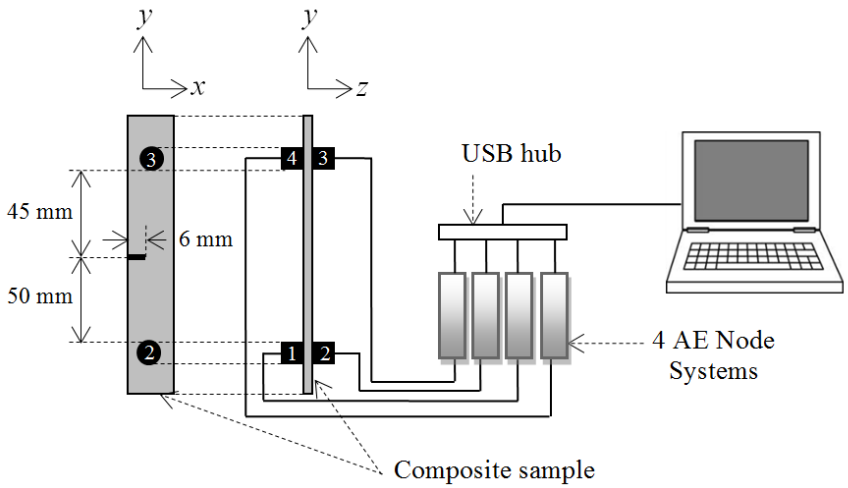

Figure 3.21: Experimental set-up for case study 3.6. Note that the specimen's dimensions is 250 mm × 25 mm × 2.9 mm.

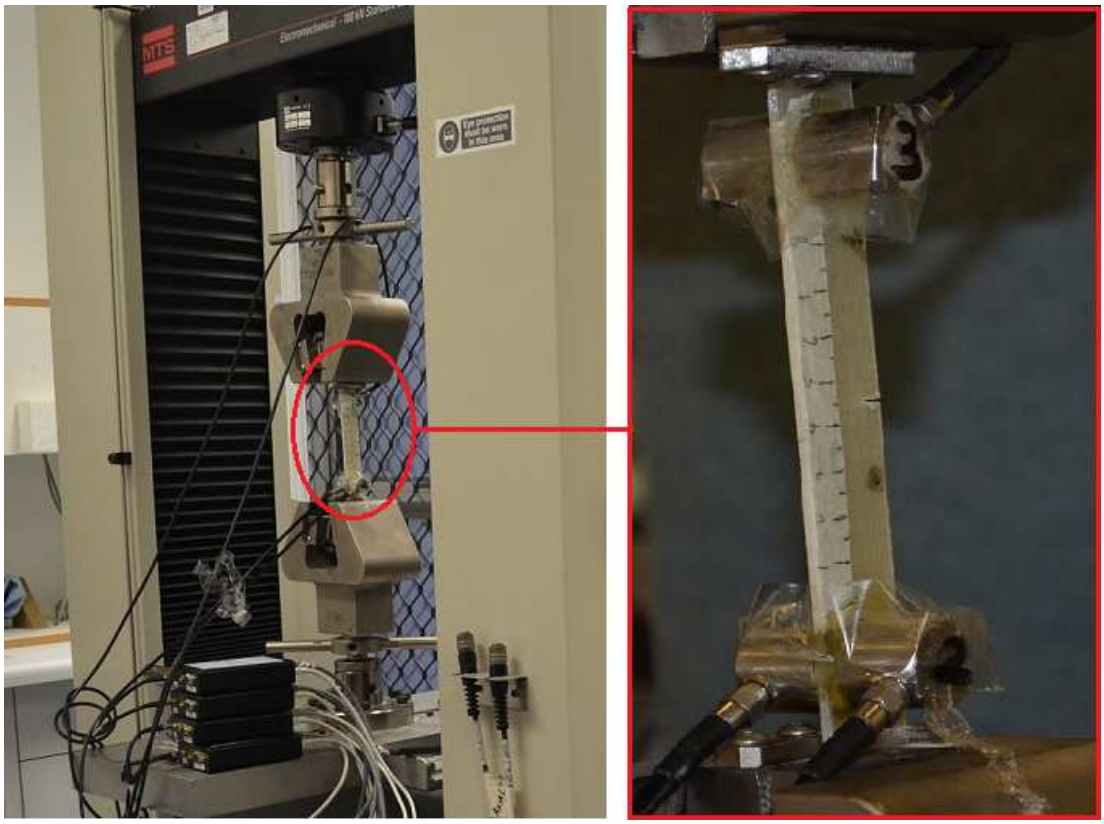

Figure 3.22: Sample under testing.

of AE signals acquired from tensile test.

3.6.1 Hsu-Nielsen test results

Typical AE signal's waveforms from Hsu-Nielsen test can be viewed as in Figure 3.23 and Figure 3.24 respectively. The dotted line indicates the AE signal from sensor 1 and the solid line shows the signal from sensor 2. In the meantime, Figure 3.25 shows the frequency spectrum comparison of typical AE signal from sensor 1 for both types of AE sources. As expected, both extensional and flexural sources gave two peak frequencies; which are symmetric S mode, and asymmetric A mode.

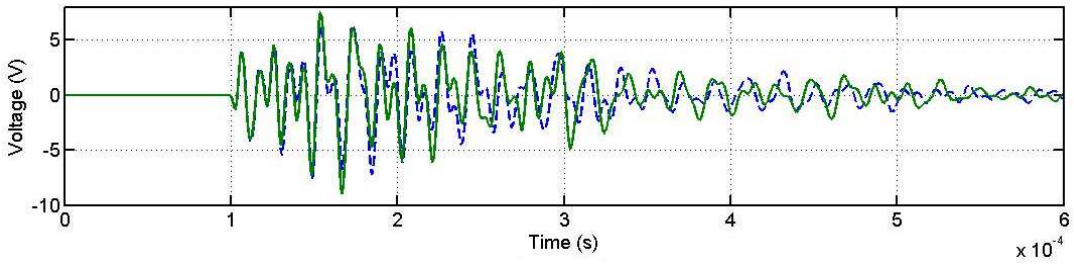

Figure 3.23: Signal waveform from extensional AE source.

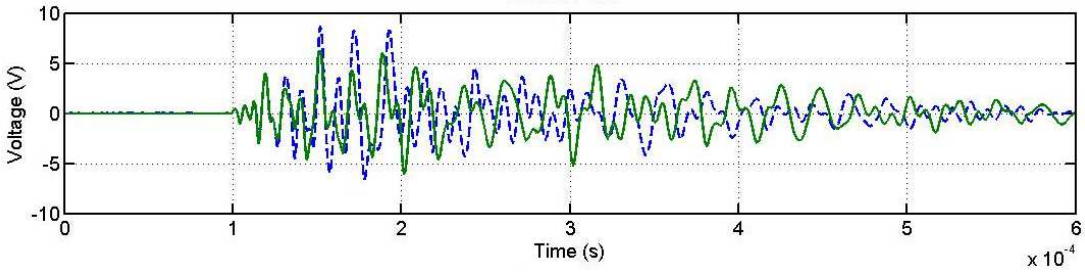

Figure 3.24: Signal waveform from flexural AE source.

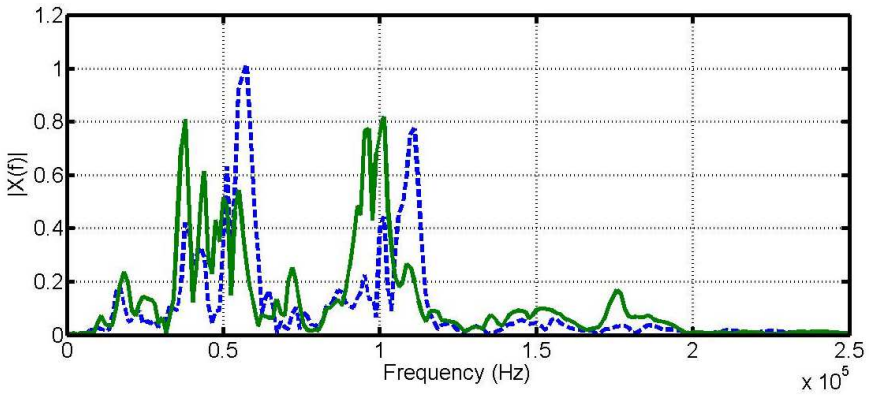

Figure 3.25: FFT comparison.The dotted blue line indicates the signal from extensional source and the solid green line shows the signal from flexural source.

The most dominant wave propagation between the two modes can be determined by looking at the waveform comparison in Figure 3.23 and Figure 3.24. It can

be concluded that the extensional source produced a symmetric wave. Although the asymmetric wave appeared approximately 0.2 milliseconds later, it still can't affect the overall domination of the symmetric mode. Note that, for the extensional source, the corresponding AE signals were in-phase until the end of the signal's duration. On the other hand, the flexural source shows the domination of an asymmetric wave; where the signals were *in-phase* at the beginning but then, start to *out-phase* approximately after 0.13 milliseconds.

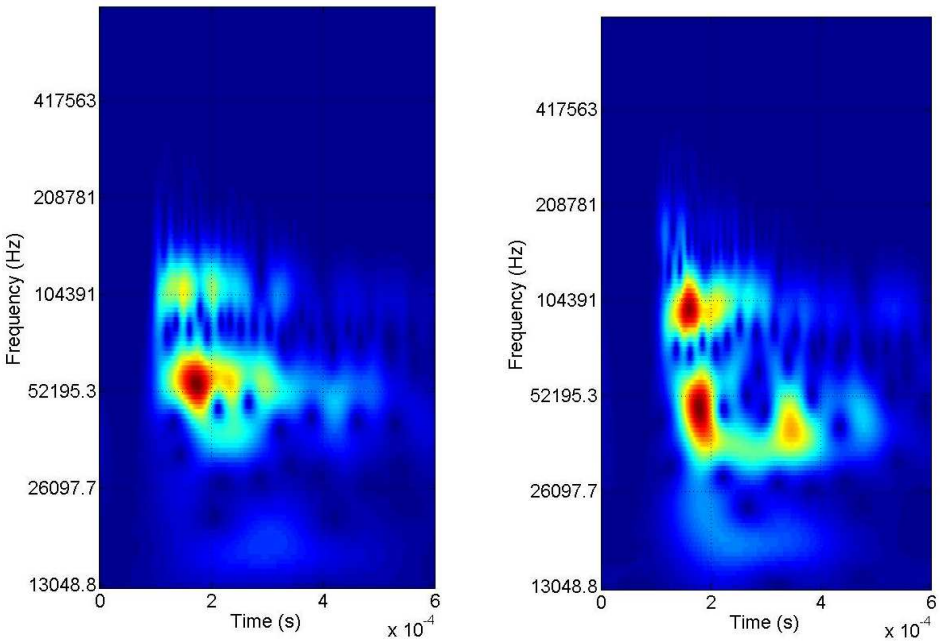

(a) Extensional source. (b) Flexural source.

Figure 3.26: Wavelet analysis of AE signals emitted by different source orientation.

Meanwhile, the wavelet analysis of the signal captured by sensor 1 for both types of AE sources were as shown in Figures 3.26. Note that, each frequency components arrived at the sensor at different arrival time. The time differences can be used for source mapping; especially using a single channel of an AE system. In order to calculate the source location using MAE, the group velocity for both A and S modes need to be determined. The group velocity dispersion curves for the sample can be used as the same as in the previous case study (see Figure 3.10). Meanwhile, the single channel source mapping can be calculated using Equation 3.3.

From Figure 3.26a, the arrival time of A_o and S_o modes were at 0.1726 milliseconds and 0.0151 milliseconds, respectively. Meanwhile, according to the group velocity dispersion curves (see Figure 3.10), the wave velocity of A_o (52 kHz) and S_o (100 kHz) modes for the same AE signal were 1359 ms-1 and 2870 ms-1, respectively. Therefore, the distance between the source location and sensor 1

was 55.76 mm; which results in 5.76 mm absolute error (11.5 % relative error) compared to the actual position. In the meantime, using the same calculation, the source detection result for the AE signal that was generated from the flexural source was 43.22 mm; which gives 6.78 mm absolute error (13.6 % relative error) if compared to the actual position.

3.6.2 Tensile test results

The tensile test for the composite sample with a small notch was done until the sample reached final fracture (see Figure 3.27b). Failure starts to develop and propagates at the notch area as shown in Figure 3.27a, where matrix cracks and fibre fracture were expected to occur due to the notch.

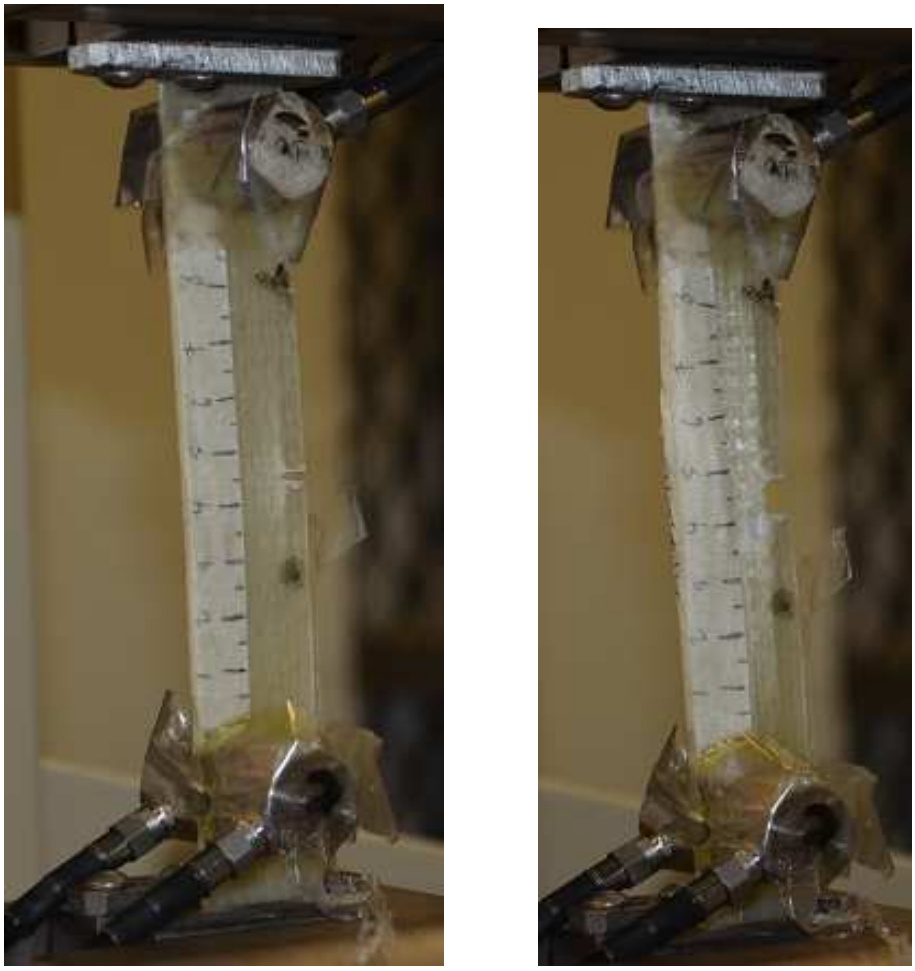

(a) Failure start to propagate. (b) Final failure.

Figure 3.27: Composite specimen during tensile test.

Approximately 9000 AE data points (hits) were successfully recorded during the

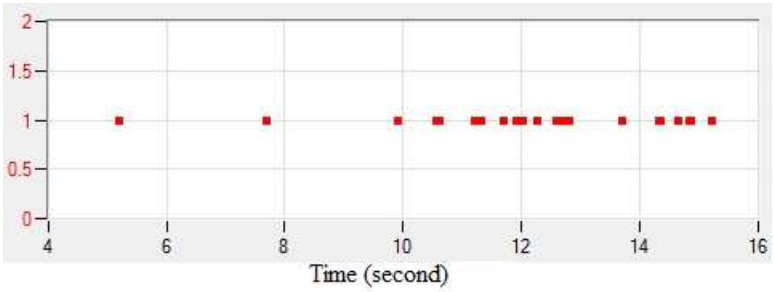

Figure 3.28: : All AE data in 16 seconds of recording time.

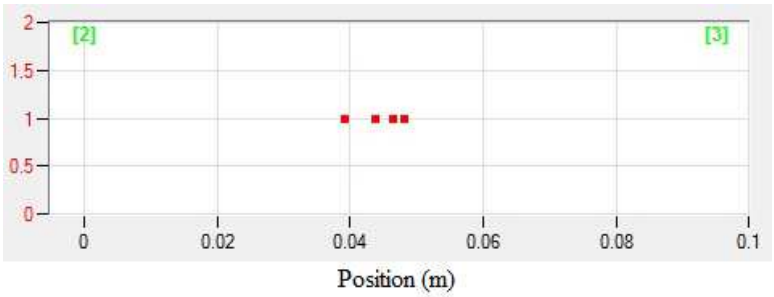

Figure 3.29: AE events at the notch area.

experiment. However, it is more attractive to view and characterize the failure mechanism at it earliest stage. Owing to that, the AE data from the first 16 seconds, as in Figure 3.28, were further processed in detail; where almost all the AE sources were from matrix cracks during this time frame, and could easily be seen by the naked eye. However, only four hits were recorded by the source mapping's algorithm in the AE win software as shown in Figure 3.29. The detection algorithm only will records the signals that have sufficient energy; that captured by two sensors for linear source mapping, and for this case the sensors are sensor 2 and 3.

Meanwhile, Figure 3.30 displays one example of all four AE hits; which was detailed by means of waveform comparison for sensors 1 and 2; together with Fast Fourier Transform and wavelet analysis of the AE signal from sensor 1. The rest of the signals can be seen in Appendix B. It is clear that, the result from CWT analysis for all signals show consistency with its FFT and waveform comparison. Unlike the signals from Hsu-Nielsen test, only one peak frequency appears from wavelet analysis of all four AE signals that were produced by matrix cracks; which makes the single channel AE source mapping difficult to be done.

In the meantime, all four signals show peak frequency values in the range between 50 and 60 kHz and have low amplitude; that were consistent with the matrix cracking source as presented in previous works (Barr & Benzeggagh 1994). Obviously, AE waveforms captured at sensor 1 and 2 for all signals were *in-phase*;

which indicate the domination of S mode, thus confirmed that matrix cracking produced symmetric wave mode signals. The similar result also was reported by Scholey et al. (2010).

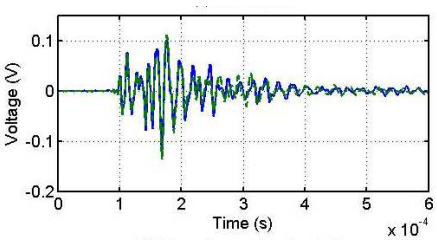

(a) Waveform comparison.

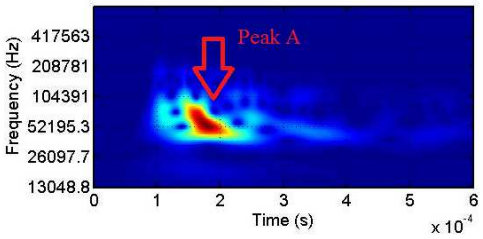

(b) Wavelet analysis.

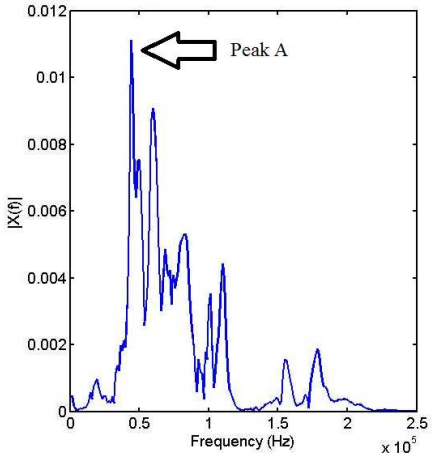

(c) FFT.

Figure 3.30: Signal analysis of AE data from matrix crack.

3.6.3 Conclusion for the GFRP plates under tensile test case study

In conclusion, the study successfully presented the MAE investigation on a thin laminated composite sample under a static tensile test. By an appropriate experimental setup, the matrix cracking can be seen producing AE signals that dominated in a symmetric (S) wave mode. However, in practice, this set up might be difficult to be achieved unless the composite plates were embedded with appropriate sensors on its top and bottom surface. This suggestion will be further detailed in the next chapter.

On the other hand, the Hsu-Nielsen test on the sample shows great accuracy using single channel source mapping utilizing MAE, however it seemed to be unpractical

in a real case since it is difficult to get signals that have two very clear dominant wave modes. As s consequence, successful source localization must use at least two sensors.

3.7 Wave Energy Attenuation of AE signals

In general, the energy of the AE signals emitted from its source is very low. Thus, the AE signal energy attenuation issue is something that needs to be emphasized; especially when involving AE wave propagation across a composite plate.

There are two conditions that need to be addressed carefully. First, is the AE signal energy attenuation from the source to the AE sensor, and the second is the energy attenuation of AE signals from the sensor to the data acquisition (DAQ) system. For the second condition, it can be easily resolved with the use of a suitable pre-amplifier. However, use of a pre-amplifier is sometimes not enough particularly, if the distance between the sensors and DAQ is too far; for instance, 10 metres. Fortunately, this problem can be solved with the use of fibre optic technology and will be detailed in the next chapter.

However, this section attempts to describe the AE energy attenuation when passing from the source to the sensor. Although composite materials can be produced to obtain the feature that allows wave propagation with less attenuation, they have a high level of damping; especially GFRP laminates. Not only that, the AE waves propagate in the ultrasonic range, and in an ultrasonic wave study, it is necessary to include the effect of wave signal attenuation.

In general, sound wave attenuates with this relation (Shull & Tittmann 2002),

$$A = A_0 e^{-\alpha z} \tag{3.4}$$

where A_0 is the amplitude of the propagating wave at the initial point or defect source. The amplitude A is the decreased amplitude as the wave travels into the distance z from the source or initial location. α value refers to the attenuation coefficient of the wave travelling in z-direction, and the dimension can be written as nepers/length.

The same model can be applied for the signal energy attenuation of AE signals

propagation on thin composite plates which can be expressed as a universal model,

$$E_i = E_0 e^{-\widehat{\beta}(|x_i - x_0|)} \tag{3.5}$$

where x_0 is referred to the location of source, x_i is the location of sensor i, E_0 is the energy at source, E_i is energy at sensor i and β is the decay constant. Equation 3.5 can be used for linear source location detection using a set of two sensors. In the case of value β being unknown, three sensors are needed and it can be expressed as,

$$(\ln \frac{E_3}{E_2} / \ln \frac{E_2}{E_1}) = \frac{|x_2 - x_0| - |x_3 - x_0|}{|x_1 - x_0| - |x_2 - x_0|} \tag{3.6}$$

3.8 Case study: Non-velocity Based Source Mapping

This case study attempts to utilize the non-time-based or non-velocity based source mapping, particularly for composite thin laminates. To achieve the goal, the attenuation behaviour of an AE wave can be used for source localization.

This technique is not new, as it is already being used in practical applications; e.g. for pipe leak location determination. It was not quite familiar, since the time-based source localization method seems easier and more reliable, yet it is true for metallic materials. The fact that composite materials usually give some errors when using a velocity-based source detection technique, as discussed in the previous section, the energy attenuation method can be an alternative solution (Hafizi, Nizwan & Lau 2012).

Three test setups were designed and prepared for signal energy attenuation, non-velocity source mapping and effective detection length study. For this purposes, $400mm \times 400mm \times 2.9mm$ GFRP laminates with a stacking sequence $[0^o]_4$ were fabricated using the hand lay-up method.

The plates' signal energy attenuation rates were plotted for several different angles; 0^o, 45^o, 60^o and 90^o, by breaking the pencil lead at several points along the given angles in a straight line, starting from one side of the composite specimen towards the other edge. As an example, Figure 3.31 shows the setup for the 45^o test. Note that the angle 0^o was referred to a line along the glass fibre. For data

acquisition two single channel Physical Acoustic Corporation (PAC) AE Node Systems were used. Each of them was connected with two different types of AE sensors (from PAC) which were NANO-30 with working frequency 100 kHz to 700 kHz (channel 1) and $R6\alpha$ with the resonance frequency 60 kHz (channel 2).

In the meantime, AE Win software was used to control the acquisition process. For instance, all the received signals were filtered in the range of 20 kHz to 1000 kHz because a fundamental wave propagation mode was targeted in this study. The sampling rate for acquisition was set up to 5 Mega samples per second, and the threshold was set to 45 dB.

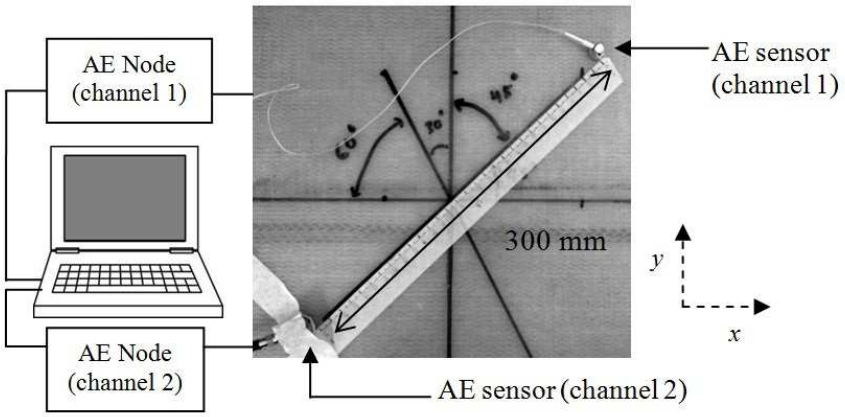

Figure 3.31: Diagram for first experiment

As a validation of the non-velocity source mapping approach, a simple test was done by applying a pencil lead break; as an artificial AE source, at several locations on the specimen. For each position, AE signals were acquired at three places (A, B and C) as indicated in Figure 3.32. Note that only one NANO-30 sensor and a single channel AE node for data acquisition was used. This procedure was repeated for angles 0^o, 45^o, 60^o and 90^o. All signals were recorded, and the linear source mapping was determined using equation 3.6 as explained in the next section.

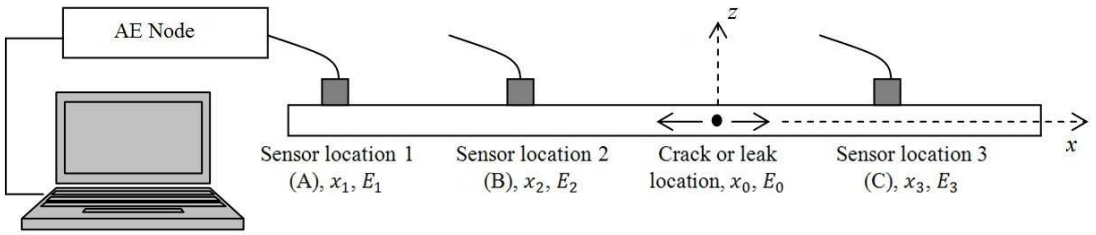

Figure 3.32: Diagram for second experiment

3.8.1 Result and discussion for non-velocity based source mapping case study

Two types of AE sensors were used in this work: broadband, NANO-30 and resonance frequency sensor, $R6\alpha$. Figure 3.33 shows the resulting comparison of AE signal capture for each sensor with the same AE source (pencil lead break). With respect to the MAE study, a broadband sensor is better due to its ability to receive more frequency content from the AE source, as seen in Figure 3.33(c) and (d), therefore, giving accurate information for composites early failure characterization. However, it is clear that the total signal energy which acquired form the broadband sensor was far less than the total energy of AE signals obtained through the resonance frequency sensor (see Figures 3.33 and 3.34). Although the total energy was different, it didn't affect the attenuation pattern of the AE signals' energy as indicated in Figure 3.34.

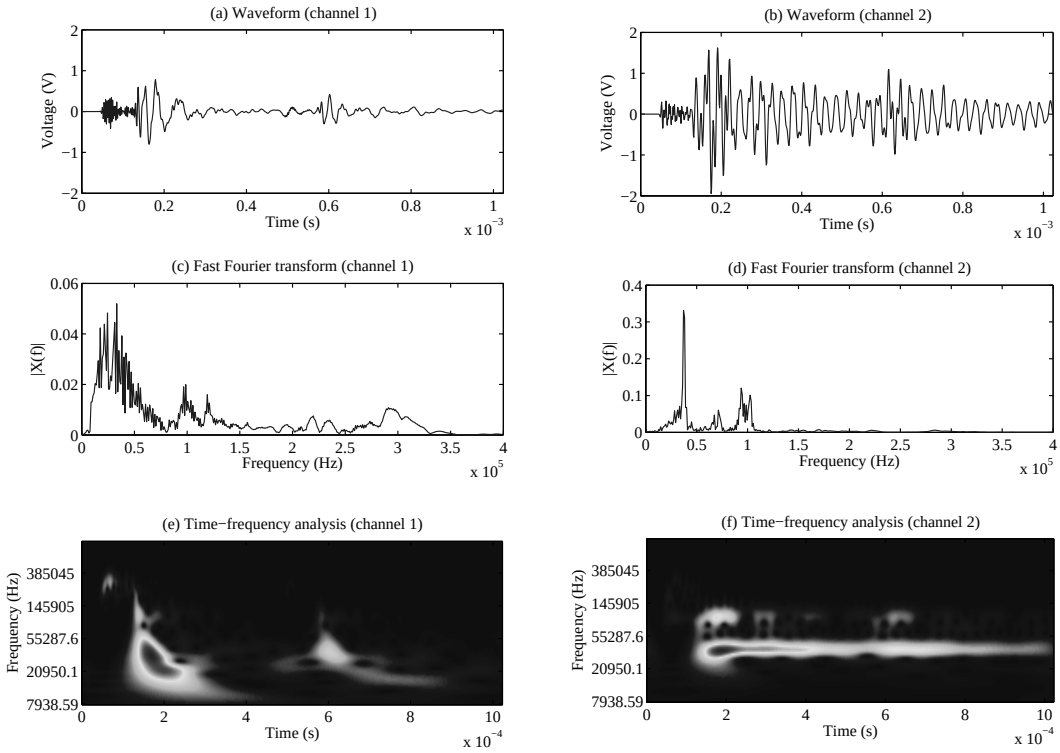

Figure 3.33: Comparison of AE signals captured by broadband and resonance frequency sensor.

Figure 3.35 illustrates the decay rate of AE signals energy in the composite specimen for four different test angles. It can be observed that, the AE signals energy attenuation for the specimen, follow the general model of ultrasonic wave attenuation; the exponential pattern as in equation 3.4, regardless of the test angles used. The R-square showed quite high values and the average decay constant for

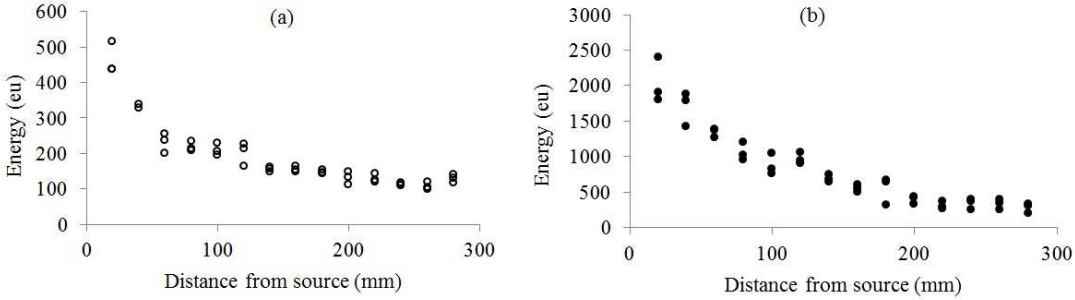

Figure 3.34: Energy attenuation of AE signals using (a) broadband sensor and (b) resonance frequency sensor for 0^o test angle.

all test angles was 0.006. However, a new attenuation model can be introduced from the results in Figure 3.35; a logarithmic pattern. The dotted line in Figure 3.35 shows the logarithmic trend line, and the R-square values were increased for all angles. Based on this, a new universal model for signal energy attenuation for source location detection algorithm is proposed,

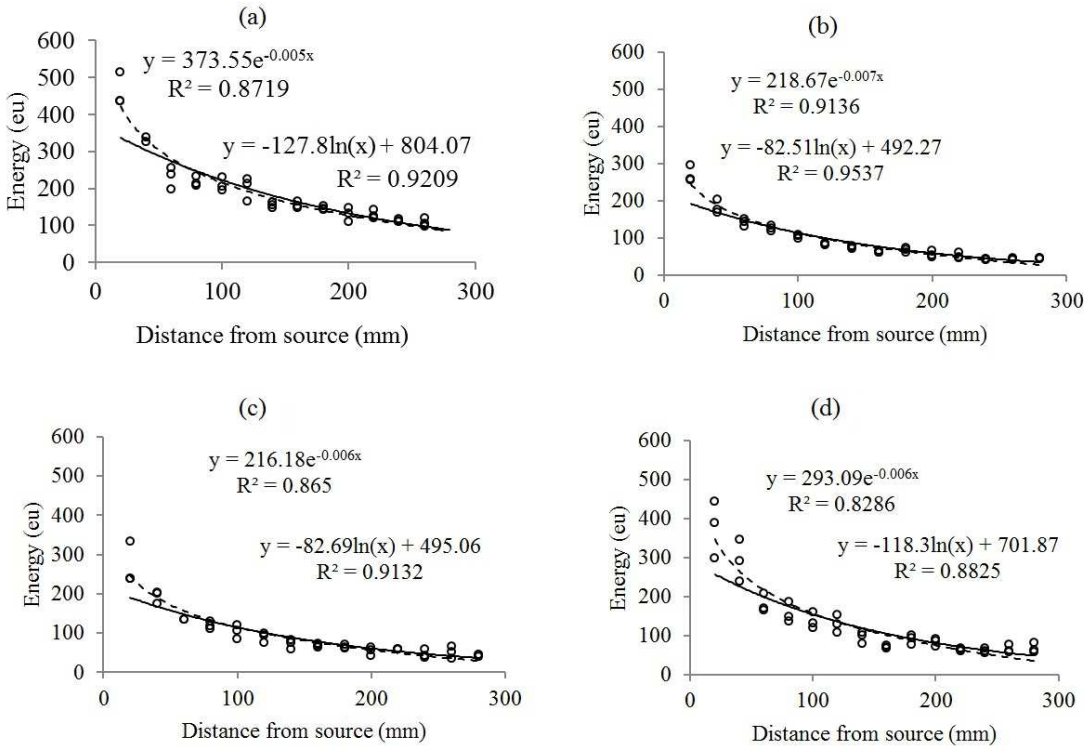

Figure 3.35: (a) Attenuation rate for 0^o, (b) attenuation rate for 45^o, (c) attenuation rate for 60^o and (d) attenuation rate for 90^o. The solid lines refer to exponential trend line while the dotted lines refer to logarithmic trend line.

$$E_i = ln(x_i - x_0)^{-\alpha} + E_0 \tag{3.7}$$

where, α is the logarithmic decay constant. For three sets of linearly arranged transducers, the equation can be expressed as,

$$\frac{E_3 - E_2}{E_2 - E_1} = \frac{\ln(|x_2 - x_0|/|x_3 - x_0)}{\ln(|x_1 - x_0|/|x_2 - x_0)} \tag{3.8}$$

or can be written as,

$$(|x_1 - x_0|)^{\gamma}(|x_3 - x_0|) = (|x_2 - x_0|)^{1+\gamma} \tag{3.9}$$

where $\gamma = (E_3 - E_2)/(E_2 - E_1)$. Equation 3.9 was used as an improved non-velocity based linear source localization.

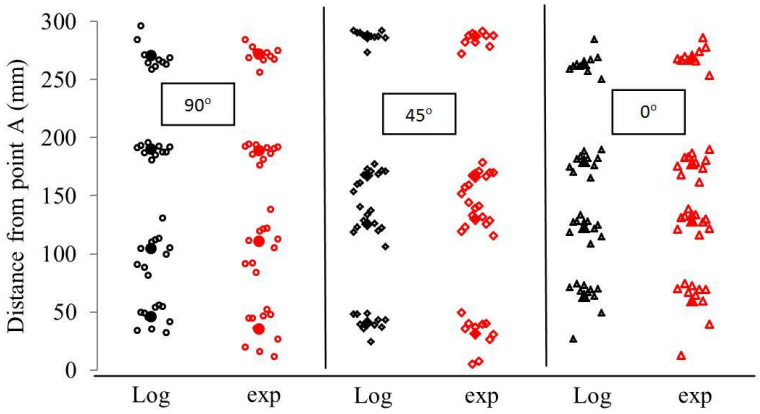

Figure 3.36: Results comparison between exponential (exp) and logarithmic attenuation model (log).

Result for the source mapping validation can be shown as in Figure 3.36. All plots randomly scattered very close to the actual source for both models; exponential and logarithmic. Although they don't look very different, it appears that the logarithmic model more stable and is spotted very closely at the same average value compared to the exponential model.

Furthermore, when the source was near to point A and C, the exponential model was not able to converge into the correct value and tended to calculate the source location with a significant error. Thus, a correction was required in order to find an accurate location. On the other hand, this problem didn't occur when calculating using the logarithmic model.

The errors for both models compared with the actual location are summarized in Table 3.4. In the meantime, Figure 3.37 reveals the average value for the

logarithmic and exponential models, comparing with actual source locations and source locations using commercial AE tools for test angle 45^o.

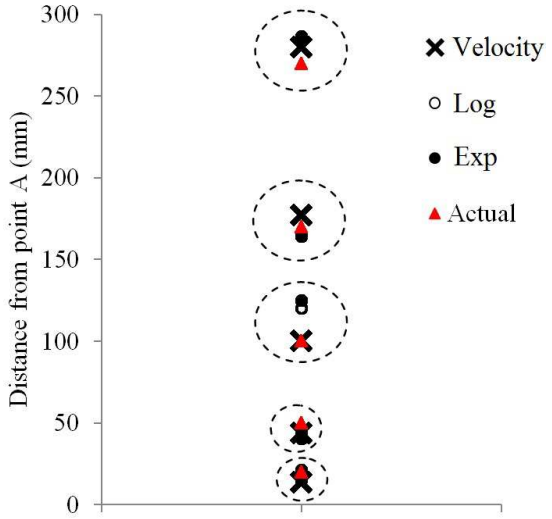

Figure 3.37: Comparison between the logarithmic model (Ln), exponential model (e), actual location and commercial AE tool (velocity).

Table 3.4: Error comparison between logarithmic and exponential source location model. Note: all values in millimeter (mm).

	Log	Exp	Actual	Error (Log)	Error (Exp)
0^o	45.65	34.97	50.00	4.35	15.03
	104.10	110.37	100.00	4.10	10.37
	189.67	188.91	170.00	19.67	18.91
	270.44	271.72	270.00	0.44	1.72
45^o	44.42	36.96	50.00	5.58	13.04
	120.23	125.27	100.00	20.23	25.27
	165.73	163.78	170.00	4.27	6.22
	284.42	283.58	270.00	14.42	13.58
90^o	63.53	59.98	50.00	13.53	9.98
	123.38	128.66	100.00	23.38	28.66
	179.68	178.28	170.00	9.68	8.28
	263.96	269.90	270.00	6.04	0.1

3.8.2 Conclusion for non-velocity based source mapping case study

This study has presented the non velocity-based source localization as an alternative for the other popular time-based methods. Although the errors still appear in the measurement, this technique offers some benefits that are not available in the conventional time-based method. Despite the independency on the velocity of the wave propagation, the other advantage is, this energy attenuation method can be used for aging structures (plates) without the need to consider its current mechanical properties.

3.8.3 Experimentation for 'Effective Distance'

Owing to the energy attenuation of AE wave propagation in composite plate, the appropriate distance between the AE source and the sensor is to be determined. To examine the effective length of AE detection, the same specimen as in the case study in Section 3.8 was cut into smaller piece; 250 mm $\times$ 25 mm (250 mm length is in the fibre direction).

Four single channel AE Node systems were combined to create a four channel AE system for data acquisition and the full set up was as shown in Figure 3.38. All AE Nodes were set to sample AE data at 1 Megahertz. One end of the specimen was clamped to a support while the other end was screwed to a shaker to form a simply supported beam condition. Four AE sensors ($R6\alpha$) were attached to the sample (numbered as in Figure 3.38), and the pencil lead break test was done to the right of sensor 1. Note that sensor 4 was located 205 mm from the shaker. Later, 100 kHz of vibration was applied to the specimen through the shaker.

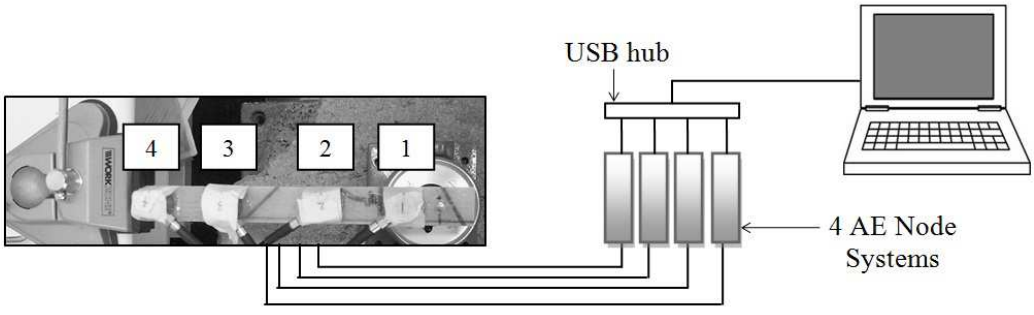

Figure 3.38: Diagram for effective distance experimentation.

Although there are big differences between the AE and acoustics studies, especially in term of their applications (Loman 2012), they share a few characteristics.

In acoustics, the area surrounding a sound source can be divided into different fields: e.g. near field and far field (Hansen 1995). Due to the attenuation behaviour of sound pressure, the near field region can be limited from the source to the distance equal to one-third of the largest energy or amplitude of the sound source. This term can be useful when relating the results presented in the previous section with the effective detection area.

Before discussed the results from the setup as in Figure 3.38, it is important to recall some of the results obtained from Case Study 3.8. Figure 3.39 reveals the detailed analysis of an AE signal which was obtained at 5 different distances from the AE source. A single AE signal may contain a reasonably large amount of information from the source, particularly due to micro-failure formation and its propagation. The frequency spectrum of the signal was proved to be one of the most important parameters that indicate the type of micro-failure characteristic (Gutkin et al. 2011).

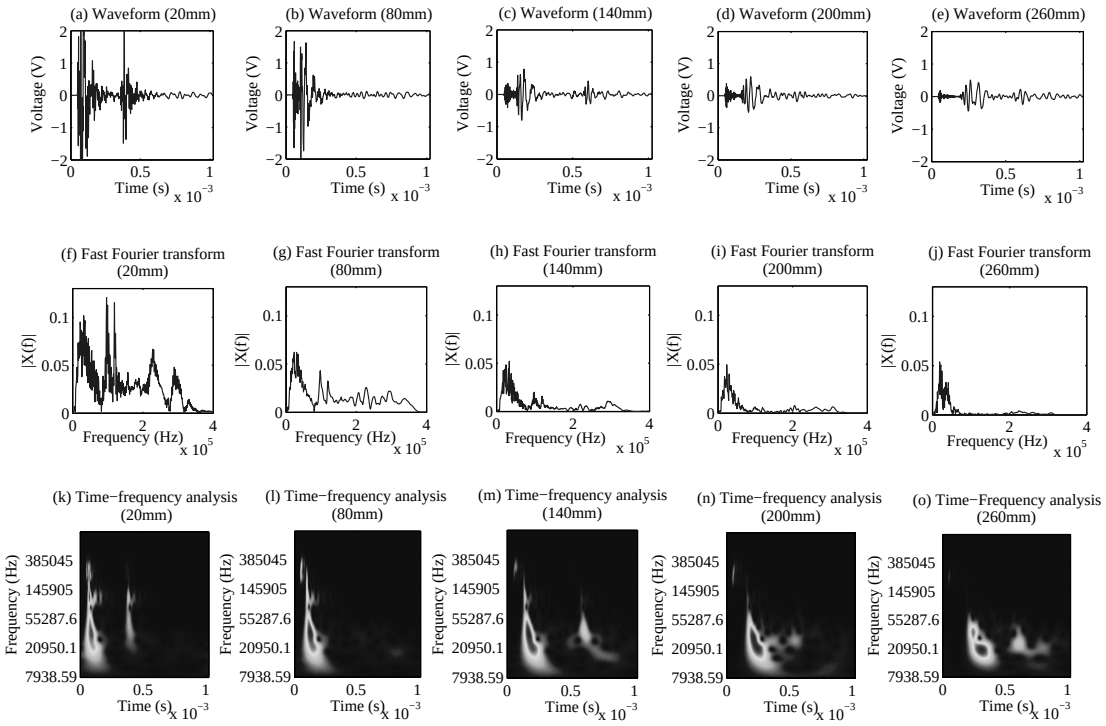

Figure 3.39: Detailed analysis of AE signals received from five different distances from AE source at test angles 0^o.

As explained earlier, the extensional wave mode conventionally has a faster velocity, higher frequency and lower amplitude (due to in-plane motion) compared with the flexural mode. By referring to the wavelet analysis, as shown in Figure 3.39 (k, l, m, n, o), the extensional mode 'signature' was consistent with the 300 kHz component which can be seen fading as the distance from the AE source

increased. In other words, the extensional mode almost disappears at the far field; approximately 140 mm from the source (refer Figure 3.34a). In practice, this will affect the accuracy of the information for micro-failure characterization since in the MAE study different failure mechanisms or source orientations can generate different frequency or wave propagation modes.

Meanwhile, with the flexural wave mode ranging from 20 kHz to 250 kHz, the signal was arriving at the sensor later than the extensional mode and became slower as the distance from AE source increased; which is consistent with antisymmetric mode behaviour. Note that at 260 mm distance from the AE source, only the lowest frequency component of the flexural wave was left (see Figure 3.39o).

3.8.4 Result and discussion for the effective distance case study

The results discussed here is corresponding with the set up as in Figure 3.38. The pencil lead break test results shown in Figure 3.40 (a to h) also reveal the same pattern as the above explanation, and can be used to describe the effective area for better AE signal detection.

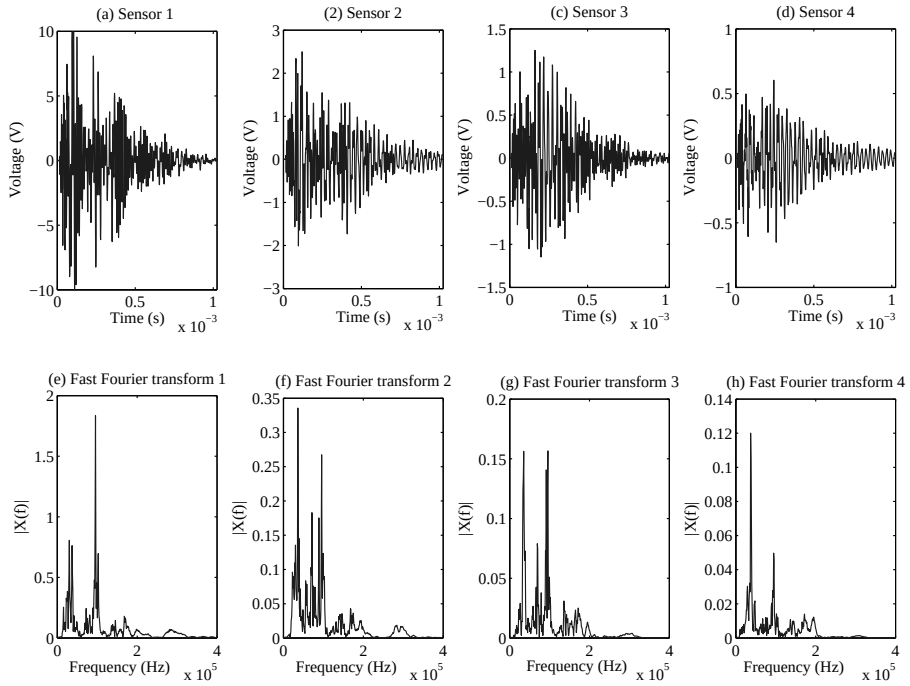

Figure 3.40: AE signal from all sensors and their respective FFT analysis.

Two main frequency components exist: high frequency (approx. 100 kHz) and low frequency (approx. 30 kHz). Signals from sensor 4 (see Figure 3.40d) had the lowest energy/RMS value and the distance from AE source was 205 mm. By comparing the frequency spectrum obtained from signal 1 (see Figure 3.40e) and signal 4 (see Figure 3.40h), it appeared that the amplitude of the higher frequency component dropped faster especially after 205 mm distance from the AE source.

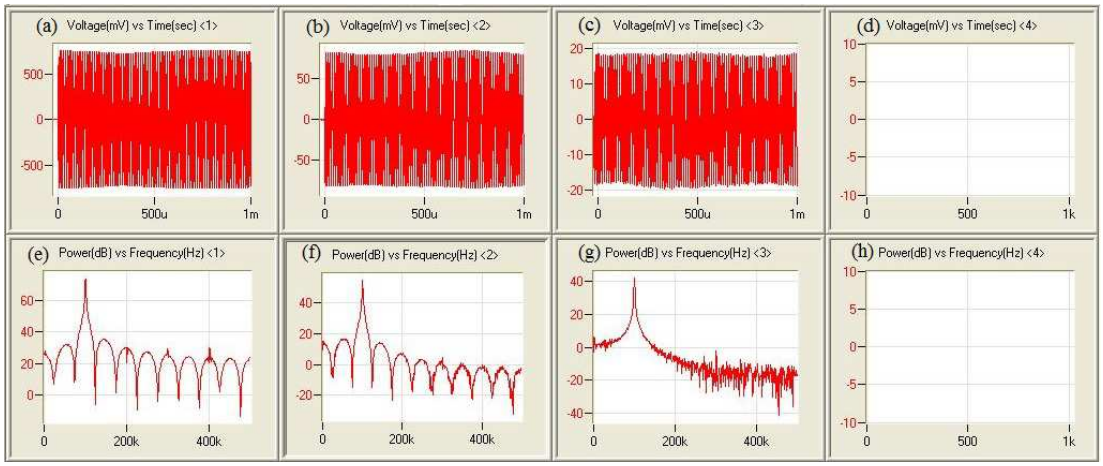

Figure 3.41: Result with 100kHz vibration applied to the specimen

Obviously, within a short distance, the propagating AE signal was dominated by low frequency signal, even though it was earlier dominated by a high frequency signal. This 'turning-over' starts approximately in between sensors 2 and 3, or 120 mm from the AE source; which is at the limit of the near field region (refer Figure 3.34b). It is clear that, a frequency more than 100 kHz was difficult to be detected in 205 mm radius (at sensor number 4) as indicated in Figure 3.41. At the same time, failure such as delamination and fibre breakage were reported to create AE signals more than 100 kHz (Gutkin et al. 2011). It explains how significant the effective detection area is necessary to be considered for a better SHM of composite materials.

3.9 Chapter Summary

This chapter has explained some detail applications on the Modal Acoustic Emission, particularly for the case of thin laminated composite plates. Four relevant case studies have been presented to show the applicability and practicality of the MAE usage in composite structures.

In conclusion, the MAE is obviously very useful and has big potential to be used further in SHM of composite structures, instead of only as an NDE technique.

However, some issues regarding the general use of the AE technique was also discussed. There are some important concerns that need to be addressed further, which are due to the limitation of current piezoelectric sensor-based system.

In Section 3.6, the MAE was proved to have the capability of revealing the *in-phase* and *out-of-phase* modes of the AE signals, thus provides accurate information in distinguishing between matrix cracking and delamination. However, the current physical size and shape of AE sensors limit the possibility of this technique to becoming practical. Thus, the replacement of the conventional AE piezoelectric transducer into a new type of sensor head, which suit the purpose, is essential.

Also stated in this chapter, is a deficiency in using an AE technique for the type of monitoring that requires a very long cable from the AE sensor to the DAQ. Apart from the problem of tangled wires during the testing, it also causes problems of energy attenuation in the signal transmission process. This problem would have been fully resolved with the use of fiber optic technology.

In order for AE techniques to become more useful for SHM of composite structures, the sensors must able to be embedded into the structures. For this purpose, *Fiber Bragg Gratings* (FBG) are proposed as a replacement to conventional piezoelectric transducers. Not only do they increase the practicality, the *FBG-AE* combination also will allow the development of smart structures.

During all the experimentation presented in this chapter, one of the most critical issues was the AE sensor mounting to specimens. Very careful initiatives were needed in order to have perfect and reliable mounting; to assure all the AE waveforms from the specimens were fully transferred to the transducer. The use of embedded sensors should eliminate this problem.

Chapter 4

Use of FBG Dynamic Sensor System for Composite Structures

4.1 Chapter Overview

The main goal of this chapter is to introduce the new proposed solution for the issues that have been listed at the end of the previous chapter. Solution to these problems is converged into the use of optical sensors, the Fiber Bragg Grating (FBG) sensors. Thus, this chapter will describe the application of FBG sensors for sensing dynamic strain. Please note that the term *FBG dynamic sensor* will be widely used until the end of this thesis.

A brief explanation of all the required components for an FBG dynamic sensor system and the basic theory of FBG dynamic sensor will be given at the beginning of the chapter. In the end, the Near Infra-Red (NIR) FBG sensors will be introduced. The details of the mechanism of embedded FBG sensors in NIR region ($\sim 830nm$) for the measurement of structural dynamic response of composite structures is also presented in this chapter.

4.2 Introduction

Recently, FBG sensors for dynamic measurement became more interesting study. It is becoming more exciting with the implementation into the health monitoring of critical structures, especially which are involving composite materials. Furthermore, the FBG dynamic sensor concept, also leads toward the development

of smart structures.

Meanwhile, the development of the hybrid SHM system, which involves the measurement of both static and dynamic strains accurately, was an emerging area of research in online-SHM systems. Since FBG sensors are able to achieve this unique capability, they have made inroads into the enhancement of in-situ SHM systems during the past few decades.

The other great benefit of using these optical sensors is the ability of utilizing the advanced technology of optical transmission systems. In other words, with the technology, distance is not a problem. It is an undeniable fact that these light-wave communication systems are very successful, especially in recent telecommunications applications. Besides having low transmission loss, this system also offers impressive advantages; small size and less weight (optical fiber cable) compared with conventional wiring.

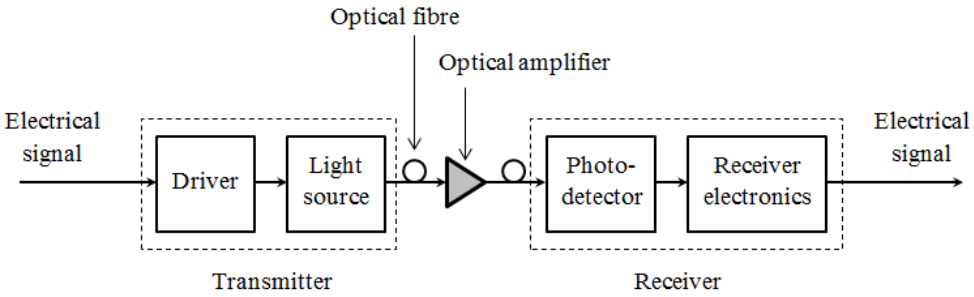

Figure 4.1: Basic block diagram of a long-distance lightwave link (Papannareddy 1997).

The general block diagram or the end-to-end signal transmission of a long-distance light-wave link can be shown as in Figure 4.1. The conversion of the electrical signals to optical signals happens in an optical transmitter. Then, the modulated light will travel using an optical fibre in a long distance before being converted back into an electrical signal by the optical receiver.

In a typical telecommunications application, the 'information' starts from the electrical signal and then converted into a modulated light; either with an intensity modulation or an external modulation process (Papannareddy 1997). Both modulations can be summarized as in Figure 4.2.

FBG dynamic sensors use the external modulation scheme. Figure 4.3 indicates how an FBG sensor is placed in an FBG dynamic measurement system. In this system, the light source provides a continuous signal, which it will be as an input to the modulator. There are other more complex arrangements, which have been proposed by researchers globally, however the main concept is to produce

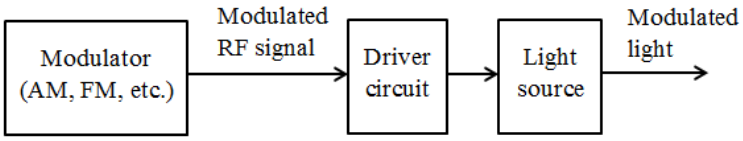

(a) Intensity modulation or direct optical modulation.

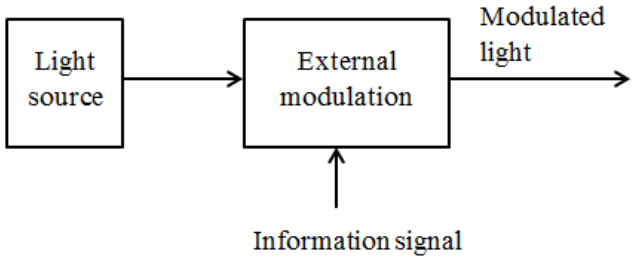

(b) External modulation.

Figure 4.2: Modulation of an information signal (Papannareddy 1997).

modulated light by which can be correlated to dynamic strain (e.g. vibration, acoustic waves).

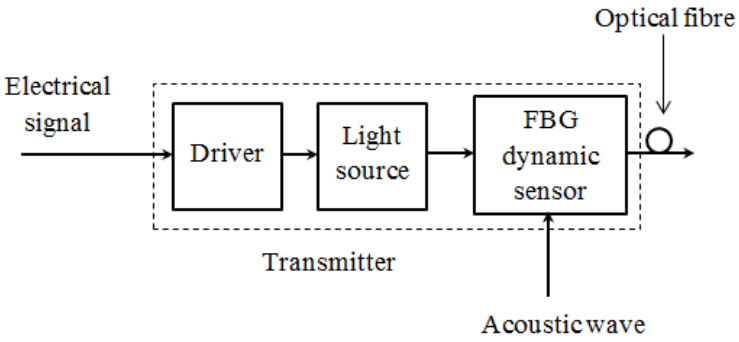

Figure 4.3: The FBG sensor work as an optical modulator.

4.3 Optical Components

In order to fully understand the capability of an FBG dynamic sensor system, it is necessary to know each of the principal components in a *lightwave link*, such as the light sources, photodiodes and optical filters. Note that, an FBG is one of the optical filters that are able to filter a particular wavelength of light.

Figure 4.4 shows the optical components in their usual position in a lightwave link. Further details of all the components, particularly which relate to the FBG dynamic sensing system, will be discussed in the next section.

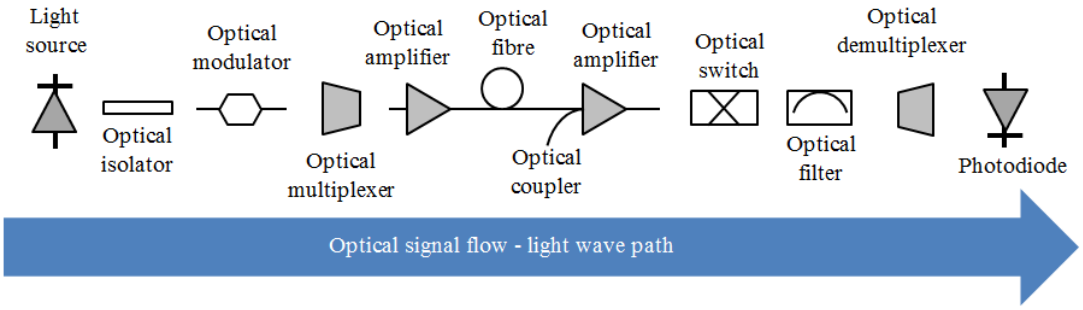

Figure 4.4: Basic optical components (Cvijetic 2004).

4.3.1 Semiconductor light sources

A light source is one of the main essential components of the system. It is the *heart* of the transmitter part, as shown by the Figure 4.1.

In a direct modulation scheme, an electrical signal will be converted by a semiconductor light source into optical radiation. Meanwhile, a constant direct current (dc) voltage provides a constant and continuous light in the external modulation scheme. Therefore, it is crucial for the external modulation type to have very stable light radiation in order to provide a sensitive and precise output. In the context of an FBG dynamic sensor system, a light source with constant output power is essential to avoid systematic error in the measurement.

The concept of a semiconductor laser was known to be introduced since 1961. However, the progress seemed very slow due to the lack of understanding of modern semiconductor technology. Although the silicon fabrication technology already matured during the time, yet the proper laser operation needed compound semiconductors, which was only to be well understood in the next decade (Chow & Koch 1999).

There are two major types of light sources, the light emitting diode (LED) and semiconductor lasers. Both are distinguished by the light emission mechanism. Meanwhile, the emitted light from the sources can be categorized as being in the short-wavelength region (700 nm - 900 nm) and the long-wavelength region (1300 nm - 1600 nm). For a short-wavelength, the GaAs-AlGaAs material is used while for a long-wavelength an InP-InGaAsP material is utilized.

The knowledge of the light source's basic operation is necessary, not only for proper selection of light source itself, but also for safety purposes. Note that, the basic principles of semiconductor light sources are also similar to the concepts applied in photodiodes, but in the opposite way.

Basic concepts of semiconductor light source

Fundamentally, electromagnetic radiation is emitted whenever a charged particle such as an electron gives up energy. In basic quantum mechanics, an electron is associated with its energy levels. When electrons 'fall' from any high level state, $\widehat{E}_2$ to lower energy state, $\widehat{E}_1$, they are radiating photons. In the other hand, the electrons also can move from lower to higher levels by absorbing photons.

A photon is referred to as the smallest particle of light energy, according to quantum mechanics study. A photon's energy, $\widehat{E}$ is determined by its frequency, f and Planck's constant, $\widehat{h}$,

$$\widehat{E} = \widehat{h}f \tag{4.1}$$

Meanwhile, the color of light is determined by its wavelength; the shorter wavelengths are the ultraviolet and the longer wavelengths are the infrared. The wavelength of the light can be expressed as,

$$\lambda = \frac{c}{f} \tag{4.2}$$

where c refers to the speed of light in vacuum.

There are three processes that are involved in basic semiconductors light sources operation: absorption, spontaneous emission and stimulated emission. These different mechanisms of light generation, distinguish the type of light sources; either LEDs or semiconductor lasers.

Light Emitting Diodes (LED)

Figure 4.5 illustrates the absorption and spontaneous emission of light. In the absorption process, the electron in the valence band will absorb the photon's energy from the incident light, to reach the conduction band. Meanwhile, the spontaneous emission is the reverse process of the absorption, and releasing light with frequency equals to,

$$f = \frac{\widehat{E}_c - \widehat{E}_v}{\widehat{h}} \tag{4.3}$$

where $\widehat{E}_c$ and $\widehat{E}_v$ are the energies of the conduction band and valence band, respectively. Spontaneous light emission is the fundamental principle for the LEDs operation. Note that the Equation 4.3 also indicates that the colour of the light depends on the band-gap energy of the materials forming the p-n junction.

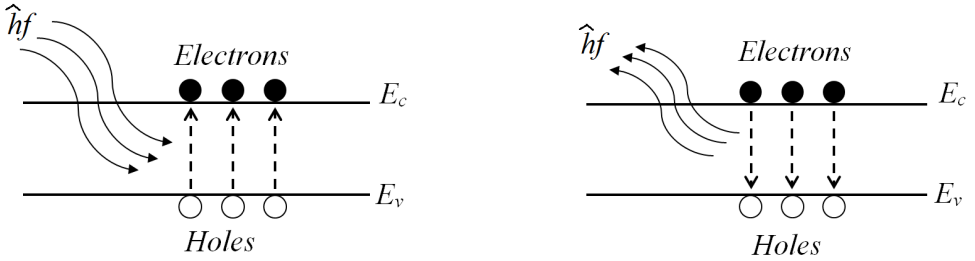

(a) Absorption of photon's energy.

(b) Spontaneous emission of light.

Figure 4.5: Absorption and spontaneous emission of light in semiconductor light sources.

The simplest structure of the LED allows for surface radiation mechanism. It is done by having semiconductors with a sandwich-like p-n junction and terminal contacts. The spontaneous emission occurs at the junction region, and the light is generated (see Figure 4.6).

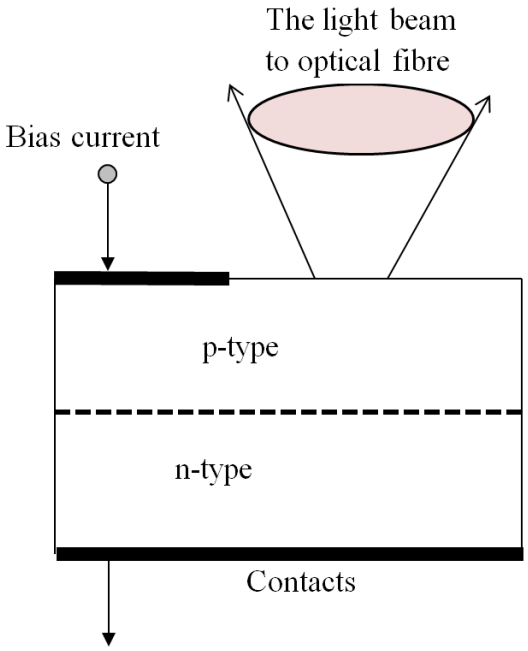

Figure 4.6: Surface radiation of LED (Cvijetic 2004).

The other LED structure causes edge emission. It can be done by having at least one or more layers in between the p-n junctions. This active layer (or region)

works as a waveguide and allows radiation to be lateral through the edges of the semiconductor structure. The refractive index of the active layer is chosen to be higher than the other layers ($n_2 > n_1$ and $n_2 > n_3$). Figure 4.7 illustrates the edge emission of the LED structure.

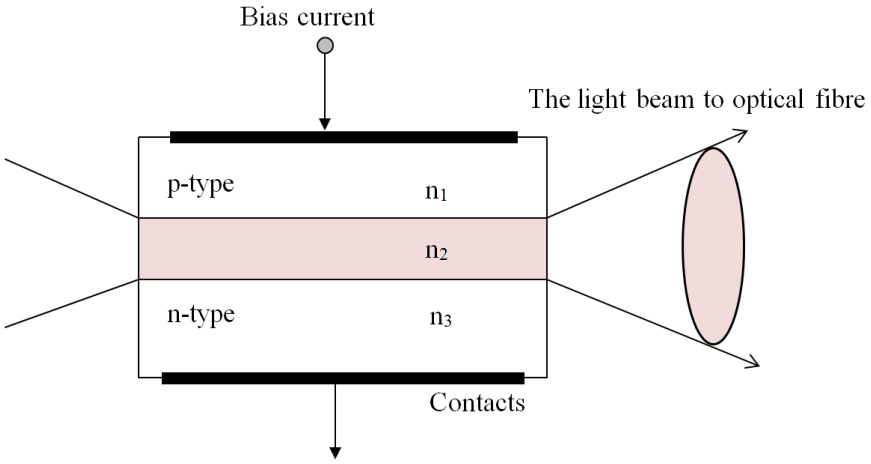

Figure 4.7: Edge emission of LED (Cvijetic 2004).

A LED is a broadband light source (spectral bandwidth 30 - 60 nm) and usually is used for a relatively low power application; 0.1 mW for bias current 100 mA (Cvijetic 2004). However, a superluminescence light emitting diode (SLED or SLD) can provide higher power, as it is an amplified spontaneous emission of a light beam (Paschotta 2013*b*). Compared to semiconductor lasers, LEDs are much cheaper.

Semiconductor Lasers

The stimulated emission of lights is required for semiconductor lasers. When a photon's energy of the incident light falls on the system, an electron from the conduction band is stimulated to drop to the valence band by means of population inversion (Papannareddy 1997). As a consequence, a coherent light is radiated; thus, the spectral width and beam divergence angle are much smaller than those of LEDs.

Population inversion in semiconductors can be illustrated by an E-**k** diagram, as in Figure 4.8. The term $\widehat{E}$ refers to energy and **k** denotes the wave space vector. The Fermi levels, $E_{F,c}$ and $E_{F,v}$ are related to the conduction and valence bands, respectively. The Fermi levels can be moved up (for p-type) and moved down (for n-type) by increasing the dopant concentration. The population inversion is done by applying an electrical current that populates the conduction band with a rate that is higher than the rate that is emptied (Cvijetic 2004).

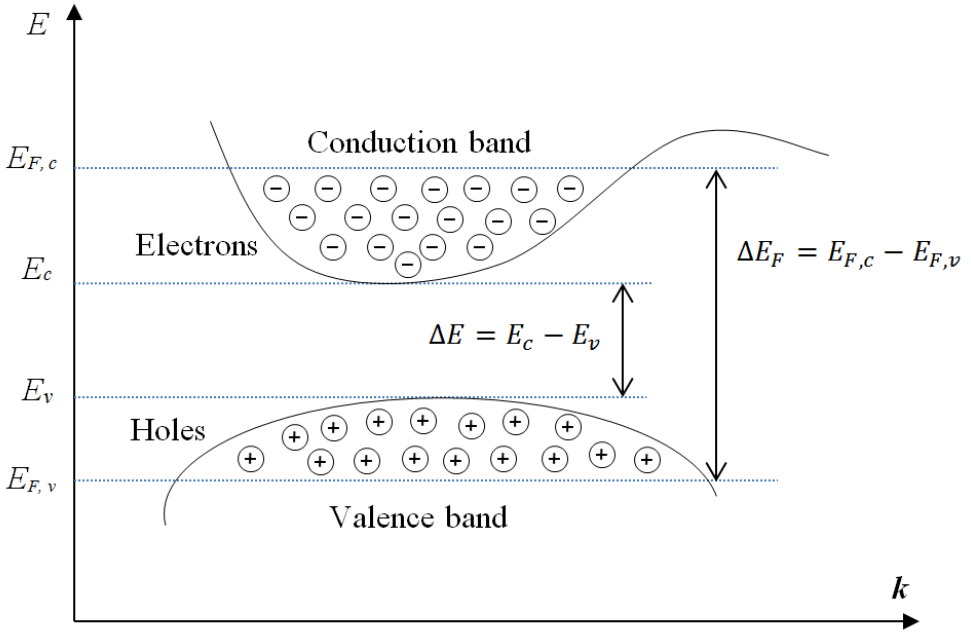

Figure 4.8: Population inversion in semiconductors (Cvijetic 2004).

Once population inversion is achieved, the electrons will jump down to the valence band and recombine with holes, and thus produce photons of the light signal. The stimulated light emission will occur if $\Delta E_F > \Delta E$. Note that, the $\Delta E_F > \Delta E$ condition will happen if the direct bias current is higher than the threshold current.

Meanwhile, the laser's output power not only depends on the current and optical characteristics, but is also influenced by the thermal characteristics. The power output of the laser inside a laser cavity due to an applied current I can be written as (Papannareddy 1997),

$$P_0 = \frac{\widehat{h}f}{q}[\eta_i(I - I_{th})] \tag{4.4}$$

for $I > I_{th}$. The term q and I_{th} in Equation 4.4 refer to electron charge ($1.6 \times 10^{-19}C$) and the threshold current density, respectively. Meanwhile, the η_i denotes the internal quantum efficiency of the laser; measured by the total photons emitted inside the laser cavity per second. If $I < I_{th}$, the Equation 4.4 becomes,

$$P_0 = \frac{\widehat{h}f}{q}\eta_i I \tag{4.5}$$

The I_{th} is temperature dependent and given by (Papannareddy 1997),

$$I_{th} = I_{th}(0)e^{(\Delta T/T_C)} \tag{4.6}$$

where $I_{th}(0)$ is the current at the reference temperature, ΔT is the temperature difference between the laser and the reference value and T_C refers to the characteristic temperature of the laser.

The basic structure of a semiconductor laser is as shown in Figure 4.9. When the applied current is higher than a certain threshold, the electron-hole recombination occurs in an organized way, with a strong correlation in phase, frequency and direction of radiated photons (Cvijetic 2004).

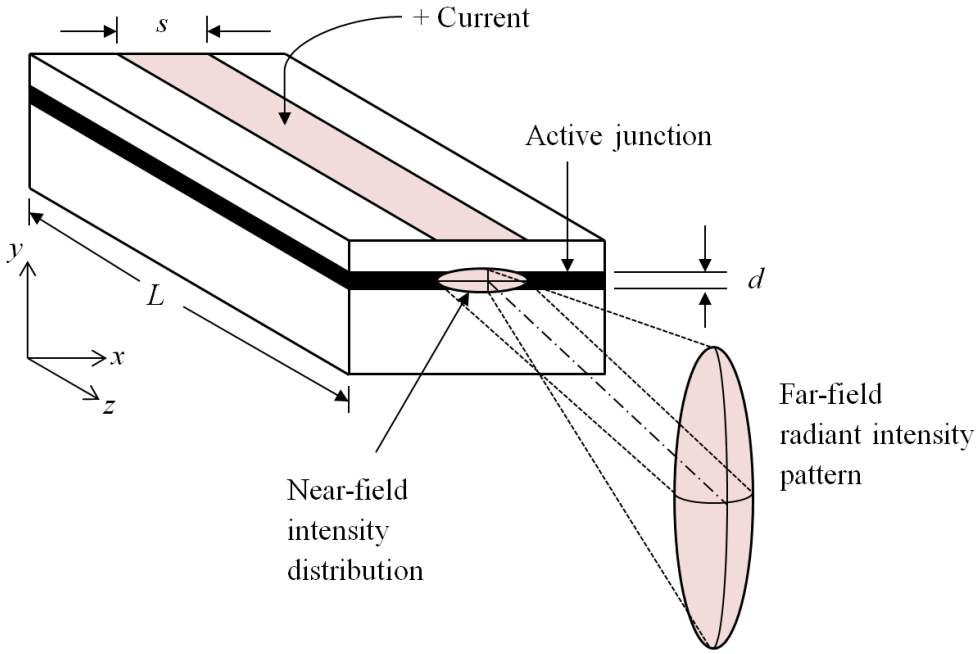

Figure 4.9: A basic semiconductor laser. The letter s denotes the stripe width, d is the thickness of the active layer and L is the length of the cavity (Papannareddy 1997).

The side view (y-z) of the basic semiconductor laser is similar to the edge emission LED structure, except, when there are reflection coatings; that act as mirrors that cover the semiconductor facets (Figure 4.10). This mechanism produces multiple reflections in the cavity area, thus amplify the stimulated light emission. As a result, this kind of device; also called as Fabry - Perot (FP) laser has an output power higher than an LED type.

Besides the basic operation being explained above, there are also other types of semiconductor lasers such as a distributed feedback (DFB) lasers, the distributed

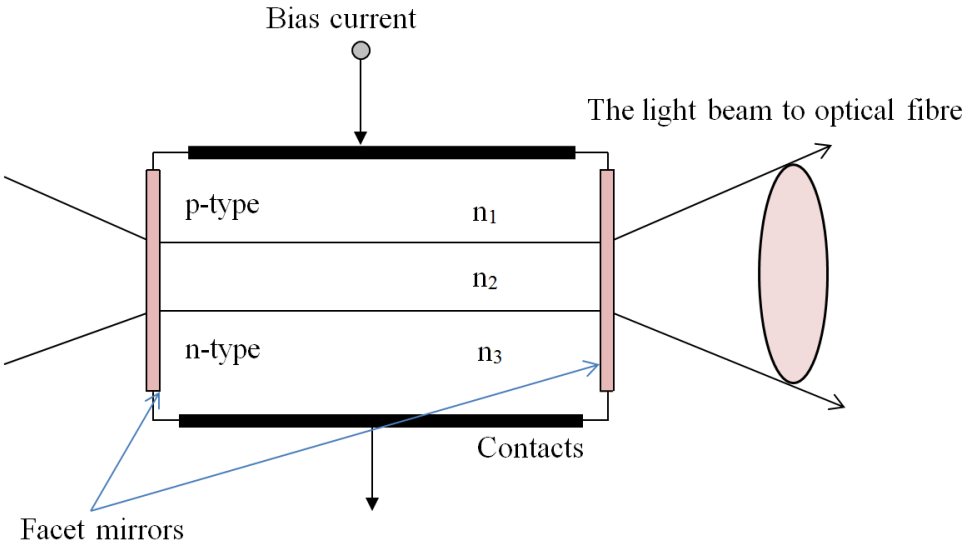

Figure 4.10: Semiconductor laser's structure in different view (Cvijetic 2004).

Bragg reflector (DBR) lasers and the vertical cavity surface emitting lasers (VCSEL). They will not be discussed further as they are not in the specific scope of this work.

4.3.2 Photodiodes

A photodiode or photodetector (PD) is one of the components in the optical receiver part (see Figure 4.1). Three major semiconductor materials are used in a photodiode's manufacture: Silicon (Si), Germanium (Ge) and Indium-Gallium-Arsenide (InGaAs). They are differentiated by the centre wavelength and the bandwidth of the incoming light frequency; as summarized in Table 4.1.

Table 4.1: Semiconductor materials used for PD manufacturing (Cvijetic 2004).

Semiconductor	Bandwidth	Center wavelength
Silicon (Si)	up to 200 nm	around 800 - 900 nm
Germanium (Ge)	up to 400 nm	around 1400 - 1500 nm
Indium-Gallium-Arsenide (InGaAs)	up to 600 nm	around 1500 - 1700 nm

There are two main groups of photodiodes; the PIN and avalanche photodiodes (APD). Both types were distinguished by the electron-hole pair generation process. As mentioned earlier, the photodiodes work in reverse to the mechanism the way a semiconductor light sources work. In other words, the photodiodes

absorb the photons from the incoming light signal and convert it into electrical signals. Specifically, the absorbed photons, which have energy higher than the band gap of the semiconductor p-n structure, will induce the electron-hole pairs. The electron-hole pairs will create the photocurrent.

The PIN photodiodes are structured as a sandwich where the lightly doped I-region is placed in the middle, between the p-type and n-type semiconductor layers. The P.I.N term is due to the arrangement of the layers. In PIN photodiodes, each photon will eventually (or high probability) caused one electron-hole pair. Which means; the photocurrent generation is proportional to the incoming optical signal.

In the APDs, each photon will generate one electron; in which, this primary electron will be accelerated in a strong electric field, thus causing the creation of several secondary electron-hole pairs due to an ionization effect. Therefore, the APDs have an additional layer to enhance the impact ionization process. This mechanism works as internal gain, yet requires higher reverse voltage compared to the PIN photodiodes. The structure of PIN and APD photodiodes are as shown in Figure 4.11.

The efficiency of the photodiode is measured by its quantum efficiency. The quantum efficiency, η is the ratio between the number of the electrons detected in the process and the number of photons that arrived. It is given by (Papannareddy 1997),

$$\eta = \frac{I_p/q}{P_{in}/\widehat{h}f} \tag{4.7}$$

where I_p denotes the average photocurrent generated by the incident optical power, P_{in}. The other parameter which is important for the photodiodes is the responsivity value, R; which can be expressed as the conversion rate between a photocurrent, I_p and optical power input, P_{in} (Cvijetic 2004),

$$I_p = RP_{in} \tag{4.8}$$

Figure 4.12 shows the general responsivity curves for three semiconductors as listed in Table 4.1.

These parameters are essential, especially when designing the optical receiver for the FBG dynamic sensor system. Typical values for some relevant specification

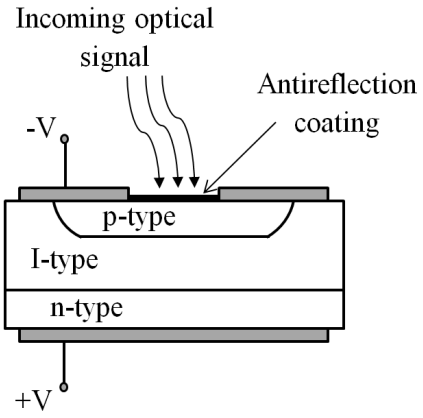

(a) PIN photodiode.

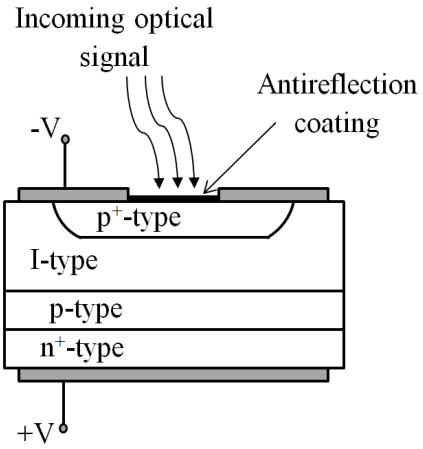

(b) APD photodiode.

Figure 4.11: The structure of semiconductor photodiodes (Cvijetic 2004).

for PIN and APD photodiodes are listed the Table 4.2.

Table 4.2: The typical values of PD's parameters (Cvijetic 2004).

Parameter	PINs	APDs
Responsivity (A/W)	0.7 - 0.95	0.7 - 0.9
Cut off frequency	up to 75 GHz	up to 15 GHz
Internal gain	1	100

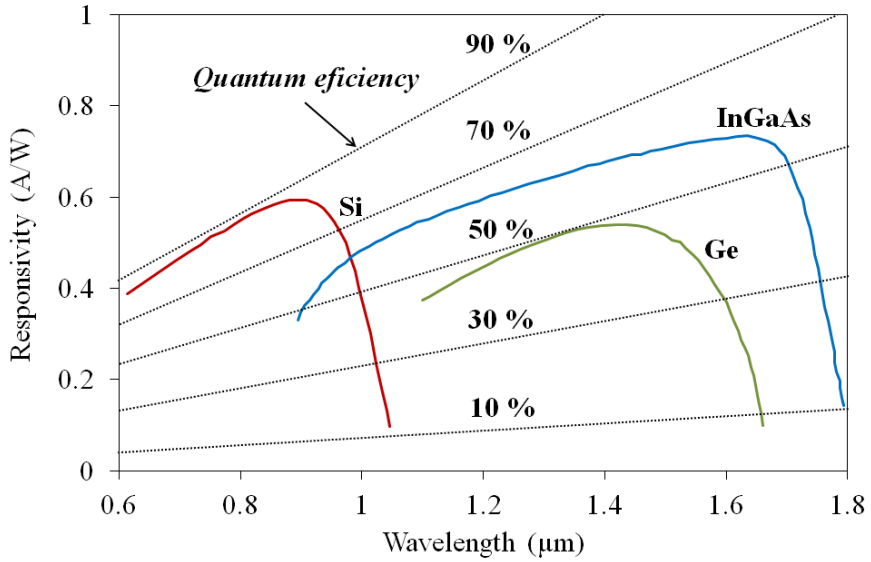

Figure 4.12: General responsivity for Si, Ge and InGaAs photodiodes as a function of wavelength (Papannareddy 1997).

4.3.3 Optical filters: the Fibre Bragg Grating (FBG)

There is a lot of optical filters available for use in optical devices or systems, but they have no specific design. Not only that, their function also varies. They can be fixed filters or tunable filters; based on the design requirements. For the purpose of this project, the optical filters used were the optical fiber grating, specifically, the fiber Bragg grating (FBG).

The FBGs are formed by constructing periodic changes in the index of refraction in the core of a single mode optical fiber (will be explained in the next part). The FBGs applications are very broad, such as, for producing single mode output from DFB and DBR lasers, as a variable mechanism in tunable lasers; strain sensors; etc. The FBGs are the optical filters which are imprinted in optical fibers; thus relatively cheap and easy for handling (Cvijetic 2004).

FBGs are also widely utilized as sensors due to several advantages. For instance, the ability to be embedded inside fibre reinforced plastic (FRP) materials in between different layers offers closer views upon defects. Besides, the attractive properties such as small size, immunity to electromagnetic fields, and multiplexing ability are the other advantages of FBG sensors (Ling et al. 2007).

Nowadays, the FBG sensors have been used widely for the SHM of composite materials (Kahandawa 2012). It is supported by increasing number of studies on the health monitoring of composite structures using FBG sensors. In the

other hand, recent advances in FBG sensor technologies have provided excellent opportunities to develop more sophisticated in-situ SHM systems. The lifetime of an FBG sensor is well above the lifetime of the FRP structures and so it also allows the measuring of multiple parameters such as load/strain, AE, vibration and temperature (Kashyap 1999).

FBG's Structure

FBGs are fabricated with a core region of specially fabricated single mode low-loss germanium doped silicate optical fibers. The grating is a laser-inscribed region which has a periodically varying refractive index. This periodic change in index of refraction is typically created by exposing the fiber core to an intense interference pattern of UV radiation. This region reflects only a narrow band of light corresponding to the Bragg wavelength λ_B (Figure 4.13), which is related to the grating period Λ_o (Kashyap 1999),

$$\lambda_B = \frac{2n_o\Lambda_o}{\widehat{k}} \tag{4.9}$$

where $\widehat{k}$ is the order of the grating and n_o is the initial refractive index of the core material prior to any applied strain. The Bragg wavelength is also frequently expressed as,

$$\lambda_B = 2n_{eff}\Lambda \tag{4.10}$$

where n_{eff} referred to the effective refractive index of the fibre core.

Meanwhile, the detail schematic diagram of an FBG can be shown as in Figure 4.14. To assure the best response due to strain or temperature differences, the FBGs must be embedded in composite layers or glued onto the surface. The Bragg wavelength shift due to temperature changes, ΔT and strain, ε can be written as (Park et al. 2003, Majumder et al. 2008),

$$\frac{\Delta\lambda_B}{\lambda_B} = (\widehat{\alpha} + \xi)\Delta T + (1 - p_e)\varepsilon \tag{4.11}$$

where the $\Delta\lambda_B$ is the wavelength change, α is the thermal expansion, ξ is the thermo-optic coefficient and p_e is the effective photo-elastic constant of the fibre

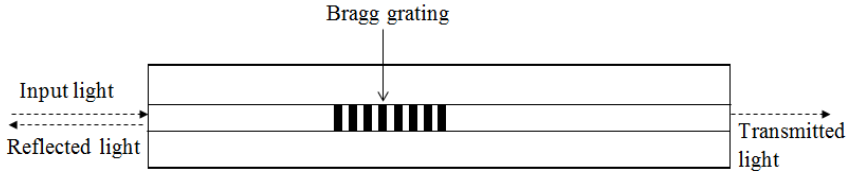

(a) An FBG.

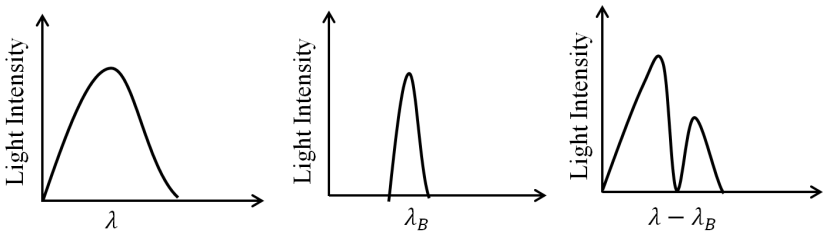

(b) Input light. (c) Reflected light. (d) Transmitted light.

Figure 4.13: Transmission and reflected light from an FBG.

core material. Figure 4.15 illustrates the wavelength changes, corresponding to the variations in the grating period, as shown by the Figure 4.16.

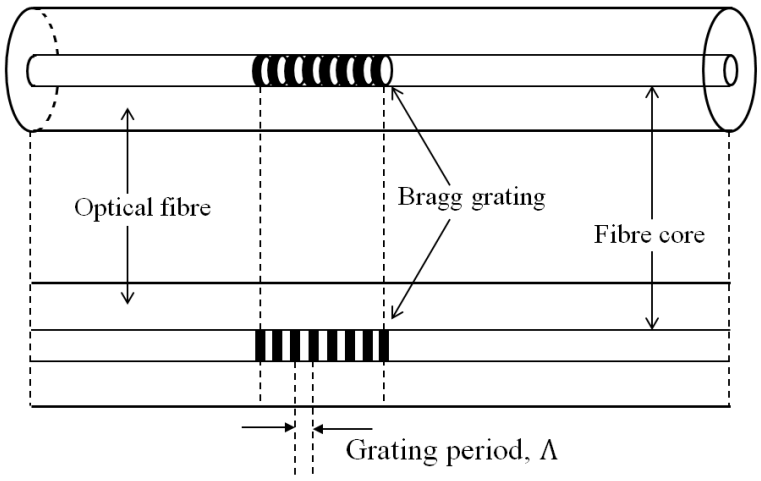

Figure 4.14: Schematic diagram of a FBG.

For this study, the temperature effect was neglected since all experiments were done in a controlled environment. Therefore, for an isothermal condition, Equation 4.11 can be reduced to (Majumder et al. 2008),

$$\frac{\Delta\lambda_B}{\lambda_B} = (1 - p_e)\varepsilon \tag{4.12}$$

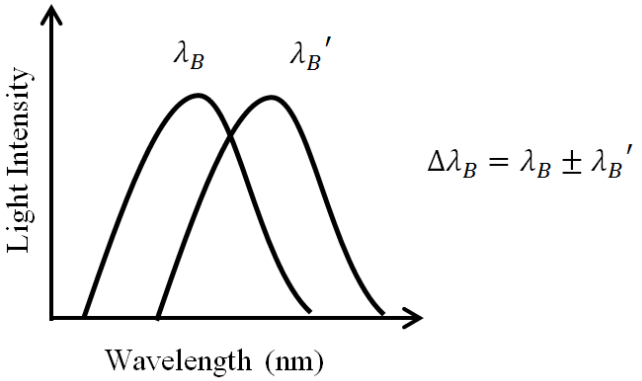

Figure 4.15: The Bragg wavelength shift as a result of grating period changes.

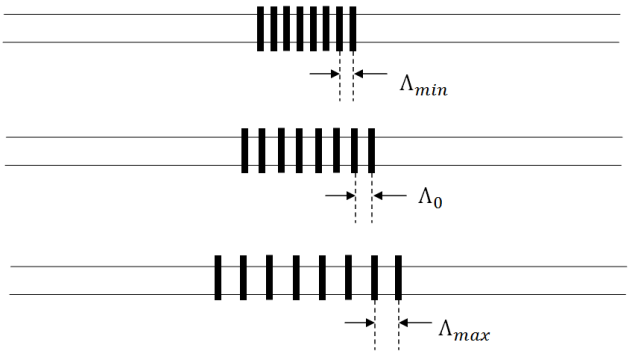

Figure 4.16: Variations of the grating period due to strain or temperature change.

4.4 FBG Sensor System for Dynamic Measurement

The brief knowledge of some major components in an optical-based system, or device, give a necessary foundation in designing an optical sensory system. Although there are other issues in the use of optical sensors such as, optical noise and signal impairments, yet, this revolutionary idea for an optical device is still at the beginning stage, and more development work is needed. Enormous benefits are awaiting if this technology can merge and mature in SHM of composite structures.

The use of FBG sensors for dynamic sensing is relatively new, and several numbers of research work were published during the last decade. This approach has been shown to work in many applications, such as composites health monitoring (Tsuda 2006, Frieden et al. 2010), mechanical testing (Lee & Tsuda 2005) and for NDE. FBG sensors for dynamic measurement work as an indirect vibration sensor; unlike the piezoelectric sensors which can convert the strain directly into

an electrical signal.

In detail, an FBG in a dynamic sensor system usually involves a special interrogation system where it can translate the wavelength variations (due to strain changes) into an electrical signal. Some proposed systems have a complicated arrangement. Although it may achieve the required results, yet, the more complicated systems may result in extra optical losses and relatively higher cost. Besides, many calibration tests need be done to obtain as accurate signals as possible. There are two interrogation methods that are available for high frequency vibration signals with FBGs, that is edge filter detection and power detection methods (Wild & Hinckley 2010).

A large number of studies has used FBG sensors in the 1550 nm range for measurement of dynamic responses. Cusano et al. (2004) introduced FBG dynamic measurement by combining the transmitted and reflected lights from an optical filter. Both reflected and transmitted optical signals were from reflection of the FBG sensor as illustrated by the Figure 4.17. The light intensities from both the reflected and transmitted spectrum were first converted into electrical signals by the photodetector (PD) and then they were fed into a unique electronic system where it did further processing to provide dynamic signals.

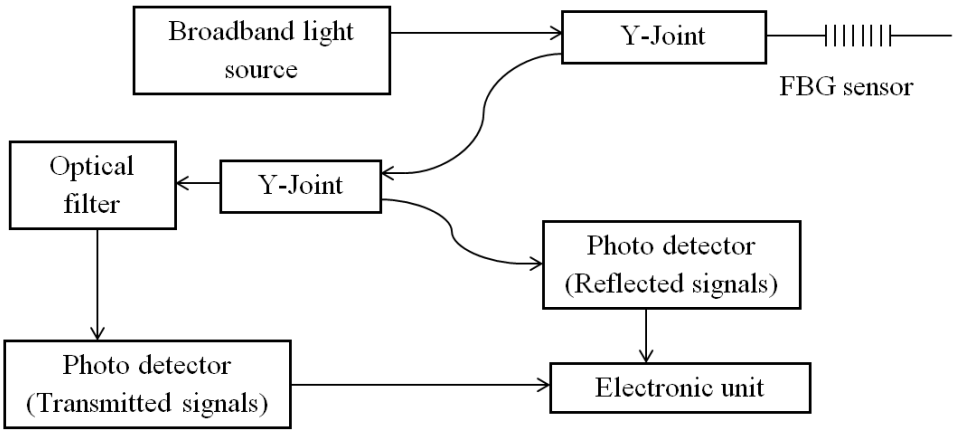

Figure 4.17: Schematic of the FBG dynamic sensing by (Cusano et al. 2004)

Tsuda (2006) performed dynamic measurement by using the matched edge filter system as shown in Figure 4.18. In this approach, the FBG filter is assumed to be constant, and broadband light source is used. The resultant optical signal, at strain-free (grating period, Λ_0 as in Figure 4.16), which is viewed at the end of FBG filter, can be illustrated by the shaded area in Figure 4.19a. Meanwhile Figures 4.19b and 4.19c show how the overlapped area increase or decrease due to strain variations.

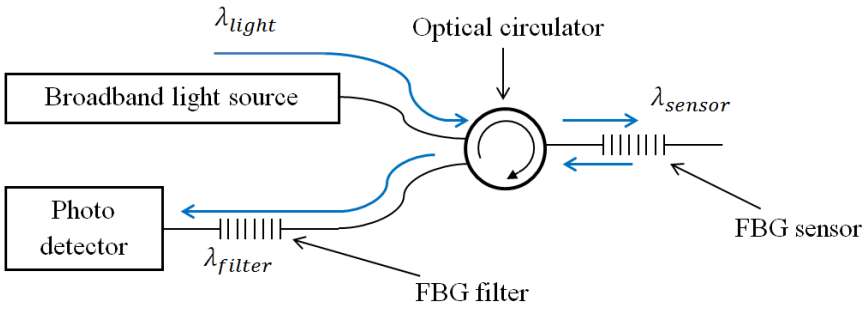

Figure 4.18: Matched edge filter arrangement for dynamic sensing.

The matched edge filter configuration is quite sensitive and Tsuda (2006) used this method to pick up ultrasonic waves propagating in composite samples. The same approach is also demonstrated in the work done by Jian & Hong (2009). However, a significant drawback of this system is a low power conversion energy as explained by Comanici et al. (2011). The idea of filtering the reflected signal from an FBG sensor, with an FBG filter will result in a small dynamic range, thus decreasing the sensitivity. This lead to the proposed system by Comanici et al. (2011), which increased the output power and a narrower bandwidth for the signal reflected by an FBG sensor.

Meanwhile, Tsuda (2006) also presented the measurement using a tunable laser system. The laser output, λ_0 was a narrow band and was set to the wavelength position where the reflectivity of the sensor at strain free is reduced by half. Figure 4.20 illustrates the detection system using a tunable laser source.

Through the set up; when the grating period expands due to strain, the Bragg wavelength becomes longer. As a result, the reflectivity of the sensor at lasing frequency rises (Figure 4.24b), thus, increases the intensity of the light reflected from the sensor. Vice versa, if the grating period reduces, the intensity of light that is reflected from the sensor will decrease. This kind of arrangement has a high power of an optical source due to the narrow band laser. Besides, it has less optical components, therefore, less optical losses. As a result, it gave better sensitivity. However, Tsuda (2006) stressed that, the configuration that utilizes a broadband light source (matched edge filter method) is enough for practical use since the application of a tuneable laser source is expensive.

Meanwhile, Frieden et al. (2010) achieved a high frequency measurement of dynamic strain by coupling the Bragg reflection spectrum (1550 nm) through a tunable Fabry-Prot (FP) filter. Note that, the interrogation system was quite similar with Tsuda (2006), except Frieden et al. (2010) used the FP filter instead of a matched FBG filter. The resultant optical signals which travel through an

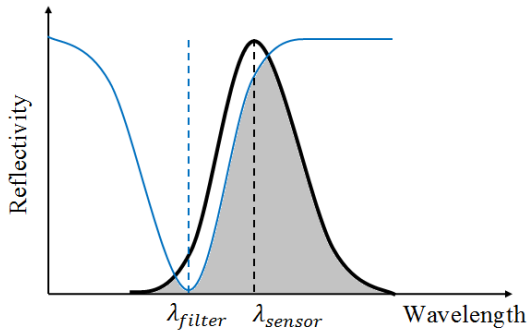

(a) Optical signal at strain free.

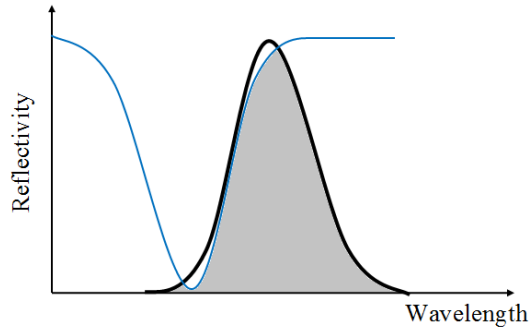

(b) Optical signal during FBG sensor in tension.

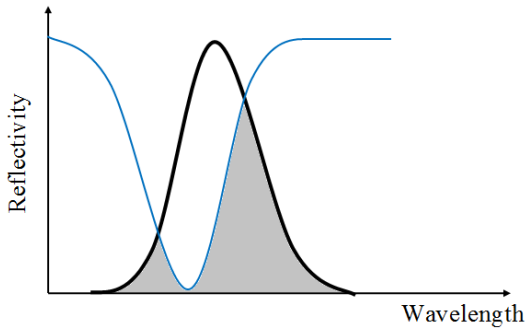

(c) Optical signal due to FBG sensor in compression.

Figure 4.19: The resultant of optical signals after passing through an FBG filter as configuration in Figure 4.18 (Tsuda 2006).

FP filter was compared to the referenced signals from reflected spectrum without an FP filter as shown in Figure 4.21. An additional electronic system was utilized to get the ratio between the intensity of the filtered and unfiltered Bragg reflection peak for the dynamic signals acquisition.

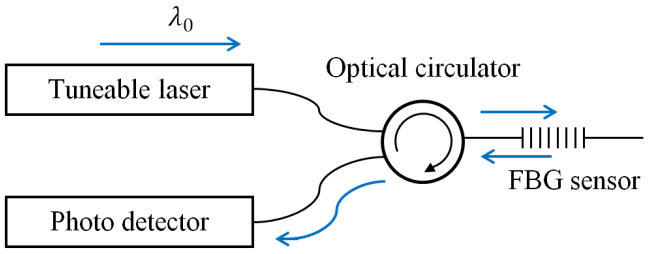

(a) Arrangement for FBG dynamic sensing using a tunable laser source.

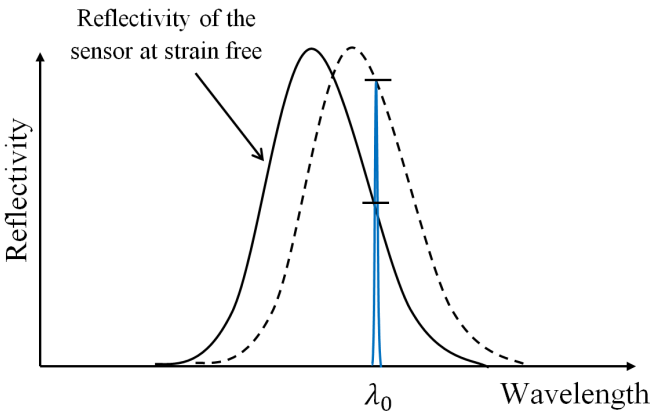

(b) Variations in reflectivity at the lasing wavelength when the grating period changes.

Figure 4.20: Principle of operation for a detection system using a tunable laser source (Tsuda 2006).

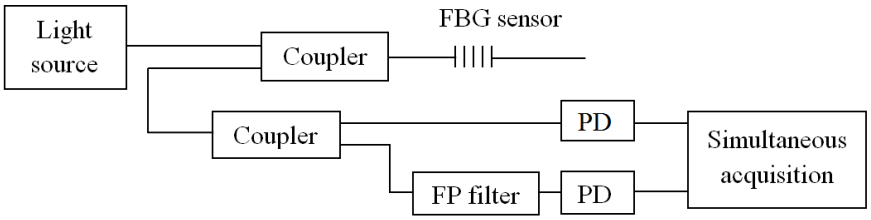

Figure 4.21: Fast FBG interrogation by (Frieden et al. 2010)

A similar approach was also done by Ling et al. (2006). They utilized an optical tunable filter (OTF) instead of an FP filter or matched FBG filter. Figure 4.22 illustrates the detailed configuration of the system. The expected resultant optical signals were the same as explained in Figure 4.18, yet the optical tuneable filter might be costly compared to the used of matched FBG filters.

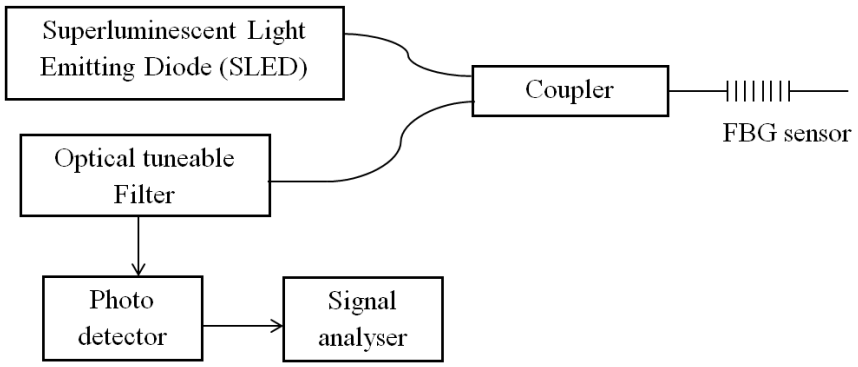

Figure 4.22: FBG dynamic strain measurement by (Ling et al. 2006)

4.4.1 General construction for FBG dynamic sensing

Among all the FBG dynamic sensor systems presented in this section, the work by Tsuda (2006) (both narrowband laser and broadband light) has become the main reference and concept for this Ph.D. work, especially for ultrasonic wave detection in AE monitoring. Most of the recent works utilized the same concept, for instance, the work done by Seo et al. (2009) and Wild & Hinckley (2007).

However, through the understanding of the basic operation of each optical component, a new design can be proposed based on requirements, such as high sensitivity, low noises and relatively low overall cost. It must follow the basic design of an FBG dynamic sensing system, whereby a variation of light power must be such that it can be summarized as in Figure 4.23.

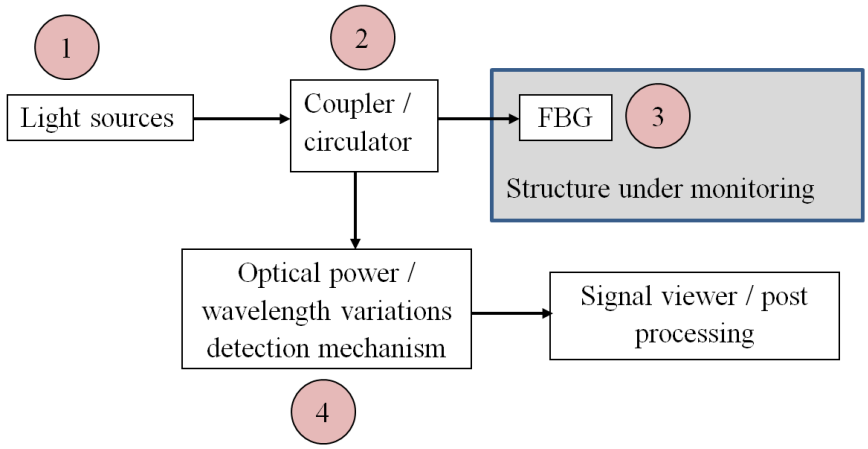

Figure 4.23: The basic schematic diagram of FBG dynamic sensing.

There are four major components in basic FBG dynamic sensing as labelled by numbers in Figure 4.23. The third component; the FBGs can be placed on the structures under monitoring by surface glue or embedding between layers.

Meanwhile the fourth element, is the most complex part; since it is the part where the optoelectronic conversion took place. The design of this part depends on the type of light sources used, either broadband or narrowband light sources. The use of photo detectors in this crucial part may provide a lot of optical noises.

4.4.2 Noise in FBG dynamic sensing

Optical noise is necessary to be considered when designing the FBG dynamic sensing. There are a lot of possible noises that can occur in an optical based system. Based on Figure 4.23, there are two parts that might contribute to the possibilities of optical noises: the light sources and the photodiodes.

The noises from light sources can be neglected if LEDs are used. If using lasers, possible optical noises can be from the *mode partition noise*, *laser intensity noise* and *laser phase noise* (Cvijetic 2004). Note that, the *mode partition noise* only appears in MML type lasers due to multi-mode effect.

Meanwhile, *laser intensity noise* and *laser phase noise* are the *microvariations* in the laser output signals, which can affect the stability of the power and spectral bandwidth size of the output signals. These noises are relatively small and usually attenuates before reaching the receiver part (Cvijetic 2004). However, if they are able to reach the photodiodes, the noise signals can appear in the resultant output signals. Usually the use of appropriate laser driver can eliminate any significant noises associated with the lasers.

The biggest noises in an FBG dynamic sensing system are due to the photodiodes. The use of PIN PD may reduce the amount of noise to only three kinds: thermal noise, quantum and dark current noise. However, the impact of the dark current noise is usually ignored; since its power is relatively so low (Cvijetic 2004).

Meanwhile, quantum noise is due to the quantum nature of light and random electron generation during the photodetection process (Cvijetic 2004). It seems not to be a major concerned in PIN PD compared to the APDs because, in PINs, each photon will generate one electron-hole pair (linear relation). However in APDs, the probability of having a random number of secondary electron-hole pairs is high, thus increasing the signal to noise ratio (SNR) of the output signals.

The impact of the thermal noise cannot be neglected for both types of photodiodes. It is always visible in the signal viewer; even if optical signals are not present. Figure 4.24 illustrates the existence of thermal noise in output signals.

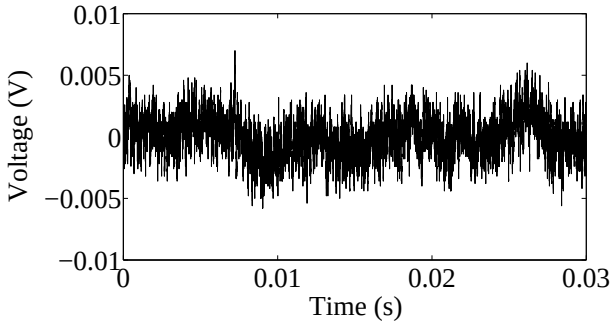

(a) Output signal without any dynamic input.

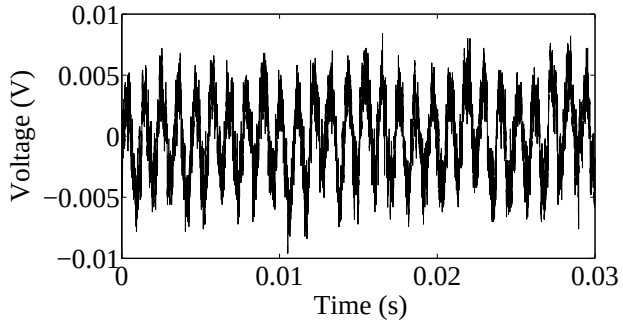

(b) Output signal due to a vibration.

Figure 4.24: Thermal noise existence in an FBG dynamic system.

The thermal noise is generated by the process of converting the photocurrent to voltage by the load resistor. The load resistor creates its own noise because of the random thermal motion of electrons (Cvijetic 2004). Increasing the load resistor may reduce the noise and increase the receiver's sensitivity, however it will also affect the receiver bandwidth - limited bandwidth.

In order to investigate the SNR of the FBG dynamic system; particularly in the thermal noise effect, a case study was done and presented in the next chapter.

4.4.3 FBG for acoustic emission detection

The incorporation of FBG sensors into an AE system was raised after FBG showed excellent capabilities for dynamic strain measurement. At the beginning of the development stage, the detection was up to a few hundred hertz. However, since the early 21st century, the growing interest of an FBG dynamic system continues in ultrasonic and acousto-ultrasonic studies where many researchers put a lot of

efforts to prove its capabilities, especially in making smart SHM into reality. For instance, Tsuda (2006) has investigated the ultrasonic failure detection in carbon fiber composites using FBG sensors. Meanwhile, Lam et al. (2009) has introduced an active failure detection system for composite laminates; utilizing FBG as the main sensor head in an acousto-ultrasonic system.

In the past decades, there were several researchers who have shown great interest in incorporating FBG sensors in AE systems for SHM, especially that involved composite structures. The system was sometimes called an FBG-AE system. An FBG-AE is a regular Acoustic Emission system but with a Fiber Bragg Grating (FBG) sensor as the sensor head. The main difference between the FBG-AE concept and FBGs in ultrasonic or acousto-ultrasonic is that the FBG-AEs provide a passive type of monitoring.

One of the earliest systematic studies of acoustic emission detection using FBGs, had been presented by Perez et al. (2001). They have reported the ability of their FBG-AE system to obtain the signals from pencil lead breaks on an aluminium plate. Not only that, they also performed an experiment to show the effect of different signal source directions to the FBG sensor's position, as illustrated in the Figure 4.25.

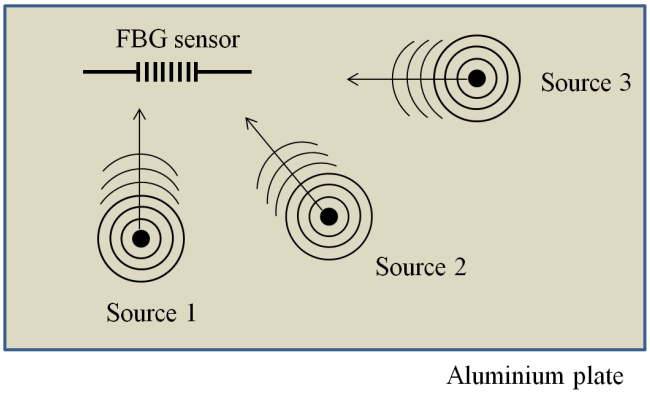

Figure 4.25: Signal sources setup with respect to FBG's position.

As a result, they had plotted the amplitude response over distance, for three different FBG sensor's direction as shown in the Figure 4.26. The attenuation of the signals over a distance is expected since the attenuation always occurs for any wave propagation on a plate. However, the directional dependencies of the FBG position to the signal source's location is significantly critical as it will affect the consistency of the measurements.

A few years later, Lee & Tsuda (2005) had designed a new FBG sensor head to replace a conventional PZT transducer for mechanical tests. It was a revolutionary idea since this new sensor head is physically very thin compared to piezoelectric

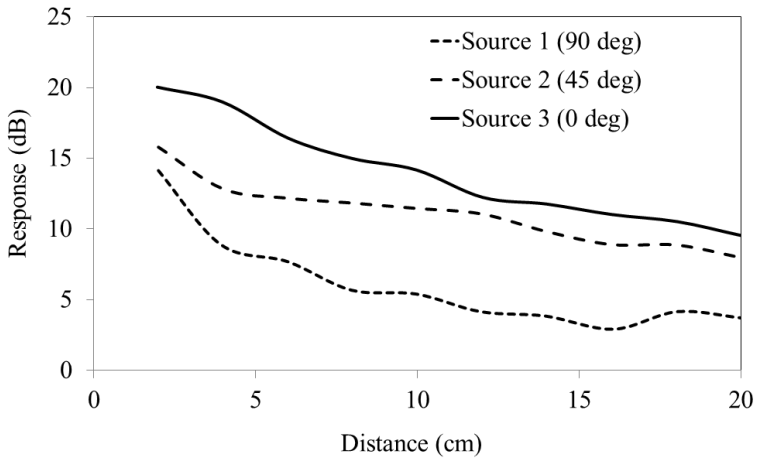

Figure 4.26: Directional dependencies of the FBG sensor positioning to the direction of the signal sources (Perez et al. 2001).

(PZT) sensors, and also mobile. The comparison between the newly designed sensor, to the conventional PZT sensor is shown in Figure 4.27.

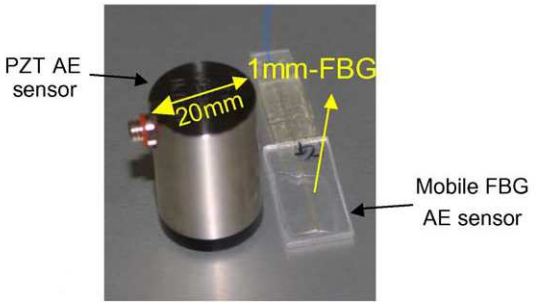

Figure 4.27: Physical comparison between FBG-AE sensor head with PZT sensor (Lee & Tsuda 2005).

Although they claimed that the proposed sensor has good SNR, yet the FFT result comparison (with the PZT sensor) shows that the FBG-AE sensor might be 'too sensitive' as it reveals the existence of too much noise. It may be a result of using an FBG grating length that was undersize (1 mm).

Seo et al. (2009) had proposed a new way to enhance the sensitivity of FBG sensors for AE monitoring. The full system was no different than the one that was used by Lee & Tsuda (2005) and Tsuda (2006) (the system with a tunable laser source). The sensitivity enhancement was achieved by partially bonding the FBG sensor to the structure under monitoring instead of fully bonding, as commonly practiced.

This kind of FBG sensor bonding was frequently mentioned in their paper as 'cantilever type FBG.' Although the signals obtained by the cantilever type FBG show a low SNR, yet it was able to acquire higher frequency contents than the one that was fully bonded. Another interesting claim which Seo et al. (2009) had in their conclusion was, the longer the FBG grating, the better its sensitivity.

Meanwhile, Wild & Hinckley (2007) introduced FBG sensors for AE detection as an intention, to be utilized in a robotic non-destructive evaluation in SHM. The validation of the FBG-AE system was done by dropping the bolts and nuts on the specimen and also the pencil lead breaking test. The results were promising as the detection of the signals were clear and the SNR was high. However, the work did not clearly indicated how accurate the frequency contents detection was by the FBG-AE system, since they were focussing on communication by acoustics transmission.

There are several more research works which had attempted to utilize the FBG-AE system. However, it is stressed that the embedded FBG sensor in a composite plate offers significant benefits if compared with a conventional PZT transducer as explained in the Chapter One (Section 1.1.4). Furthermore, the battle for developing smart materials that can react or adapt their characteristics due to signals from embedded sensors is undeniable. In conclusion, up to date, the development FBG-AE systems are still in the stage of AE signal detection.

4.5 NIR-FBG System for Dynamic Measurement

Despite the growing numbers of research work that utilize 1550 nm range FBG for dynamic sensing, there is also an alternative option, that is the Near-Infrared Region (NIR) FBG. In optical transmission systems, there are three main light-wave ranges which often used: 850 nm, 1300 nm and 1550 nm.

The 1550 nm FBGs are suitable for a long-wavelength transmission system. According to Figure **??**, the 1550 nm wavelength of optical signals has the lowest attenuation coefficient. However, a practical dynamic sensing system does not need hundreds of meters of long cables. Thus, a short-wavelength ($\sim 830nm$) light-wave system also can be used.

From the photodiodes perspective, the 1550 nm range, needs a smaller band gap compared to the silicon based 830 nm range detectors. Recall the Equation 4.3 and 4.2 in Section 4.3.1, the higher wavelength requires a smaller band gap to produce an electron-hole pair. As a consequence, the carrier (hole and electron)

not only can be excited by photons, but also possibly via thermal energy. In other words, the InGaAs (1000 nm - 1700 nm) detectors may need to operate at a suitable temperature for good sensitivity.

Meanwhile, the probability of n numbers of electron-hole pairs to occur during a time interval of Δt, can be written in terms of Poisson probability distribution (Cvijetic 2004),

$$p(n) = \frac{N^n e^{-N}}{n!} \tag{4.13}$$

where N denotes the mean number of photoelectrons detected at Δt. The N value can be obtained by,

$$N = \frac{\eta}{\widehat{hf}} \int_0^{\Delta t} P(t)dt \tag{4.14}$$

Although equation 4.14 reveals that the longer the wavelength (higher light frequency, f), the greater the probability of having electron-hole pairs (thus more sensitive), it, however, also depends on the quantum efficiency, η. According to the Figure 4.12, silicon-based photo detectors always have a higher quantum efficiency than the InGaAs based PDs. In other words, the performance of both wavelength ranges of PDs is almost equal.

In comparison to the 1550 nm range, the NIR range FBG's are widely available and are comparably cheaper silicon-based technologies. However, the excessive noise levels that are experienced in NIR FBGs have caused the rejection of these sensors for SHM systems. Fortunately, the use of the dynamic response for in-situ SHM systems requires only the frequencies of the dynamic strain and, therefore, the embedded noise levels in the measured signal can be processed cheaply without scarfing the signal frequencies (Kessler et al. 2001).

Therefore, NIR-FBG sensors are more suited to the development of low cost SHM systems which use relatively cheaper silicon sources and detectors, with comparable performance as the 1550 nm based systems. For instance, the Silicon based photodiodes offer almost the same capabilities as the InGaAs type: low dark current and high speed (Paschotta 2013*a*).

4.5.1 Principle operation of the NIR-FBG system for dynamic measurement

In this Ph.D. work, two arrangements for NIR-FBG dynamic sensing were suggested. Each of the configurations was distinguished by the optical power detection mechanism as illustrated by the basic diagram of an FBG dynamic sensing system (see Figure 4.23).

The first proposed system is the concept as explained by (Tsuda 2006), that is the one with a broadband light source and fixed FBG filter. The arrangement of the system can be shown as in Figure 4.28.

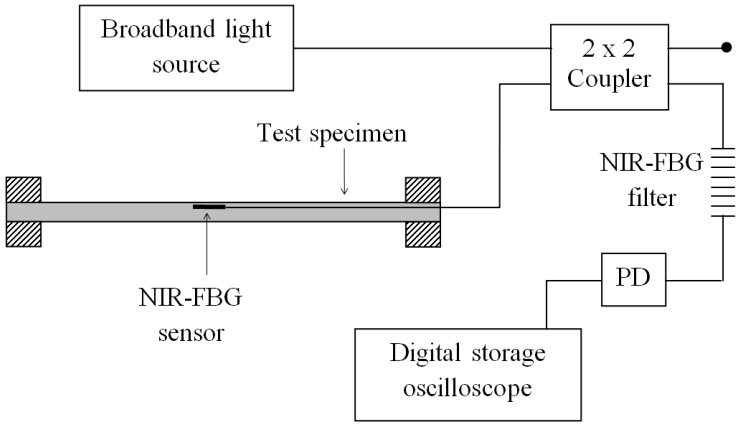

Figure 4.28: Schematic diagram of the optical components arrangement for the fixed NIR-FBG filter system.

To explain the basic principle of the system, consider a clamp-clamp position of thin composite sample with an embedded FBG and having a point force in the center of the plate, as illustrated by Figure 4.29. The NIR-FBG sensor will experience the stretching or compression due to the bending of the sample as shown in the figure. Please note that, if the NIR-FBG is located at the bottom of the sample, it will be in the compression state. As consequences, there will be a variation to the optical signal before reaching the photodiodes as shown as in the Figure 4.30. These optical power variations are significant. As a result, it caused big changes to the output current of the PD, due to the photocurrent generation as explained in the Section 4.3.2.

Figure 4.31 illustrates the demodulation of the NIR-FBG spectral shift due to the bending (or compression) of the composite sample. The spectral shifts of the NIR-FBG sensor, labeled as A in the Figure 4.31, will cause optical power

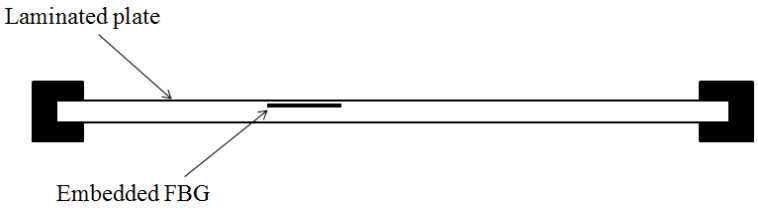

(a) Sample of laminated plate with embedded NIR-FBG.

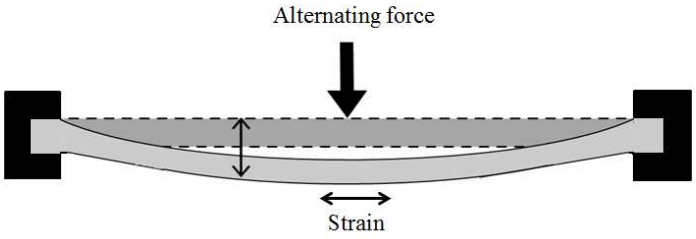

(b) Laminated plate in bending due to applied force.

Figure 4.29: Laminated plate under applied force.

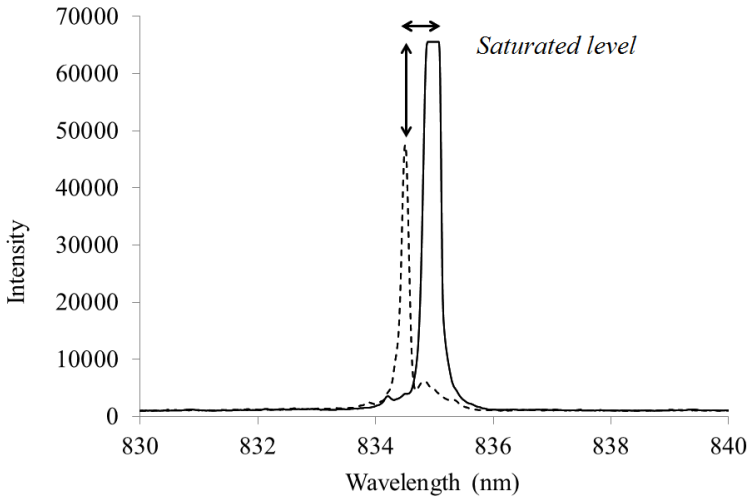

Figure 4.30: Optical spectrum variations from matched FBGs system.

variations (labeled as B) as the optical signal passes through the NIR-FBG filter. Consequently, this will cause the changes in the voltage reading (labeled as C) if viewed from the signal viewer.

The fixed FBG filter (or matched-FBGs) system was proved to be very useful with 1550 nm based system as discussed in earlier section. However, its applica-

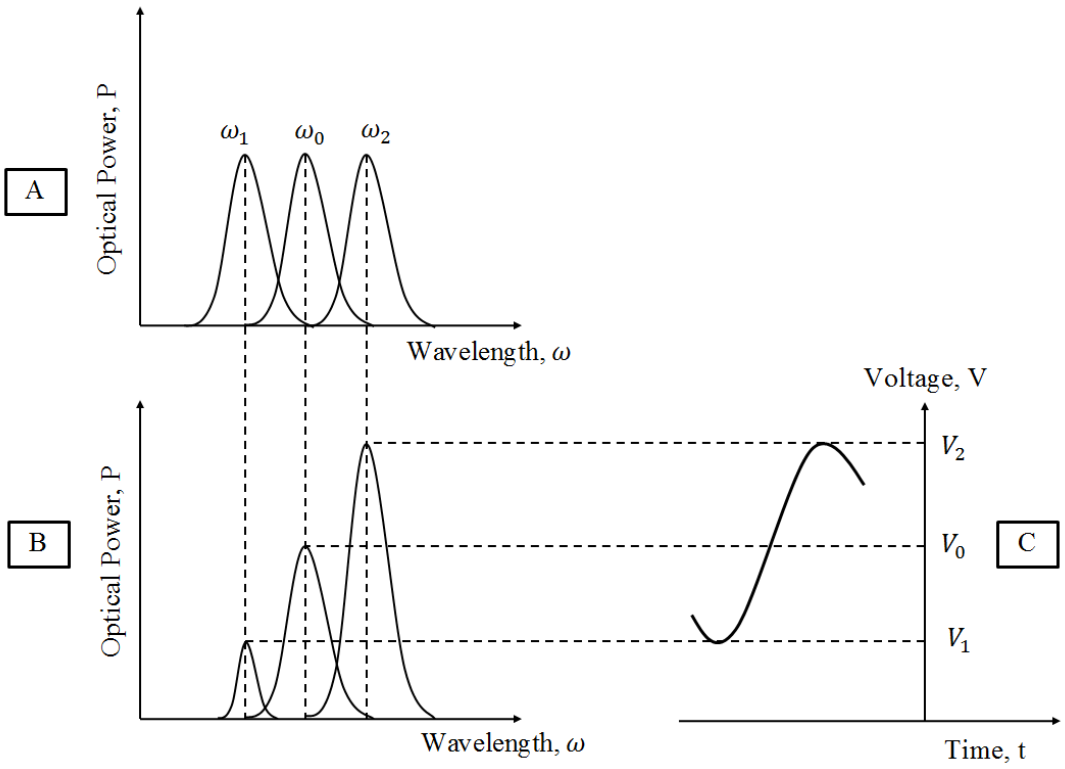

Figure 4.31: Demodulation of the NIR-FBG spectral shift for the fixed NIR-FBG filter system.

tion with the 830 nm optical components has never been tested. The usage of matched-FBGs might be impractical since it is difficult to control the 'matching condition' in the long term, especially if the FBG sensor is embedded in laminated structures.

Due to the limitation, the second setup for the NIR-FBG sensor-based dynamic measurement was introduced, as shown as in Figure 4.32. The basis was very similar to the first proposed NIR-FBG dynamic system, except with no matched-FBGs; thus, only a single NIR-FBG was used. The performance of this system was never examined; thus, the experimental validation of the system will be presented in the next chapter.

Through the arrangement in Figure 4.32, any changes of the reflected light from FBG sensor due to dynamic strain will be detected by photodetectors. The PDs convert the wavelength variations into an electrical signal which can be observed from the oscilloscope. This approach utilized the *responsivity curve* which relates to the wavelengths and PD output currents, as explained in next Subsection (4.5.2).

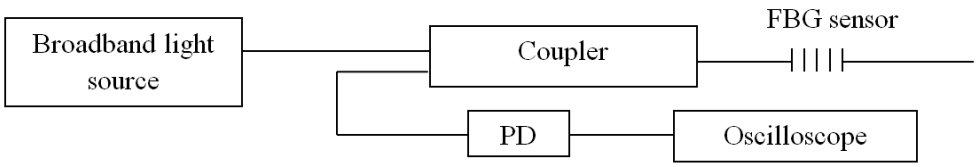

Figure 4.32: The second arrangement for NIR FBGs dynamic sensing; the single-FBG system.

The optical power intensity which is proposed in the system is considered constant due to the selection of broadband light source which operates with a flat power between $822 - 870$ nm, as indicated in Figure 4.33. Thus, assuring only the wavelength variations will cause the changes in PD's voltage output.

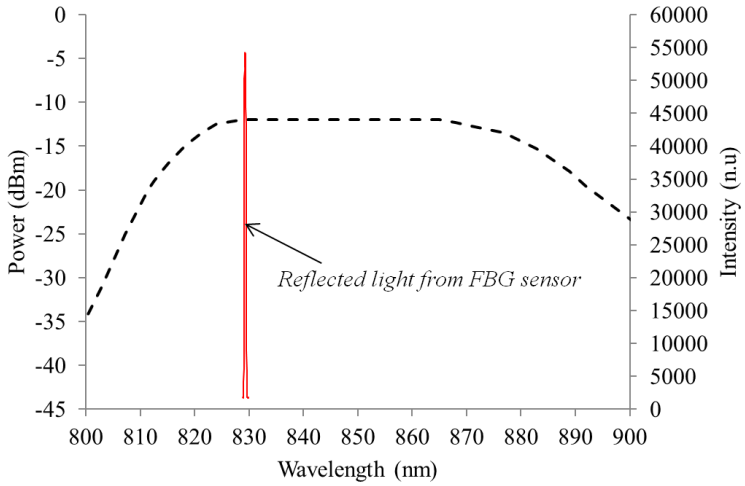

Figure 4.33: Power spectrum of the broadband laser source. The red line shows the spectrum of the NIR-FBG.

For this research work, the broadband light source, SLED type has been used. It has a maximum power of 3.93 ± 2 mW at the highest applied current, 200 mA. It is a product from the *Amonics* company, and the model is ASLD85-050-B-FA as shown by the Figure 4.34.

4.5.2 Responsivity curve manipulation in the single NIR-FBG system

To explain the working principle of the second proposed NIR-FBG system's arrangement, consider the same composite thin sample, as indicated in Figure 4.29. With the system as in the Figure 4.32, there are two main variations that will

Figure 4.34: The SLED lights source.

occur to the reflected light as illustrated in the Figure 4.35.

The main variation was due to the wavelength change (left-right arrow) which is caused by the grating motion, therefore, causing to the output current from the PD. The light intensity changes (up-down arrow) might be caused by noises from the optical system; however, it only shows very little differences and can be ignored.

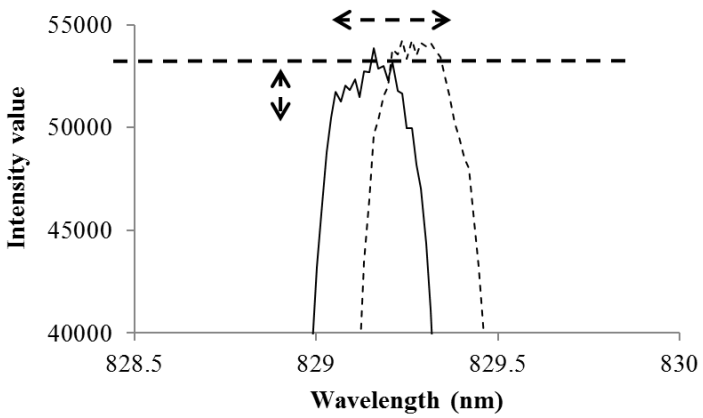

Figure 4.35: Variations of reflected light from FBG sensor viewed during simple static three-point bending of the composite sample. The dotted line indicates the original plot before loading.

Meanwhile, Figure 4.36 shows the responsivity, R, curve of a PD. The value R, can be expressed as the conversion rate between a photocurrent, I_p and optical power input, as explained the Section 4.3.2. The concept of using an NIR-FBG based system still can be proved with the PD's in 1550 nm range. However in the future, a silicon-based PD is recommended since it usually has a higher quantum

efficiency and is obviously cheaper than InGaAs PDs.

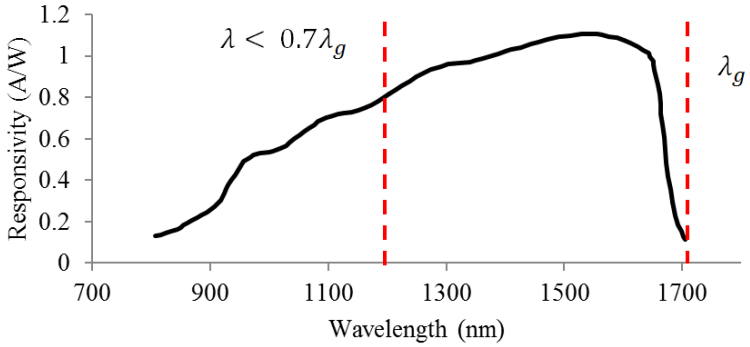

Figure 4.36: Responsivity of the photodetector; model PD10CS (InGaAs) detector.

Figure 4.37: The PD10CS (InGaAs) detector.

Recall the Equation 4.7, and the relation of wavelength, λ and frequency, f as in Equation 4.2. Rearranging both equations and assuming that the optical power input is constant, the wavelength, and the PDs output current, I_p can be related by a linear relation,

$$\lambda\eta(\frac{e}{\widehat{hc}}) = I_p/P_{in} \tag{4.15}$$

$$I_p = \lambda(P_{in})(\eta\frac{e}{\widehat{hc}}) \tag{4.16}$$

for $\lambda < 0.7\lambda_g$ where λ_g is the cut-off wavelength. The wavelength of the FBG must fall below $0.7\lambda_g$ to assure the linearity of Equation 4.16. Please note that increasing optical power input, P_{in} will increase the current (and voltage) output reading.

Differ from the fixed FBG-filter systems, the single-NIR-FBG system only uses the reflected light from the grating. Theoretically, this will reduce the extra

connection, such as adding an FBG as a matched filter. Therefore, the optical power loss can be decreased.

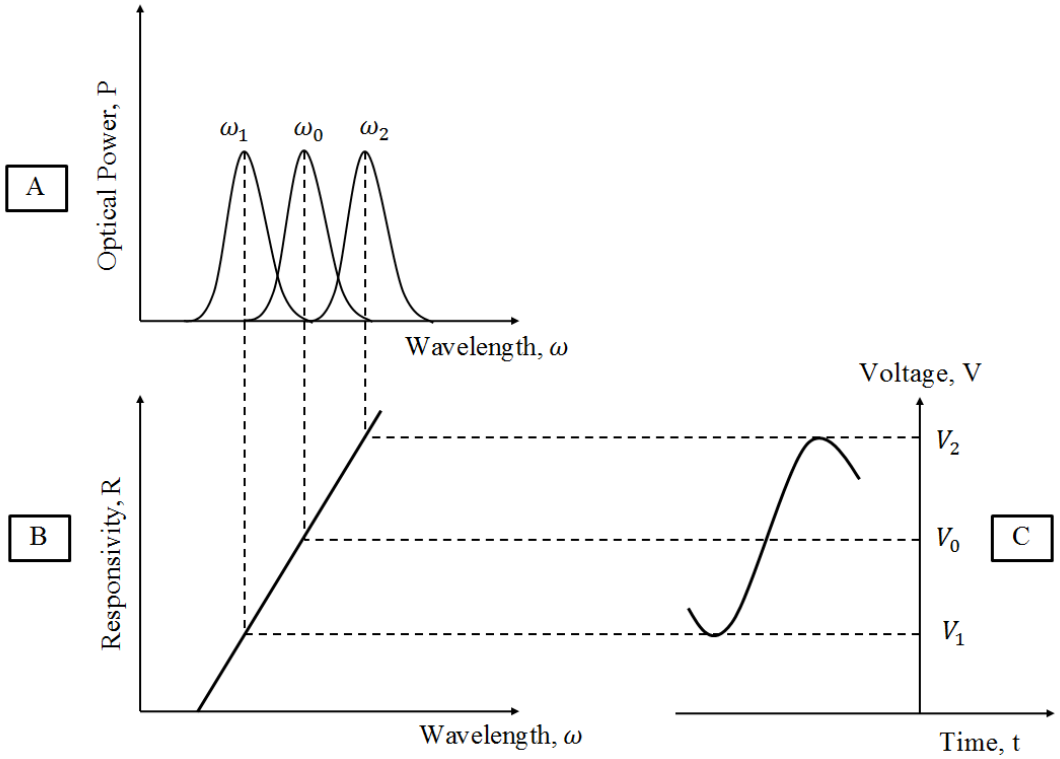

Figure 4.38: Demodulation of the NIR-FBG spectral shift for the single NIR-FBG system.

In the meantime, the demodulation of the NIR-FBG spectral shift for the single NIR-FBG system can be illustrated by the Figure 4.38. The demodulation concept is the same as for the fixed NIR-FBG filter systems, except the single NIR-FBG systems utilize the linear region in the responsivity curve to convert the spectral shifts to voltage changes.

4.6 Chapter Summary

This chapter successfully explained the FBG sensor based system for dynamic measurements. Some essential elements which are necessary for a complete sensor system, also were reviewed. It is essential to have full understanding of the main optical components since they can be manipulated to provide a better performance to an FBG dynamic sensor system.

The small size of the FBGs also offers an additional superiority, especially as a replacement to the conventional PZT transducers. However, this new concept of dynamic sensors, particularly for the applications in wave propagation based SHM is still in the developmental stage and need more work before it can be established in the field.

Hence, the introduction of NIR-FBG sensor based system for FBG dynamic measurement is in the right time. In the vision to have a cheaper system in the future, the NIR range of optical equipments (e.g. lasers, photodiodes, etc.) can be used with the NIR-FBG sensor-based system. Two NIR-FBG systems have been proposed, and the fundamental principle was fully explained in this chapter. As these systems have never been examined in any published work, the next chapter will present and discuss the validation of this system and its applications in SHM.

Chapter 5

NIR-FBG sensors for Dynamic Response of Composite Plates

5.1 Chapter Overview

This chapter will present the validation of the proposed NIR-FBG sensor system, particularly in wave propagation based SHM. The main objective is to use this innovative system in several applications that usually done traditionally with PZT. Note that in Chapter 3, the applications of AE have been explored particularly for the use in SHM of composite thin plates. As a result, significant drawbacks of the conventional AE system were noted as elaborated in the Section 3.9. In the other hand in Chapter 4, the NIR-FBG sensor system for dynamic strain measurement has been explained. This optical fiber based measurement system was developed as an alternative to the traditional PZT in AE applications.

Every experimentation in this chapter was carefully planned and completed in order to prove the practicability of the developed system. All these include the dynamic response due to impact source and shaker excitation, SNR investigation, wave propagation attenuation effects and signal source mapping. For this purpose, two types of NIR-FBG based sensor systems for dynamic measurement were proposed, and their application will be validated by a series of case studies. They are:

1. Single FBG sensor system.
2. Fixed FBG filter system.

All two of them have been discussed thoroughly, particularly in Section 4.5.1. However, further findings will be discussed through some experimental studies and are presented in the next sections.

In the final section of this chapter, the usage of the NIR-FBG systems in some significant applications in SHM of composite thin structures will be presented.

5.2 The NIR-FBG System with Single-FBG

An experimental study was conducted in order to examine the use of the novel NIR-FBG dynamic sensing system with a single FBG, particularly for composite thin laminate structures. The main aim of this study is to investigate the response of the proposed system from two kinds of wave propagation sources, that is impact hammer and shaker excitation. Through the experiment, the highest frequency component that can be captured by the sensor system was targeted.

5.2.1 Case study: The validation single-FBG system

Two samples of glass / epoxy resin laminates, with a stacking sequence of $[0^o]_8$, were fabricated by hand lay-up method. An 830 nm FBG sensor was embedded during the lay-up. It was placed in between the 7^{th} and 8^{th} layer, since the most displacement occurs closer to the surface of the plates. The details of the geometry of both samples are summarized in Table 5.1. In the meantime, the material properties for the GFRP composite that was used in the experiment can be summarized as in Table 5.2.

Table 5.1: Detail geometry of the samples.

	Dimensions ($l \times w \times h$)
Sample 1	270 mm × 123 mm × 4.25 mm
Sample 2	265 mm × 97 mm × 4.4 mm

The samples and the NIR-FBG system were set up as the arrangement in Figure 5.1. A piezoelectric sensor was placed as close as possible to the FBG sensor, as shown in Figure 5.2. This condition was applied for both samples.

An impact with a hammer has been done on the composite samples. The impact hammer, model 086C04, was from PCB Piezotronics Inc. The impact initiated

Table 5.2: Material properties of the samples (Rajadurai et al. 2008).

	Values
E_1	34412 MPa
E_2	6531 MPa
v_{12}	0.217
G_{12} and G_{13}	2433 MPa
G_{23}	1698 MPa
Density	$2.0 \times 10^{-9} T/mm^3$

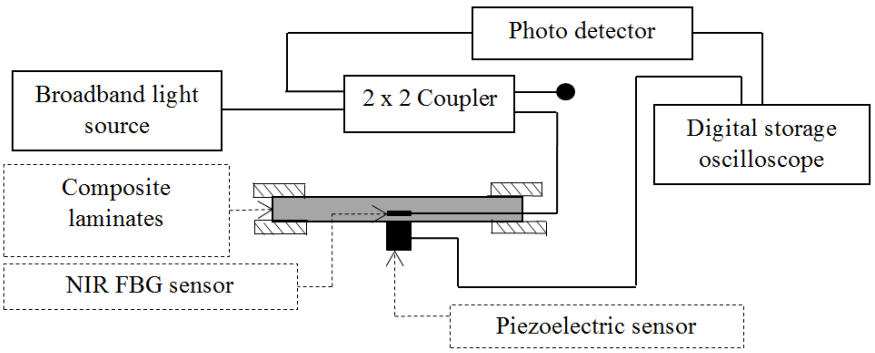

(a) Schematic diagram of the NIR-FBG dynamic sensor system and measurement setup.

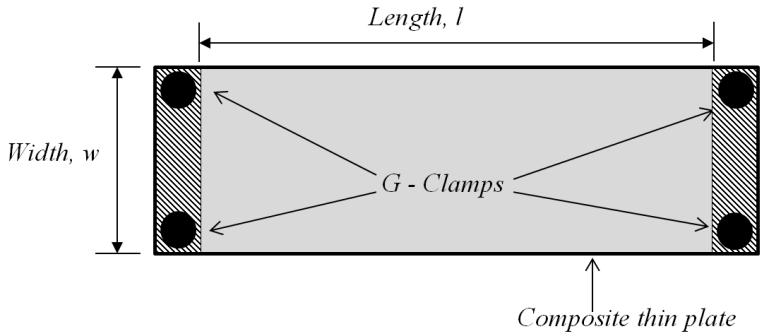

(b) Clamping positions.

Figure 5.1: Specimens and the system arrangement for the experiment.

wave propagation on the samples, which in turn can be used to obtain the natural frequency of the samples and the results are compared with theoretical results from Strand7 software. For this case, the soft tip of the impact hammer was used to induce the lower modes of the natural frequency.

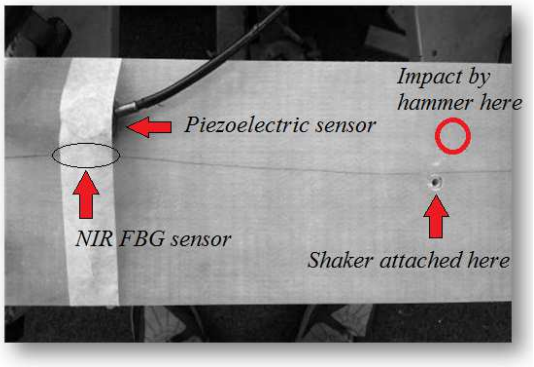

Figure 5.2: Sensors position on the composite sample.

Subsequently, the plate was excited with a shaker at frequency 250 and 500 Hz to investigate the dynamic response from the NIR-FBG sensor system. The shaker (Figure 5.3), model number V201-M4-CE, was from the LDS Test and Measurement Ltd; has the highest useful frequency at 13 kHz. All responses obtained from both sensors were recorded by a digital storage oscilloscope and stored for post processing. Note that the sampling rate for the acquisition was set to 25000 samples per second.

Figure 5.3: The shaker used for the experiment.

5.2.2 Results and discussion for the validation of single-FBG system

Theoretical calculations are essential in ensuring the accuracy of the results obtained from the experiments. The experimental study is considered successful if the results are in the acceptable range (below 10 % error). Therefore, the Finite

Element Analysis (FEA) software, Strand7, was used in order to calculate the theoretical natural frequencies of the samples.

The results of the natural frequency calculation by Strand7 software for both samples is shown in Figures 5.4. The figures reveal the first four mode shapes of the samples.

When the composite thin plates were given an impact at varies points, they were set into vibration. The wave propagations started and propagated along the sample's surface. A number of modes took part in the propagations, as indicated by the free vibration analysis using Strand7 (Figure 5.4a and 5.4b). These modes correspond to the natural frequencies of the thin plates. Figures 5.5 shows the signal waveform due to an impact and its corresponding wavelet transform for both samples.

Meanwhile, the Fast Fourier Transform (FFT) comparison between NIR-FBG and piezoelectric sensor are shown in Figure 5.6. It reveals that the PZT was able to obtain the signal from various modes of vibrations (mode 1, 2, 3 etc.). The NIR-FBG sensor shows a very good response to the mode 1 vibration, which was a flexural wave in nature and has the highest amplitude. The NIR-FBG dynamic system still can capture the other modes of vibration as well, however the magnitudes were relatively small compared to the first mode.

The comparison between the first natural frequencies (mode 1) of the two samples to the theoretical values from the software can be concluded as in Table 5.3. It shows good agreement between both the simulation and the experimental results (error $< 10\%$); thus indicates the accuracy of the NIR-FBG system in capturing the important frequency contents.

Table 5.3: Theoretical natural frequencies of the samples

	Theoretical (Hz)	Experiment (Hz)	Error (%)
Sample 1	157.0	152.6	2.8
Sample 2	184.5	170.9	7.4

Shaker excitations

Figure 5.7 to 5.10 shows the waveform and FFT of signals from the NIR-FBG sensor and piezoelectric sensor for one of the samples for given input excitation of 250 Hz and 500 Hz, respectively. Note that, the lower frequencies which appear

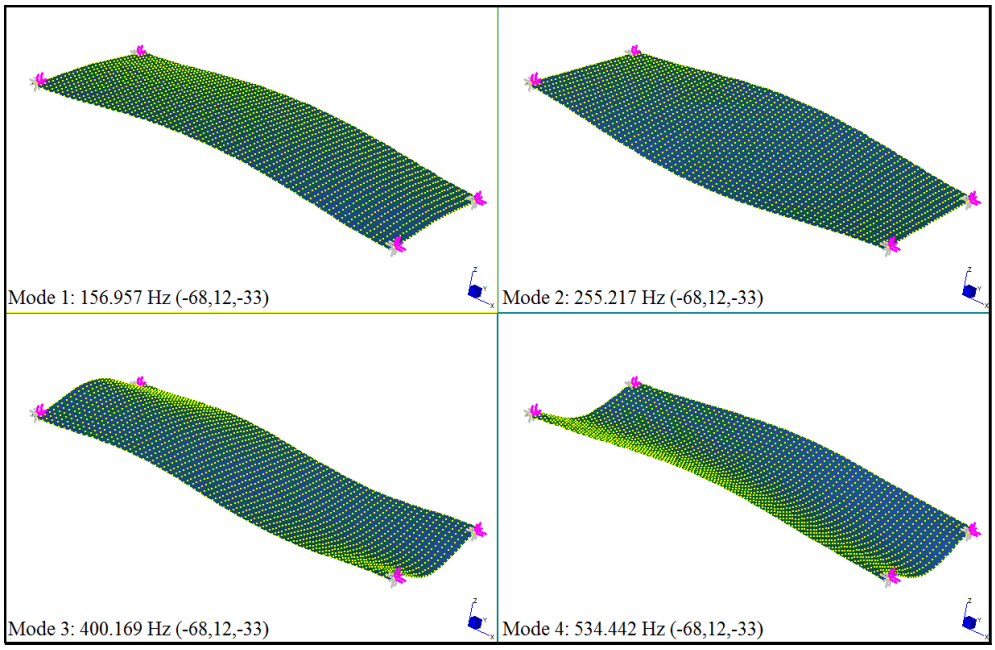

(a) Sample 1.

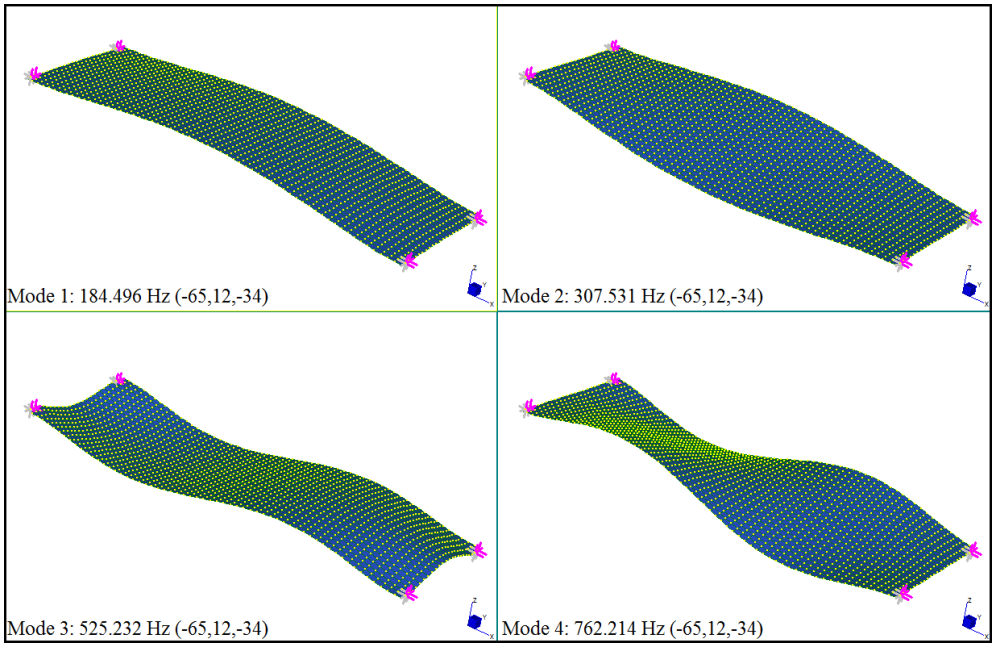

(b) Sample 2.

Figure 5.4: The first four natural frequencies of both samples.

in the spectrum for the NIR FBG sensor response (50 Hz) were the noises due to utility (power line) frequency.

The excitations at 250 Hz and 500 Hz to the sample had generated a vibration

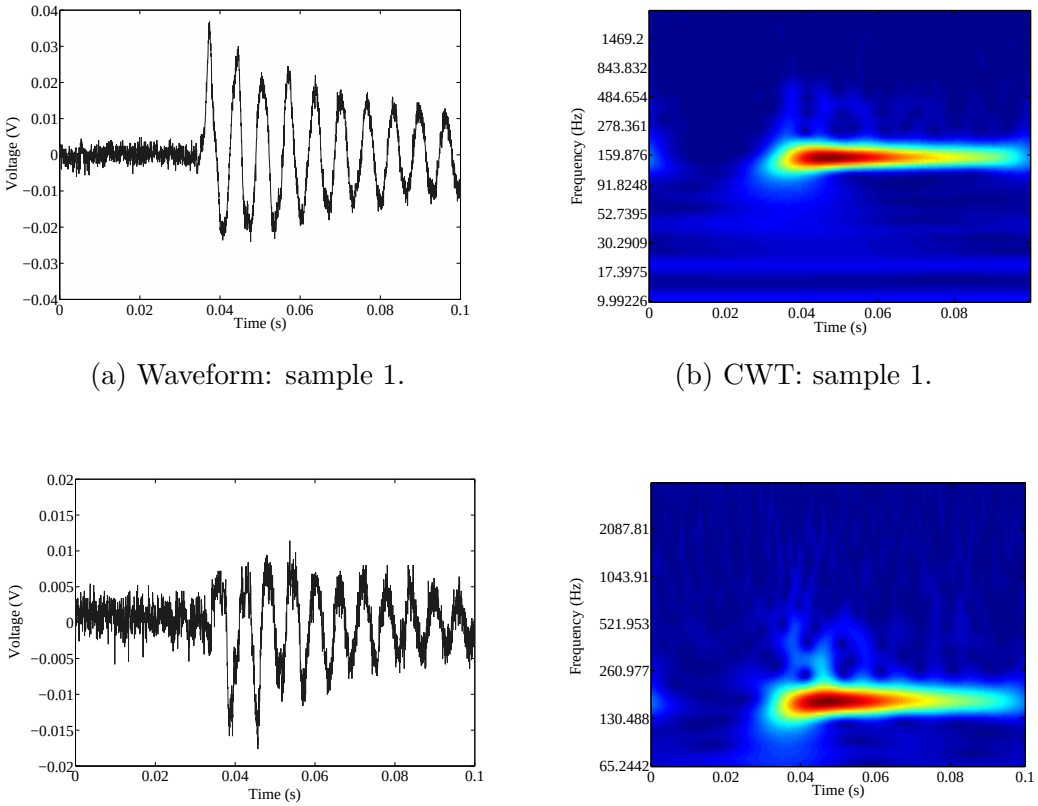

(a) Waveform: sample 1.

(b) CWT: sample 1.

(c) Waveform: sample 2.

(d) CWT: sample 2.

Figure 5.5: NIR FBG sensor response due to an impact for both samples.

with a number of mode shapes, as shown by the FFT analysis (Figure 5.8 and 5.10). The NIR-FBG sensors were able to detect the first natural frequency which was 152.6 Hz, for both excitations. It is observed that both sensors (NIR-FBG and PZT) have different sensitivity to difference wave propagation frequencies. It can be explained by looking at the basic working principles of both sensors, whereby the PZT is sensitive to the out-of-plane propagation, while FBG sensor is better on in-plane wave propagation, particularly the axial strain.

Obviously, the highest frequency obtained by the NIR-FBG dynamic system was 2026 Hz, at 500 Hz excitation. Meanwhile for 250 Hz of excitation, the highest frequency that observed through the NIR-FBG was the excitation frequency itself. In conclusion, the NIR-FBG sensor is able to obtain an accurate frequency response from a sinusoidal excitation source. However, its sensitivity to the higher frequency was limited to the type of propagation mode. For instance, the wave propagation at 2026 Hz was probably the in-plane propagation. In this case, there are possibilities for the other higher frequency contents fail to be obtained by the sensor, such as the wave which propagating with low amplitude of flexural

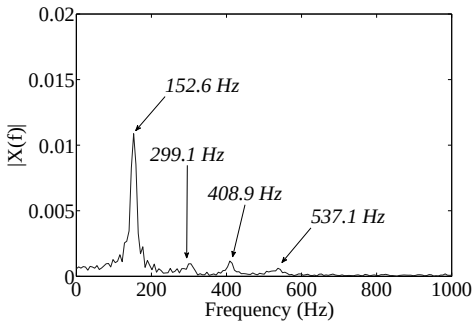

(a) NIR FBG sensor: sample 1.

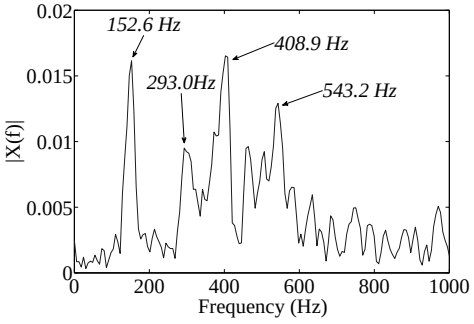

(b) Piezoelectric sensor: sample 1.

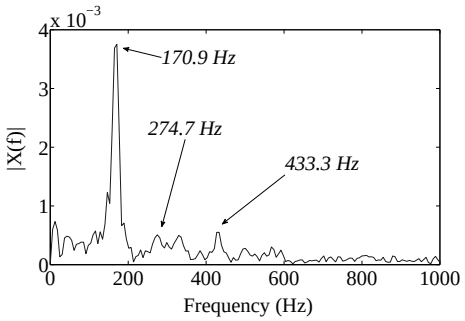

(c) NIR FBG sensor: sample 2.

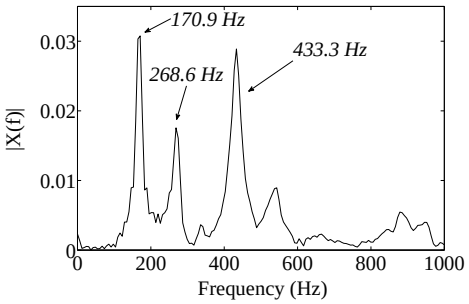

(d) Piezoelectric sensor: sample 2.

Figure 5.6: FFT comparison between NIR FBG sensor and piezoelectric sensor for both samples.

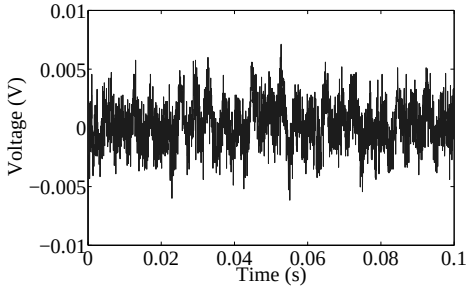

(a) Waveform from NIR-FBG sensor.

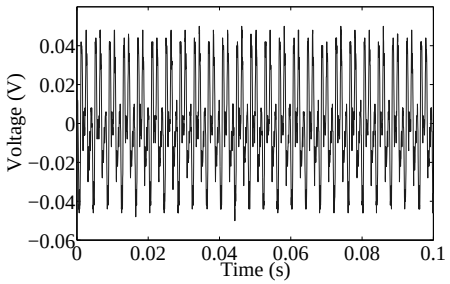

(b) Waveform from PZT.

Figure 5.7: Waveform comparison for 250 Hz excitation.

mode.

On the other hand, higher frequencies were also mixed with noisy signal. However, proper filtering needs to be done in order to screen the noisy signals. Therefore,

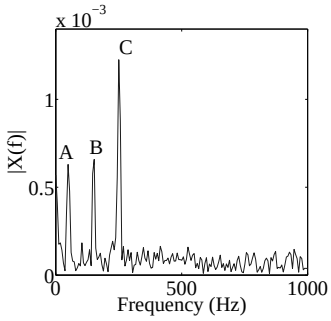

(a) FFT analysis of the signal from NIR-FBG sensor.

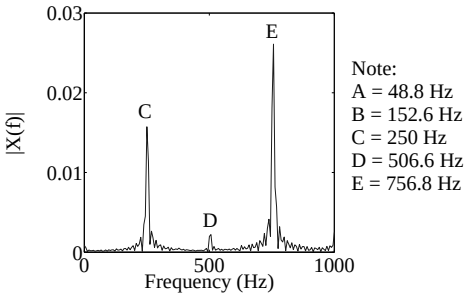

(b) FFT analysis of the signal from PZT.

Figure 5.8: FFT comparison for 250 Hz excitation.

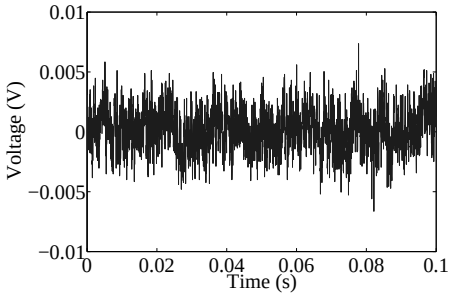

(a) Waveform from NIR-FBG sensor.

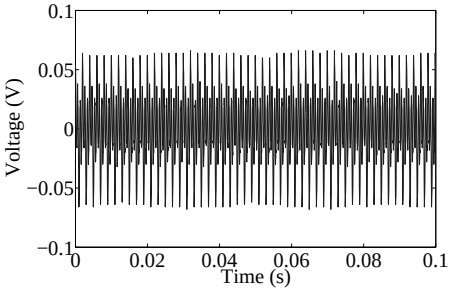

(b) Waveform from PZT.

Figure 5.9: Waveform comparison for 500 Hz excitation.

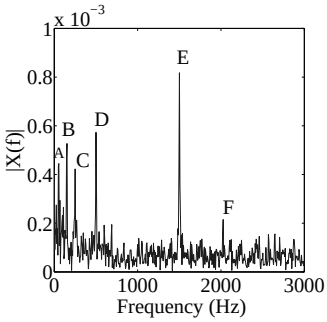

(a) FFT analysis of the signal from NIR-FBG sensor.

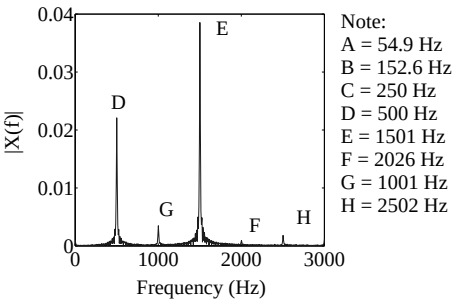

(b) FFT analysis of the signal from PZT.

Figure 5.10: FFT comparison for 500 Hz excitation.

wavelet 'denoising' was proposed in this Ph.D. work and further explanation will be presented in the next section.

5.3 Signals' Denoising

The signal to noise ratio (SNR) is one of the big issues when applying FBG dynamic sensing; including all ranges of FBG wavelength. Although many previous works have shown a remarkable ability in acquiring the dynamic signals with FBGs, the signals actually have relatively low SNR (Tsuda 2006, Tsuda et al. 2004, Perez et al. 2001, Seo et al. 2009, Wild & Hinckley 2007).

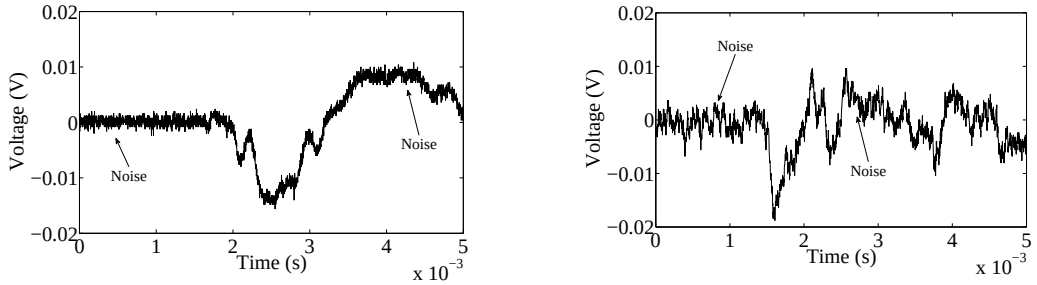

(a) 1550 nm FBG sensor.

(b) 830 nm (NIR) FBG sensor.

Figure 5.11: Waveform signals due to an impact, captured by FBG dynamic sensing.

The noise levels of NIR-FBGs are very high as indicated by the signal response due to an impact, in Figure 5.11. However, the noise signal, which is behaving like *white noise*, can be reduced or eliminated by using appropriate signal processing tools such as wavelet analysis.

5.3.1 Wavelet *denoising*

As discussed in Chapter 2, Section 2.5.2, the Discreet Wavelet Transform (DWT) can be utilized as a filtering tool for any noisy signals. The process is often known as wavelet *denoising*. The term denoising was found to be claimed by Donoho (1995) where he had shown comprehensively how a wavelet transform can be used to optimally reduce signal noise. 'Denoising' is very useful in many applications such as image compression (Boix & Cant 2010), trends analysis (Nalley et al. 2012) and smoothing kinematic data (Ismail & Asfour 1999). The theory of DWT for 'denoising' was discussed thoroughly in many previous works (Ergen 2012, Tsai 2002, Alfaouri & Daqrouq 2008, Cao et al. 2003).

The main procedure of 'denoising' can be summarized in three steps, which are signal decomposition, thresholding and signal reconstruction (Ergen 2012). In

the thresholding stage, noise elimination is done by setting the threshold to the coefficients in the detailed parts, after the decomposition process. There are many threshold estimation methods, however the hard and soft thresholding by Donoho (1995) is widely used and included in this present work.

In order to perform 'denoising' to the signals, as obtained in the experimental validation of the NIR-FBG dynamic system, a case study was performed. The main objective of this study is to reduce the noise level in the impact signal captured by NIR-FBG dynamic sensing which has a low SNR using DWT.

Note that, a smooth signal can be very useful in some specific applications such as impact location and damage monitoring on composite thin plates. Smoother signals can help to provide better accuracy of the arrival time between the sensors and impact source. It can also clearly indicate whether the wave signal from any impact has variations when traveling through any damage across the thin plates.

5.3.2 Case study: An application of 1D digital wavelet analysis for signal *denoising*

Consider the impact signals from sample 1 and 2 as shown as in Figure 5.5. Both signal waveforms have a very low SNR and difficult to determine some important signal parameters, such as the accurate starting points of the impact and the rise time. This study shows the application of a DWT analysis for signal 'denoising'.

To determine the best level, m, of decomposition process (see Section 2.5.2), the calculation must be done based on the scale relation, as in Equation 2.49. Generally, for a sampling rate, f_n, of 25k, the decomposition levels can be represented as in table 5.4. Note that, considering the Nyquist theorem, the frequency must be multiplied by 2 to give an appropriate sampling rate, thus for the case of 170 Hz signal, at least, it must be sampled by 340 Hz. From the table 5.4, decomposition up to level 6 is suitable, as the 340 Hz is within this range.

Figure 5.12 and 5.13 show the approximation result of the signal from an FBG sensor (due to an impact), at three different levels of decomposition; including its respective FFT spectrum. The 'denoised' signal was obtained by setting up all the details coefficients of all levels to be below the threshold value; except the level which has the important frequency range.

Setting all levels to below the threshold value will give only the first natural frequency for this particular case. However, there is an additional frequency

Table 5.4: DWT frequency domain representation.

Level, m		Frequency range	
6	Approximation	0 to $f_n 2^{-6}$	0 - 390.625 Hz
	Detail	$f_n 2^{-6}$ to $f_n 2^{-5}$	390.625 - 781.25 Hz
5	Approximation	0 to $f_n 2^{-5}$	0 - 781.25 Hz
	Detail	$f_n 2^{-5}$ to $f_n 2^{-4}$	781.25 - 1562.5 Hz
4	Approximation	0 to $f_n 2^{-4}$	0 - 1562.5 Hz
	Detail	$f_n 2^{-4}$ to $f_n 2^{-3}$	1562.5 - 3125 Hz
3	Approximation	0 to $f_n 2^{-3}$	0 - 3125 Hz
	Detail	$f_n 2^{-3}$ to $f_n 2^{-2}$	3125 - 6250 Hz
2	Approximation	0 to $f_n 2^{-2}$	0 - 6250 Hz
	Detail	$f_n 2^{-2}$ to $f_n 2^{-1}$	6250 - 12500 Hz
1	Approximation	0 to $f_n 2^{-1}$	0 - 12500 Hz
	Detail	$f_n 2^{-1}$ to $f_n 2^{-0}$	12500 - 25000 Hz

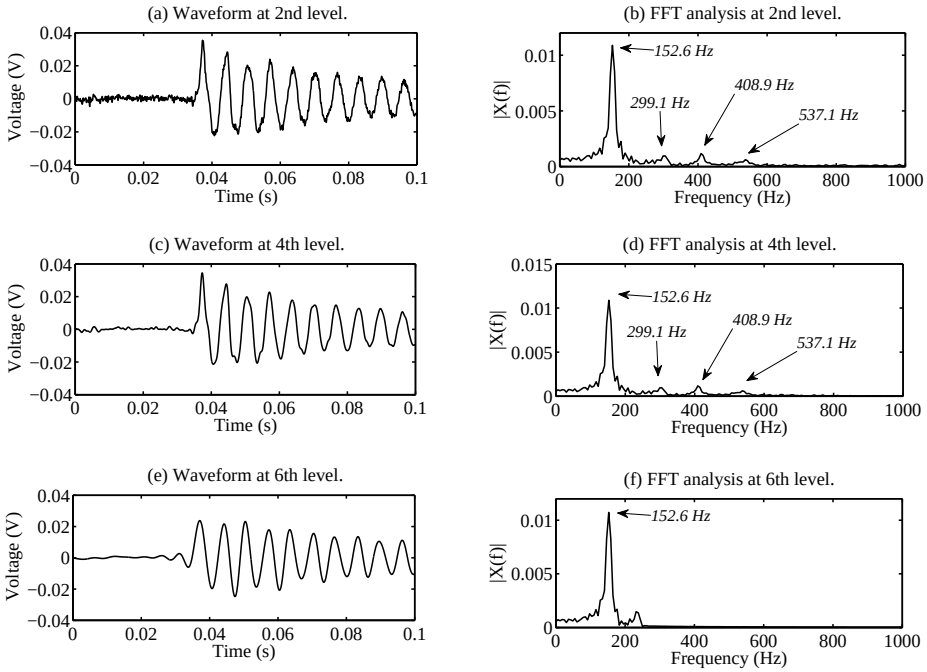

Figure 5.12: Impact signal from sample 1 and its corresponding FFT, at three different decomposition levels.

that appeared in the FFT spectrum (see Figure 5.12f and 5.13f); which is not consistent with any of the natural frequency contents, either from theoretical calculations or from piezoelectric sensor results.

This fake frequency is formed as a result of over 'denoising'. In other words,

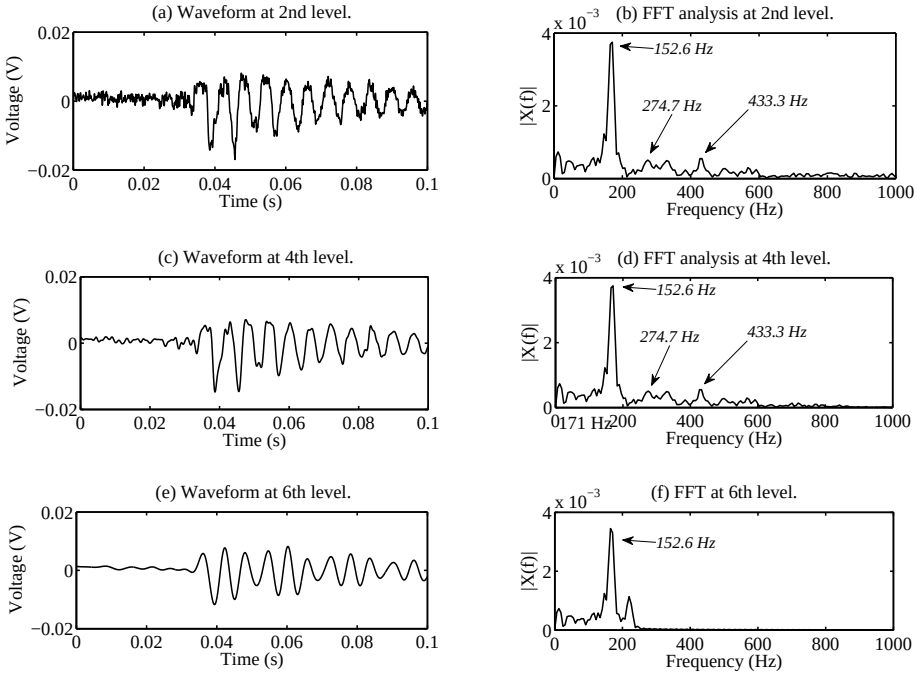

Figure 5.13: Impact signal from sample 2 and its corresponding FFT, at three different decomposition levels.

some of the important details on coefficients were not recovered correctly during the reconstruction of the signal. Reducing to a lower level of decomposition will solve the problem. Since the NIR-FBG dynamic sensing can capture the first three natural frequencies; thresholds for level 5 and 6 were set to zero to give the result as in Figure 5.12 (c, d) and 5.13 (c, d). Thus, all those frequencies were well recovered. Meanwhile, Figure 5.14 shows the comparison of the *denoised* waveform from an FBG and the waveform from a piezoelectric sensor.

When considering the FBG dynamic system response to a shaker excitation, the

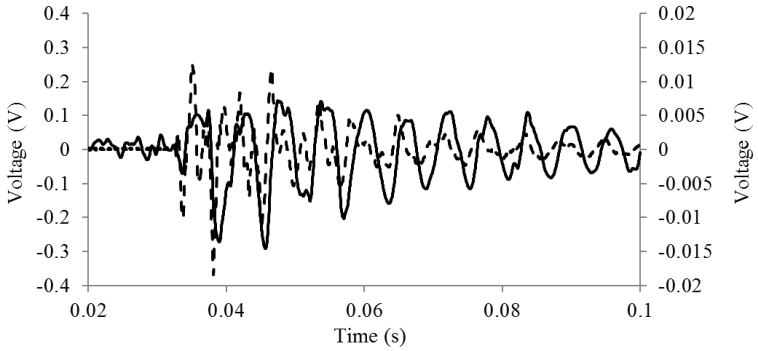

Figure 5.14: Waveform comparison between *denoised* waveform from an FBG (solid line) and the waveform from a PZT (doted line).

thresholding process also needs to consider the corresponding frequency range. This is to assure all important frequency information will not diminish during signal reconstruction.

As an example, consider the case of 500 Hz excitation. Figure 5.15 shows the original waveform captured by a NIR-FBG dynamic sensor. The 150 Hz, 250 Hz and 1500 Hz, which appear in the FFT analysis in Figure 5.15(b), are the natural frequencies which also vibrate as the result of shaker excitations.

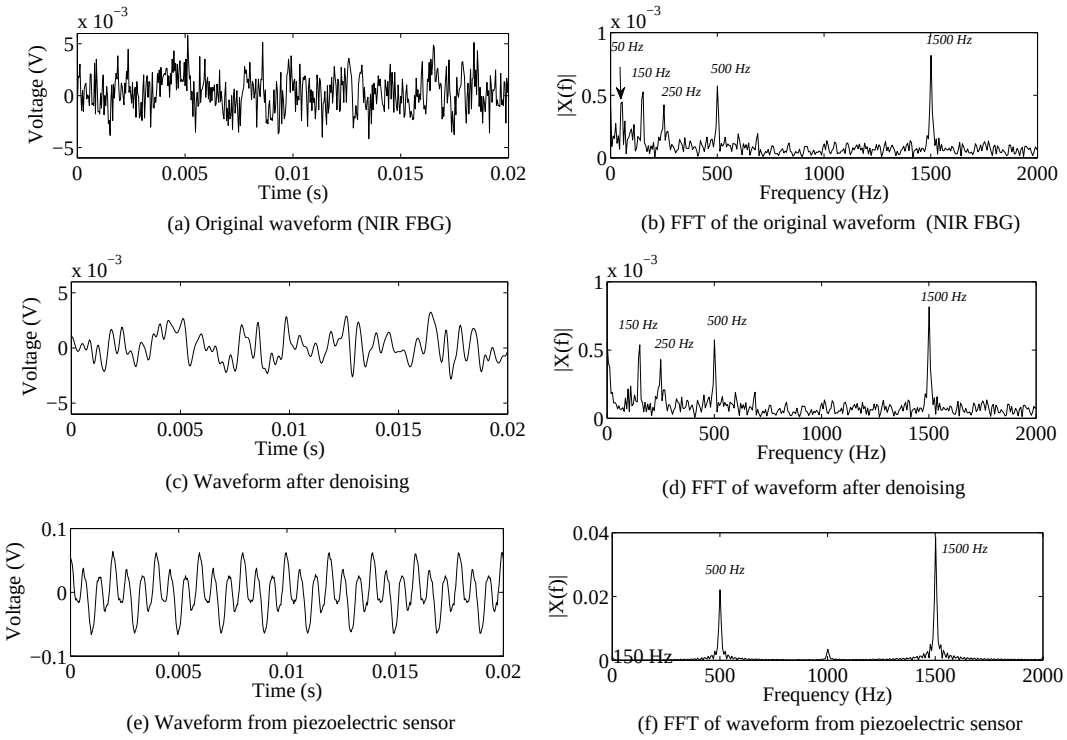

Figure 5.15: Original response from an NIR-FBG due to excitation and its denoised version; and the response from a PZT.

Meanwhile, Figure 5.15c and 5.15d specifies the 'denoised' version of the signal and its FFT spectrum. It can be seen that all the original natural frequencies were preserved after the 'denoising' process. Note that, the 'denoising' also can be used to eliminate the utility frequency (50 Hz) which exists in the original waveform. In comparison with the 'denoised' version, the signal response from the piezoelectric sensor is presented as in Figure 5.15e and 5.15f.

5.4 The NIR-FBG System with a Fixed FBG-Filter

The fixed FBG filter or the matched-FBG system configuration is based on the optical power changes due to the filtering process by the FBG filter. The basic arrangement of the fixed NIR-FBG filter system has been explained in details in Section 4.5.1. Besides, the detailed mechanism also has been discussed in the previous chapter (Figure 4.18). However, for this present work, an optical coupler was used instead of the optical circulator as used by Tsuda (2006). Yet, the effect of using either a coupler or a circulator is significant, as it can affect the SNR and the overall sensitivity of the sensor system (see further explanation in Section 5.5.1).

Theoretically, the matched-FBG system has a better sensitivity and higher SNR compared to the single-FBG system. Recall the illustration presented in the Figure 4.30. The changes of the optical signal relative to the strain is predicted to be higher than the single FBG system, since the optical variations not only occur in wavelength, but also with immense changes in intensity. Consequently, the matched FBG system can provide better dynamic readings.

5.4.1 Case study: The validation of a fixed FBG-filter system

300 mm × 154 mm × 4 mm of GFRP sample was prepared for the experiment. The thin unidirectional, 8 ply sample was manufactured by the hand lay-up method and an NIR-FBG was placed in between the 7^{th} and 8^{th} layers, along the fiber direction. The thin plate was positioned as a cantilever, as indicated in details by the Figure 5.16. For validation purposes, a piezoelectric sensor was located on the sample's surface, as close as possible to the FBG sensor, as illustrated by Figure 5.17.

To validate the performance of the system with matched FBGs, experiments with the impact source and shaker excitations were performed. Since the system is predicted to have better sensitivity than the single-FBG system, testing was planned carefully on aiming at capturing the higher frequency components. For that reason, an impact hammer test was done using the hard tip.

According to the specification (PCB hammer model 086C04), an impact with the hard tip is able to produce vibrations with frequency up to 5000 Hz, depending

(a) Top view.

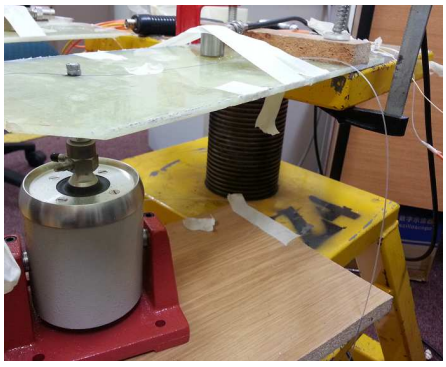

(b) View showing shaker and piezoelectric sensor.

Figure 5.16: The real sample in the lab.

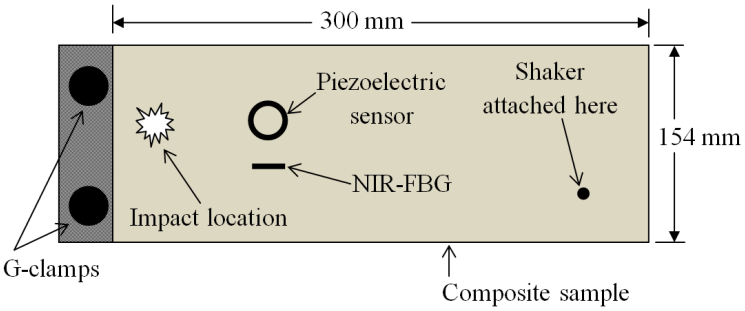

Figure 5.17: Schematic diagram of the sample set-up.

on how the impact was done and its position. The force spectrum of an impact by the hammer can be illustrated by the hammer response curves in Figure 5.18.

Meanwhile, the shaker excitations were applied to the composite plate, using the maximum usable frequencies, 13 kHz and 20 kHz. All the equipment used in this case study (i.e., the light source, PD, oscilloscope, hammer and shaker) were the same as in the experimental validation of the single FBG system (Section 5.2).

5.4.2 Results and discussion for the validation of fixed FBG-filter system case study

Figure 5.19 shows the impact signals which were acquired from both the NIR-FBG and the piezoelectric sensor. Note that, the signal from the matched-FBG system was presented after the denoising process. It indicates a very good signal and identical to the signal's acquired by the piezo sensor. Thus, revealing the

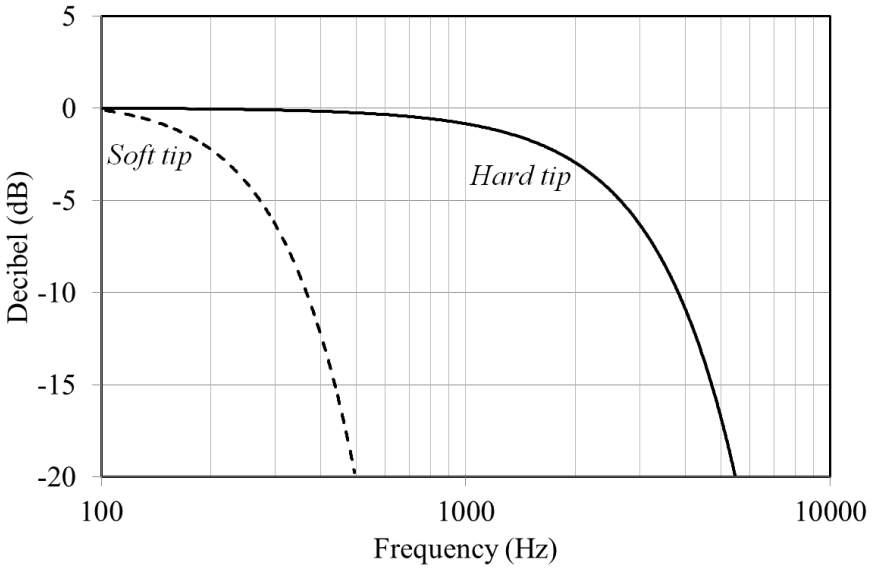

Figure 5.18: Model 086C04 impulse hammer response curves.

potential of a NIR-FBG sensor system for replacing the conventional PZT.

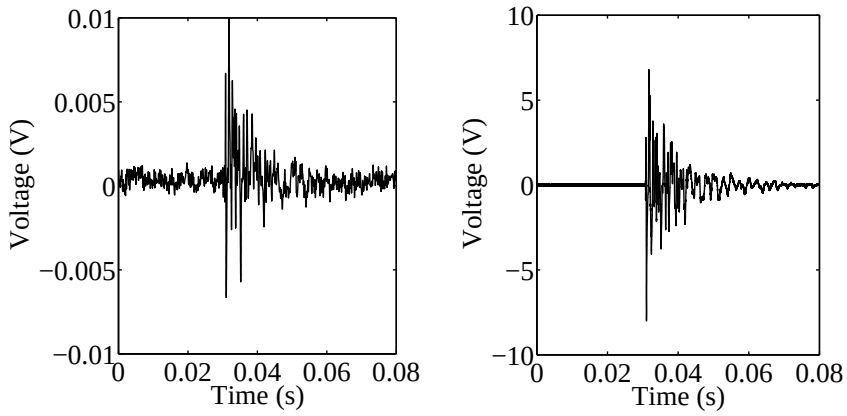

(a) NIR−FBG matched filter system (after filtering).

(b) Piezoelectric sensor.

Figure 5.19: The comparison of impact's signal from two different sensors.

Meanwhile, the respective FFT analysis for both sensors can be shown as in Figure 5.20 and Figure 5.21. The FFT analyses reveal that the NIR-FBG system (with fixed FBG filter) was able to obtain the frequency contents up to 2000 Hz. Furthermore, it was also capable to acquire most of the natural frequencies which were obtained by the piezo sensor, particularly for the components below 2000

Hz.

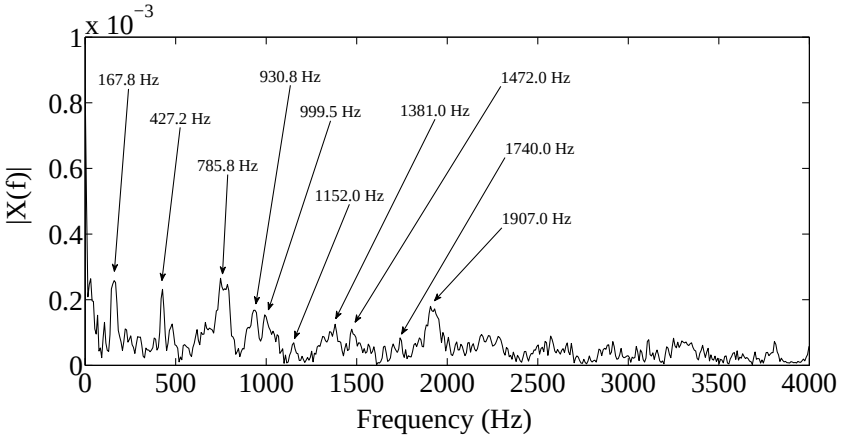

Figure 5.20: The FFT analyses of the impact's signals from the NIR-FBG sensor system.

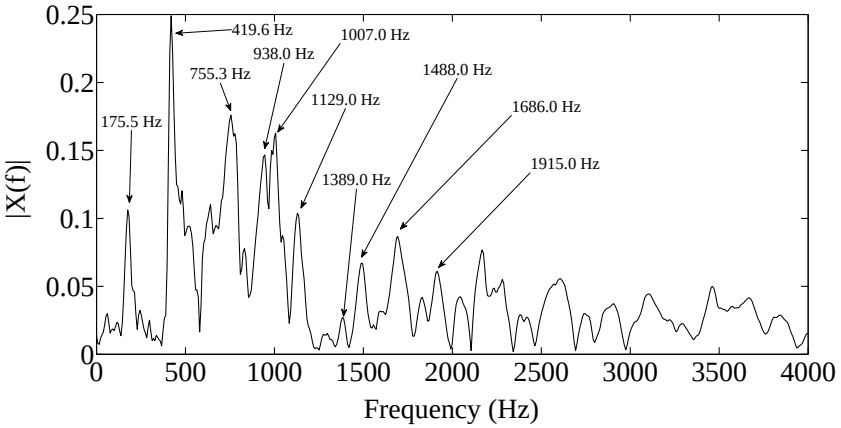

Figure 5.21: The FFT analyses of the impact's signals from the piezoelectric sensor.

In the meantime, the free vibration analysis by the Strand7 software was done to calculate natural frequencies of the sample. The sample is modelled as illustrated by the Figure 5.22. Material properties of the GFRP sample were set, as the same as in the Table 5.1. The natural frequency solver was chosen and set to produce up to 25 mode shapes.

Figures 5.23 show some of the mode shapes, corresponding to the natural frequencies of the sample. The full result for all 25 mode shapes can be viewed in the Appendix. It is obvious that not all frequencies will be detected by the sensors, especially the NIR-FBG sensor, due to its positioning on the sample and

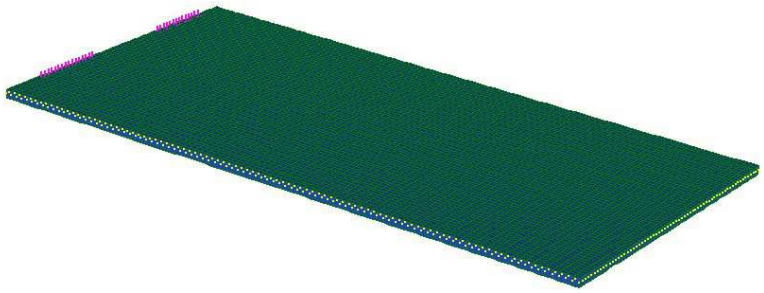

Figure 5.22: The FEA model of the thin composite sample.

the sensing mechanism of the NIR-FBGs. Table 5.5 tabulated the natural frequencies displayed by the FFT analysis of the signal obtained by the NIR-FBG and piezoelectric sensors along with the respective results from the FEA analysis.

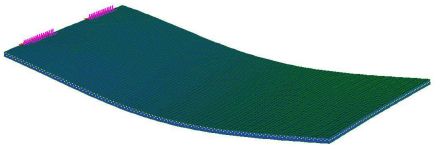

(a) Mode 3: 175.2 Hz.

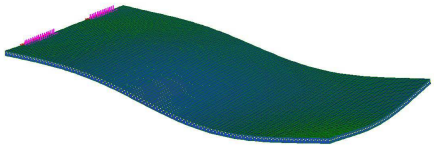

(b) Mode 7: 496.4 Hz.

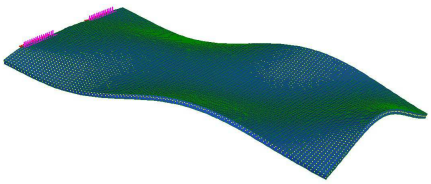

(c) Mode 10: 755.5 Hz.

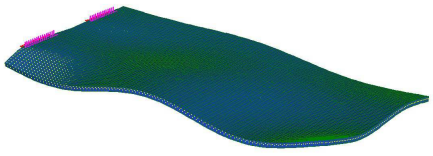

(d) Mode 12: 953.9 Hz.

Figure 5.23: Some example of FEA results.

Meanwhile, the results from the shaker excitation testing revealed promising out-

Table 5.5: Frequency content comparisons between the results from FEA, NIR-FBG and piezoelectric sensors.

Mode	FEA (Hz)	NIR-FBG (Hz)	Piezoelectric (Hz)
3	175.2	167.8	175.5
7	496.4	427.2	419.6
10	755.5	785.8	755.3
12	953.9	930.8	938.0
14	1020.3	999.5	1007.0
15	1190.1	1152.0	1129.0
16	1261.1	1381.0	1389.0
17	1491.0	1472.0	1488.0
21	1773.4	1740.0	1686.0
23	1983.1	1907.0	1915.0

comes. As expected, the NIR-FBG matched filter system has shown its capabilities of acquiring high frequency contents, up to the kilohertz (kHz) range. Yet, the responses due to both excitation frequencies display the existence of noise, as shown by the Figures 5.24 and 5.25.

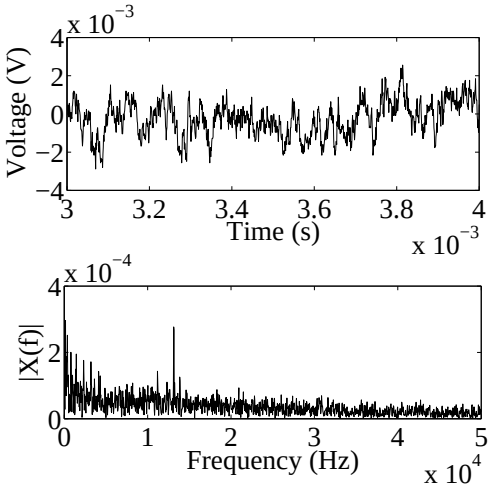

Figure 5.24: Signal waveform (top) and its respective spectrums (bottom) for a 13 kHz input, captured by NIR-FBG sensor.

It can be seen that, the lower frequency components are also visible in the frequency spectrum, for both excitation inputs. These lower frequencies, which obviously are some of the specimen's natural frequencies, usually have a high amplitude. Therefore, they almost conceal the excitation frequency.

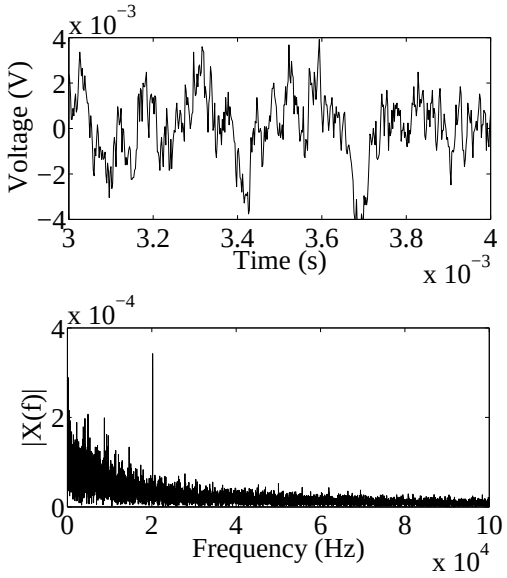

Figure 5.25: Signal waveform (top) and its respective spectrums (bottom) for a 20 kHz input, captured by NIR-FBG sensor.

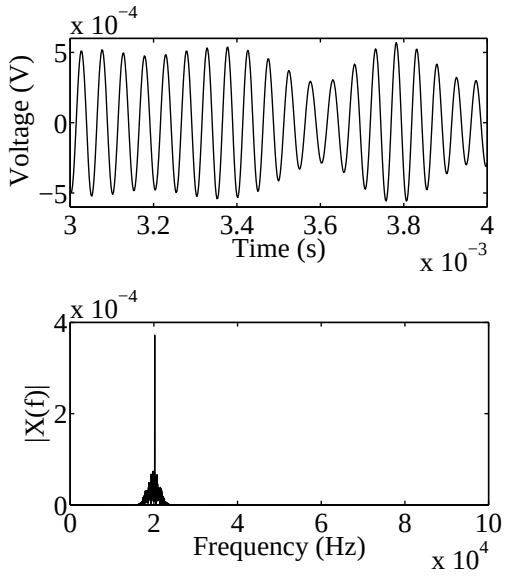

Figure 5.26: NIR-FBG sensor's response to the 20 kHz shaker excitation, after signal filtering.

However, with the application of an appropriate bandpass filter, the actual excitation components can be easily exposed. For instance, Figure 5.26 shows the filtered version of the signal response from a NIR-FBG sensor due to the 20 kHz input. The bandpass filter was specially designed to stop all the other spectrums except the excitation frequency. Note that, the filter design was done

using the *Signal Processing Toolbox*, in MATLAB software. Meanwhile, Figure 5.27 presents the signal response from a piezoelectric sensor due to the 20 kHz vibration.

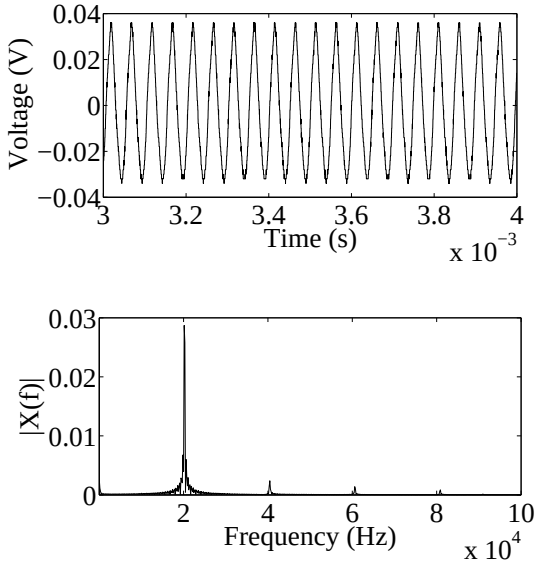

Figure 5.27: The response from a piezoelectric sensor at 20 kHz vibration.

5.5 Signal to Noise Ratio Analysis

The theory of the SNR has been explained in many texts (Vasilescu 2005, Semmlow 2005), as the ratio of signal power to the noise power. It should be noted that, the better the SNR of the system, the sensitivity to the higher frequency contents of wave propagations will also increase. There are many ways that have been investigated in order to improve the SNR of an FBG-based dynamic system; such as using smaller grating (Lee & Tsuda 2005) and cantilever type FBG bonding (Seo et al. 2009). However in general, one of the main criteria for having a sensitive system is the ability of providing higher optical power to the system.

In terms of power, P, the SNR in decibel (dB) can be written as

$$SNR_{dB} = 10\log(\frac{P_s}{P_n}) \tag{5.1}$$

where P_s and P_n indicate the average power of the signal and noise, respectively. Meanwhile, it also can be expressed by the root mean square (RMS) amplitude

ratio;

$$SNR_{dB} = 20\log(\frac{A_s}{A_n}) \tag{5.2}$$

where A_s is the RMS of the signals and A_n denotes the RMS value of the noise.

As stated in Section 4.4.2, the noise from an FBG dynamic sensing system is mainly from the thermal noise. To investigate the SNR performance of the FBG dynamic sensing system, an experiment with several types of FBG dynamic sensing systems was conducted. The case study will be explained in the next subsection.

5.5.1 Case study: The SNR analysis

A thin glass / epoxy sample was prepared. The symmetric sample was manufactured with 8 plies of laminates; thickness 4 mm and has the orientation of $[0^o, 90^o, -45^o, 45^o, 45^o, -45^o, 90^o, 0^o]$.

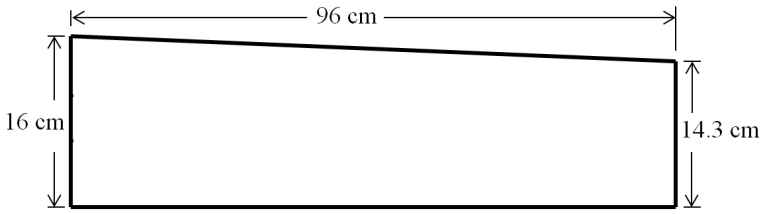

Figure 5.28: Long composite thin plate.

Figure 5.28 shows the detailed geometry of the sample. Two FBGs with different wavelengths, 830 nm and 1550 nm, were surface-glued by using the epoxy resin and were placed near to each other as illustrated by Figure 5.29. A shaker (the same model as used in the previous experiments) was attached approximately at the middle of the composite specimen. Meanwhile, Figure 5.30 presents the actual picture in the laboratory.

Each FBG, was connected with two different kinds of arrangements in order to measure the SNR from each system. In other words, four types of FBG dynamic sensing systems were tested and they are summarized in Table 5.6. Note that the System C and System D were distinguished by the use of two different opti-

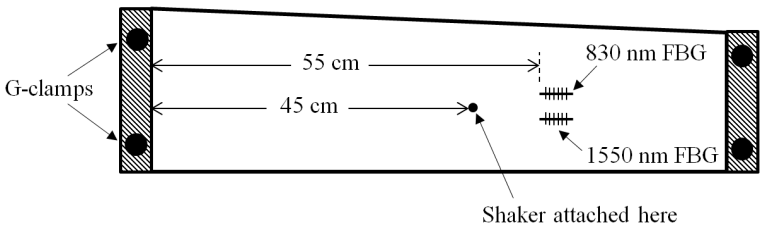

Figure 5.29: Setup diagram for the testing.

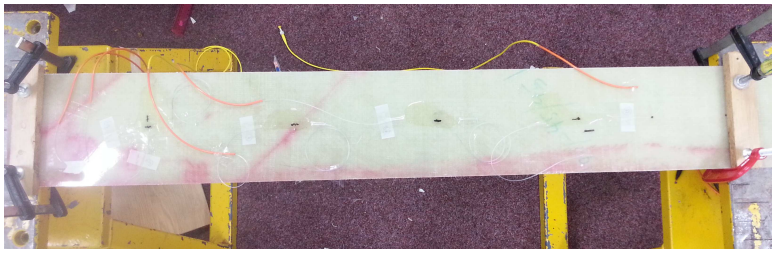

Figure 5.30: The actual composite sample's set-up in the laboratory.

cal components: the optical coupler and optical circulator, as illustrated by the Figure 5.31.

Table 5.6: Detail geometry of the samples.

	Type of arrangement
System A	NIR-FBG dynamic sensing with a single FBG
System B	NIR-FBG dynamic sensing with a fixed FBG filter
System C	1550-FBG dynamic sensing with a fixed FBG filter (use optical coupler)
System D	1550-FBG dynamic sensing with a fixed FBG filter (use optical circulator)

An excitation with constant amplitude and frequency, was applied to the composite sample. The response due to the excitation was measured by the Systems A, B, C and D. Prior to the shaker excitation, an impact with an impact hammer was done to the sample. The FFT result of the impact signal revealed some of the sample's natural frequencies, as shown in the Figure 5.32. The resulting frequency values as labeled by letter 'a' to 'g', are presented in the Table 5.7. Note that, the impact signal was acquired using the System B. One of the natu-

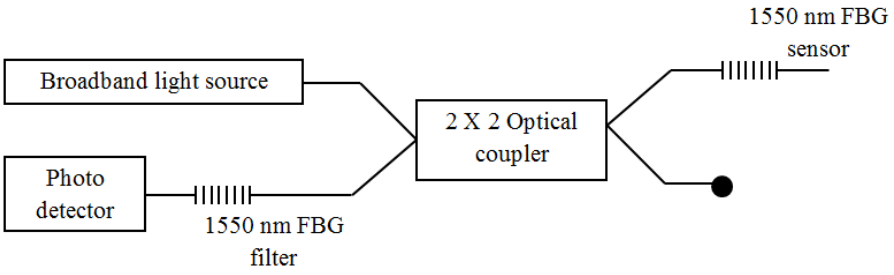

(a) System C.

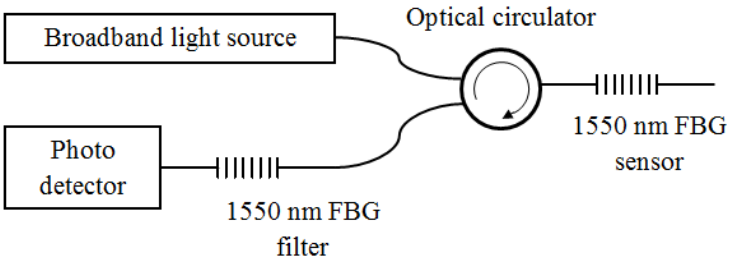

(b) System D.

Figure 5.31: Schematic diagram of System C and System D.

ral frequencies, approximately 1100 Hz (Peak 'g'), was selected as the excitation frequency.

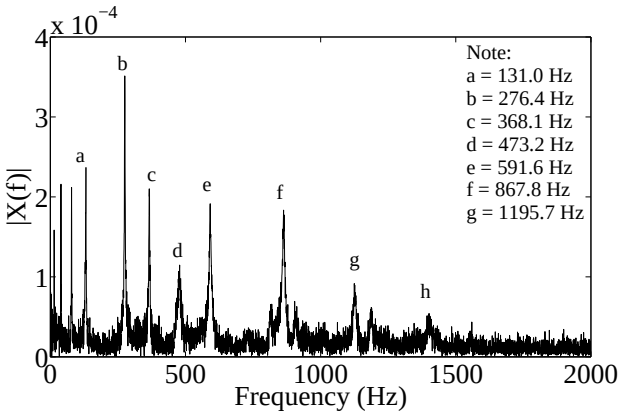

Figure 5.32: Frequency spectrums of the impact signal.

In the meantime, a free vibration analysis by Strand7 software was also done to the sample, for better understanding of its behaviour during the vibration. Figure 5.33 shows the FEA model of the composite specimen. The natural frequency solver was chosen to calculate up to 40 mode shapes.

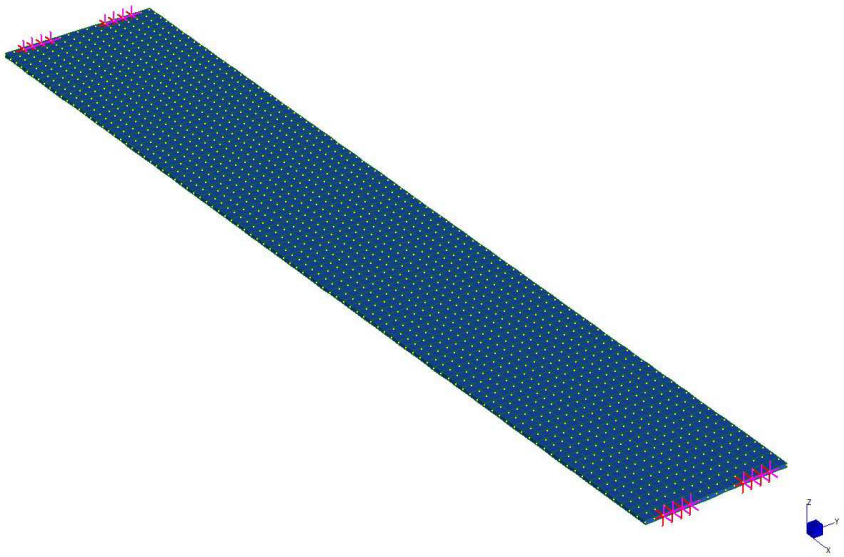

Figure 5.33: FEA model of the composite sample.

5.5.2 Results and discussion for the SNR analysis

All the 40 mode shapes which were determined by the Strand7 software can be viewed in the Appendix. Meanwhile, the Table 5.7 tabulated some of the natural frequencies by the theoretical results (FEA) and its comparison to the experimental results (NIR-FBG dynamic sensor).

Table 5.7: List of selected frequencies as shown by the Figure 5.32.

Frequency peak	FEA (Hz)	NIR-FBG (Hz)
a	131.6	131.0
b	275.4	276.4
c	366.0	368.1
d	478.5	473.2
e	591.4	591.6
f	862.9	867.8
g	1126.0	1195.71

Some of the selected mode shapes, specifically the ones which correspond to the peaks as shown in the Figure 5.32, can be presented by the Figures 5.34. The results reveal an important sensing characteristic of general FBG dynamic sensing which obviously shows better response is obtained from the flexural type of wave propagations.

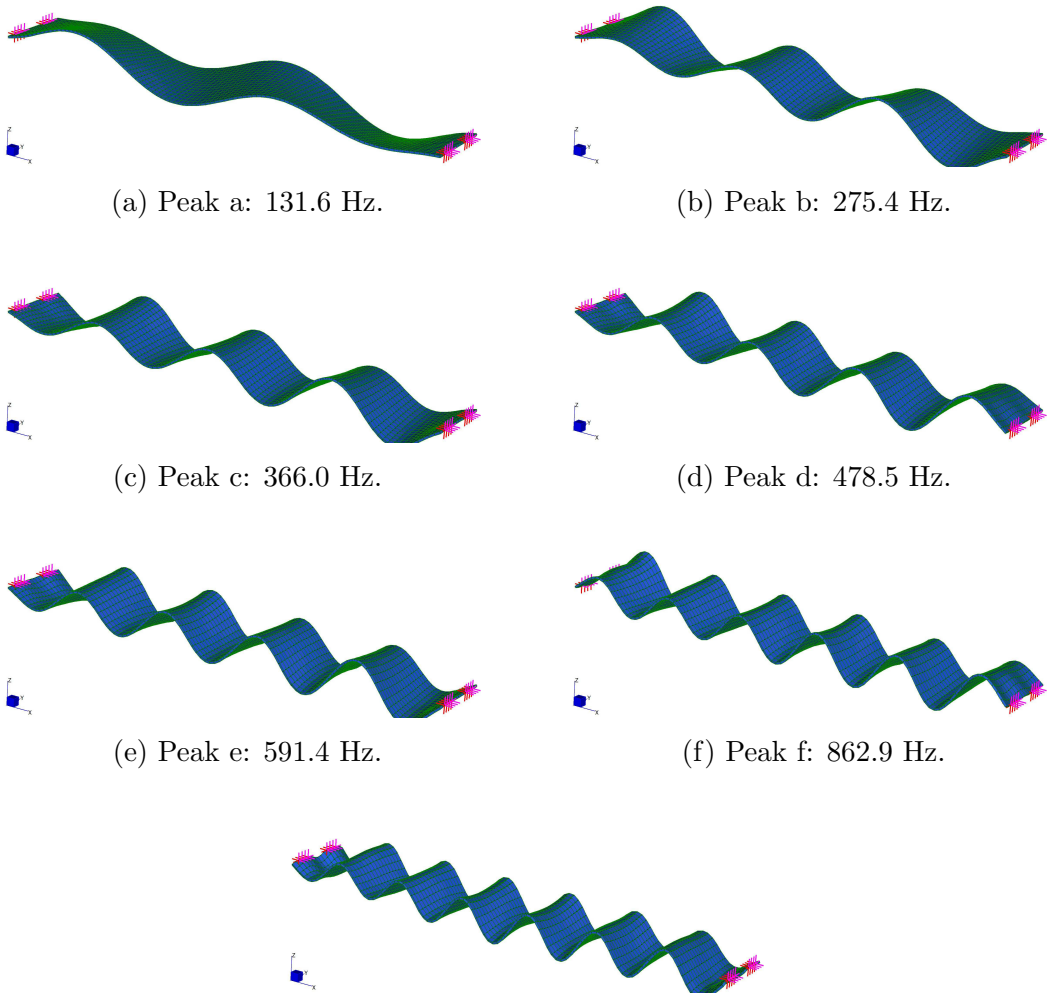

(a) Peak a: 131.6 Hz.

(b) Peak b: 275.4 Hz.

(c) Peak c: 366.0 Hz.

(d) Peak d: 478.5 Hz.

(e) Peak e: 591.4 Hz.

(f) Peak f: 862.9 Hz.

(g) Peak g: 1126.0 Hz.

Figure 5.34: The selected mode shapes which simulated by the Strand7 software.

In the meantime, the Figures 5.35 to 5.38 reveal the responses from all the FBG dynamic systems to the given 1100 Hz of excitation. In all figures, the plots which are labeled as (a), (b) and (d), correspond to the the signal with the vibration, signal without the vibration (noises) and the FFT of the signal with the vibration, respectively. Note that, all the results are presented without signal filtering or denoising.

Table 5.8 summarized the SNR values, for all systems. Note that, the SNR values was determined by using the Equation 5.2. It is obvious that, system A and C have relatively weak responses among others. Although system A has a higher SNR than system C, yet, it was not able to show a stable response as obtained by using system C.

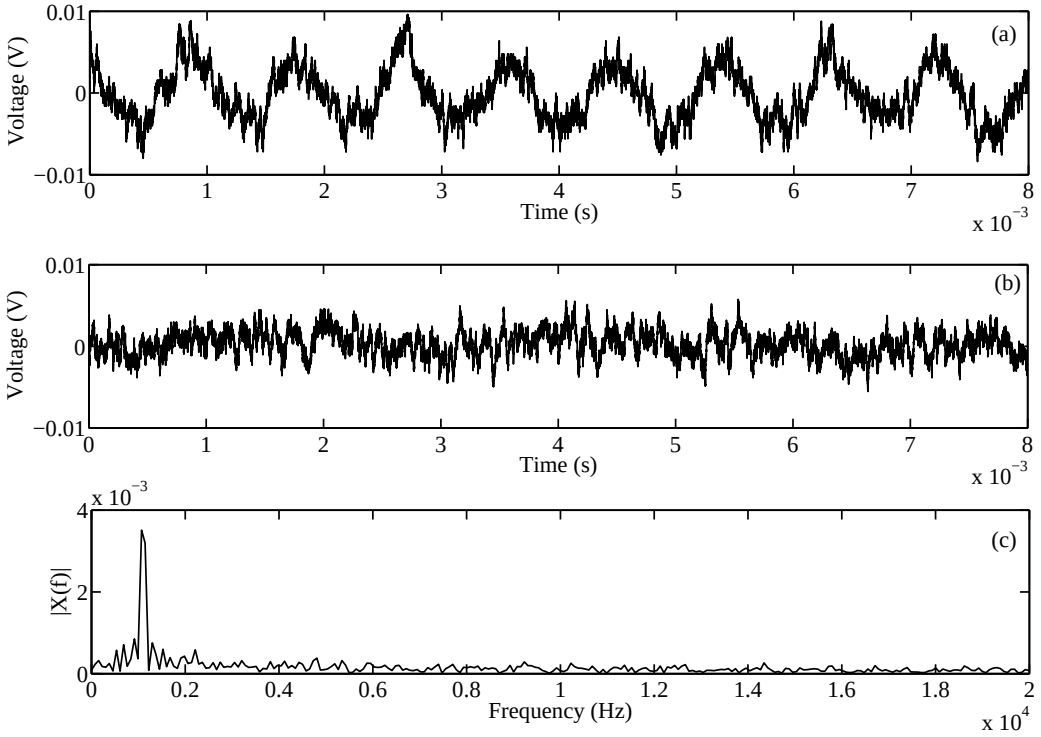

Figure 5.35: Response of System A.

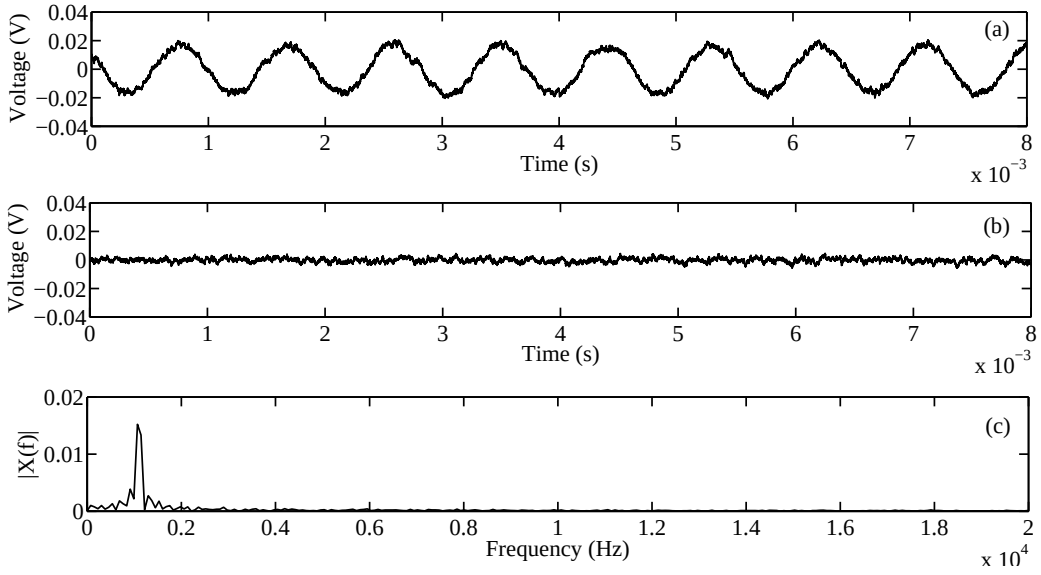

Figure 5.36: Response of System B.

System A had its own advantage compared to others, whereby it only required a 'stand alone' NIR-FBG sensor, without a fixed FBG filter. Based on the SNR result, System A might be useful (at least for this stage), for the application of

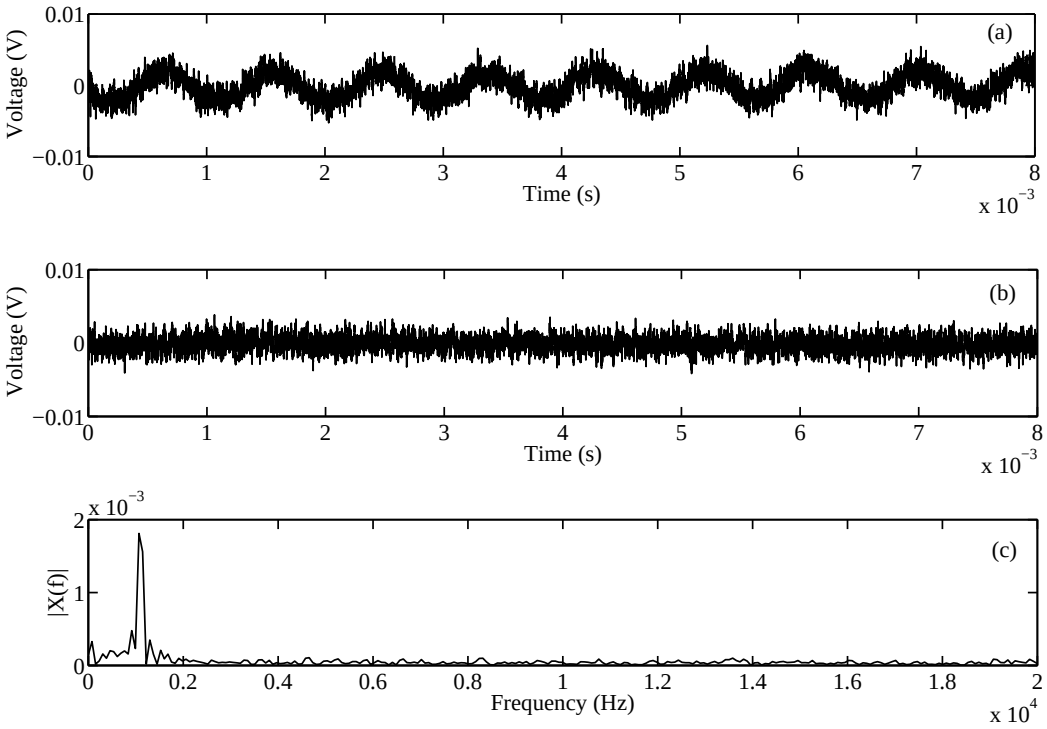

Figure 5.37: Response of System C.

detecting a high energy impact with low frequency contents.

Table 5.8: SNR of the samples.

	SNR (dB)
System A	6.15
System B	17.97
System C	4.74
System D	19.41

The comparison between the use of optical couplers and optical circulators

The results comparison between the 1550 nm based FBG dynamic systems, C and D, reveals a significant difference between the usage of two optical components; the optical circulator and optical coupler. Both components are known to be able to transmit the reflected light from the FBG sensor to the photo diodes. Yet, the optical power received by the PDs, using an optical circulator are much greater

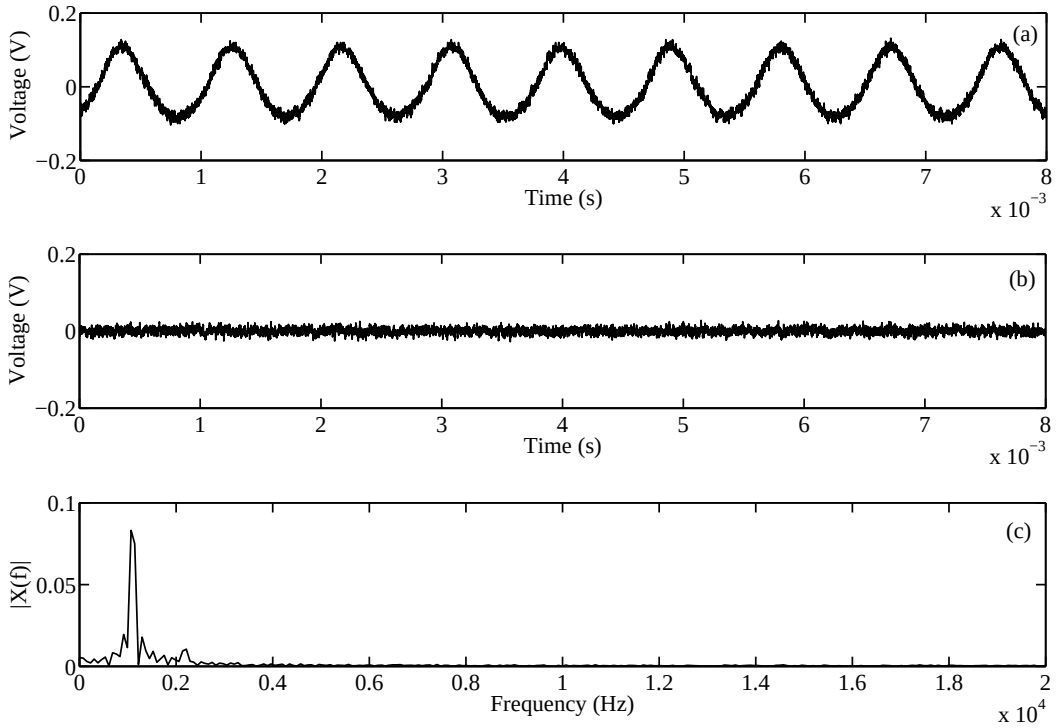

Figure 5.38: Response of System D.

than the one with an optical coupler. However, the usage of an optical coupler also has its own advantage.

Consider an FBG dynamic system which utilizes an optical coupler with 50:50 ratio, as illustrate by the Figure 5.39. The broadband light will enter the coupler and continue to the FBG sensor with half the optical power. Next, the reflected light from the FBG will enter the coupler, and again, divided into half, before going straight to an FBG filter or PD. Consequently, the optical power that is received by the PD will be only 25% of the original power from the broadband light source.

Meanwhile, the light power in the circulator-based FBG dynamic system will remain at the same level, until it reaches the fixed FBG filter. As a result, a small wavelength variation due to dynamic strain at the FBG sensor will give big changes to the optical power level before being received by the PD. This condition not only increases the SNR, it also increases the sensitivity of the sensor system.

Despite the disadvantage in terms of the optical power, the coupler-based system actually can allow many connections to be made through the system, as the coupler can also perform as an optical divider. Thus, the system allows several series

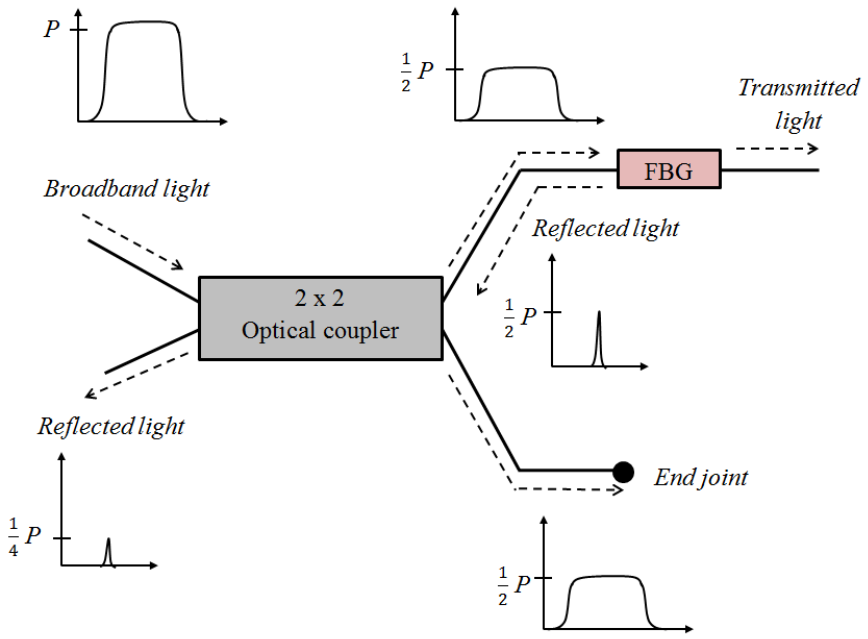

Figure 5.39: Schematic diagram of the movement of light in the coupler-based system.

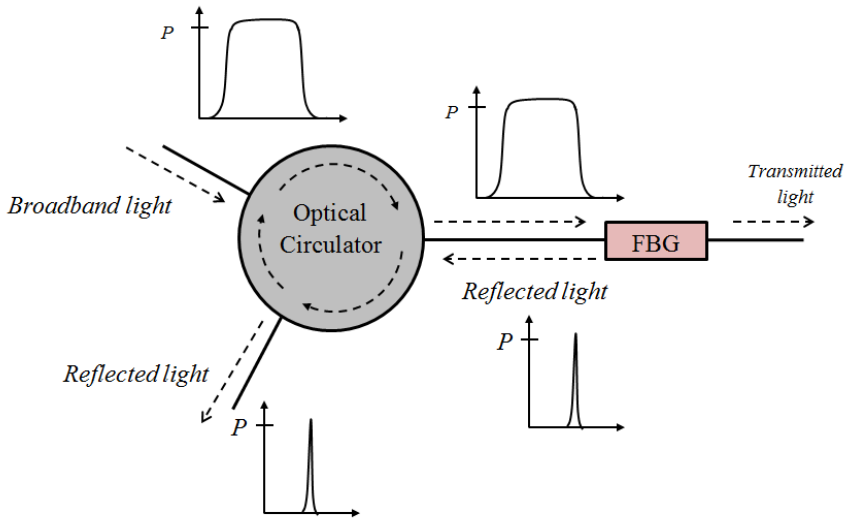

Figure 5.40: Schematic diagram of the movement of light in the circulator-based system.

of parallel systems (i.e., combining with FBG static measurement), or dynamic measuring system with several channels and etc. These extra capabilities would not be achievable with the circulator-based system.

The System B, or the NIR-FBG dynamic sensing with a fixed FBG filter actually

utilized an optical coupler. However, its SNR value was high, almost the same as the System D. Therefore, it is expected that if an optical circulator is used in the System B, instead of the coupler, the SNR and sensitivity of the system will increase.

5.6 Applications Using NIR-FBG Systems

In the previous section, the validation of single and fixed-FBG-filter systems has been successfully performed and presented with convincing results. Further, each system was utilized in some applications, particularly which involved the detection of acoustic wave propagation on thin composite plates. The selected applications will be carried out, based on one of the objectives of this Ph.D., which is to use the NIR-FBG system for monitoring progressive failure in composite structures. The applications are;

1. Impact location detection.
2. Wave mode identification with a NIR-FBG system.

All the experiments in this section use the same sample as in the SNR case study (Section 5.1), including the boundary conditions of the sample. Therefore, some of the results from Section 5.1 were valid to be used for discussion in the next coming case studies. However, the sensors placement (i.e., piezoelectric and FBG sensors) was varied, depending on the objectives of each experiments.

5.6.1 Impact location detection

One of the most important capabilities of an SHM system is to determine the location of internal defects or external impacts. For that reason, linear source-location-detection testing was prepared and was successfully performed to validate the NIR-FBG dynamic sensing system in performing the impact location detection.

For this case study, the NIR-FBG system with a single FBG was used, since it has a lower SNR than the system with the fixed FBG filter. Note that, if a lower SNR system can prove its capability in providing reasonable source location mapping, then the systems with greater SNR (and sensitivity) obviously can give better results.

The conventional time arrival (TOA) method was applied to calculate the linear impact location. Specifically, the arrival of the first signal's peak was used. Two NIR-FBG sensors were placed at two different locations on the composite sample for the determination of the time difference between sensors. In other words, a two-channel system was utilized. The Figure 5.41 shows the sensor's set up.

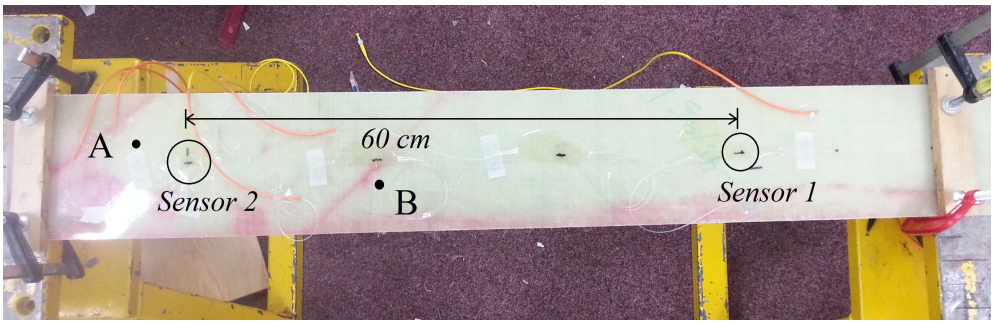

Figure 5.41: Experimental setup for impact location detection.

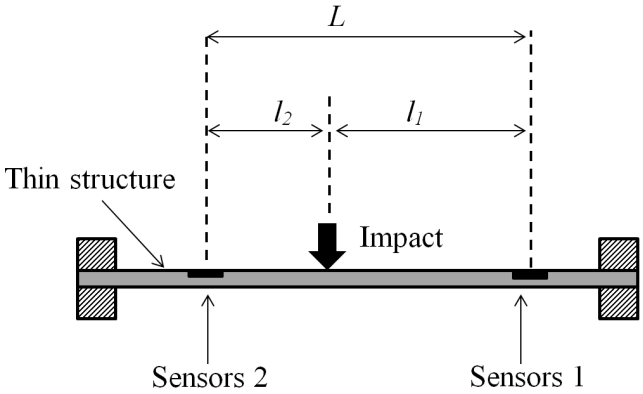

Figure 5.42: Set-up diagram for the linear source location detection.

Consider a one dimensional structure with two sensors, as shown in Figure 5.42. The equation for linear source location can be written as,

$$l_2 = \frac{1}{2} \times (\Delta t \times c_g + L) \tag{5.3}$$

The c_g in Equation 5.3 refers to the group velocity of the waves travelled on the sample. Note that, for an impact on a thin composite sample, the flexural mode will be the most dominant wave propagation to occur. The group velocity for the flexural mode will be easily determined from the dispersion curves of the sample. Figure 5.43 shows the group velocity curve, calculated using *PACshare Dispersion Curves* software.

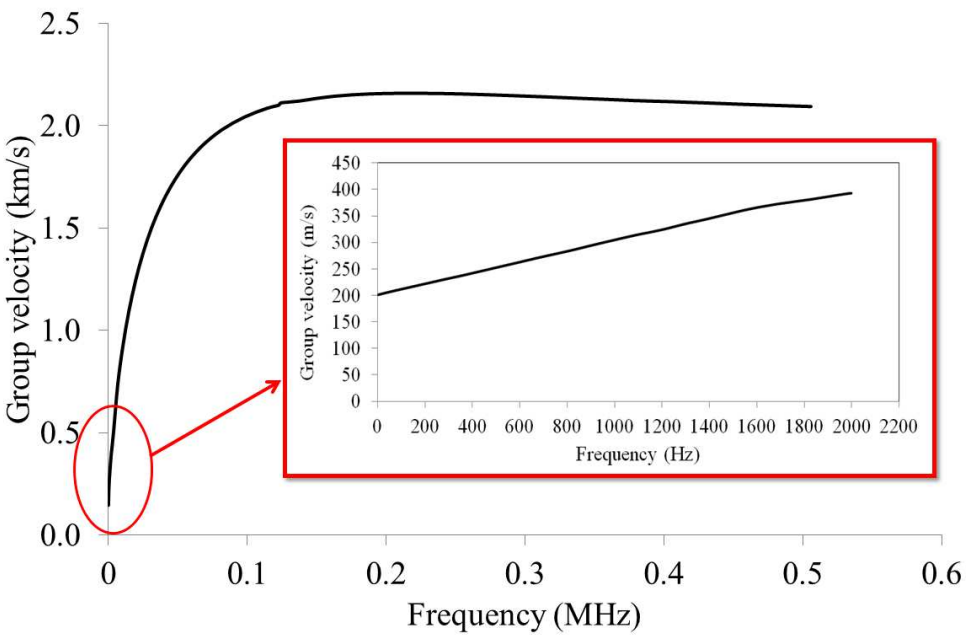

Figure 5.43: Group velocity curve for the flexural wave (A_0).

Two impacts at two different locations were done. The first hit location, point A, was done at 5 cm to the left of sensor 2. Meanwhile, the second hit location (point B) was done at 20 cm, to the right of sensor 2. The hits, using the hard tip of an impact hammer (model 086C04), were repeated for four times at each location.

For the data acquisition set-up, the threshold was set based on the arrival of the signal obtained from sensor 1 and the sampling rate was set to 250,000 data per second. All the acquired data was recorded by a digital storage oscilloscope and stored for post-processing.

Source mapping results

An example of the acquired signals due to impact at point is shown in Figure 5.44. Although both signals from each channel indicate low SNR values, the first peak from both signals were clear and can be utilized for the TOA determination. The variations between the time arrival of signals' peak for each channel, Δt, was used in the source location calculation (see Equation 5.4). Note that, to avoid any loses to the time domain signal, filtering was not done.

Meanwhile, the FFT analysis of one of the impact's signals reveals that the excited frequencies were in ranges from 40 - 600 Hz as shown in Figure 5.45. According

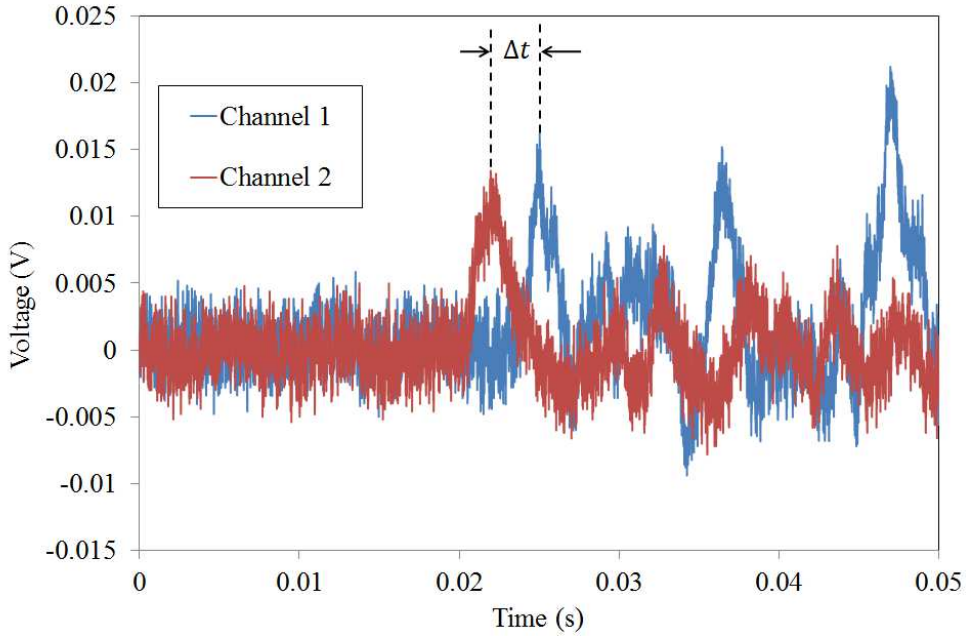

Figure 5.44: Example of signals from both channels due to an impact at point A.

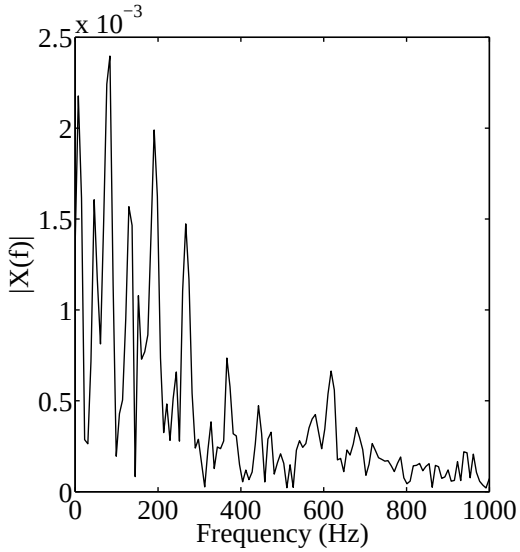

Figure 5.45: FFT analysis of a signal due to an impact on the composite specimen.

to the dispersion curves, as in Figure 5.43, all the propagated waves in that frequency range will have velocities in the range of $200 - 250ms^{-1}$.

By further examination of the signal using CWT, it was found that the frequency component which first arrived at the sensor was the frequency of 190 Hz. It is shown by the white arrow in the Figure 5.46; and the frequency is also consistent

with the time arrival of the signal as shown in the Figure 5.44. It should be noted, from Figure 5.43, the respective group velocity for frequency of 190 Hz is $220ms^{-1}$; thus was chosen for the general c_g value for all the source location calculations in this case study.

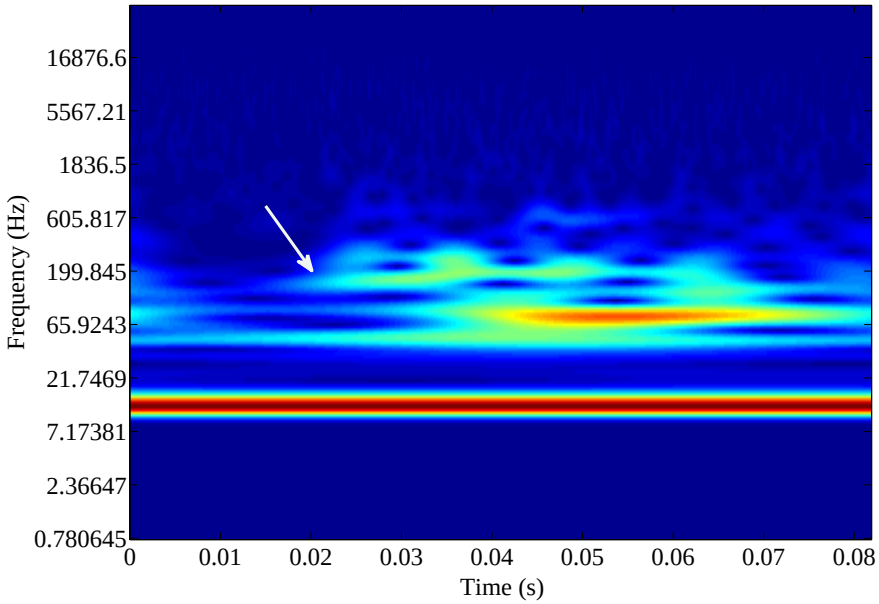

Figure 5.46: Wavelet analysis of the impact's signal. The white arrow indicates the first frequency arrival.

Table 5.9 summarizes the results for the linear impact source locations. The results reveal that all the relative errors were below 10 %. The negative sign indicates that the location was to the left of the sensor 2 and positive values mean the location was to the right side of sensor 2. Note that the relative errors were calculated based on the normalized value of the absolute error with respect to the total length of the specimen. For the sample length, L, the relative error can be calculate as,

$$Error(\%) = (\frac{(Measured + L) - (Actual + L)}{Actual + L}) \times 100 \tag{5.4}$$

In the meantime, Figure 5.47 illustrates the mapping of the measured locations versus the actual hit locations. The figure indicates that all the measured locations were close to the actual hits. These results clearly reveal the capability of NIR-FBG systems in locating the external impact location on thin composite plates.

Table 5.9: Linear impact source distances.

	Trial	Measured (cm)	Actual (cm)	Abs. error (cm)	Rel. error (%)
A	1	-3.75	-5	1.25	1.24
	2	-1.06	-5	3.94	3.90
	3	-0.84	-5	4.16	4.11
	4	-8.85	-5	3.85	3.81
B	1	28.64	20	8.02	7.44
	2	27.18	20	7.18	6.19
	3	28.02	20	8.02	6.91
	4	21.99	20	1.99	1.72

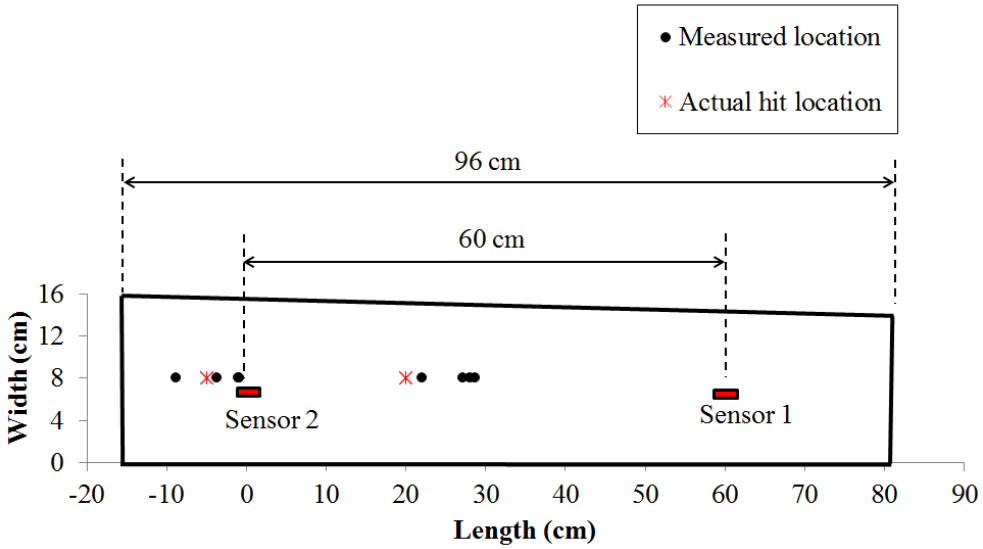

Figure 5.47: Experimental setup for impact location detection.

5.6.2 Wave mode identification using an NIR-FBG system

One of the important items that has been listed at the end of Chapter 3 was the problem during identification of the wave propagation modes in thin plates using an acoustic sensor. The determination of the most dominant wave mode in acoustic wave propagation may help to characterize the failure mechanisms in a composite plate under monitoring. As discussed in the previous chapter, some internal damage will generate either the extensional-dominated wave propagation or the flexural-dominated wave propagation.

An appropriate sensor arrangement for the specimen under testing is important in order to distinguish between those types of wave propagation. The idea was already explained by the case study in the Section 3.6. However, instead of utilizing the common piezoelectric sensors, the use of NIR-FBG was proposed and presented in this section.

The benefits of using the NIR-FBGs, in this particular case, are much greater than the PZT. One of them, is the improvement of the sensor-specimen mounting problem, which is always experienced by the PZT in most of its applications. It is critical to attach the PZT properly on the specimens surface to ensure it acquires the best response, especially for the arrangement as shown in Figure 5.48.

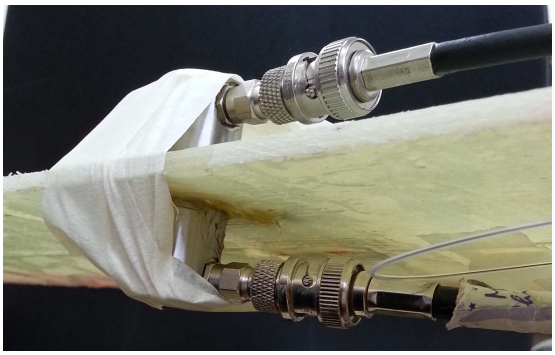

Figure 5.48: Example of piezoelectric sensors' mounting.

This section will focus on identifying both typical wave modes in Lamb's wave, that is the flexural wave modes and extensional waves. Consider a thin composite sample, which has two PZTs arranged on the top and bottom surface, as illustrated by the Figure 5.49a.

When a flexural wave *'hits'* the sensors' location, PZT 1 will experience an upwards displacement and the PZT 2 will go the opposite direction, as shown by the Figure 5.49c. As a consequence, the voltage reading at the signal viewer, theoretically, will indicate the out-phase signals from both sensors. Meanwhile during the extensional waves, both PZT 1 and 2 will be in the same upwards displacement. If translated into a voltage reading, the respective responses will be in the same phase.

Figure 5.50 illustrates the same mechanism, but with the NIR-FBG sensors instead of the PZTs. Note that, the sensors can be surface-glued or embedded in the composite sample during manufacturing. However, embedding too close to the mid-plane of the plate must be avoided, since it is the neutral axis and has no displacement.

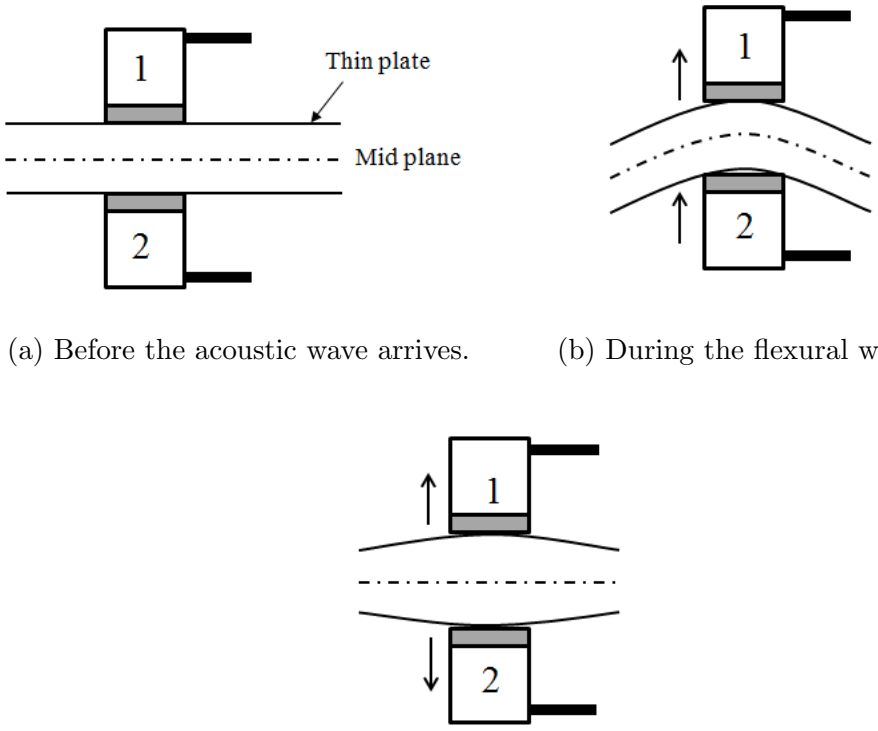

(a) Before the acoustic wave arrives.

(b) During the flexural wave.

(c) During the extensional wave.

Figure 5.49: The illustration of a piezoelectric sensor sensing mechanism for wave modes identification.

During the occurrence of flexural waves, the NIR-FBG sensor on the top surface will be tensed, while the bottom sensor will experience compression, as shown by the Figure 5.50b. Due to this opposite behavior of each FBG, the signal viewer will show the out-phase signals. For the case of extensional waves, both the top and bottom sensor will be in the same stretching condition, as illustrated by the Figure 5.50c, thus gives the in-phase responses for both sensors.

Case study for the wave mode identifications

An experiment was prepared in order to validate the capability of NIR-FBG sensors in performing wave mode identification. Note that, the NIR-FBG system used in this case study, was the one with a fixed FBG filter. The NIR-FBG sensors were surface-glued with epoxy resin and arranged as in the Figure 5.50a. Meanwhile, the Figure 5.51 illustrates the position of the NIR-FBG sensor pair. Also, a pair of PZTs, the $R6\alpha$ from PAC company, were located close to the

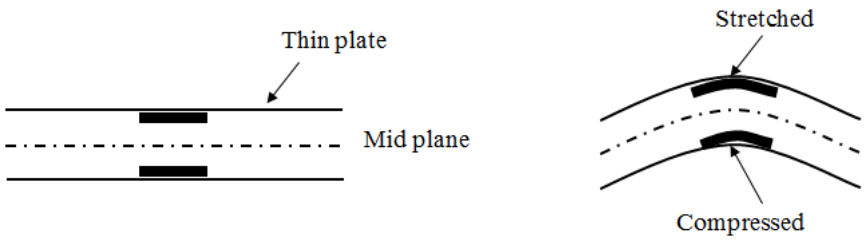

(a) Before the acoustic wave arrives. (b) During the flexural wave.

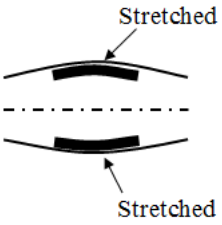

(c) During the extensional wave.

Figure 5.50: The illustration of NIR-FBG sensors' sensing mechanism for wave modes identification.

NIR-FBGs for the results' comparison.

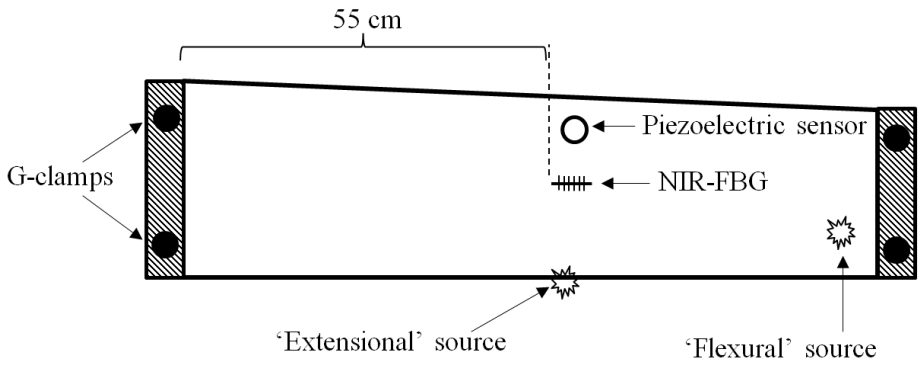

Figure 5.51: The position of the NIR-FBG and piezoelectric sensors on the composite specimen.

The signal acquisition was done using the digital storage oscilloscope, with a data sampling rate of 1.25 MHz. Two channels were activated, whereby the sensors

(NIR-FBG and piezo sensor) located on the bottom surface of the sample were set as channel 1. Meanwhile, channel 2 was for the sensors which were located on the top surface of the sample.

Two hits of impact hammer were done, whereby each hit would give two different kinds of wave modes, that is the extensional and flexural wave modes. The discussion of these two wave sources has been introduced in the case study in Section 3.6.

Results and discussion for the wave mode identifications case study

The signals response due to the 'flexural source' from the piezoelectric sensor pair can be presented as in Figure 5.52. The green plot indicates the results from channel 2, while the blue dotted line depicts the channel 1 reading (this will be the same for the next figures). The waveforms seem to be out of phase, as predicted. Furthermore, both signals does not seem fully identical, even though both were acquired from the same type of PZTs.

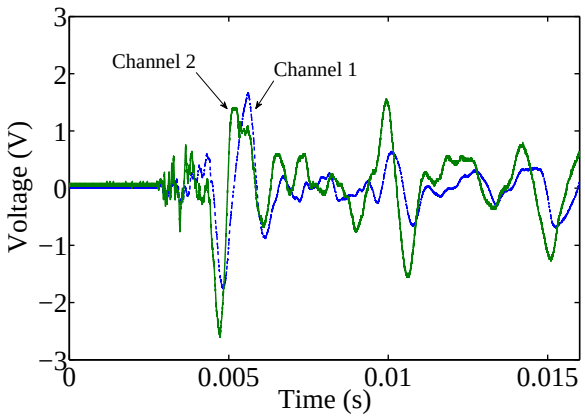

Figure 5.52: The signals obtained by the pair of piezoelectric sensors (flexural source).

Meanwhile, Figures 5.53 show the piezoelectric sensors' pair signals due to the 'extensional source'. The lower amplitude value, compared to the result from 'flexural source', is one piece of evidence of the extensional modes; besides the in-phase responses as shown in the figure. However, the result does not show fully identical signals from the PZTs' pair.

The non-identical response can happen due to the existence of a very small gap between the sensor and the sample's surface during the acquisition process. This empty space between the sensor and the surface of the sample, results in only part

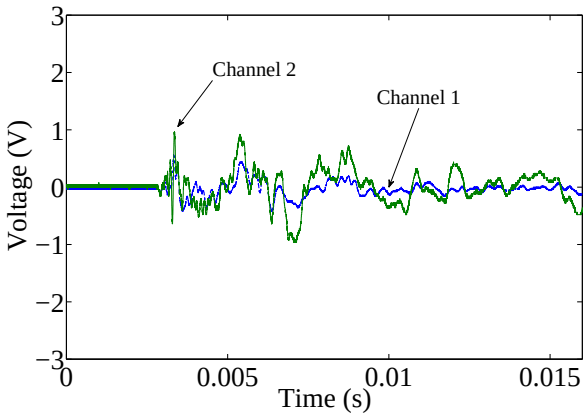

Figure 5.53: The signals obtained by the pair of piezoelectric sensors (extensional source).

of the wave propagation being captured by the sensor. Figure 5.54 illustrates the gap between a PZT and sample's surface. Note that, this problem is not critical at all if the sensor is used in common practice, such as for location detection of an AE source and defect characterization using an ultrasonic technique. Furthermore, in standard applications (ASTM-E1067-01 2001), grease is applied to close any gap between the sensor and the surface of the material under monitoring. Therefore, the problem tends to be ignored because a single piezoelectric sensor is capable of obtaining most of the frequency contents from an acoustic wave which propagates on the monitored structure. However, the issue of non-identical signals is necessary to be addressed, especially when it comes to the comparison of pairs, as used in the wave modes identification process.

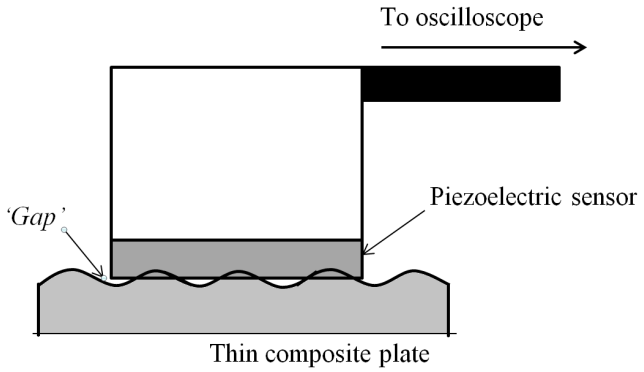

Figure 5.54: The illustration of empty space between specimen's surface and the PZT.

In the meantime, Figure 5.55 shows the waveforms comparison of the responses from the NIR-FBG sensors due to the 'flexural source'. The signals seem iden-

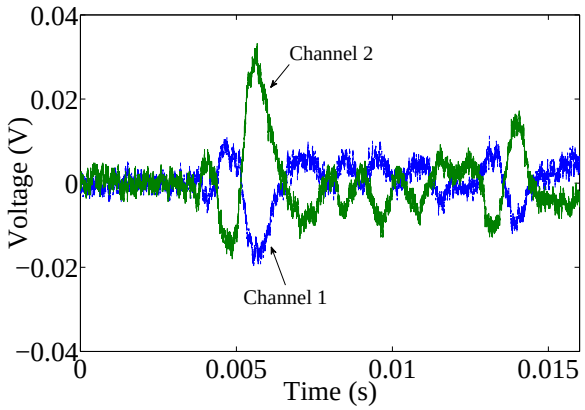

Figure 5.55: The signals obtained by a pair of NIR-FBG sensors (flexural source).

tical, but in out-of-phase position. In other words, the signal from channel 2 is completely a 'mirror image' of the signal from channel 1. The condition is caused by the ability of the NIR-FBG sensors, at top and bottom sample's surface, to move together with the composite sample as a whole. This become more obvious, after *denoising* of the signals, as shown by the Figure 5.56.

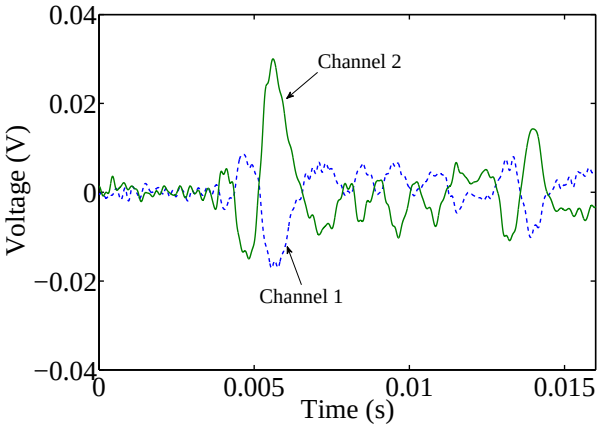

Figure 5.56: The 'denoised' version of the NIR-FBG signals comparison.

For the case of an 'extensional source', the NIR-FBG sensor pair show the in-phase responses as seen in Figure 5.57. Note that, the responses were presented after the signal 'denoising'. Please note that the amplitude of the signal from an extensional source was not much difference, if compared to the signal due to a flexural wave. This is owing to the sensing mechanism of the NIR-FBG sensor, which is different to the PZTs, as explained in the Section 1.1.4.

To see clearly the 'mirror image' signals that obtained from the NIR-FBG sensor pair, the same test has been repeated. In this simple experiment, a 10 Hz vibra-

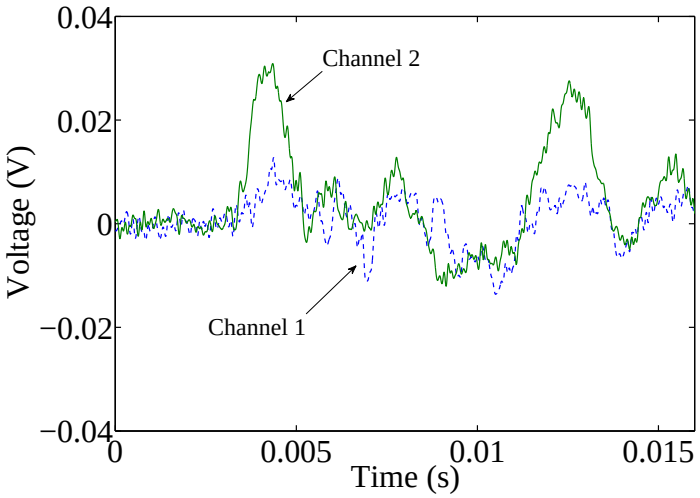

Figure 5.57: The signals obtained by the NIR-FBG sensors (extensional source).

tion by a shaker was applied onto the composite plate sample, instead of using the impact hammer. The results show that the dominant wave mode propagation is the flexural mode, and the vibration of the plate can be seen clearly by naked eye. The waveforms comparison between the signals from both channels is shown in Figure 5.58.

In conclusion, the signals' responses which acquired from both piezoelectric sensor and NIR-FBG sensor pair were agreed well with the prediction, as explained previously. More importantly it also proved the ability of the NIR-FBG system for wave modes identification, which later, can lead to its use in the characterization of damage type in composite materials. NIR-FBGs are more practical than PZT, particularly for wave mode identification purpose.

5.7 Chapter Summary

This chapter has presented the validation for two types of dynamic sensing systems based on NIR-FBG sensors. It was very promising, whereby the NIR-FBGs were capable on providing good results and consistent with the simulation by FEA. Although the study is still in early stage, it has the potential to be a high demanding optical fiber based dynamic sensing system in the future, especially in composite structures applications.

On the other hand, the NIR-FBG-based system also has revealed better performance compared to the conventional 1550 nm range of FBG-based systems,

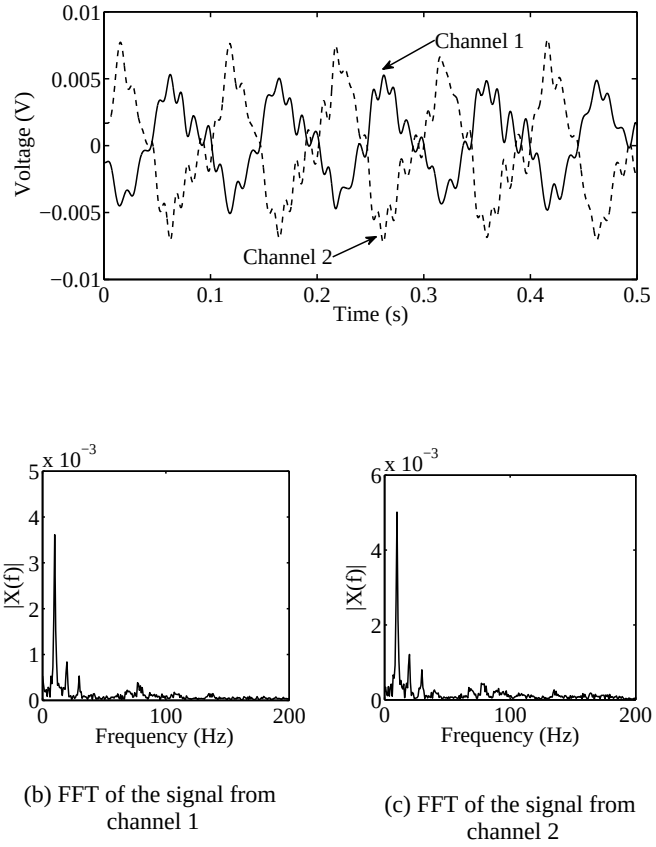

(b) FFT of the signal from channel 1

(c) FFT of the signal from channel 2

Figure 5.58: The waveforms' comparison for the signal due to 10 Hz excitation.

particularly in dynamic strain measurement. The conclusion is based on the observation through SNR comparison for both types of systems, as reported in Section 5.5.1. Not only that, signal noise from NIR-FBG system also can be filtered with a proper filtering such as wavelet 'denoising' (as proposed in Section 5.3.1). Therefore, it will increase the SNR.

This chapter has ended with convincing results from the experiments in the Section 5.6. The study was carefully prepared to simulate real SHM applications in the lab scale. The impact location detection results indicated a relatively small error, that is below 10 %, and it is sufficient for a global monitoring of the composite structures. Meanwhile, the application of NIR-FBGs for wave propagation mode identification is a new insight for modal acoustic emission (MAE) technique. In conclusion, the capability of an FBG dynamic sensing system for SHM of thin composite plates was proven, particularly the one which uses NIR-FBGs.

Chapter 6

Conclusions and Further Work

This Ph.D. work was carried out to investigate the FBG-based dynamic sensor as an alternative replacement to the conventional piezoelectric sensors, in particular for monitoring composite structures. Specifically, this study proposed the use of NIR-FBG sensor system for wave propagation based SHM. The utilization of FBG sensors that are in the NIR wavelength range is something unconventional, whereby the regular and widely used FBG sensor is in the range of 1550 nm. However, a system based on NIR-FBG sensors have the potential to be a relatively low cost optical sensor based SHM system as it mainly utilized relatively cheaper silicon sources and detectors. Not only that, the NIR-FBG system also offers a comparable performance as the 1550 nm based systems. It has been proved by a number of well planned case studies, that were presented throughout this dissertation.

Furthermore, the NIR-FBGs also were successfully applied in some of the wave propagation based SHM applications, whereby the piezoelectric sensors were typically used. The utilization of this FBG-based sensor was motivated by a few drawbacks of PZT usage, particularly which involving the SHM of thin composite laminates (see Section 3.9).

6.1 Principle Achievements

At the beginning of this thesis (Chapter One), three main objectives have been stated:

1. To investigate the use AE in composite structures, especially regarding its

applicability and robustness for SHM of composite structures.

2. To develop the an FBG dynamic sensing utilizing Near-Infra-Red FBG sensors.

3. To implement FBG-AE system in plate-like composite laminates for damage monitoring.

All of the objectives have been successfully achieved with a significant level of achievement.

6.1.1 Investigation of AE SHM in composites

In this study, an investigation of the AE technique for the use in SHM of composite thin plate structures has been performed. It was discussed in details, including the applications of more quantitative approach, the modal acoustic emission (MAE). Compared to the traditional AE method, the MAE is more focused on the analysis of wave propagation and involves better theoretical calculations thus giving more robust and accurate results.

In the road to fully understand the use of AE for composite structures, two case studies have been done successfully. They are the determination of the source location of an AE signal based on the velocity determination (see Section 3.5) and non-velocity approach (see Section 3.8). It was found that the non-velocity approach can be used as an alternative to the conventional time-based technique. The superiority of the non-velocity based source mapping can eliminate the inconsistent problem in determining the wave propagation velocity, particularly for anisotropic materials such as composite laminates. However, for global source mapping, the velocity-based calculation still can be a reliable technique.

Meanwhile, the failure characterization of the damages in composite laminates were also presented (see Section 3.6). It was found that, a special arrangement of sensors is needed to be used before it can successfully characterize the damages in composite laminates by using MAE. However, with the traditional piezoelectric sensors, this approach looks impractical.

Despite the excellent capabilities of the AE systems for progressive monitoring in composite structures, there are several weaknesses also noted as detailed in the summary of the Chapter Three. The drawbacks are, as a result, of the conventional piezoelectric-based transducers for the use in the composite laminates. One of the major problem was the size of the PZT itself, whereby it has become

a significant concern if it is used in difficult access area. Not only that, PZT requires a good cabling to avoid the attenuation of signal strength. Low impedance cable and preamplifier is the regular solution especially for AE technique. However, for a monitoring which requires hundred of meters of access, the overall cost will significantly increase. Consequently, this leads to the proposed new generation sensors system which has the capability to be implanted into the structures without significantly affect its mechanical properties, while still maintaining the sensor's performance.

6.1.2 The development of the NIR-FBG dynamic sensor system

This newly developed NIR-FBG-dynamic-sensor-system is a new generation of sensing systems that are based on the optical sensor. With its significant advantages, especially in the contribution to smart structures development and long distance monitoring, the use of an optical-based sensing system will bring great potentials for future applications.

A dynamic measurement system based on FBG sensors has been developed in this Ph.D. study. Not only that, the FBG sensors used are from the NIR range. Therefore, this will allow the production of cheaper optical sensing systems, with a performance comparable to the systems based on conventional 1550 nm FBG sensors.

The validation studies for the NIR-FBG based system has been achieved up to a significant level, particularly for thin composite plate applications. The system is competitive and able to replace the piezoelectric based sensors. It has shown an excellent capability in capturing the propagation of waves, which were generated either from an external impact or vibration. Not only that, in one of the experiments performed, the NIR-FBG based systems was able to acquire the wave frequencies of up to 20 kHz (see Section 5.4.1). In the meantime, the NIR-FBG system also was found to have a better performance than the conventional FBG based system (1550 nm), in particular, with the fixed filter NIR-FBG system (see Section 5.5.1).

6.1.3 Implementation of the NIR-FBG system in SHM of thin composite structures

The success of implementing the NIR-FBG system for structural monitoring is among the significant achievement in this study. The case studies which were presented in Section 5.6 have shown that the NIR-FBG system is able to provide excellent and reliable results, particularly for composite thin laminates. It was found that, the system shows an ability that is equivalent to a piezoelectric sensor system particularly in the SHM of laminated composites. Yet from some angles, the NIR-FBG system has the significant advantages, such as ability to embedded into laminated structures, multiplexing, immune to electromagnetic disturbance and allowing a long cabling without significantly loosing the signal strength.

In the Section 5.6.1, the impact location case study has proved the excellent use of the NIR-FBG for SHM. In the experiments, the TOA technique was utilized to calculate the linear impact location. It was found that the method is able to give a consistent result, particularly with the help of wave velocity determination using Lamb's wave frequency equation and wavelet analysis. Not only that, the errors were relatively small, thus perfect to be used for global impact location monitoring with the fixed location of NIR-FBG sensors.

On the other hand, the wave mode determination case study has shown the ability of the NIR-FBG system in distinguishing two different wave modes (see Section 5.6.2). This is a new approach to be used in MAE analysis for composite failure characterization, whereby it eliminate the impractically of using the traditional piezoelectric sensor head although the PZT is capable to provide excellent result. Therefore, it has potential to replace the use of PZT in MAE for damage mode characterization in laminated composite plates.

6.2 Summary

In conclusion for this Ph.D. study, it appears that the NIR-FBG sensors for the use in wave propagation based SHM, has high potential for future development, especially towards achieving smart structures. For a global monitoring of composite structures, the use of this system has a significant superiority than the piezoelectric sensor system, particularly from the aspect of monitoring the external impact onto the structures, as well as performing measurements for dynamic analysis of the structures. Not to forget, the NIR-FBG based sensor system also has opened a space for the production of a cheaper system compared with the

conventional 1550 nm FBG based optical sensor system.

6.3 Further Work and Recommendations

Throughout this Ph.D. work, only one grating length (for FBG) was used, that is 10 mm. It was selected due to its availability and for simplicity of the study. However, for the future work, the effect of different grating lengths must be considered. Obviously, a variation of the grating length will give a different effect to the sensing performance of the sensor system; therefore, further investigation on the optimum grating length is required. However, it should be noted that, the more the grating length, the better the reflectivity as well as the sensitivity (Seo et al. 2009).

In the meantime, the NIR-FBG sensor system should be extended to more than two channels. With the use of four channels (or more), better applications can be performed, for example, locating an impact and mapping the damage in composite structures in two or three dimensions. It will require additionally optical components, especially the light source and photo detector. It is recommended for future use, to either add a light source (LED) or increase the power of the light source which later, can be divided for a few sensor systems. In addition, the use of an optical circulator is recommended instead of the optical coupler as it can give a better and higher power of the reflected light.

As mentioned in the introductory chapter, there are few more wave propagation based SHMs, such as the acousto-ultrasonic, ultrasonic testing and Lamb waves inspection. For future studies, the study of the NIR-FBG system applications should also be expanded into the other types of wave propagation based SHM. In this Ph.D. study, the selection of the AE technique is because it is a passive monitoring system; therefore, it narrowed the scope of the study to the sensing part only. However, passive monitoring system is only suitable for a global examination of composite structures. Therefore, it is important for the usage of NIR-FBG system to be further investigated in the active SHM techniques such as ultrasonic and acousto-ultrasonic inspection since they can provide more local and specific monitoring.

Finally, to enable the system to mature in SHM usage, its performance should be tested in actual applications. For instance, the system should be tested further on civil structures such as bridges and building cores. It is believed; the NIR-FBG system that has been developed is robust and able to provide effective monitoring of structural conditions and measuring its dynamic behaviour.

Last but not least, is the comparative cost study between the 1550 nm based optical sensor and NIR-FBG based sensors should be done in the next research. In this thesis, a well known reasons have been repeatedly stated, whereby the NIR-FBG system used cheaper silicon-based optical components such as the photo detectors. However, a detailed analysis should be included since it is also one of the main motivation for introducing the NIR-FBG, instead of using the common 1550 nm FBGs.

References

Abrate, S. (1998), *Impact on Composite Structures*, Cambridge University Press.

Alfaouri, M. & Daqrouq, K. (2008), 'Ecg signal denoising by wavelet transform thresholding', *American Journal of Applied Sciences* **5**(3), 276 281.

Altmann, J. (1996), 'Wavelet basics, wavelet tutorial : surfing the wavelets'. viewed 21 March 2013.

Arumugam, V., Shankar, R. N., Sridhar, B. & Stanley, A. J. (2010), 'Ultimate strength prediction of carbon/epoxy tensile specimens from acoustic emission data', *J. Mater. Sci. Technol.* **26**(8), 725–729.

ASTM-D3039/D3039M-08 (2008), 'Standard test method for tensile properties of polymer matrix composite materials'.

ASTM-E1067-01 (2001), 'Standard practice for acoustic emission examination of fiberglass reinforced plactic resin (frp) tanks/vessels'.

ASTM-E1316-13D (2013), 'Standard terminology for nondestructive examinations'.

Balageas, D. (2010), *Structural Health Monitoring*, ISTE, London, UK.

Barr, S. & Benzeggagh, M. L. (1994), 'On the use of acoustic emission to investigate damage mechanisms in glass-fibre-reinforced polypropylene', *Composites Science and Technology* **52**(3), 369376.

Beard, S. J., Kumar, A., Qing, X., Chan, H. L., Zhang, C. & Ooi, T. K. (2005), Practical issues in real-world implimentation of structural health monitoring systems, *in* 'Industrial & Commertial Application of Smart Structure Technologies', Vol. 5762, San Diego, California, USA, pp. 196–203.

Beukema, R. P. (2012), Embedding technologies of fbg sensors in composites: Technologies, applications and practical use, *in* '6th European Workshop on Structural Health Monitoring - Tu.4.C.4', Dresden, Germany.

Black, S. (2008), 'High-performance composites, structural health monitoring: Composites get smart', http://www.compositesworld.com/articles/structural-health-monitoring-composites-get-smart. Viewed September 16, 2013.

Bohse, J. (2000), 'Acoustic emission characteristics of micro-failure processes in polymer blends and composites', *Composites Science and Technology* **60**, 1213 – 1226.

Boix, M. & Cant, B. (2010), 'Wavelet transform application to the compression of images', *Mathematical and Computer Modelling* **52**, 1265–1270.

Boller, C. & Meyendorf, N. (2008), State-of-the-art in structural health monitoring for aeronatics, *in* 'Proceeding of International Symposium on NDT in Aerospace', Bavaria, Germany.

Brondsted, P., Lilholt, H. & Lystrup, A. (2005), 'Composite materials for win power turbine blades', *Annu. Rev. Mater. Res.* **35**, 505–538.

Brunner, A. J., Barbezat, M., Fleler, P. & Huber, C. (2004), 'Composites from piezoelectric fibres as sensors and emitters for acoustic applications', *J. Acoustic Emission* **22**, 127 – 137.

Campbell, F. C. (2010), *Structural composite materials*, ASM International.

Cao, W., Chen, X., Yang, X. & E. Wang, . (2003), 'Discrete wavelets transform for signal denoising in capillary electrophoresis with electrochemiluminescence detection', *Electrophoresis* **24**, 3124 3130.

Carlos, M. F. (2003), 'Acoustic emission: Heeding the warning sounds from materials', `http://www.astm.org/SNEWS/OCTOBER_2003/carlos_oct03.html`. viewed September 3, 2013.

Chen, B. L. & Shin, C. S. (2010), 'Fiber bragg gratings array for structural health monitoring', *Materials and Manufacturing Processes* **25**, 255–258.

Chow, W. W. & Koch, S. W. (1999), *Semiconductor - Laser Fundamentals: Physics of the Gain Materials*, Springer-Verlag Berlin Heidelberg.

Chui, C. K. (1992), *An introduction to wavelets*, Academic Press Professional, Inc, San Diego, CA, USA.

Ciang, C. C., Lee, J.-R. & Bang, H.-J. (2008), 'Structural health monitoring for a wind turbine system: a review of damage detection methods', *Measurement Science and Technology* **19**, 122001 (20pp).

Comanici, M., Chen, L., Kung, P. & Wang, L. (2011), Measurement of dynamic strain using a fiber bragg grating-based laser sensor system, *in* '2011 ICO International Conference on Information Photonics (IP)', pp. 1 –2.

Cusano, A., Cutolo, A., Nasser, J., Giordano, M. & Calabro, A. (2004), 'Dynamic strain measurements by fibre bragg grating sensor', *Sensors and Actuators A: Physical* **110**, 276–281.

Cvijetic, M. (2004), *Optical transmission systems engineering*, Artech House, Inc, 685 Canton Street, Norwood, MA 02062, USA.

Datta, S. K. & Shah, A. H. (2009), *Elastic Waves in Composite Media and Structures with Application to Ultrasonic Nondestructive Evaluation*, CRC Press Taylor & Francis Group.

Daubechies, I. (1990), 'The wavelet transform, time frequency localization and signal analysis', *IEEE Transactions on Information Theory* **36(5)**, 961–1005.

de Groot, P. J., Wijnen, P. A. M. & Janssen, R. B. F. (1995), 'Real-time frequency determination of acoustic emission for different fracture mechanisms in carbon/epoxy composites', *Composites Science and Technology* **55**, 405412.

Diamanti, K. & Soutis, C. (2010), 'Structural health monitoring techniques for aircraft composites structures', *Progress in Aerospace Sciences* **46**, 342–352.

Donoho, D. L. (1995), 'De-noising by soft-thresholding', *IEEE Transactions on Information Theory* **41**, 613 627.

Einde, L. V. D., Zhao, L. & Seible, F. (2003), 'Use of frp composites in civil structural applications', *Construction and Building Materials* **17**, 389–403.

Eitzen, D. G. & Wadley, H. N. G. (1984), 'Acoustic emission: Establishing the fundamentals', *Journal of Research of the National Bureau of Standards* **84**(1), 75–100.

Ergen, B. (2012), *Signal and Image Denoising Using Wavelet Transform, Advances in Wavelet Theory and Their Applications in Engineering, Physics and Technology*, InTech.

Frieden, J., Cugnoni, J., Botsis, J., Gmr, T. & oric, D. C. (2010), 'High-speed internal strain measurements in composite structures under dynamic load using embedded fbg sensors', *Composite Structures* **92**, 1905 1912.

Giurgiutiu, V. & Yu, L. (2003), Comparison of short-time fourier transform and wavelet transform of transient and tone burst wave propagation signals for structural health monitoring, *in* '4th International Workshop on Structural

Health Monitoring September 15-17,', Stanford University, Stanford, CA, USA.

Giurgiutiu, V. & Zagrai, A. N. (2002), 'Embedded self-sensing piezoelectric active sensors for on-line structural identification', *Journal of Vibration and Acoustics* **124**, 116 – 125.

Godin, N., Huguet, S., Gaertner, R. & Salmon, L. (2004), 'Clustering of acoustic emission signals collected during tensile tests on unidirectional glass/polyester composite using supervised and unsupervised classifiers', *NDT and E International* **37**, 253 264.

Gorman, M. R. & Prosser, W. H. (1991), 'Ae source orientation by plate wave analysis', *Journal of Acoustic Emission* **9(4)**, 283–288.

Graff, K. F. (1975), *Wave motion in elastic solids*, Courier Dover Publications.

Gutkin, R., Green, C. J., Vangrattanachai, S., Pinho, S. T., Robinson, P. & Curtis, P. T. (2011), 'On acoustic emission for failure investigation in cfrp: Pattern recognition and peak frequency analyses', *Mechanical Systems and Signal Processing* **25**, 1393 – 1407.

Hafizi, Z. M., Epaarachchi, J. & Lau, K. T. (2012), Modal analysis of high frequency acoustic signal approach for progressive failure monitoring in thin composite plates, *in* 'MPC 2012: 2nd Malaysian Postgraduate Conference', Gold Coast, Australia.

Hafizi, Z. M., Epaarachchi, J. & Lau, K. T. (2013), 'Modal acoustic emission investigation for progressive failure monitoring in thin composite plates under tensile test', *Key Engineering Materials* **558**, 65–75.

Hafizi, Z. M., Nizwan, J. E. C. K. E. & Lau, K. T. (2012), 'Non-velocity based analysis of passive ultrasonic signal for source location detection in composite plates: A pilot study', *IOP Conf. Series: Materials Science and Engineering* **36**, –.

Hamstad, M. A., r, A. O. & Gary, J. (2002), 'A wavelet transform applied to acoustic emission signals part 2: Source location', *Journal Acoustic Emission* **20**, 62–82.

Hansen, C. H. (1995), *Occupational exposure to noise: evaluation, prevention and control*, World Health Organization. pp. 23 - 52, viewed February 5, 2013.

Hollaway, L. C. (2010), 'A review of the present and future utilisation of frp composites in the civil infrastructure with reference to their important in-service properties.', *Construction and Building Materials* **24**, 2419–2445.

Huang, M., Jiang, L., Liaw, P. K., Brooks, C. R., Seeley, R. & Klarstrom, D. L. (1998), 'Using acoustic emission in fatigue and fracture materials research', *JOM* **50**(11), –.

Huguet, S., Godin, N., Gaertner, R., Salmon, L. & Villard, D. (2002), 'Use of acoustic emission to identify damage modes in glass fibre reinforced polyester', *Composites Science and Technology* **62**, 1433–1444.

Ismail, A. R. & Asfour, S. S. (1999), 'Discrete wavelet transform: a tool in smoothing kinematic data', *Journal of Biomechanics* **32**, 317 321.

Jalili, M. M., Pirayeshfar, A. S. & Mousavi, S. Y. (2010), Non-destructive acoustic test (ndat) to determine elastic modulus of polymeric composites, *in* 'Engineering Working Group on Acoustic Emission (EWGAE 2010)', Vienna, Austria.

Jeong, H. (2001), 'Analysis of plate wave propagation in anisotropic laminates using a wavelet transform', *NDT and E International* **34**, 185–190.

Jeong, H. & Jang, Y.-S. (2000), 'Wavelet analysis of plate wave propagation in composite laminates', *Composites Structures* **49**, 443–450.

Jian, Z. & Hong, Z. (2009), Matched fbg application research on dynamic sensing and demodulation, *in* 'Photonics and Optoelectronics, 2009. SOPO 2009. Symposium on', pp. 1–5.

Jiao, J., He, C., Wu, B., Fei, R. & Wang, X. (2004), 'Application of wavelet transform on modal acoustic emission source location in thin plates with one sensor', *International Journal of Pressure Vessels and Piping* **81**, 427431.

Jimenez, C. R. R., Papadakis, N., Reynolds, N., Gan, T. H., Purnell, P. & Pharaoh, M. (2004), 'Identification of failure modes in glass/polypropylene composites by means of the primary frequency content of the acoustic emission event', *Composites Science and Technology* **64**, 18191827.

Jing-Pin, J., Cun-Fu, H., Bin, W., Ren-Yuan, F. & Xiu-Yan, W. (2006), 'A new acoustic emission source location technique based on wavelet transform and mode analysis', *Front. Mech. Eng. China* **3**, 341?345.

Jingpin, J., Bin, W. & Cunfu, H. (2008), 'Acoustic emission source location methods using mode and frequency analysis', *Structural Control and Health Monitoring* **15**, 642651.

Johnson, M. (2002), 'Waveform based clustering and classification of ae transients in composite laminates using principal component analysis', *NDT and E International* **35**, 367–376.

Kahandawa, G. C. (2012), Monitoring Damage in Advance Composite Structures using Embedded Fibre Optic Sensors, PhD thesis, Faculty of Engineering and Surveying, University of Southern Queensland, University of Southern Queensland, Toowoomba QLD, 4350 Australia.

Kahandawa, G. C., Epaarachchi, J., Wang, H. & Lau, K. T. (2012), 'Use of fbg sensors for shm in aerospace structures', *Photonic Sensors* **2**(3), 203214.

Kashyap, R. (1999), *Fiber Bragg Gratings*, Vol. 1, San Diego: Acadamic Press.

Kessler, S. S., Spearing, S. M., Atalla, M. J., Cesnik, C. E. S. & Soutis, C. (2001), 'Structural health monitoring in composite materials using frequency response methods', *Proc. SPIE 4336, Nondestructive Evaluation of Materials and Composites V, 1* **-**, 1–11.

Kim, K.-S. (2004), 'Dynamic strain measurement with fiber bragg grating sensor system for smart structure', *Key Engineering Materials* **270-273**, 2114–2119.

Lacidogna, G., Manuello, A., Carpinteri, A., Durin, G., Niccolini, G., Schiavi, A. & Agosto, A. (2010), Acoustic and electromagnetic emissions related to stress-induced cracks, *in* e. a. B. H. Oh, ed., 'Fracture Mechanics of Concrete and Concrete Structures 7', Korea Concrete Institute, Seoul.

Lam, P.-M., Lau, K.-T., Ling, H.-Y., Su, Z. & Tam, H.-Y. (2009), 'Acousto-ultrasonic sensing for delaminated gfrp composites using an embedded fbg sensor', *Optics and Lasers in Engineering* **47**, 10491055.

Lamb, H. (1917), 'On waves in an elastic plate', *Proceedings of the Royal Society, Series A* **93**, 114–128.

Leaird, J. D. (1980), Acoustic emission as applied to rock & soil its history, basic theory and several case studies, *in* 'The 21st US Symposium on Rock Mechanics (USRMS)', Rolla, Missouri, U.S.A.

Lee, J.-R. & Tsuda, H. (2005), 'A novel fiber bragg grating acoustic emission sensor head for mechanical tests', *Scripta Materialia* **53**, 1181–1186.

Lempriere, B. M. (1968), 'Poisson's ratio in orthotropic materials', *AIAA Journal* **6**(11), 2226–2227.

Lin, J. (2001), 'Feature extraction of machine sound using wavelet and its application in fault diagnosis', *NDT and E International* **34**, 25–30.

Ling, H. Y., Lau, K. T., Cheng, L. & Jin, W. (2006), 'Viability of using an embedded fbg sensor in a composite structure for dynamic strain measurement.', *Measurement* **39**, 328334.

Ling, H.-Y., Lau, K. T., Jin, W. & Chan, K.-C. (2007), 'Characterization of dynamic strain measurement using reflection spectrum from a fiber bragg grating', *Optics Communications* **270**, 25–30.

Loman, M. (2012), 'Between acoustics and acoustic emission; a justification', http://asivr.ump.edu.my/. Viewed February 3, 2013.

Majumder, M., Gangopadhyay, T. K., Chakraborty, A. K., Dasgupta, K. & Bhattacharya, D. (2008), 'Fibre bragg gratings in structural health monitoring present status and applications', *Sensors and Actuators A: Physical* **147**, 150164.

Mandalgiri, P. D. (1999), 'Composite materials for aerospace applications', *Bulletin Materials Sciences* **3**, 657–664.

Marec, A., Thomas, J. H. & Guerjouma, R. E. (2008), 'Damage characterization of polymer-based composite materials: Multivariable analysis and wavelet transform for clustering acoustic emission data', *Mechanical Systems and Signal Processing* **22**, 1441–1464.

Miller, R. K. & v. K. Hill, E. (2005), *Nondestructive Testing Handbook: Acoustic Emission Testing*, Vol. 6, 3 edn, American Society for Nondestructive Testing Inc., USA.

Morscher, G. N. (1999), 'Modal acoustic emission of damage accumulation in a woven sic/sic composite', *Composites Science and Technology* **59**, 687– 697.

Muravin, B., Muravin, G. & Lezvinsky, L. (2010), The fundamentals of structural health monitoring by the acoustic emission method, *in* 'Proceedings of the 20th International Acoustic Emission Symposium', Kumamoto, Japan, pp. 253 – 258.

Nalley, D., Adamowski, J. & B. Khalil, . (2012), 'Using discrete wavelet transforms to analyze trends in streamflow and precipitation in quebec and ontario (19542008)', *Journal of Hydrology* **475**, 204228.

Orifici, A. C., Herszberg, I. & Thomson, R. S. (2008), 'Review of methodologies for composite material modeling incorporating failure', *Composite Structures* **86**, 194210.

Oskouei, A. R. & Ahmadi, M. (2008), Using wavelet transform to locate acoustic emission source in composite plate with one sensor., *in* 'Acoustics '08', Paris, France.

Oskouei, A. R., Ahmadi, M. & Hajikhani, M. (2009), 'Wavelet-based acoustic emission characterization of damage mechanism in composite materials under mode i delamination at different interfaces', *Express Polymer Letters* **3(12)**, 804–813.

Paget, C. A. & Levin, K. (1999), *Structural integrity of composites with embedded piezoelectric ceramic transducers*.

Panopoulou, A., T.Loutas, D.Roulias, S.Fransen & V.Kostopoulos (2011), 'Dynamic fiber bragg gratings based health monitoring system of composite aerospace structures', *Acta Astronautica* **69**, 445457.

Papannareddy, R. (1997), *Introduction to Lightwave Communication Systems*, Artech House, Inc.

Park, J.-M., Lee, S.-I., Kwon, O.-Y., Choi, H.-S. & Lee, J.-H. (2003), 'Comparison of nondestructive microfailure evaluation of fiber-optic bragg gratings and acoustic emission piezoelectric sensors using fragmentation test', *Composites: Part A* **34**, 203–216.

Paschotta, R. (2013*a*), 'Photodiodes', http://www.rp-photonics.com/photodiodes.html. Viewed 21 November 2013.

Paschotta, R. (2013*b*), 'Superluminescent diodes', http://www.rp-photonics.com/superluminescent˙diodes.html. Viewed 21 November 2013.

Perez, I. M., Cui, H. & Udd, E. (2001), Acoustic emission detection using fiber bragg gratings, *in* 'Smart Structures and Materials 2001: Sensory Phenomena and Measurement Instrumentation for Smart Structures and Materials', Vol. 4328, Newport Beach, CA.

Prosser, W. H. (1991), The propagation characteristic of the plate modes of acoustic emission waves in thin aluminium plates and this graphite/epoxy composite plates and tubes, PhD thesis, The Johns Hopkins University.

Prosser, W. H. & Gorman, M. R. (1994), 'Plate mode velocities in graphite/epoxy plates', *Journal of the Acoustical Society of America* **96**, 902–907.

Prosser, W. H., Gorman, M. R. & Dorighi, J. (1992), 'Extensional and flexural waves in a thin-walled graphite/epoxy tube', *Journal of Composite Materials* **26(14)**, 418–427.

Prosser, W. H., Jackson, K. E., Kellas, S., Smith, B. T., McKeon, J. & Friedman, A. (1995), 'Advance waveform based acoustic emission detection of matrix cracking in composites', *Materials Evaluation* **53 (9)**, 1052 – 1058.

Qi, G. (2000), 'Wavelet - based ae characterization of composite materials', *NDT & EInternational* **33**, 133144.

Rajadurai, J. S., Christopher, T., Thanigaiyarasu, G. & Rao, B. N. (2008), 'Finite element analysiswith an improved failure criterion for composite wind turbine blades', *Forsch Ingenieurwes* **72**, 193207.

Rao, Y. J. (1999), 'Recent progress in applications of in-fibre bragg grating sensors', *Optics and Lasers in Engineering* **31**, 297324.

Reddy, J. N. (2004), *Mechanics of Laminated Composite Plates and Shells*, second edn, CRC Press.

Reifsnider, K. (1998), *Handbook of Composites*, 2 edn, Chapman & Hall.

Rhee, S. H., Lee, J. K. & Lee, J. J. (2007), 'The group velocity variation of lamb wave in fiber reinforced composite plate', *Ultrasonics* **47**, 5563.

Schiavi, A., Niccolini, G., Tarizzo, P., Carpinteri, A., Lacidogna, G. & Manuello, A. (2011), 'Acoustic emission at high and low frequencies during compression tests in brittle materials', *An International Journal for Experimental Mechanics* **47**(2), 105 – 110.

Scholey, J. J., Wilcox, P. D., Lee, C. K., Friswell, M. I. & Wisnom, M. R. (2006), 'Acoustic emission in wide specimens', *Advanced Materials Research* **13-14**, 325–332.

Scholey, J. J., Wilcox, P. D., Wisnom, M. R. & Friswell, M. I. (2009), 'A practical technique for quantifying the performance of acoustic emission systems on plate-like structures', *Ultrasonics* **49**, 538–548.

Scholey, J. J., Wilcox, P. D., Wisnom, M. R. & Friswell, M. I. (2010), 'Quantitative experimental measurements of matrix cracking and delamination using acoustic emission', *Composites: Part A* **41**, 612 – 623.

Semmlow, J. L. (2005), *Circuits, Systems and Signals for Bioengineers: A Matlab-Based Introduction*, Elsevier Inc.

Seo, D.-C., Yoon, D.-J., Kwon, I.-B. & Lee, S.-S. (2009), Sensitivity enhancement of fiber optic fbg sensor for acoustic emission, *in* 'Nondestructive Characterization for Composite Materials, Aerospace Engineering, Civil Infrastructure, and Homeland Security', San Diego, California.

Shull, P. J. & Tittmann, B. R. (2002), *Nondestructive Evaluation: Theory, Techniques and Applications*, Vol. 3 (Ultrasound), Marcel Dekker Inc., 270 Madison Avenue, New York, NY 10016.

Simonovski, I. & Boltezar, M. (2003), 'The norms and variances of the gabor, morlet and general harmonic wavelet fiunctions', *Journal of Sound and Vibration* **264**, 545–557.

Staszewski, W. J., Mahzan, S. & Traynor, R. (2009), 'Health monitoring of aerospace composite structures - active and passive approach', *Composites Science and Technology* **69**, 1678–1685.

Su, Z. & Ye, L. (2008), *Delamination behaviour of composites*, Woodhead Publishing Limited and CRC Press.

Su, Z. & Ye, L. (2009), *Identification of Damage Using Lamb Waves: From Fundamentals to Applications: Volume 48 of Lecture notes in applied and computational mechanics*, Springer-Verlag Berlin Heidelberg.

Surgeon, M. & Wevers, M. (1999), 'Modal analysis of acoustic emission signals from cfrp laminates', *NDT and E International* **32**, 311322.

Takeda, N., Okabe, Y., Kuwahara, J., Kojima, S. & Ogisu, T. (2005), 'Development of smart composite structures with small-diameter fiber bragg grating sensors for damage detection: Quantitative evaluation of delamination length in cfrp laminates using lamb wave sensing', *Composites Science and Technology* **65**, 25752587.

Tsai, S. J. S. (2002), Power transformer partial discharge (pd) acoustic signal detection using fiber sensors and wavelet analysis, modeling, and simulation, Master's thesis, Virginia Polytechnic Institute and State University, USA.

Tsuda, H. (2006), 'Ultrasound and damage detection in cfrp using fiber bragg grating sensors', *Composites Science and Technology* **66**, 676–683.

Tsuda, H., Toyama, N., Urabe, K. & J. Takatsubo, , . (2004), 'Impact damage detection in cfrp using fiber bragg gratings', *Smart Mater Struct* **13**(4), 719724.

Vasilescu, G. (2005), *Electronic Noise and Interfering Signals: Principles and Applications*, Springer-Verlag Berlin Heidelberg New York.

Wang, H. & Zou, L. (2013), 'Interfacial effect on the electromechanical behaviors of piezoelectric/elastic composite smart beams', *Journal of Intelligent Material Systems and Structures* **24**(4), 421 – 430.

Wang, L. & Yuan, F. G. (2007), Lamb wave propagation in composite laminates using a higher-order plate theory, *in* 'SPIE Proceedings Vol. 6531: Nondestructive Characterization for Composite Materials, Aerospace Engineering, Civil Infrastructure, and Homeland Security'.

Wilcox, P. D. (1998), lamb wave inspection of large structures using permanently attached transducers, PhD thesis, Imperial College of Science, Technology and Medicine.

Wilcox, P. D., Lee, C. K., Scholey, J. J., Friswell, M. I., Wisnom, M. R. & Drinkwater, B. W. (2006), *Quantitative structural health monitoring using acoustic emission*.

Wild, G. & Hinckley, S. (2007), Fiber bragg grating sensors for acoustic emission and transmission detection applied to robotic nde in structural health monitoring, *in* 'Proceedings of IEEE sensors applications symposium', IEEE, San Diego, California, USA, pp. 1–6.

Wild, G. & Hinckley, S. (2010), Optical fibre bragg gratings for acoustic sensors, *in* 'Proceeding of 20th International Congress on Acoustics (ICA 2010)', Sydney, Australia.

Wu, F. & Chang, F. K. (2006), 'Debond detection using embedded piezoelectric elements in reinforced concrete structures part i: Experiment', *Structural Health Monitoring* **5**(1), 5 – 15.

Yan, Y. & Yam, L. (2002), 'Online detection of crack damage in composite plates using embedded piezoelectric actuators/sensors and wavelet analysis', *Composite Structures* **58**(1), 29 – 38.

Ziola, S. M. (1991), Source Location in thin plates using crosscorrelation, PhD thesis, Naval Postgraduate School, Monterey, CA 93943-5000.

Zou, H., Liang, D. & Zeng, J. (2012), 'Dynamic strain measurement using two wavelength-matched fiber bragg grating sensors interrogated by a cascaded long-period fiber grating', *Optics and Lasers in Engineering* **50**(2), 199 – 203.

Appendix A

Some Supporting Information

Table A.1: Important terminology to composite materials.

Term	Definition
Isotropic	The mechanical properties are same in all directions.
Laminate	A material consisting of many layers bonded together.
Quasi-isotropic	One plane having the same mechanical properties at any direction in that plane. For instance, a laminate will have the same stress-strain behaviour at any direction in the plane of the material. Also can be called transversely isotropic.
Orthotropic	A material that has different mechanical properties in three mutually perpendicular planes. The properties of the material are direction dependent.
Homogenous	Material properties do not change within any points in the material. Laminated composites may be generalized as homogenous but in reality all composites are heterogenous.
Symmetric laminate	The plies of the laminate are a mirror image at the midplane.

Table A.2: Engineering constant for several materials - part 1 (Reddy 2004).

Materials	E_1(MPa)	E_2(MPa)	G_{12}(MPa)	G_{13}(MPa)	G_{23}(MPa)
Aluminium	73,084	73,084	23,304	23,304	23,304
Copper	124,106	124,106	44,058	44,058	44,058
Steel	206,843	206,843	77,497	77,497	77,497
Graphite-epoxy (AS/3501)	137,895	8,963	7,102	7,102	6,205
Graphite-epoxy (T300/934)	131,000	10,342	6,895	6,205	6,205
Glass-epoxy (1)	53,779	17,926	8,963	8,963	3,447
Glass-epoxy (2)	38,610	8,274	4,137	4,137	3,447
Boron-epoxy	206,843	20,684	6,895	6,895	4,137

Table A.3: Engineering constant for several materials - part 2 (Reddy 2004).

Materials	E_3(MPa)	G_{23}(MPa)	ν_{12}	ν_{13}	ν_{23}
Aluminium	73,084	23,304	0.33	0.33	0.33
Copper	124,106	44,058	0.33	0.33	0.33
Steel	206,843	77,497	0.29	0.29	0.29
Graphite-epoxy (AS/3501)	8,963	6,205	0.30	0.30	0.49
Graphite-epoxy (T300/934)	10,342	6,205	0.22	0.22	0.49
Glass-epoxy (1)	17,926	3,447	0.25	0.25	0.34
Glass-epoxy (2)	8,963	3,447	0.26	0.26	0.34
Boron-epoxy	20,684	4,137	0.30	0.25	0.25

Appendix B

Some Supporting Information

Figures B.1 - B.3 are next three results from matrix cracks that produced during case study in chapter 3 (section 3.6). Meanwhile Figure B.4 show the result from fiber breakage.

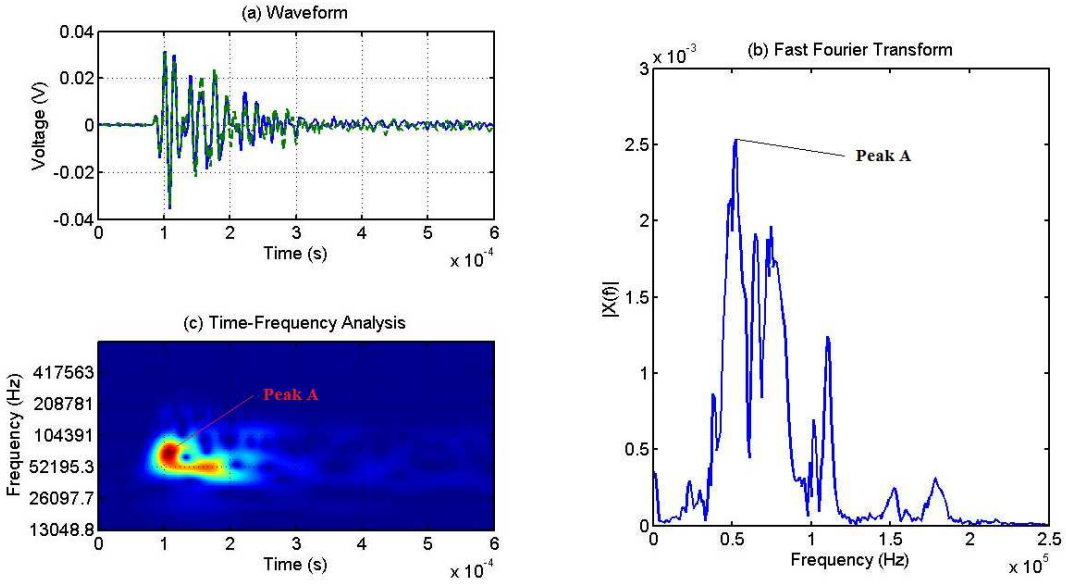

Figure B.1: AE signal from matrix crack; second data.

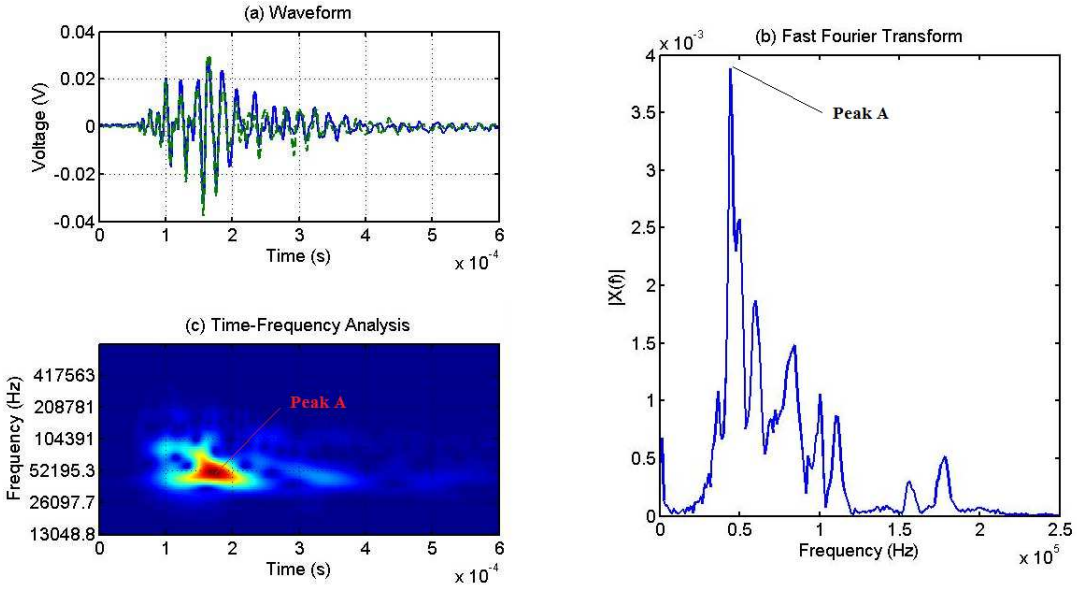

Figure B.2: AE signal from matrix crack; third data.

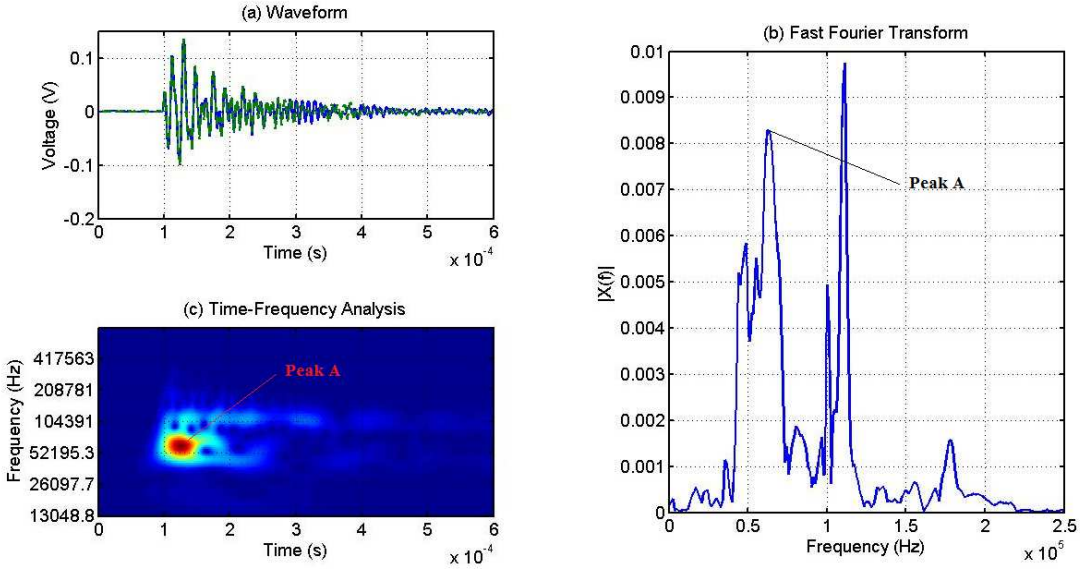

Figure B.3: AE signal from matrix crack; fourth data.

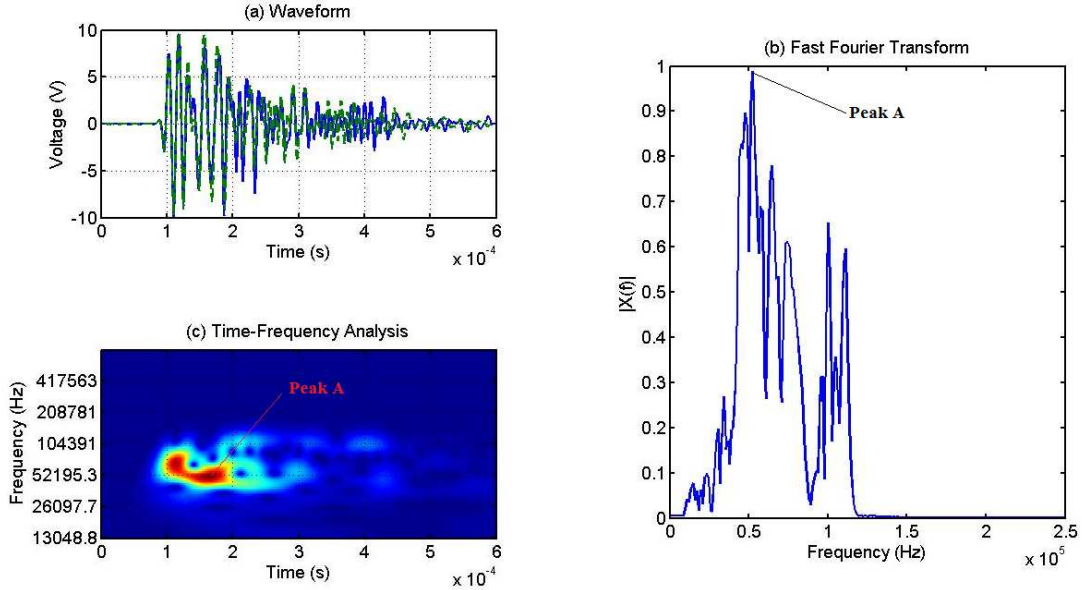

Figure B.4: AE signal from fiber breakage.